Long range order in 3D nanoparticle assemblies

Elisabeth Josten

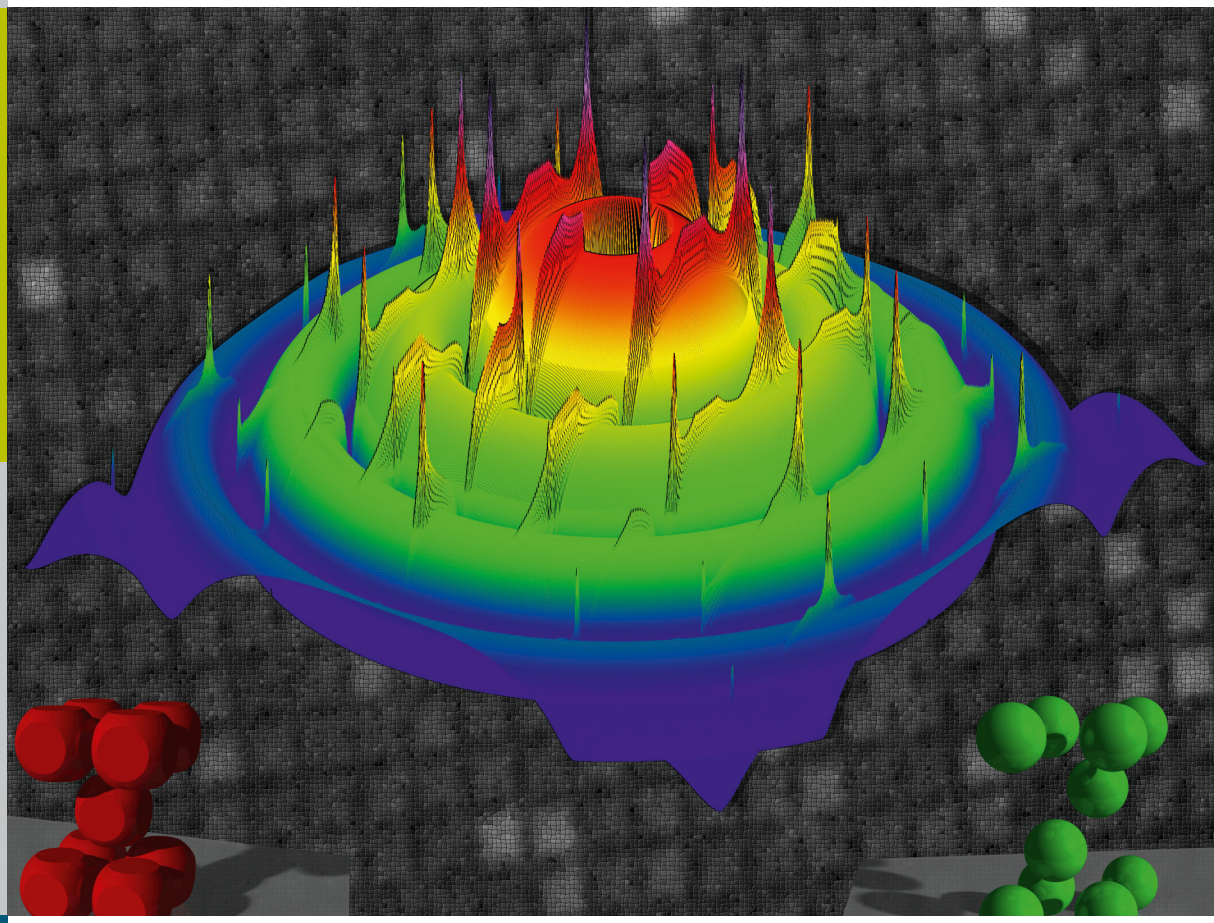

Member of the Helmholtz Association

Schlüsseltechnologien / Key Technologies
Band / Volume 111
ISBN 978-3-95806-087-6

JÜLICH FORSCHUNGSZENTRUM

Schriften des Forschungszentrums Jülich
Reihe Schlüsseltechnologien / Key Technologies Band / Volume 111

Forschungszentrum Jülich GmbH
Peter Grünberg Institute (PGI)
Scattering Methods (PGI-4 / JCNS-2)

Long range order in 3D nanoparticle assemblies

Elisabeth Josten

Schriften des Forschungszentrums Jülich
Reihe Schlüsseltechnologien / Key Technologies Band / Volume 111

ISSN 1866-1807 ISBN 978-3-95806-087-6

Bibliographic information published by the Deutsche Nationalbibliothek.
The Deutsche Nationalbibliothek lists this publication in the Deutsche Nationalbibliografie; detailed bibliographic data are available in the Internet at http://dnb.d-nb.de.

Publisher and Distributor: Forschungszentrum Jülich GmbH
Zentralbibliothek
52425 Jülich
Tel: +49 2461 61-5368
Fax: +49 2461 61-6103
Email: zb-publikation@fz-juelich.de
www.fz-juelich.de/zb

Cover Design: Grafische Medien, Forschungszentrum Jülich GmbH

Printer: Grafische Medien, Forschungszentrum Jülich GmbH

Schriften des Forschungszentrums Jülich
Reihe Schlüsseltechnologien / Key Technologies, Band / Volume 111

D 82 (Diss. RWTH Aachen University, 2014)

ISSN 1866-1807
ISBN 978-3-95806-087-6

The complete volume is freely available on the Internet on the Jülicher Open Access Server (JuSER) at www.fz-juelich.de/zb/openaccess.

Long range order in 3D nanoparticle assemblies

Abstract

Magnetic nanoparticles and their assembly in highly correlated structures are of great interest for future applications as e.g. spin-based data storage. These systems are not only distinguished by the obvious miniaturization but by the novel physical properties emerging due to their limited size and ordered arrangement, as well. The superstructures are formed from nanometer sized building blocks, ordered like atoms in a crystal, which renders them a new class of materials. To gain a profound understanding of these systems it is necessary to perform experiments on all length scales.

The present work supplies an extensive and novel contribution to the investigation of the structural properties and the self-assembly of iron oxide nanoparticle superstructures. The unique combination of microscopy and scattering techniques allows a new understanding of the structural features of three dimensional structures that develop from the self-organization of these particles.

In this thesis, magnetic nanoparticles have been deposited for this purpose using a self organization method to form long range ordered structures, so called mesocrystals. The process of self-assembling has been investigated for the influence of different deposition parameters and these parameters have been optimized. An in-situ study using grazing incidence x-ray scattering during the growth of the mesocrystals allowed the identification of different stages of the mesocrystal growth and its spatial position. From the combination of these different experiments it was possible to establish a model for the growth process governed by a shape and size selective arrangement of the particles.

Another highlight of this work is the measurement on a single mesocrystal, which had only a volume of $2.5\,\mu m^3$, leading to a challenging diffraction experiment. It was possible to extract structural quality parameters from this investigation, as e.g. the mosaicity, which would normally be masked by the distribution of the orientation and lattice parameters generally present in the normal samples that contain a large number of mesocrystals.

A detailed analysis of the scattering patterns of different samples with mesocrystal ensembles yielded a refined structure model, which allowed the quantitative analysis of the data collected as well for in-situ created as for already deposited samples. In addition, a new rounded cubes form factor was developed for the modeling of small angle x-ray scattering and the single mesocrystal diffraction data.

In conclusion, this work shows the large correlation in these nanoparticle superstructures, the distribution of different structural parameters that can be present in the samples and how much information can be extracted from the scattering patterns.

Langreichweitige Ordnung in 3D Nanopartikelüberstrukturen

Zusammenfassung

Magnetische Nanopartikel und ihre Anordnungen in hochkorrelierten Strukturen sind von großem Interesse für zukünftige Anwendungen wie z.B. in der Spin-basierten Datenspeicherung. Nicht nur die durch sie ermöglichte Miniaturisierung, sondern auch die durch ihre endliche Größe und Anordnung hergerufenen neuartigen physikalischen Eigenschaften der Partikel zeichnen diese Systeme aus. Solche Nanopartikelüberstrukturen mit ihren Nanometer großen Bausteinen sind eine neue Klasse von Materialen, welche sich wie Atome in einem Kristall ordnen. Um ein grundlegendes Verständnis zu erhalten, müssen Experimente auf allen Längenskalen durchgeführt werden.

Die vorliegende Arbeit leistet einen umfassenden und neuartigen Beitrag zur Erforschung der Selbstanordnung und der strukturellen Eigenschaften von Eisenoxid Nanopartikelüberstrukturen. Die Kombination von Mikroskopie und Streuexperimenten ermöglicht ein neues Verständnis der strukturellen Eigenschaften der dreidimensionalen Nanopartikelanordnung, welche sich aus der Selbstorganisation dieser Nanopartikel enwickeln.

In dieser Dissertation wurden hierzu magnetische Nanopartikel mittels Selbstorganisation langreichweitig in sogenannten Mesokristallen geordnet, dieser Prozess auf den Einfluss von diversen Depositionsparametern hin untersucht und diese Parameter optimiert. Eine in-situ Studie mit Röntgenstreuung unter streifendem Einfall während des Wachstumsprozess der Mesokristalle ermöglichte die Eingrenzung des Ortes und die Identifizierung verschiedener Phasen des mesokristallinen Wachstums. Die Kombination dieser verschiedenen Untersuchungen erlaubte es ein Modell des Wachstums aufzustellen und in diesem Zuge eine form- und größenselektive Selbstanordnung als Ursache des mesokristallinen Wachstums zu identifizieren.

Einen weiteren Höhepunkt der Arbeit stellt die Untersuchung eines einzelnen Mesokritalls dar, welcher durch sein Volumen von nur $2.5\,\mu m^3$ das durchgeführte Diffraktionsexperiment zu einer großen Herausforderung machte. Hier konnten Parameter der strukturellen Qualität, wie z.B. die Mosaizität, ohne den störenden Einfluss von Richtungs- und Gitterkonstantenverteilungen extrahiert werden, wie sie in den sonst untersuchten Proben mit Ansammlungen von sehr vielen Mesokristallen zu finden waren .

Eine neu entwickelte detaillierte Analyse von Streubildern des Ensembles führte zu einem neuen, verfeinerten Strukturmodell, welches zur quantitativen Untersuchung der in-situ hergestellten und auch der bereits deponierten Proben herangezogen wurde. Weiterhin wurde ein neuer, abgerundeter kubischer Form Faktor vorgestellt, der für die Modellierung abgeschnittener Würfel sowohl für Röntgenkleinwinkelstreuung als auch in der Streuung an einem einzelnem Mesokristall verwendet wurde.

Zusammenfassend zeigt diese Arbeit, wie hoch korreliert die einzelnen Nanopartikelüberstrukturen sind, welche Verteilung die strukturellen Parameter auf den Proben haben können und wie viele Informationen aus den komplexen Streubildern gewonnen werden können.

Contents

Chapter 1

Introduction

Two thousand years ago in Greece, lodestone was discovered, a naturally occurring magnetized mineral known today as magnetite [1]. This finding marked the beginning of a new scientific era: the research on magnetism. Mankind's curiosity to comprehend, explain and make use of this phenomenon had been piqued. Today, the optimization and further development of products based on magnetism is still a field of immense interest to science and technology. An example, taken from the last few decades of research, of the application of magnetism in daily life is the giant magnetoresistance (GMR) effect used in today's hard disc drives. This phenomenon was observed independently by Peter Grünberg and Albert Fert in 1988, who were awarded with the Nobel Prize in Physics in 2007 for their work in this area [18, 23]. The application of this effect allows the construction of smaller magnetic field sensors with higher sensitivity. These sensors have successfully been implemented as read heads in hard disks with highly increased data density. The effect utilizes the change of resistance depending on the relative alignment of the magnetization inside two ferromagnetic layers, which are separated by a non-magnetic layer.

Fundamental research on magnetic nanostructures is an important part of the current scientific efforts in spin-based information technology [63]. The goal is to reach a higher readout rate and also an increase of the bit density in data storage, which continuously requires miniaturization. Self-assembled structures of nanocrystals are promising candidates for a new generation of magnetic storage media [43], in which a single particle represents one information unit. To build even higher density magnetic storage devices in the future using the approach of today's standard devices of a two-dimensional media, would require that ferromagnetic single domain nanoparticles, magnetically decoupled, order perfectly on a two-dimensional lattice. The process of such self-organization is a relevant scientific question, which becomes even more interesting and more challenging to investigate when it involves three dimensions. For applications, the magnetic properties of the nanoparticles and the correlations inside their lattice play a significant role, as neighbouring bits should not influence each other.

In addition to novel optical and electronic properties found in nanoscale materials these particles exhibit exciting magnetic characteristics induced by the increased surface-to-volume ratio. Below a critical particle size, which is material-specific (e.g. a diameter of 15 nm for Fe, 35 nm for Co and 30 nm for γ-Fe_2O_3 [20]), the development of domain walls is energetically unfavorable and the nanoparticles consist of only a single magnetic domain. Another important property of these particles is superparamagnetism caused by the instability of the magnetization due to thermal excitations [20]. Furthermore, many nanoparticles possess the capacity to assemble into long-range ordered structures, organizing spontaneously in superstructures without external intervention [94]. Inside such an assembly, where the particles are separated by an organic

shell, the long-ranged dipole-dipole interaction is expected to be the only magnetic interaction as the direct electronic exchange interaction between them through the ligand shell is negligible [20].

In order to reach further miniaturization for data storage and avoid greater loss of information, the superparamagntic limit must be overcome. This can be achieved, for example, using larger magnetic anisotropies; the dipole influences of neighbouring particles must be limited and the self-assembling process must be reliable. Success was first achieved by Sun et al., who prepared ferromagnetic nanoparticle superstructures, which can be used as small nanomagnets to store information [89]. Further possible applications of these systems are magnetic field sensors with superparamagnetic nanoparticle assemblies reaching high sensitivities with extremely small sensing volumes. Applications in other scientific fields are possible e.g. in biology and medicine, in terms of treatment for hyperthermia, drug-delivery and cancer treatment. Research in the field of nanoparticles has increased in the last few decades with advances in nanoparticle synthesis and new possibilities for its investigation. Intensive research on the magnetic properties of single particles as well as nanoparticle clusters and the process of self-assembly is necessary for all these applications.

The investigation of the phenomenon of self-assembly and the resulting nanoparticle superstructures has opened up a new field in science. Not only have nanoparticles been identified as a novel type of material with special properties, but nanoparticle superstructures are mow recognized as a new class of ordered systems, where the particles order in a similar way to atoms in a solid. Nanoparticle superspins (single domain magnetic moments) correspond to atomic spins and the nanoparticle superlattices (or supercrystals, mesocrystals,..) are the analogous to crystals. S.C. Glotzer and M.J. Solomon pointed out the importance of these systems by commenting "These new particles are poised to become the ‘atoms’ and ‘molecules’ of tomorrow’s materials" [46]. The novelty of the new systems is the nm dimension of the building blocks that raises many new questions and high hopes for new scientific findings of new properties and possible applications.

To acquire insights into the basic physics in these systems, experiments on all length scales must be performed. This dissertation aims at contributing to the comprehension of self-assembly and the structural properties of γ-Fe_2O_3 nanoparticle ensembles, using the combination of a variety of advanced microscopy and scattering methods. Complex scattering experiments were performed yielding new and fascinating insights, adding more and more aspects to the understanding of the subject. With these methods the structural properties of the nanoparticle superstructure could be investigated three dimensional and depth resolved over a large area of the sample.

For the experiments in this thesis, well known γ-Fe_2O_3 particles were used, which have a sizable magnetization, can be reproduced at high quality [14, 15] and which have already been investigated in terms of their atomic structural and magnetic properties [33, 34, 103]. Furthermore it was known that these particles could be grown in ensembles of 3D superstructures, called mesocrystals [33, 35]. These known characteristics are the basic requirements for advanced experiments on nanoparticle superstructures and thus for this dissertation. Iron oxide particles are used to guarantee a stable system, as these are relatively insensitive to oxygen and moisture from the environment and permit an easy sample handling.

One goal of this PhD thesis is to understand and control the process of self assembly in more detail. Thus the influence of different preparation parameters on the mesocrystals characteristics is

investigated and the feasibility of tuning the ensemble of grown mesocrystals using external parameters such as particle shape, magnetic field and evaporation time is shown. An optimization of the sample preparation was realized. Conditions have been identified under which the process of self-assembly leads to shape-selective self-segregation during the drying of the droplet and this result is the first direct observation of well-separated 3D ordered structures within one sample. Using an extreme magnetic field configuration, a nanoparticle macro-polycrystal in the mm-range was grown for the first time. All these experiments undertaken to achieve a profound understanding and optimization of the ensemble of mesocrystals can be found in **chapter 4**.

An in-situ GISAXS study during the drying process was carried out to gain a deeper understanding of the process of time-dependent self-assembly (**chapter 6**). To carry out this experiment, a specialized in-situ cell with several extra components was built to ensure precise control of the system and the possibility of an accurate identification of key influences. Therefore new insights into the drying and self-assembly process of an ensemble of 3D highly ordered assemblies were gained and four stages of the mesocrystals growth could be identified.

A highlight of this work is the diffraction experiment on a separated single mesocrystal (**chapter 7**). With the outstanding intensity and precision of state-of-the-art synchrotron beamlines it is possible to push the already established limits in diffraction from Å-size [39, 57, 78, 79] and nm-size unit cells [62, 97] further to 10 nm large building blocks with samples of only 2.5 μm^3 scattering volume. So far, the smallest crystals investigated in the atomic structure are reported to have a volume in the 10^3 μm^3 range [16, 17, 48]. The achievable data quality is, as expected, not yet comparable to conventional single crystal XRD. Nevertheless a lot of new information could be gained complementary to GISAXS on a 2D powder of mesocrystals. A quantitative structural analysis of a single mesocrystal was performed, revealing the mosaicity in the range of good atomic crystals, extracting the lattice constant and size distribution inside one mesocrystal. This challenging experiment proved the feasibility of the investigation of single, small mesocrystals of nanoparticles and opened a new field for further investigations of mesocrystal properties.

For a more detailed analysis of the scattering patterns a new structure model was developed to interpret the time-resolved in-situ as well as the post deposition GISAXS and the single mesocrystal diffraction images (**chapter 5**). With the help of the new model, more features of the scattering patterns could be interpreted and a new insight in the system was gained. Furthermore the cubic form-factor was refined, which describes the integrated intensities of the single mesocrystal as well as the SAXS measurements.

Finally, all conclusions from these experiments were included in a first approach to model the process of self-assembly of an ensemble of mesocrystals with magnetic nanoparticles (**chapter 4**).

In this PhD thesis, it was possible with the combined effort of these various experiments to find the optimal deposition conditions to produce high-quality nanoparticle superstructures. The resulting structures have been characterized in more detail than has been done before, revealing for example a clear distinction between single mesocrystal and ensemble variations of structural parameters. A four-stage process self-organization could be identified and explained using a detailed model.

Chapter 2

Theoretical Background

This chapter gives an overview over the physics that governs nanoparticles in general and that is needed to understand the experiments performed in this work. For most of the subjects described in the following sections, a variety of literature exists which describes the theory in more detail. The literature used is referenced in the according paragraphs.

2.1 Properties of magnetic nanoparticles

The nanoparticles that have been used for our investigations are microscopic single crystals exhibiting special characteristics not present or notable in macroscopic materials. It is crucial to know the physics behind these effects especially for the understanding of self-assembly and magnetic interactions.

2.1.1 Brownian motion

When particles reside in a liquid the thermal motion of the liquids molecules leads to a random motion of the particles first observed by Robert Brown in 1827 on pollen grains and explained by Einstein in 1905 [40]. The motion of the particles follows the diffusion equation $\frac{\partial f}{\partial t} = D\frac{\partial^2 f}{\partial x^2}$. The diffusion coefficient of this motion is a function of the liquids viscosity, the absolute temperature and the particle size as given by [40]:

$$D = \frac{R}{6\pi N_A}\frac{T}{\eta \cdot r_{NP}} \tag{2.1}$$

where r_{NP} is the particle radius, η the friction coefficient, R the ideal gas constant, N_A the Avogadro constant and T the temperature. Obviously, larger particles will move slower and increasing temperature will speed up the motion.

The diffusion equation can be used to derive the average displacement of a particle after a given time to be [40]:

$$\langle \Delta \mathrm{x} \rangle = \sqrt{2Dt} = \sqrt{\frac{R}{3\pi N_A}\frac{T \cdot t}{\eta \cdot r_{NP}}} \tag{2.2}$$

This result is of crucial importance for the self organization process described in **section 4.2.2** as it limits the possibility for particles to find suitable vacancies in a given time.

2.1.2 Magnetic single-domain nanoparticles

Below a critical size of ferromagnetic particles, the development of domain walls is energetically unfavorable and the nanoparticles consist of only a single magnetic domain. The critical radius r_c, which is material-specific, is given by [2, 20]:

$$r_c \approx 9\frac{\sqrt{\mathrm{AK}}}{\mu_0 M_s^2} \tag{2.3}$$

with μ_0 the vacuum permeability and M_s the saturation magnetization. K is the anisotropy constant, the energy density needed to rotate the magnetic moment away from a single easy axis, which is a result of the spin-orbit interaction of the electrons in the crystal lattice. A is the exchange constant, which is a characteristic figure of a ferromagnetic material proportional to the microscopic exchange constant J and the quantity characterizing the strength of the exchange coupling. Together, both effects determine the energy needed for the formation of domain walls and thus the maximal size of a single domain particle. Example values for the critical radius are 15 nm for Fe, 35 nm for Co and 30 nm for γ-Fe_2O_3 [20].

2.1.3 Superparamagnetism

Thermal fluctuations can flip the magnetic moment of magnetic materials when their size is reduced as the thermal energy gets in the order of magnitude of the magnetic anisotropy, which is responsible for keeping the magnetic moment aligned in a specific direction. This is typically the case for single domain nanoparticles, as investigated in this dissertation at room temperature. An important measure for this effect is the Néel relaxation time τ_N (eqn. 2.4) [2, 8, 12, 20, 66], which describes the average time between two flips and depends on the particle volume V, the anisotropy constant K, the characteristic attempt time τ_0 of the material and the temperature T. When measuring the magnetic moment of a sample of such particles, this effect leads to paramagnetic like behavior described by the Langevin function L(x) (eqn. 2.5) [2, 8, 20] above the so called blocking temperature T_B (eqn. 2.6) [2, 8, 20]. In this case the magnetic moment is constantly flipped by thermal fluctuations so that no macroscopic magnetization can be measured without applying an external magnetic field. In this connection N_{NP} is the number of particles, m the magnetic moment of each particle and H the external applied field. This magnetic state is called superparamagnetism.

$$\tau_N = \tau_0 \exp\left(\frac{KV}{k_B T}\right) \tag{2.4}$$

$$M(H) \approx N_{NP} \cdot m \cdot \mathrm{L}\left(\frac{\mu_0 H m}{k_B T}\right) \quad \text{with} \quad \mathrm{L(x)} = \coth(\mathrm{x}) - \frac{1}{\mathrm{x}}, \quad \text{for} \quad k_B T \gg KV \tag{2.5}$$

$$T_B = \frac{KV}{k_B \ln\left(\frac{\tau_m}{\tau_0}\right)} \tag{2.6}$$

Below the blocking temperature a ferromagnetic hysteresis of the macroscopic magnetic moment can be measured, which can be calculated by the Stoner Wohlfarth model [2, 8, 20, 87]. As the magnetic moments flip with the Néel relaxation time, the blocking temperature measured depends on the time scale of the experiment τ_m. If the timescale for the relaxation time τ_N is bigger than the experimental measuring time the system appears to be static (or so called blocked).

2.1.4 Interactions between nanoparticles

The process of self-assembly is governed by the interaction of different attractive and repulsive forces. The main influences on our system will be introduced in this section.

2.1.4.1 Van der Waals interaction

As is possible for any molecule and bound or unbound atom, quantum fluctuation induced arbitrary electric dipole moments of nanoparticle surface atoms can induce electron displacement of another particles atoms leading to a dipole-dipole attraction of both particles, which drops with r^{-6} on the atomic level, where r is the distance between the atoms/molecules. An approximation for the "macroscopic" van der Waals interaction between objects consisting of many atoms/molecules is a pairwise summation of all molecular interactions inside the macroscopic bodies in dependence on their shape [24]. For example, the van der Waals potential for spherical particles with radii $\mathrm{r_{NP_1}}$ and $\mathrm{r_{NP_2}}$ in a center to center distance $r = \mathrm{r_{NP_1}} + \mathrm{r_{NP_2}} + a$, where a is the distance between the surfaces, results in [24]:

$$U_{vdW}(r) = -\frac{A}{3}\left(\frac{\mathrm{r_{NP_1}}\cdot\mathrm{r_{NP_2}}}{r^2-(\mathrm{r_{NP_1}}+\mathrm{r_{NP_2}})^2}+\frac{\mathrm{r_{NP_1}}\cdot\mathrm{r_{NP_2}}}{r^2-(\mathrm{r_{NP_1}}-\mathrm{r_{NP_2}})^2}+\frac{1}{2}ln\left(\frac{r^2-(\mathrm{r_{NP_1}}+\mathrm{r_{NP_2}})^2}{r^2-(\mathrm{r_{NP_1}}-\mathrm{r_{NP_2}})^2}\right)\right) \tag{2.7}$$

A is the material-dependent Hamaker-constant, which specifies the effective strength of the van der Waals force. In the approximation for very close objects, where the radii of spherical nanoparticles are large compared to the distance between the surfaces ($a \ll \mathrm{r_{NP_1}}, \mathrm{r_{NP_2}}$), the eqn. 2.7 gets simplified to [10]:

$$U_{vdW}(a) = -\frac{A}{6\cdot a}\left(\frac{\mathrm{r_{NP_1}}\cdot\mathrm{r_{NP_2}}}{\mathrm{r_{NP_1}}+\mathrm{r_{NP_2}}}\right) \tag{2.8}$$

The force of the van der Waals interaction is the negative derivative with respect to a. An estimate for γ-Fe_2O_3 nanoparticles with a radius of 5 nm, a surface distance of 1 nm and a Hamacker-constant of $18\cdot10^{-21}$ J [42] yields a force in the order of magnitude of $10^{-12}N$.

For electrically neutral particles this van der Waals interaction (vdW) is an important, often dominating, contribution to the interaction potential when in solution. All particles will have a basic interaction potential governed by their vdW attraction, which depends mainly on the surface chemical composition and size, and the electrostatic repulsion of the surface atoms at Å distances, which can be modified by other interactions in specific cases. This interplay of attractive and repulsive forces leads to a potential that always has its minimum at an particle distance comparable to the size of an atom, while the binding strength increases with the particle radius [24]. In consequence, the interaction length scale relative to the particle size decreases with

increasing radius, which has implications on the NP self organization process when changing the particle size.

2.1.4.2 Gravity and external magnetic field

In the case of iron oxide particles dissolved in toluene the buoyant force does only compensate a small fraction of the particle weight (toluene density is $0.87\,\frac{\mathrm{g}}{\mathrm{cm}^3}$ compared to $5.242\,\frac{\mathrm{g}}{\mathrm{cm}^3}$ of γ-Fe_2O_3) leading to an effective gravitational acceleration constant g_{eff} of eqn. 2.9 for the particles in dependence to the gravitational acceleration constant g, and leading to an effective force in the order of $5{\cdot}10^{-20}\,\mathrm{N}$ on a $(10\,nm)^3$ particle pointing towards the substrate. Together with the Brownian motion this leads to a particle concentration ρ inside the solvent which follows the barometric distribution eqn. 2.10 [5], where m is the mass of the particle and h height difference.

$$g_{eff} = \left(1 - \frac{0.87}{5.242}\right) \cdot g \tag{2.9}$$

$$\rho = \rho_0 e^{-\frac{m g_{eff} h}{k_B T}} \tag{2.10}$$

The second external force acting on the particles is an applied magnetic field. This will have two effects on the super-paramagnetic moment of the particles. The field itself applies a torque $\vec{\tau}$ that tries to align the moment into the field direction (eqn. 2.11) [2, 4], which will compete with the thermal fluctuations, yielding a Langevin type behavior for the average magnetic moment as given in eqn. 2.12. In addition, any magnetic field gradient will accelerate moments aligned within the field direction with a force F given in eqn. 2.13 [2, 4]. In consequence, the superparamagnetic particles will be partially aligned by the magnetic field and dragged in the direction of the field gradient. Considering a induced moment of $1000\,\mu_B$ in a field with gradient $10\,\frac{mT}{cm}$ leads to a force of $10^{-20}\,\mathrm{N}$, comparable with the influence of gravitation.

$$\vec{\tau} = \vec{m} \times \vec{B} \tag{2.11}$$

$$M(H) \approx N_{NP} \cdot m \cdot \mathrm{L}\left(\frac{\mu_0 H m}{k_B T}\right) \tag{2.12}$$

$$F = \vec{m} \cdot \vec{\nabla} \vec{B} \tag{2.13}$$

2.1.4.3 Dipole-dipole force

The magnetic field produced by the dipole moments of individual particles introduces an additional inter-particle interaction which may be altered by an external field. The force between two dipoles is given in equation 2.15 [96], which has a component perpendicular to the connection vector $\hat{e}_r$ (first two terms) as well as an attractive/repulsive component. The latter is strongest when both moments are aligned in parallel directions and attractive when they point

into the direction of their connecting vector $\vec{r}$.

$$B(\vec{r}) = -\frac{\mu_0}{4\pi} \vec{\nabla}\frac{\vec{m}\cdot\hat{e}_r}{r^2} \tag{2.14}$$

$$\begin{aligned}\vec{F}(\vec{r},\vec{m}_1,\vec{m}_2) = \frac{3\mu_0}{4\pi r^4}[& (\hat{e}_r\times\vec{m}_1)\times\vec{m}_2+(\hat{e}_r\times\vec{m}_2)\times\vec{m}_1 \\ & -2\hat{e}_r(\vec{m}_1\cdot\vec{m}_2)+5\hat{e}_r((\hat{e}_r\times\vec{m}_1)\cdot(\hat{e}_r\times\vec{m}_2))]\end{aligned} \tag{2.15}$$

In the absence of an external magnetic field and above T_B the moments of individual particles in solution will be oriented arbitrarily. This case is very similar to the van der Waals interaction, as the field of one dipole aligns the other (induced dipole in parallel direction) leading to an attractive force. As an induced dipole is involved in this interaction it drops fast with increasing distance ($\approx r^{-6}$ as the inducing dipole field, eqn. 2.14 [2, 96], drops with the square of the distance) and effectively leads to a small correction of the van der Waals potential. An estimate of the dipole force for two interacting spherical γ-Fe_2O_3 nanoparticles without an external field results with the use of eqn. 2.12, 2.14 and 2.15 in a force of $10^{-13}N$. This estimate was done for room temperature, particle radii of 5 nm, a center to center distance of 13 nm and a saturation moment of $10286\mu_B$ calculated from a magnetization per iron atom of $0.72\mu_B$ [103], a cell volume of 586 Å [72] and 8 formula units per unit cell [72]. The comparison to the van der Waals interaction shows that the dipole-dipole force is about one order of magnitude lower and therefore has less influence on the self-assembly for the considered case. In an applied magnetic field, however, the moments are aligned to the field direction as given in eqn. 2.12, leading to a much stronger attractive force between particles separated in field direction and repulsion perpendicular to it, which only drops with r^{-4}. This effect can lead to the formation of particle chains inside the solution as was reported in [58, 90].

2.1.5 Free energy

In order to spontaneously form clusters the attractive force between particles needs to overcome the free energy associated with the entropy loss due to limitation of degrees of translational and rotational degrees of freedom [24]. In other words, the thermally activated movements of the particles should not break dipole-dipole bonds between particles faster than the typical time between collision and new bond formation. This mainly depends on the range and strength of the attractive forces between individual particles and the particle density inside the solution. From a microscopic point of view this corresponds to the probability of two particles to stick together long enough to bond with additional particles and not to be broken apart by thermal fluctuations. This situation can be described by the equilibrium theory of physical clusters [9, 24], which describes the average number of n-sized clusters N_n related to each other by the canonical partition functions. For the dimer case $n = 2$ this number relates to the number of free particles N_1 of spherical shape with radius R, interaction range λ, the interacting volume V_ε and interaction strength ε in a volume V by [24]:

$$N_2 = N_1^2\left(\frac{V_\varepsilon}{8\pi V}\right)\exp\left(\frac{\varepsilon}{k_BT}\right) \tag{2.16}$$

$$V_\varepsilon = \frac{4}{3}\pi\left[(2R+\lambda)^3-(2R)^3\right] \tag{2.17}$$

To increase the number of dimers and consequently of larger clusters one therefore needs to increase the interaction strength, the interaction range or lower the available volume of the particle. For small length scale interactions ($\lambda \ll R$) this leads to a free energy difference when forming a dimer that depends linearly on the interaction strength and logarithmically on the range [24]:

$$\Delta F = -k_B T \ln(N_2/N_1^2) \tag{2.18}$$

2.2 Scattering methods

In this section the fundamental theory of the scattering methods used is introduced. The concept is mainly taken from [3], where the theory is described in more detail.

2.2.1 Fundamentals

Scattering experiments investigate the angular dependent intensity of a defined radiation, which gets scattered by interaction with a sample. The scattered intensities detected in different directions on a detector are described by the angles 2θ and φ. The geometry of a scattering experiment is shown in **figure 2.1**. The angular dependent detected intensity is directly proportional to the differential scattering cross section $\frac{d\sigma}{d\Omega}$. **Equation 2.19** describes the intensity I as measured over a solid angle element $d\Omega$ for a given incident beam intensity I_0.

$$I = I_0 \frac{d\sigma(\omega,\varphi)}{d\Omega} d\Omega = I_0 \left| f_k(\omega,\varphi) \right|^2 \tag{2.19}$$

Dependant on the radiation type used for the experiment the derivation of the scattered intensity and thus an expression for $\frac{d\sigma}{d\Omega}$ starts from the stationary Schödinger (particles with mass) or Maxwell's equations (photons, in the limit where a macroscopic description is appropriate), leading to the wave equation (**eqn. 2.20** just with different prefactors - the gray colored term is only used for neutrons) with wave function $\Psi(\vec{r})$ and scattering potential $V(\vec{r})$ for elastic scattering processes. Elastic implies scattering without energy transfer between radiation and sample.

$$V(\vec{r})\Psi(\vec{r}) = \frac{\hbar^2}{2m_{red}} \left(\nabla^2 + k^2\right) \Psi(\vec{r}) \tag{2.20}$$

$$\Psi(r) \underset{r\to\infty}{\sim} e^{i\vec{k}_i\vec{r}} + f_k(\omega,\varphi) \frac{e^{i\vec{k}_f\vec{r}}}{r} \tag{2.21}$$

The solution of the equation must be of the form of **eqn. 2.21**, describing a plane incident wave (with wave vector $\vec{k}_i$) and a second scattered wave contribution (with wave vector $\vec{k}_f$ and $k_i = k_f = \frac{2\pi}{\lambda}$ as the process is elastic). The Fraunhofer approximation can be assumed as the size of the sample is much smaller than the distance between sample and source/detector and allows the description of the monochromatic radiation as a plane wave, which is described by the corresponding wave vectors. This equation for the solution can be used to retrieve an approximate solution of the wave equation, brought into integral form **eqn. 2.22**, by using the

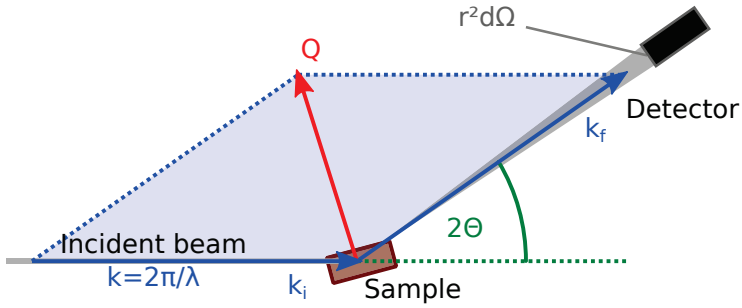

Figure 2.1: General scattering geometry for a scattering event of a particle with incoming wavevector k_i, outgoing wavevector k_f and with an outgoing angle 2θ. The angles φ, ω define the angle of the sample (see **figure 2.4**).

plane wave ($\Psi_{(0)}(\vec{r}) = e^{i\vec{k}_i\vec{r}}$) as first approximation for the wave function and than using the result of the integral as better guess for Ψ.

$$\Psi_{(n+1)}(\vec{r}) = e^{i\vec{k}_i\vec{r}} + \frac{2m_{red}}{4\pi\hbar^2}\int \frac{e^{ik|\vec{r}-\vec{r}'|}}{|\vec{r}-\vec{r}'|} V(\vec{r}')\Psi_{(n)}(\vec{r}')d^3r' \tag{2.22}$$

Equation 2.22 represents a superposition of the incident plane wave - the first term - with the scattered wave - the second term. This iterative approximation is known as Born series, where the first integration is already a reasonable approximation for the case of a weak interaction potential. It assumes that the incident wave is only scattered once from the sample (potential $V(\vec{r}')$). For stronger interaction potentials and larger samples multiple scattering events and thus higher order terms of the Born series need to be taken into consideration. Using the definition of the scattering vector $\vec{Q} = \vec{k}_f - \vec{k}_i$, $e^{ik|\vec{r}-\vec{r}'|} = e^{i\vec{k}_f(\vec{r}-\vec{r}')}$ and the far field approximation $r \approx |\vec{r}-\vec{r}'|$ one finds that the wave function amplitude of this so called first Born approximation is the Fourier transform of the scattering potential V:

$$\overset{2.22+2.21}{\Longrightarrow} \qquad f_k^{(Born)}(\vec{Q}) = \frac{2m_{red}}{4\pi\hbar^2}\int V(\vec{r}')e^{-i\vec{Q}\vec{r}'}d^3r' \propto \mathfrak{F}(V) \tag{2.23}$$

As described in the beginning of this section, the scattering experiment measures the scattering intensity eqn. 2.19, where taking the modulus square of f_k removes the phase information of this result, so it is not possible to directly conclude the scattering potential from the intensity. Therefore it is necessary to calculate the scattering intensity from a model for the scattering, which largely depends on the radiation used, the sample composition and the length scales accessible within the $\vec{Q}$-range measured in the experiment. Details of such model descriptions important for this thesis are described in the subsequent sections.

2.2.2 Interaction of radiation with matter

The following paragraphs will address the basic interactions between the X-rays and the matter in the sample, which is the basis for the models used to analyze the scattered intensity. As the

scattering amplitude is connected to the potential by a Fourier transform integral, it is possible to build up the scattering amplitude starting from the atoms, when the scattering cross section for each atom is known. Therefore the discussion will focus on the derivation of the single atom scattering cross section, the atomic form factor.

The Coulomb force accelerates electrons inside the electromagnetic field of the X-ray wave, making them a source of radiation themselves. This results in the single electron Thomson scattering cross-section **equation 2.24** with the *classical electron radius* $r_e = \frac{e^2}{4\pi m_e c_0^2 \varepsilon_0}$ and polarization vectors of the incoming and outgoing wave $\hat{e}_{i/f}$, always perpendicular to the wave vectors $\vec{k}_{i/f}$.

$$\frac{d\sigma}{d\Omega_{Thomson}} = r_e^2 (\hat{e}_i \cdot \hat{e}_f)^2 \tag{2.24}$$

As photons are preponderantly interacting with the electrons of the sample, the atomic form factor of the scattered X-ray wave is proportional to the Fourier transform of the charge density distribution ρ_e within the atom (**eqn. 2.25**). This is valid for electrons bound in an atom and high photon energies compared to the binding energy.

$$f_0(\vec{Q}) = \frac{r_e}{e} \int_V \rho_e(\vec{r}) e^{i\vec{Q}\cdot\vec{r}} d\vec{r} \tag{2.25}$$

When measuring at low angles and therefore small $\vec{Q}$ values this cross section is proportional to the atomic number Z. Consequentially, the elemental composition and density is the determining factor for the contrast (variation of scattering potential) in small angle X-ray experiments [110]. In the case of higher angle diffraction, on the other hand, the electron distribution of the atom needs to be taken into account, but generally is substituted by an empirical approximation to the real distribution function as can be found in e.g. [6]:

$$f_0(\vec{Q}) \approx \sum_{j=1}^{4} a_j e^{-b_j (2\pi\vec{Q})^2} + c \tag{2.26}$$

Obviously, the scattering cross section drops for large values of $\vec{Q}$. In addition, the polarization dependence of the Thomson scattering needs to be taken into account, leading to an additional polarization dependent prefactor for the scattered intensity:

$$(\hat{e}_i \cdot \hat{e}_f)^2 = \begin{cases} 1, & \text{polarization} \perp \text{scattering plane} \\ cos^2(2\Theta), & \text{polarization} \parallel \text{scattering plane} \\ \frac{(1+cos^2(2\Theta))}{2}, & \text{unpolarized} \end{cases} \tag{2.27}$$

The deviation of the atomic form factor from the equations above due to absorption effects is known as anomalous scattering factor or anomalous dispersion correction [51]. The atomic form factor f is given by [51]:

$$f(\vec{Q}, E) = f_0(\vec{Q}) + f'(E) + if''(E) \tag{2.28}$$

where f_0 is the known Thomson scattering factor, f' the real part and f'' the imaginary part of the anomalous scattering factors. The large absorption μ of X-rays (compared to neutron

scattering) has to be taken into account. It enters the atomic form factor as an imaginary part proportional to the absorption length[1] μ and to the absorption cross-section σ_{abs} via

$$\mu = \rho_{atom}\sigma_{abs} = \rho_{atom} 2 r_0 \lambda f''(E). \tag{2.29}$$

2.2.3 Nanoparticles and assemblies

In contrast to the case of atomic crystals, the size of nanoparticle building blocks in the investigated structures is relatively large compared to the typical wavelength used in X-ray experiments, which are in the order of Å. Therefore the investigations on nanoparticle superstructures are carried out at small $\vec{Q}$ values and therefore small angles. The atomic crystal structure inside the nanoparticle can be probed with wide angle scattering as is the case for solids with structures on the atomic length scale.

Here we focus on such experiments carried out at small angles, as most of the measurements done in the scope of this dissertation were carried out in such a geometry[2]. In this case one only observes the area of reciprocal space[3] which is insensitive to the atomic structure of the system and can work with a smooth scattering potential derived from the atomic density instead of using the full atomic structure. For most nano-sized objects this density will be constant over large regions of the particle. In our case of iron oxide nanoparticles this would be the constant scattering power density of γ-Fe_2O_3 inside the particle with a small organic shell of smaller scattering power. The Fourier transform integral is additive, so one can retrieve the scattering cross section by adding up the Fourier transforms of each component separately. The part of the scattering cross section that is defined from a single particle scattering potential is called single particle form factor. It can be measured directly on particles in a dilute solution as there is no interference between scattered waves from different particles with distance far greater than the coherence length of the radiation. The form factor functions for shapes relevant in this thesis are given in **chapter 5**.

For densely packed particles inside an assembly, interference between individual particles is not negligible any more and the combined scattering potential of the particles needs to be taken into account. To simplify the model one can make use of the convolution theorem for Fourier transforms (**eqn. 2.30**) to separate the single particle from the lattice contribution.

$$\mathfrak{F}(A \circledast B) = \mathfrak{F}(A) \cdot \mathfrak{F}(B) \tag{2.30}$$

In general the nanoparticle superstructure in real space can mathematically be described as a convolution of the nanoparticle scattering potential in a basis defining the nanoparticle positions and an infinite lattice (see **figure 2.2**). For the scattering the convolution theorem can be used, as each corresponding element can be separately Fourier transformed and the results in reciprocal space only need to be multiplied afterwards [3]. If the assembly consists of similar particles (or unit cells of atoms in crystals) arranged in a regular lattice pattern, the form factor included in the unit cell structure factor and lattice contribution can be separated by individually transforming each contribution to get **eqn. 2.31**, as the real space structure is a convolution of a particle with the lattice position.

[1] Typical absorption lengths are in the order of μm for hard X-rays.
[2] The description of atomic crystals for larger scattering angles is carried out analogously.
[3] the Fourier transform of real space

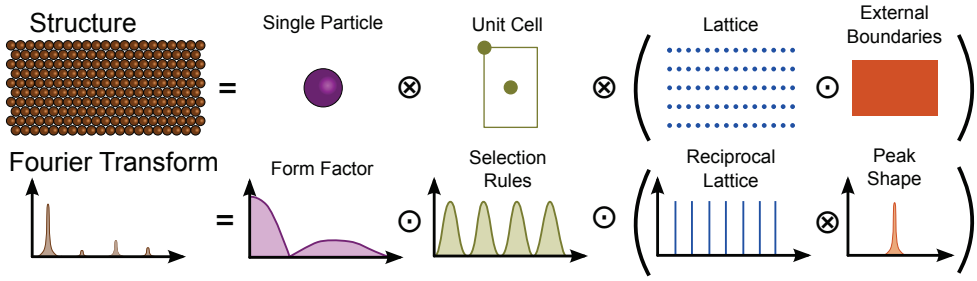

Figure 2.2: Application of the convolution theorem to simplify the modeling and allow a model independent understanding of a scattering experiment.

$$S(\vec{Q}) \sim \overbrace{\sum_j \underbrace{f_j(\vec{Q})}_{\text{Form Factor}} e^{i\vec{Q}\vec{r}_j}}^{\text{Unit Cell Structure Factor}} \cdot \overbrace{\sum_{h,k,l} \delta(\vec{Q} - (h\vec{a}_1^* + k\vec{a}_2^* + l\vec{a}_3^*))}^{\text{Reciprocal Lattice}} \tag{2.31}$$

with $$\vec{a}_i^* = 2\pi \frac{\vec{a}_{(i+1)_{mod3}} \times \vec{a}_{(i+2)_{mod3}}}{\vec{a}_1 \cdot (\vec{a}_2 \times \vec{a}_3)} \tag{2.32}$$

This means that the scattering pattern of an infinite lattice of particles consists of delta functions with intensities modulated by the single particle form factor. If the lattice is finite (which means it is a product of an infinite lattice with some kind of box function), the lattice term has a Fourier transform, which again can be derived using the opposite direction of the convolution theorem, leading to peak shape functions at the same position as the infinite lattice delta functions (see **figure 2.2** external boundaries). These peak shapes correspond to the Fourier transformation of the outer shape of the assembly. The monodisperity of the particles allows one to describe the cross section as a product of form factor and structure factor [71] (local monodisperse approximation [70]), thus the form factor part can be separated from all lattice contributions in **eqn. 2.31** and it is possible to derive the pure lattice contribution directly from a measurement by dividing by a known particle form factor.

2.2.4 Influences of the measurement method and structural imperfections

For real experiments, there are several aspects which need to be taken into account to derive the true peak intensity and shape. Even for a perfect crystal the peak shape is not described by a delta function and a minimal peak width is present due to the instrumental resolution. This resolution is dependent on the angular uncertainties due to the collimation apertures and the finite size detector elements, as well as the wavelength spread determined by the monochromator. The limited coherence of the radiation is larger than a single mesocrystal and only becomes relevant when looking at crystal ensembles (see **chapter 5**).

For a diffraction experiment an intensity correction of individual reflection's integrated intensities is necessary due to the measurement geometry. The corresponding scaling term is called

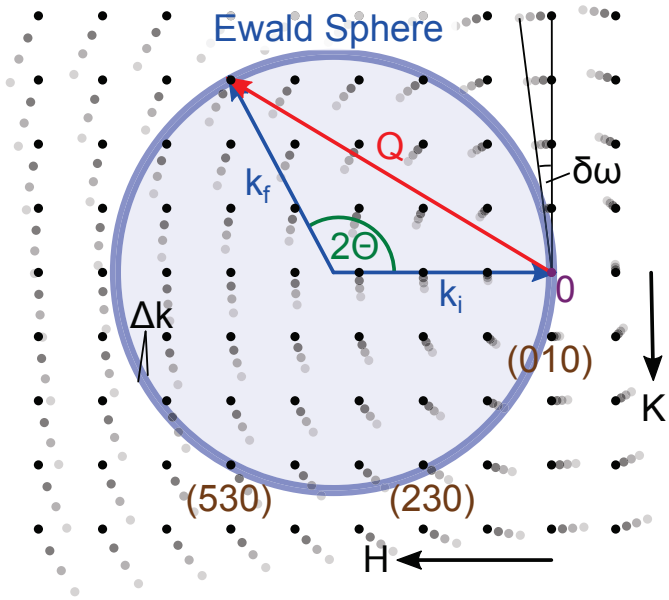

Figure 2.3: Schematic view of an Ewald sphere.

Lorentz-factor [85]:

$$L = \frac{1}{sin(\theta) \cdot sin(2\theta)}, \tag{2.33}$$

valid in this form only for measurements, where the sample is rotated in the scattering plane by the angle ω (see **figure 2.4**). The effect can be described very well in the framework of the Ewald construction shown in **figure 2.3**.

The Ewald sphere illustrates all possible elastic scattering processes, as it constructs any orientation of the vector $\vec{k}_f$ with the same length $|\vec{k}|$ as the vector $\vec{k}_i$. In this construction the Bragg condition $2d_{hkl} \cdot sin(\theta) = n\lambda$ (or $Q = G(hkl)$) is fulfilled for each reciprocal lattice point on the sphere's edge when the reciprocal space origin is placed at the end of $\vec{k}_i$. Obviously, a single crystal has to be rotated around the ω-axis to observe different Bragg reflections.

The Ewald sphere has a finite thickness Δk due to the finite instrument resolution. When rotating the sample (and therefore the reciprocal lattice) the movement of reciprocal lattice points through the circle arc gets faster for larger $|\vec{Q}| \sim sin(\theta)$ as illustrated in **figure 2.3**. In addition, the time of the reflex on the arc depends on the ω position, where the reciprocal lattice point overlaps the Ewald sphere. For $2\theta = 90°$ the reflection moves through the sphere almost radially, while for $2\theta = 180°$ the movement is tangential and therefore the intersection area is larger than for the former case. These two effects combined lead to the Lorentz-Factor (**eqn. 2.33**) given in the last paragraph.

In addition to the considerations given above, sample influences can impact the reflection intensities and shapes. Different imperfections can influence the scattering result and are categorized into local and global imperfections. A local imperfection is an arbitrary offset of an individual

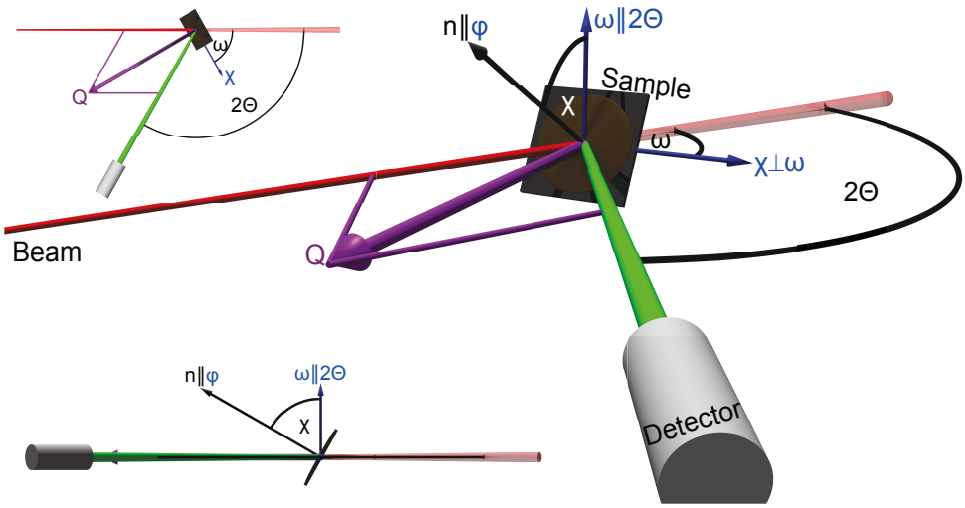

Figure 2.4: Geometry of a scattering experiment with different rotation axis (blue arrows) and their corresponding angles.

particle from its perfect lattice position and can be described by the Debye-Waller factor,

$$I(\vec{Q}) \propto |S(\vec{Q})|^2 \cdot e^{-\frac{1}{3}|\vec{Q}|^2|<u>|^2}, \tag{2.34}$$

derived for the equivalent case of thermal atomic displacements for atomic crystals and is multiplied additionally to the scattering intensity $|S(\vec{Q})|^2$ lowering the intensity for higher Q's. Global imperfections can be grain boundaries, stacking faults or e.g. large scale lattice deformations. They are limiting the coherence of the nanoparticle superstructure. The limitation of the structural coherence is described through the correlation length ε

$$P(r) = e^{\frac{-r}{\varepsilon}}, \tag{2.35}$$

which statistically describes how fast the two particle correlation function vanishes with the spatial particle separation r. The correlation is reduced by $\frac{1}{\varepsilon}$ at a distance of the correlation length ε. Further details on the influence of different imperfections on the scattering pattern for the system used can be found in **chapter 5**.

2.2.5 Structures on surfaces

Nanoparticle structures, as the ones described in the last section, are generally produced on top of large substrate surfaces and consist of relatively low amounts of material. To be able to characterize these structures different kinds of grazing incidences scattering techniques are applied: The specular reflectivity, off-specular scattering (**figure 2.5**) and grazing incidences small angle scattering (GISAS) (**figure 2.6**). Common to all these three techniques is that the incident beam hits the sample under a small angle α_i and is scattered from the surface under the angle α_f with a possible in-plane scattering angle φ. The components of the scattering vector

$\vec{Q}$ are given by

$$Q_x = \frac{2\pi}{\lambda}(cos(\alpha_f)cos(\varphi) - cos(\alpha_i)) \tag{2.36}$$

$$Q_y = \frac{2\pi}{\lambda}(cos(\alpha_f)sin(\varphi)) \tag{2.37}$$

$$Q_z = \frac{2\pi}{\lambda}(sin(\alpha_f) + sin(\alpha_i)) \tag{2.38}$$

The specular reflections are observed at $\alpha_i = \alpha_f$ and $\varphi = 0$, giving information parallel to the substrate's surface normal in the nm-range such as layer thicknesses, roughnesses, or layer sequence. Off-specular scattering ($\alpha_i \neq \alpha_f$ and $\varphi = 0$) gives additional information in-plane in beam direction in the µm-range. For an optimal characterization of the nanoparticle superstructure in both directions, GISAS (in general $\alpha_i \neq \alpha_f$ and $\varphi \neq 0$ is possible) experiments were performed, achieving an additional nm resolution in-plane perpendicular to the beam with an angular resolution in two dimensions. In the GISAS case the specular reflectivity is detected at point (1) in **figure 2.6**, the off-specular scattering on a line perpendicular to the sample horizon on the detector plane at e.g. (2) and arbitrary refections are observed at e.g. (3) with $\varphi \neq 0$. The Yoneda[4] line is detected at $\alpha_f = \alpha_c$, with α_c the critical angle of total reflection.

For all approaches, the incident beam gets close to the sample angle of total external reflection, where the prerequisite of a small scattering probability used to derive the Born approximation no longer holds. Therefore the intensity can no longer be described by the Born approximation. To be able to analyze the scattering intensity one can use a two step approach by separating the sample into layers of average scattering potential, where the wave equation **2.20** is solved exactly with an optical approach, and than introducing in-plane deviations from this average as small perturbation, treatable with the Born approximation. This so called Distorted Wave Born Approximation (DWBA) leads to several Fourier transform components for the in-plane structure for each possible wave propagation inside the medium.

The treatment of the average potential uses the result of a wave traveling across a potential step $V(z)$, getting partly reflected and transmitted according to the Fresnel coefficients, well known from optics or quantum mechanics:

$$r_{j,j+1} = \frac{k_{z,j} - k_{z,j+1}}{k_{z,j} + k_{z,j+1}} \qquad \text{with } k_{z,j} = k_0\sqrt{n_j^2 - \cos\alpha_i^2} \tag{2.39}$$

$$t_{j,j+1} = \frac{2\sqrt{k_{z,j}k_{z,j+1}}}{k_{z,j} + k_{z,j+1}} \qquad \text{and } n_j = 1 - \delta + i\beta \tag{2.40}$$

Here the scattering power density δ and absorption β, derived from the atomic density and the low $\vec{Q}$ form factors, leads to the reflective index n. These single interface parameters can be used in an iterative approach introduced by Paratt [69] to derive the reflection and transmission coefficients R_j and T_j used in the DWBA:

$$X_j = \frac{R_j}{T_j} = e^{-2ik_{z,j}z_j}\frac{r_{j,j+1} + X_{j+1}e^{2ik_{z,j+1}z_j}}{1 + r_{j,j+1}X_{j+1}e^{2ik_{z,j+1}z_j}} \tag{2.41}$$

[4] a surface wave, containing mainly information about the lateral structure

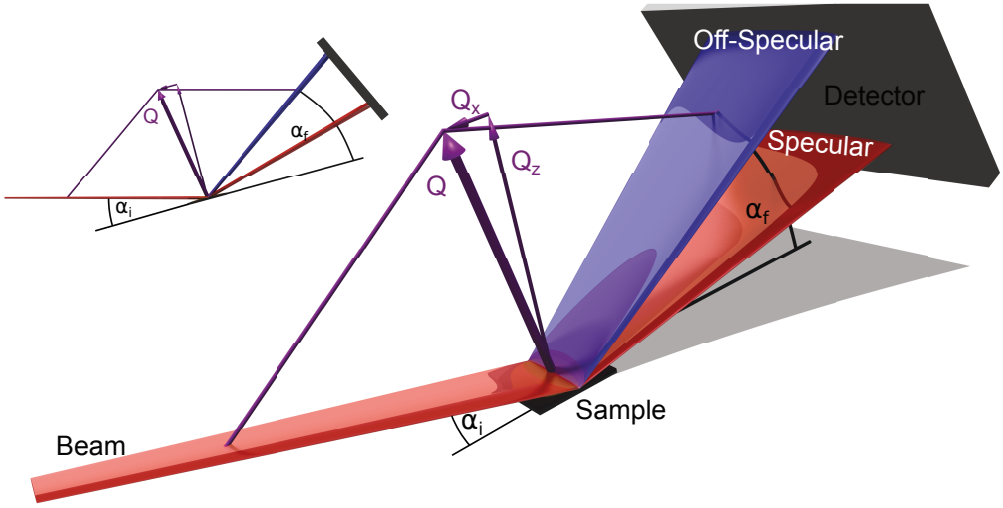

Figure 2.5: Geometry of a specular and off-specular scattering experiment.

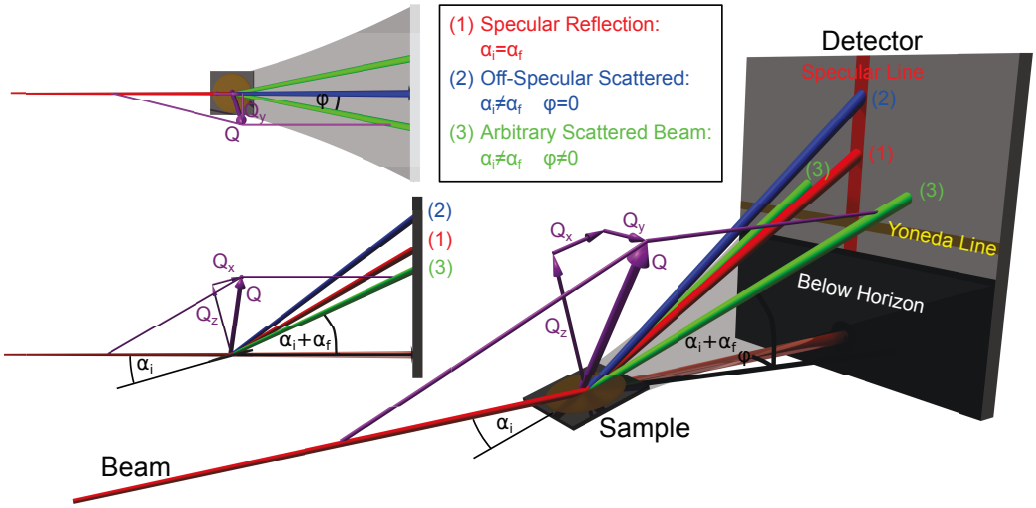

Figure 2.6: Geometry of a grazing incidence small angle scattering experiment (GISAS).

To solve the equation one can start from the substrate, which imposes the boundary condition $X_N = R_N = 0$, working upwards layer by layer up to the surface where the second boundary condition $T_0 = 1$ yields the absolute value of all coefficients. The surface reflectivity index R_0 yields the intensity of a reflectivity experiment, where the scattered beam has the same angle to the substrate as the incident beam (specular condition). Therefore the reflectivity experiment only measures the average scattering power density of these layers. Rough interfaces between layers can be introduced by a Debye-Waller type modification of the Fresnel coefficients as described in [30]:

$$r_{j,j+1}(\sigma) = r_{j,j+1}(0)e^{-2\sigma_j^2 k_{z,j} k_{z,j+1}} \tag{2.42}$$

Chapter 3

Experimental Methods

The structural and magnetic investigation of three dimensional assemblies of nanoparticles necessitates the application of several complementary advanced methods. Scattering methods are powerful tools to look at the average correlations on a large sample area with depth resolution. Microscopy, on the other hand, yields a snapshot of the surface structure in a specific, small area. For the comprehension of the structure of such complex systems, only the combination of microscopy (e.g. SEM, TEM, AFM, ...) and x-ray scattering methods (e.g. diffraction, GISAXS,...) leads to a complete picture. A precise determination of the complete 3D structure is necessary in order to understand the magnetic correlations present in the nanoparticle superstructures.

In this chapter, the methods and instruments used to investigate the complex assemblies are described. Microscopy techniques characterize the morphology in real space imaging. For example, Scanning Electron Microscopy (SEM) visualizes information about the nanoparticle superstructure, topography, material and larger structures on the surface of the sample, while Transmission Electron Microscopy (TEM) illustrates these properties inside a crystal and additionally gives information about the atomic structure and the shape of single particles. Atomic Force Microscopy (AFM) was used to obtain the height profile of the samples as well as an independent check of the lateral size of the mesocrystals grown, an estimate of their shape and the mesocrystal density on the substrate in comparison to the SEM. For a first, not too time-consuming, check of the mesocrystal distribution on the substrate optical Light Microscopy (LM) was utilized. These methods give a local view on the mesocrystals and their supercrystal structure in real space and yield important sample parameters such as the height of the mesocrystals.

A depth resolved structural characterization over a large sample area can be achieved with X-ray scattering experiments. For this work, a study of the morphology of the individual nanoparticles in a solution was done with Small Angle X-ray Scattering (SAXS). Nanoparticle superlattices were investigated by Grazing Incidence Small Angle X-ray Scattering (GISAXS) in either lateral or specular directions, giving information on the structure of the mesocrystals. X-ray reflectometry was used to investigate the correlations along the direction of the substrate's surface normal in the nm range with high intensities. In contrast to the small angle techniques, the x-ray diffraction method allows the study of correlations on the atomic scale and thus was used to analyze the crystal structure within the nanoparticles and their orientations in the assembly.

3.1 Light microscopy

Optical Microscopy using a LEICA INM100 system was performed to investigate the mesocrystal distribution on the substrate, as scanning electron microscopy techniques often have a too high magnification to get a good overview and are too time-consuming for large samples. A light microscope works with visible light and an optical lens system to magnify small structures. We worked in a magnification range from 50x to 1000x with a theoretical resolution from 1.8 µm to 0.3 µm, using bright field contrast imaging. The real resolution is lower due to the usage of white light and imperfections of the optical setup and can be estimated to be 1.5 to 2 times worse. The mesocrystals of a few µm size were big enough to be observed with the light microscope (see **figure 3.1**). The optical microscope is a fast and efficient way to test if mesocrystals have grown and to have a look at their distribution on the sample surface.

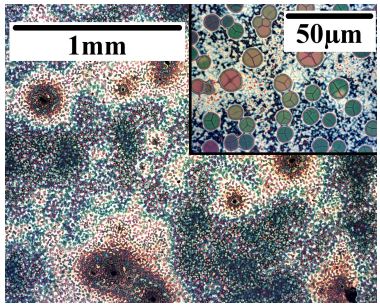

Figure 3.1: Example picture of a light microscope image with 50x magnification and a resolution of 1.8 µm (inset: 1000x , 0.3 µm).

3.2 Scanning electron microscopy

The Scanning Electron Microscope (SEM) works in reflection mode, scanning a focused electron beam over the sample and measuring the flux of scattered electrons to create an image. The image contains information about the topography as well as about the material composition as the interaction of the electrons is element dependent. For imaging, the low energy Secondary Electrons (SE) emitted from the sample after an inelastic scattering process and the high energy BackScattered Electrons (BSE), which are fully elastic scattered, are utilized. The SE escape due to the impact of the primary electrons from the upper atomic layers and thus the surface atoms determine the image contrast, so that edges appear bright and cavity dark [105]. The information about the bulk material is deduced from the BSE intensity, which depends on the atomic number of the material [105]. The intensity of the interaction signal is measured with spatial resolution and is illustrated with variations in luminosity on the SEM picture. More information about this technique can be found in [13, 105].

In this work the SEM was used to probe a bulk sample of self-assembled mesocrystals on a substrate from the top. It yielded the lateral size of the mesocrystals grown, the mesocrystal density on the substrate surface, an estimate of their shape as well as in higher magnification ($\geq$250000) the 2D order of the single particles at the top of a mesocrystal. This method allowed us to receive a first surface sensitive characterization of the quality of the crystal structure without destroying or cutting the sample. These intact samples could be used for further investigation where we needed the full size samples e.g. for neutron scattering. The SEM investigation was done in collaboration with Elke Brauweiler-Reuters and Hans-Peter Bochem from the Helmholtz Nanoelectronic Facility (HNF).

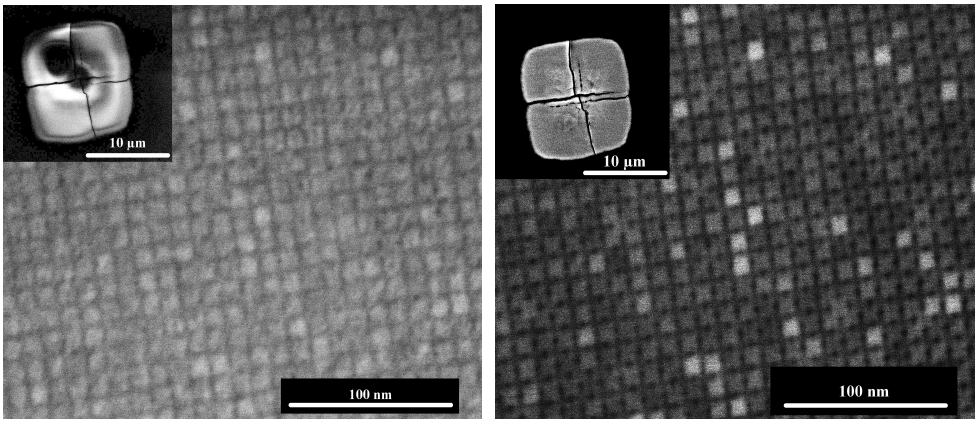

(a) SEM image made with TLD detector with electrons from the near surface area. Burning points and a blurry view are visible.

(b) SEM image made with vCD detector with electrons from deeper parts under the organic shell. The picture has a better contrast and the structure is clearly visible.

Figure 3.2: Comparison between SEM pictures using the TLD and the vCD detector. The pictures have been recorded simultaneously.

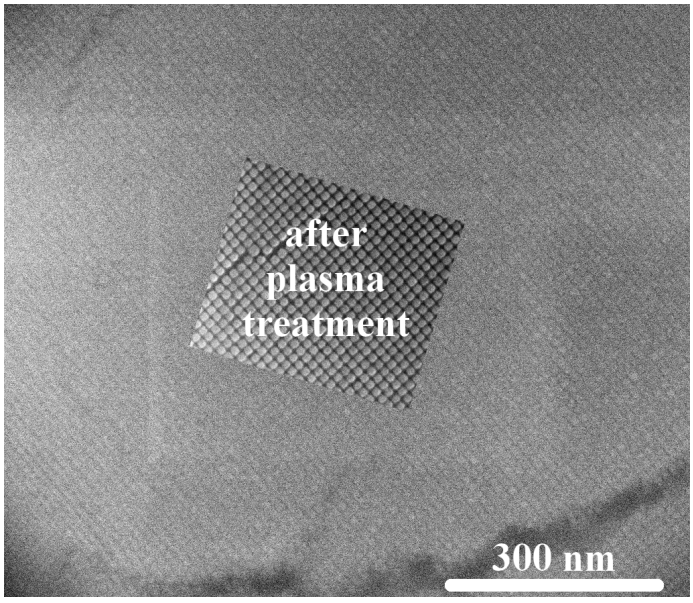

Figure 3.3: The sample structure before the plasma treatment, where the structure can only be estimated. The picture inset shows an equivalent position of the same sample after applying the plasma. A good contrast between the nanoparticles is visible.

The earlier SEM images presented in this dissertation were obtained using a Gemini 1550VP SEM from Zeiss. This instrument has a typical resolution of 1 nm at 20 kV [106] and uses a high resolution in-lens detector (TLD). For the imaging it was operated at 20 kV in the high resolution mode at a working distance between 2 and 3 mm. For the sample characterization we recorded routinely pictures with different magnifications at several positions on the sample surface to get a good overview over the mesocrystal structures and order on every sample.

At a later stage of this work a new SEM was available. The Magellan 400 SEM from FEI offers a nanometer resolution over the full 1 keV to 30 keV electron energy range [104]. It allowed us to use a lower acceleration voltage for higher resolution, surface sensitive information [104] and a lower probability for sample damage. An Everhart Thornley detector (ETD) for secondary electrons was used for lower magnification. Images with higher magnification were recorded with an in-lens detector (TLD) for secondary electrons. The operation mode used was 10 kV with a working distance of around 4 mm. The characterization procedure was the same as with the Zeiss microscope we used before.

The organic shell around the nanoparticles is always a big problem for SEM imaging, as an excessive accumulation of this material produces charging effects. Furthermore, the organic layer generates an additional electron signal (SE), which makes high resolution imaging due to the appearing luting effect impossible. The new SEM is equipped with a retractable low-voltage high-contrast solid state detector (vCD) for backscattered electrons [104]. Only the higher energetic electrons from deeper layers trigger this detector and one gets more information of the structure below the organic material (see **figure 3.2**). The additional SE electrons from the upper organic layer are not disturbing the signal in this case. The black areas in the middle of the particle faces (looking like holes in the structure) in **figure 3.2b** are a result of long, tube-like voids present in the bct structure, where the empty planes between particle faces of subsequent layers intersect so that no particle is present in any of the subsequent layers. If the organic layer was too thick and the sample was not to be characterized magnetically afterwards, an oxygen plasma was applied to remove the organic surface layer. The plasma generator was operated for one hour to remove a few atomic layers. The success of this treatment is shown in **figure 3.3**, where the difference due to the plasma treatment is clearly visible.

3.3 Transmission electron microscopy

Transmission Electron Microscopy (TEM) studies were used to reveal essential information about the morphology of the single nanoparticle, stacking of nanoparticles layers and the presence of stacking defects and/or dislocations in the mesocrystals. In TEM, a highly coherent electron beam passes through a thin, electron transparent specimen. The transmitted electron beam can be used to record images (real space) or diffraction patterns (reciprocal space). The TEM characterization was done on cross-sectional specimens that were prepared by Focused Ion Beam (FIB) (see **section 7.1**). Different TEM images and diffraction patterns are recorded using a 2k x 2k CCD camera. The TEM studies were performed in collaboration with Andras Kovacs from the Ernst Ruska-Centre for Microscopy and Spectroscopy with Electrons, Peter Grünberg Institute 5, Forschungszentrum Jülich.

The shape, size and atomic crystal structure of individual nanoparticles was investigated using aberration-corrected High-Resolution TEM (HRTEM). The specimens are prepared from drop

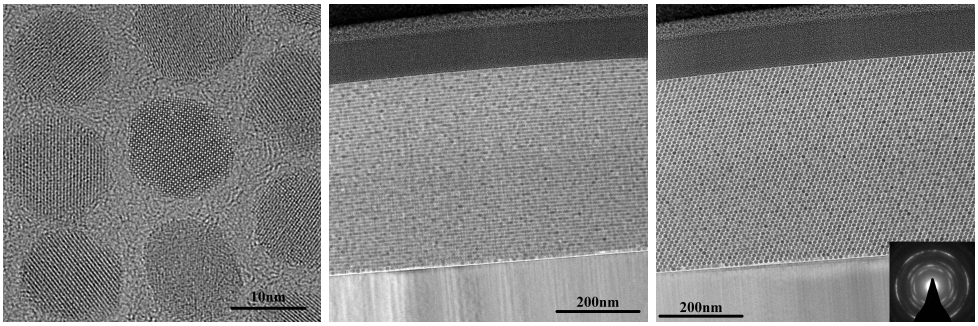

(a) HRTEM **(b)** TEM - off-zone **(c)** TEM - in-zone (inset: SEAD)

Figure 3.4: Example pictures for every operating mode: The HRTEM (a) picture shows a high resolution image of spherical particles, where the lattice planes are visible. The TEM picture yields information about the stacking of the nanoparticle layer perpendicular to the substrate. (b) shows an imperfectly aligned specimen, where the nanoparticles are aligned off-zone and the silica in-zone. (c) shows a TEM picture where the nanoparticles are aligned in-zone. The inset shows a SEAD pattern containing information about the nanoparticle orientation inside the mesocrystal.

casting of a low concentrated nanoparticle solution onto a carbon layer. Important for this study is that the particles do not lie on top of each other to produce a good image. If this is the case, the probability is high that the particles have different crystal orientations which will lead to blurred images. The images are recorded using a FEI Titan microscope operated at 200 kV. The aberration functions are corrected up to fourth order.

The TEM images of low and medium resolution were made from vertical cuts through a mesocrystal. This study was performed to reveal essential information about the stacking of nanoparticle layers perpendicular to the substrate surface, in comparison to the SEM where the structure on top of the mesocyrstals can be investigated. The presence of stacking defects and/or dislocations in the mesocrystals can be analyzed. Selected Area Electron Diffraction (SAED) patterns were used to confirm the crystal structure of the nanoparticles and their relative orientation within the mesocrystals (see **figure 3.4c inset**). For this investigation an FEI Tecnai G^2 microscope was used, operated at 200 keV acceleration voltage with a point resolution of 0.24 nm. The samples were fixed on a FEI double-tilt sample holder to align the nanocrystals. The holder permits a tilting of the specimen in two directions perpendicular to each other, so that the mesocrystal lattice planes are in focus (in-zone) aligned (see **figure 3.4c**). If this is not the case, the nanoparticles inside the mesocrystal are projected on top of each other in the image (see **figure 3.4b**).

3.4 Atomic force microscopy

Atomic Force Microscopy (AFM) was used as a complementary surface sensitive technique. A thin tip, sitting on a flexible cantilever, is used as a measuring sensor to scan over the sample surface. In this work, all AFM images were obtained in a standard AC mode (non-contact),

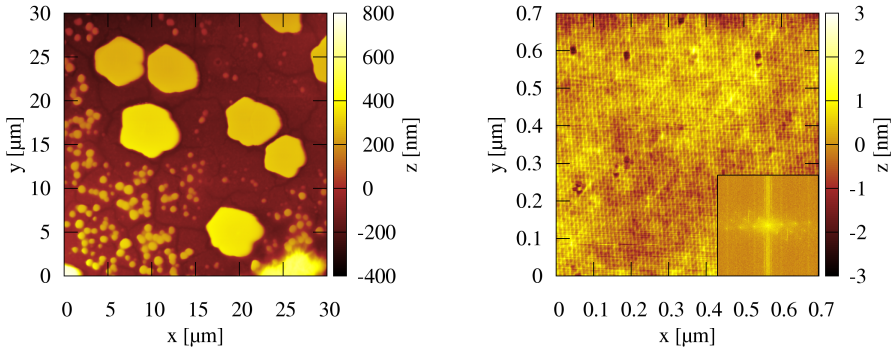

(a) Topography of an ensemble of mesocrystals

(b) Topography of nanoparticle order on top of a mesocrystal (inset:Fourier transformation)

Figure 3.5: Example pictures for a height profile in different magnifications measured with an AFM in non contact mode.

where the tip does not touch the sample surface. In this mode the cantilever is oscillating near the resonance frequency and is scanned over the sample. The changing cantilever amplitude and phase due to the modification of the interaction between specimen and tip is recorded, while keeping the distance constant via a feedback loop. The topography of the specimen investigated is constructed from the necessary readjustment to reach a constant amplitude of the cantilever's oscillation.

This method was used to obtain the height profile of the samples as well as an independent check of the lateral size of the mesocrystals grown, an estimate of their shape and the mesocrystal density on the substrate in comparison to the SEM. An example of a height profile measured with AFM is shown in **figure 3.5a**. The advantage of measuring the height of mesocrystals by AFM is that these datasets contain information in three dimensions. The relative height of the sample surface is measured at every position (x,y) in dependence on the position of the raster. So a more quantitative determination of the height of single mesocrystals is possible, in comparison to the SEM where only a two dimensional image is obtained.

For this study an Agilent 5400 scanning probe instrument was used [101]. The organic shell around the particles does not allow a contact mode due to the high probability of snagging organic material on the tip. The additional material leads to an overshoot and makes measurements impossible. Furthermore it could happen that a nanoparticle is graped with the tip and moved [54]. The mesocrystal samples implicate a slow scan speed to avoid contact and edge artefacts, due to the large difference in height of up to 800 nm and the large scanning area. The possible lateral resolution is mainly determined by tip shape and size. For a higher resolution a sharper tip is required. In this work a cantilever with $\approx$4 nm tip size is used at $\approx$250 kHz, which allows a lateral resolution of approximately 10 nm. The difficulty to resolve the order of the nanoparticle stacking on top of a mesocrystal is increased by the organic material, which lies in the void between the particles and masks the structure of the individual particles. Additionally it is known that the AFM tip follows the height variations on a hard surface with higher fidelity than on soft areas [100]. But despite all these difficulties, it was possible to resolve the nanoparticle structure in rare cases (see **figure 3.5b**). The inset shows the Fourier transformation of

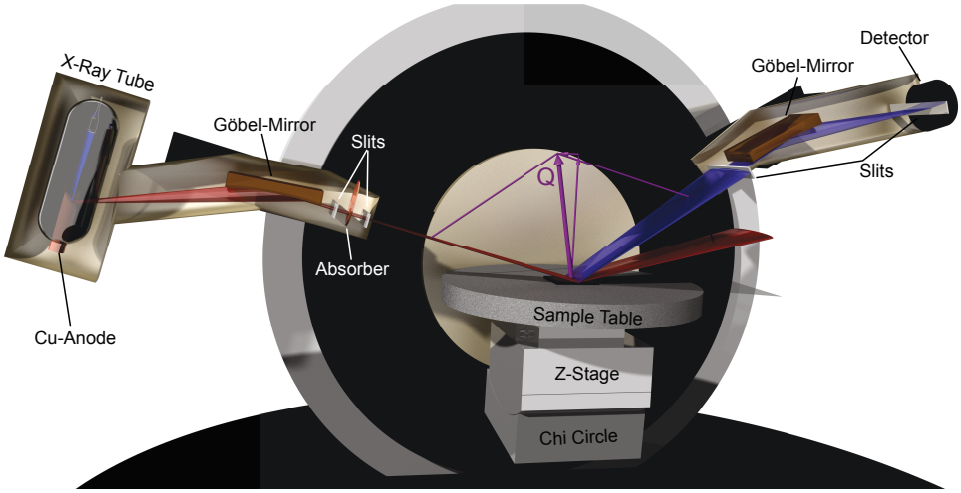

Figure 3.6: Setup of the Bruker D8 reflectometer

the topography image and the presence of long-range order with sharp peaks. The coherence in the vertical direction is lower, as the tip was scanned in horizontal direction. The *PicoView* instrument software was used to apply leveling, polynomial form removal and line correction to the images to remove sample tilt, non-linearity effects of the piezo drives and electronic noise from the images, respectively.

3.5 X-ray reflectometry

A Bruker AXS D8 X-Ray Reflectometer (XRR) was used to investigate the structural correlation along the direction of the surface normal in the nm range with high intensity. In-plane correlations can only be resolved in the µm range. The Göbel mirror monochromator parallelizes the Cu K_α radiation generated from a sealed tube X-ray source (see **figure 3.6**). The first two slits define the beamsize and reduce the background. A switchable attenuator is installed between these slits, to reduce the intensity to avoid over illumination of the detector. The sample table has motors for z translation and the χ angle. Another Göbel mirror is mounted on the detector arm to focus the scattered beam onto the last slit, which is responsible for the angular resolution. The slits were chosen to achieve a beam size between 0.2 and 0.4 mm. The used detector is a NaI scintillator. The setup allows measurements in specular and off-specular scattering geometries and up to a 2Θ angle of about 110° in the specular case. The X-ray reflectometer was used for a first fast evaluation of the nanoparticle stacking in c direction (perpendicular to the substrate) averaging over the sample. Only a few minutes are needed to get a reflectometry curve with good statistics. The existence of strong Bragg peaks indicate a good order along the c direction. The average interparticle distances perpendicular to the substrate can be deduced from the distance of the peaks. Additionally, a clear distinction between monolayer, multilayer or an ensemble of mesocrystals can be done. Due to the possibility of accessing the atomic scale at large angles, a first evaluation of the atomic crystal structure of

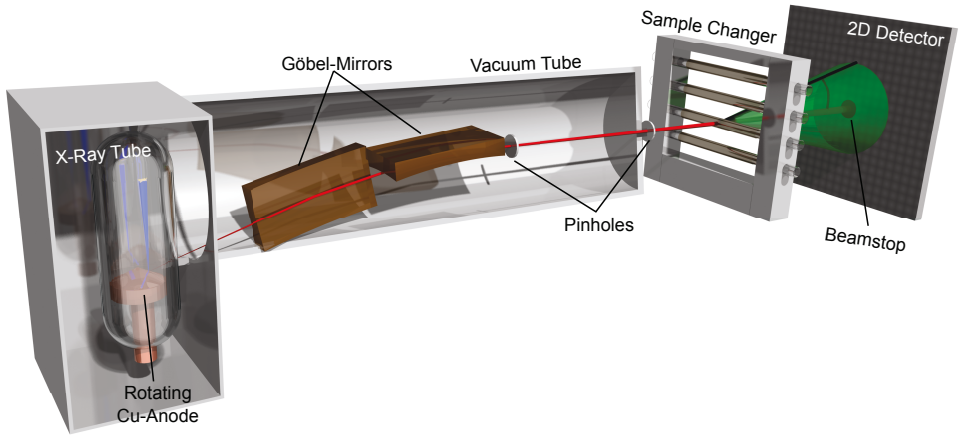

Figure 3.7: Setup of the SAXS instrument

the single nanoparticles and their preferred orientation inside the mesocrystals was possible as well. A sketch of the principle design of the instrument is shown in **figure 3.6**.

3.6 Small angle X-ray scattering

The morphology of the nanoparticles in solution was investigated with a Bruker AXS Nanostar® laboratory Small Angle X-Ray Scattering (SAXS) instrument [102]. The extracted particle size distribution and the average radius of the nanoparticles in the solution are important precharacterizations for the process of self-assembly and further investigations. The sample solutions were filled into quartz capillaries with an inner diameter of 1.5 mm and a wall thickness of 0.01 mm.

The SAXS measurements were performed with Cu K_α radiation (1.54 Å wavelength), produced by a rotating anode source operated at 40 kV, 40 mA with a double Göbel mirror monochromator. A pin-hole collimation system defines a precise x-ray beam which hits the sample inserted in a multi-sample holder. This holder is mounted on an yz-stage in a vacuum chamber. Scattered from the sample, the beam hits a 2-dimensional VANTEC 2000 xenon gas filled detector with 2048x2048 pixels on a 14x14 cm^2 area. The distance between sample and detector is fixed at 1.07 m. The accessible Q-range was defined by the primary beamstop of 2 mm diameter positioned at a distance of 1.05 m from the sample and the detector size to 0.007 - 0.25 $Å^{-1}$. A sketch of the instrument design is shown in **figure 3.7**.

3.7 Grazing incidence small angle X-ray scattering

Grazing Incidence Small Angle X-ray Scattering (GISAXS) was used to determine the 3 dimensional structure of the assemblies in the nm range. While the reflectometer has only a nm resolution in the out-of-plane direction, GISAXS provides access to both directions resolving the nanometer scaled structure of the ensemble of mesocrystals. The subtleties of the in-plane

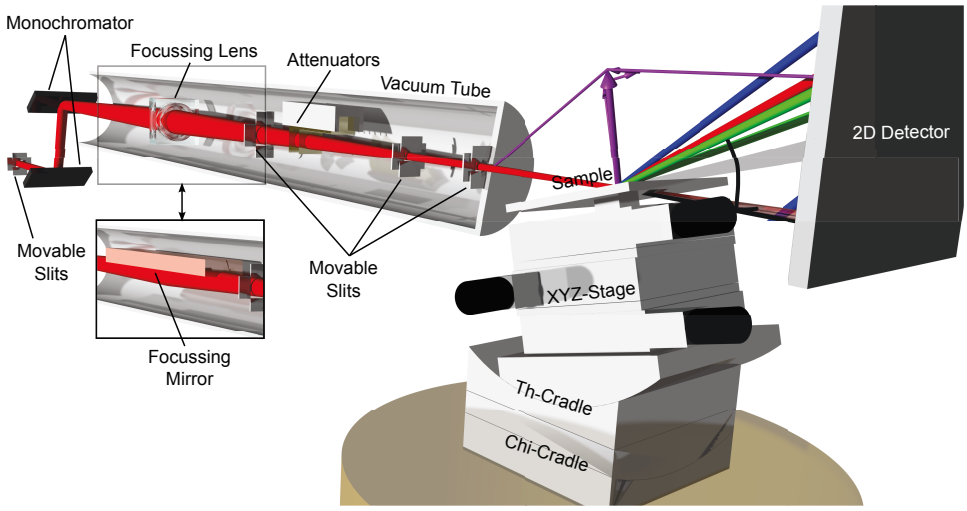

Figure 3.8: General setup of an GISAXS instrument

ordering can be visualized and a full quantitative interpretation can be made by extracting the space group as well as the coherence length, lattice constant size and distribution and tilting angle. The sample properties and the measured intensity pattern resulting from them, are an average over a large sample area, that is illuminated by the beam (footprint). In this measurement geometry, the ensemble of mesocrystals can be investigated as grown on the substrate without cutting the sample.

The general setup of a GISAXS experiment is shown in **figure 3.8**. The X-rays from the source are guided through a vacuum system to the sample by the use of various lenses and mirrors, monochromators and slits to achieve a monochromatic and sufficiently collimated/focused beam. The beam size can be influenced by the last set of slits in front of the sample position. Together with the detector resolution and distance these optics define the experimental resolution. The beamsize at the sample position is of importance, as it controls the footprint on the sample and thus the scattering area. The X-rays hit the sample under a small angle of incident (usually 0.1 - 0.5 °). A 2-dimensional detector records the scattered intensity pattern as in the SAXS experiments, but with a higher detector position to access more of the upper hemisphere above the sample horizon. Typically, three translation and two inclination motors are installed to align the sample and change the angle of incidence. The Q range can not only be changed by the choice of the energy but as well by variation of the distance between sample and detector. A GISAXS beamline can be used for SAXS measurements as well if it is equipped with the appropriate beamstop. For both experiments the central area around the direct beam needs to be shadowed, especially for alignment when the unattenuated beam can hit the detector. The strong specularly reflected beam in GISAXS experiments necessitates the full coverage of the specular line to avoid detector damage or saturation effects, so a long, rectangular shaped beamstop is needed in addition (only for synchrotron setups).

The configuration of a GISAXS setup varies from beamline to beamline, the measurements presented in this thesis were obtained at the following instruments:

- The **SWING beamline at the synchrotron Soleil, Gif sur Yvette, France** [112] was

used to measure GISAXS for structural characterization of dried samples where the influence of different self-assembly parameters was investigated. An in-vacuum U20 undulator provides an incident energy of 7 keV. A beam focus of 40x400 µm was used. We fixed our dedicated vacuum sample holder on a standard micro control holder to have an available sample size of up to 5 cm in diameter. In this configuration, a z translation adjusts the sample to the center of the beam and a θ-cradle changes the of incidence angle. The detector is a stack of 2x2 Aviex CCD detectors with 2048x2048 pixels each in a distance of 0.91 m to the sample position. Software binning of 4x4 pixels is applied to reach a final resolution of 1024x1024 pixels of 165x165 μm^2 size. The detector position was off-centered to allow the measurement with a maximum Q of 0.6 $Å^{-1}$. For the GISAXS measurements the angle of incidence was varied from 0.1 to 1.0°. The exposure time used was 0.5 s per image.

- The **ID01 beamline at the Synchrotron ESRF, Grenoble, France** [111] was used for the real time monitoring of the mesocrystal growth by in-situ SAXS and GISAXS (see **chapter 6**). The synchrotron light from the 3^{rd} generation source is produced by an undulator, which was set to the 9.8 keV incidence energy, well above the Fe K-edge at 7.112 keV. This was a compromise to be high enough above the absorption edge while staying in the detector sensitivity range. The focusing of the beam to 25x1000 µm was done with a lense, to achieve a stable beam with small footprint. Our self developed sample setup (see **section 6.1**) was mounted on a Huber Tower with xyz-translation and θ χ rotation stage. A Princeton CCD detector with 1242 x 1151 pixels and a pixel size of 54x54 μm^2 was set at a distance of 1 m from the sample. In this configuration the available Q-range was $\pm$ 0.16 $Å^{-1}$. The CCD was coupled to a fast shutter system, so that the sample and CCD were only exposed during acquisition. This is necessary for a correct readout of the CCD and protects the sample from radiation damage. The acquisition time of 1 s and a readout time of 7 s defined our time resolution.
- The **laboratory GISAXS setup at the Technical University of Denmark, Risø Campus**, was used to characterize the mesocrystal structure of other dried samples. The measurements were performed using Cu K_α radiation from a rotating anode operated in fine focus mode, monochromatized and focused by a single reflection graded multilayer optics and further collimated by 3 pinholes. The entire beam path is evacuated to prevent air scattering. Two translations and a rotation are available to align the sample. A two dimensional delay line gas detector [44] with a sample-to-detector distance of 1.435 m allows a Q-range of 0.01-0.35 $Å^{-1}$. A 4 mm diameter circular SAXS beam stop was positioned directly in front of the detector and thus the specular line was measurable, too. Such a measurement is possible at this instrument without destroying the detector because of the lower incident intensity compared to a synchrotron source and by selecting an angle of incidence above the critical angle of total reflection. This way it is possible to measure the specular line in the GISAXS pattern, as well. The exposure time was obviously much longer than at a synchrotron (10-30 minutes).

3.8 X-ray diffraction

X-Ray Diffraction (XRD) is the traditional method to investigate the atomic structure and orientation of crystals. An Eulerian cradle with a large angular range is a standard part of a four circle

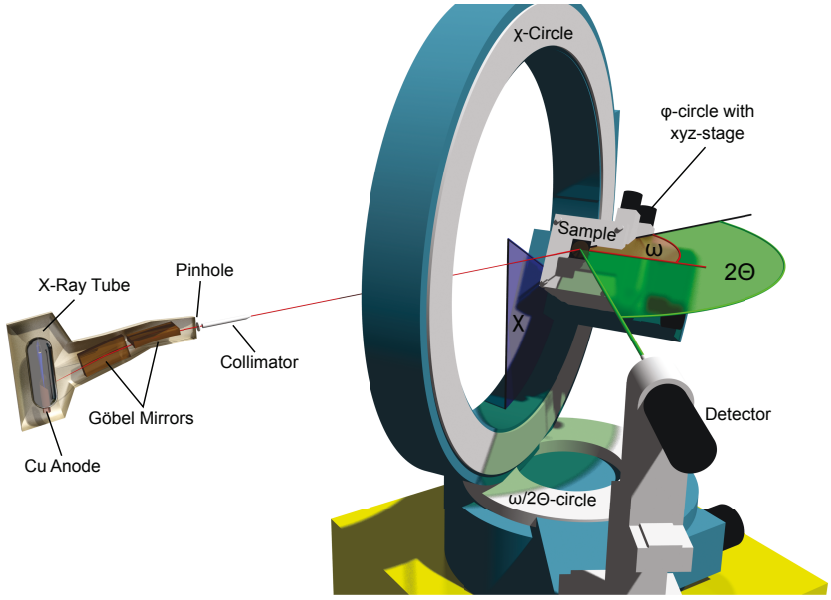

Figure 3.9: Setup for a diffraction experiment- here the inhouse 4circle diffractometer.

or a six circle diffractometer. In this work we used two kinds of diffraction studies, wide angle crystal diffraction on a laboratory 4-circle diffractometer and small angle single mesocrystal measurements on a synchrotron source.

The investigation of preferred orientations of the nanoparticle crystalline lattice inside the mesocrystals was performed at our **Huber 4-circle diffractometer** equipped with a Cu K_α sealed tube X-ray source and a double Göbel mirror monochromator to monochromatize and parallelize the beam. The collimator, which only confines the beamsize, was not used to get more flux on the sample. The beam size was about 2x2 mm^2. The detector arm has slits to define the resolution at the detector and the scattering pattern is recorded by a NaI scintillation detector. The 4-circle diffractometer allows a higher degree of freedom than the D8 instrument because of its 4 angles (ω, 2Θ, ϕ, χ). For $\chi = 90°$ and $\phi = 0°$, a normal $\omega/2\Theta$ -scan geometry is achieved. Other ϕ and χ values allow to reach any Q-position with $Q_z > 0$ in reflection geometry. Additionally, an x y z translation stage is installed for alignment purposes. For approaching the different (hkl) values, the *SPEC* instrument software is used to calculate the angles from the lattice information of γ-Fe_2O_3 given in [72]. While the D8 reflectometer (see **section 3.5**) gives only the out-of-plane information about a preferred orientation with higher intensities, a 4-circle diffraction experiment enabled us to characterize peaks in any direction.

At the **high resolution diffraction beamline P08 of the synchrotron radiation source PETRA III at DESY in Hamburg** [80], small angle diffraction studies have been carried out to investigate the structure of single mesocrystals (see **chapter 7**). To be able to investigate crystals of µm size some requirements are absolutely mandatory: The x-rays have to be focused down to the size of the crystal to achieve high photon flux densities, the beam position has to be stable within a fraction of the sample diameter, the background has to be virtually zero and the motor resolution has to be significantly better than the sample size and the width of the Bragg

reflections.

To achieve focusing with a spot size of 5 µm vertically and 10 µm horizontally, sets of compound refractive lenses [59] have been utilized. The photon energy of 12.4 keV provides a high integrated flux (10^{11} photons/second at the sample) and is sufficiently far away from the iron K-edge at 7.1 keV, avoiding high background due to x-ray fluorescence. The detector of choice was a Princeton Instruments Quad-RO 4096 CCD with 4096x4096 pixels at a pixel size of 15x15 μm^2, mounted 0.77 m from the sample. This detector has a very good efficiency at 12.4 keV. To reduce the background scattering an evacuated pipe was installed between sample and CCD.
The experiment was done in a typical SAXS geometry in transmission (see **figure 3.7**) but with additional rotational degrees of freedom (see **figure 3.9** - This figure also holds for this setup, because we only used 4 degrees of the 6-circle diffractometer.) to enable high resolution diffraction analysis similar to that for atomic crystals, but now on the length scale of nanometers. To translate the sample into the beam an xyz-stage was used, to orient it a double goniometer on top of this stage. After full spatial and orientational alignment, sample-tilt (ω) and sample-azimuth (ϕ) angles have been scanned to take the diffraction patters. The resolution in Q-space is basically determined by the pixel size of the detector and the divergence of the beam. The energy resolution δE/E was $0.5 \cdot 10^{-4}$.

3.9 Space group evaluation of GISAXS data

The analysis of the space group is done according to well established crystallographic methods [7, 11], but with the special case that all reflections hkl from different directions arise in one single GISAXS pattern without any rotation of the sample, as in a powder sample, but with additional directional information for the out-of-plane axis. In other words, the 2D powder leads to reciprocal space rings in the Q_x-Q_y plane and the experiment measures one slice through this plane. The pure (00l) reflections have a ring radius of 0 and therefore lead to much stronger reflections in the measured plane. The flat Ewald sphere in small angle scattering, as well as the 2D powder property with the in-plane orientation average induce this phenomenon. The structural symmetries and inter-particle correlations are described by the structure factor (SF) (see **section 5.1.1**) consisting of the nanoparticle and mesocrystal form factor (FF) convoluted with the unit cell Fourier transform times the reciprocal lattice. In comparison to atomic crystals the nanoparticle FF complicates the analysis as several FF minima lie in the observed Q-range and can lead to additional extinction of reflections allowed by the selection rules. Dividing by the corresponding FF leads to equalized intensity for the peaks. Devision by zero is avoided in this process, as the formfactor always contains a size distribution, leading to non zero values over the whole Q-range. The Q_z direction of the GISAXS pattern contain information of the correlations perpendicular to the substrate, while Q_y exhibits in plane nanoparticle correlations, with a component in a* or the combination of a* and b* as reciprocal lattice vectors. In our case of simple unit cell structure, the first peak in Q_y direction gives the reciprocal lattice constant a* and the smallest distance between any two reflections in Q_z direction, measured at higher Q values to eliminate refraction, is the reciprocal lattice constant c* in c direction of the cyrstal (out-of plane of the substrate). Using this procedure one has to check if a second structure or superstructure exists. If this is the case the structures have to be separated and the same treatment can be used. Indexing of the peak is done by taking multiples of the reciprocal lattice

constants (a* and c*). The existing peaks and the extinguished reflections yields the selections rules, which lead to the possible space groups.

Chapter 4

Fabrication and properties of γ-Fe_2O_3 nanoparticle assemblies

Fundamental research on nanocrystals and self-assembled nanostructures is a major part of today's scientific effort for the design of novel materials [46, 94]. A reproducible production of highly ordered nanoparticle systems is an important step for its further development. The process of self-assembly is a promising way for the fabrication as it allows mass production processes of very small structures over a large area without the use of expensive equipment. The physical process itself is complex, including several interactions between nanoparticles, solvent and substrate [83]. Understanding and optimizing the arrangement of nanoparticles in structures like supercrystals or superlattices at all length scales is an important step towards controlled design.

If the resulting superstructures are μm sized discrete islands of three dimensionally highly ordered particles they are called mesocrystals. This chapter will provide the post deposition properties of the self-assembled structures observed after different deposition conditions and herefrom deduce the properties of the self-assembly process. The gathered knowledge was used to improve the self-organization procedures and tune the resulting parameters of the sample.

Basic requirement for an optimal self-assembly process is the quality of the nanoparticles, especially the size distribution. An overview of the results of the atomic order, magnetic and morphological precharacterization of the single γ-Fe_2O_3 nanoparticles is summarized. Here, the focus is in the morphological characterization including particle size and size distribution.

The main point of this chapter is the preparation and the three dimensional structural characterization of highly ordered assemblies of iron oxide nanospheres and nanocubes. A short overview of the known mechanisms of self-assembly is given and discussed with respect to the system used. The structural characteristics of the assemblies are introduced and analyzed with the application of several complementary methods for a good overview. The influences of the preparation conditions on the resulting structures have been studied, allowing to optimize and selectively influence the system. Under extraordinary conditions completely different macroscopic structures can evolve. Preferred directions of the single nanocrystals inside the mesocrystals may lead to a change of the overall magnetic behavior due to the aligned anisotropy axis. These aspects are also discussed in the present chapter.

4.1 γ-Fe_2O_3 nanoparticles

This section provides an introductory description of the γ-Fe_2O_3 nanocrystals used, showing the good quality of the samples as revealed by the morphological characterization including particle size and size distribution.

4.1.1 Preparation

Spherical and cubic particles were used for the investigations described in this work. The samples in the form of pastes or solutions were obtained through a collaboration with Prof. L. Bergström and his group from Stockholm University, Sweden. The synthesis of the nanoparticles [14] is a modification of the nonhydrolytic thermal decomposition of iron-oleate in an high-boiling organic solvent [68]. The following information about the particle fabrication was provided in a private communication with German Salazar Alvarez and Erik Wetterskog from the mentioned group.

The iron-oleate complex was prepared following a procedure similar to what has been previously reported [14]: 10.8 g of iron chloride ($FeCl_3 \cdot 6H_2O$, 40 mmol, Aldrich, 98 %) were refluxed with 36.5 g of sodium oleate (120 mmol, Sigma, 82 %) in a solvent mixture of 140 cm^3 hexane, 80 cm^3 ethanol and 60 cm^3 distilled water at 70 ° for 4 hours. The organic phase was washed three times in 30 cm^3 of distilled water prior to the removal of hexane using a rotary evaporator. A dark brown iron-oleate residue is achieved from this process.

The synthesis was performed in a solution of 36 g of the iron (III) oleate (40 mmol) and 200 cm^3 1-octadecene (Aldrich, 90%) degassed under vacuum at 80 °C for 1 hour to remove water prior to the addition of oleic acid and increasing the temperature up to the reflux temperature of 320 °C. The synthesis process by thermal decomposition of iron-oleate in an high-boiling organic solvent allows a perfect control of nanoparticle size and size distribution due to the separation of the nucleation and growth kinetics, which result from the separate temperature dependence of the processes [68]. Nucleation centers are produced through a decomposition of the iron oleate by heating up the precursor solution slowly through the nucleation temperature range of 200-240 °C to higher temperatures. The slow increase of the temperature enables the nucleation process to finish before the growth process starts. The growth rate of the particles accelerates above 300 °C and is temperature dependent. To reach smaller nanoparticles, a lower boiling solvent and shorter heating time at the boiling point is necessary. The additional amount of oleic acid during the synthesis influences the particle size, too. In the case of the particles used the shapes were controlled by the amount of additional oleic acid (the iron-oleate:oleic acid molar ratio) and the heating rate [14]. The small decrease of the heating rate from 3 °C/s to < 2.6 °C/s together with a lower additional amount of oleic acid supports the production of nonsperical nanocrystals. For the synthesis of nanospheres, 5.7 g (20 mmol) of oleic acid was added and a regular reflux apparatus setup was used and heated up with 3 °C/min up to 320 °C, whereas for the synthesis of nanocubes, a Dean-Stark condenser was incorporated, the solution was heated up at 2.6 °C/min to 320 °C and 3.2 g (11.3 mmol) of oleic acid was needed. Both mixtures were refluxed for 30 min under N_2 after which the vessel was allowed to cool down.

The nanoparticles were separated by centrifugation through several precipitation cycles using a solvent/non-solvent pair (n-heptane/ethanol) resulting in a concentrated paste. At the end

Solution ID	shape	concentration	solid content in paste (from TGA)	solvent
$S_S^{0.1}$:	spherical	$0.1{\cdot}10^{14}$ NP/ml	61 wt%	toluene
$S_C^{0.1}$:	cubic	$0.1{\cdot}10^{14}$ NP/ml	43.5 wt%	toluene
$S_S^{1.0}$:	spherical	$1.0{\cdot}10^{14}$ NP/ml	61 wt%	toluene
$S_C^{1.0}$:	cubic	$1.0{\cdot}10^{14}$ NP/ml	43.5 wt%	toluene
$S_S^{4.7}$:	spherical	$4.7{\cdot}10^{14}$ NP/ml	61 wt%	toluene
$S_C^{4.7}$:	cubic	$4.7{\cdot}10^{14}$ NP/ml	43.5 wt%	toluene
$S_S^{8.4}$:	spherical	$8.4{\cdot}10^{14}$ NP/ml	61 wt%	toluene
$S_C^{8.4}$:	cubic	$8.4{\cdot}10^{14}$ NP/ml	43.5 wt%	toluene

Table 4.1: Produced nanoparticle solutions which were used.

a black nanoparticle paste is achieved with 61 wt% iron oxide for the spheres and 43.5 wt% iron oxides for the cubes. The fraction of inorganic content of this paste was estimated from the residual mass after heating to 800 °C in air employing a Perkin Elmer Thermogravimetric Analyzer TGA-7 at a heating rate of 10 °/min.

The dispersions were produced by diluting the paste in toluene in a ratio determined from the iron oxide content to achieve the desired particle concentrations. For a nicely dispersed solution, manual shaking and subsequently sonication for 15 minutes is applied to produce stable solutions. The solutions used and their sample IDs are listed in **table 4.1**. The capital S is the symbol for solution, the subscript character for the shape (S:spherical, C:cubic) and the superscript the concentration. These sample ID's will be used for the identification of the nanoparticle solutions in the subsequent chapters.

4.1.2 Structural characterization

The structural characterization of the nanoparticles inside the solution is an important prerequisite to understand the results of the investigations of the ordered particle assemblies. In addition to the characterization done in this work, an extensive collection of results published in the PhD thesis of S. Disch [103] is available.

Structure on the atomic scale

The nanoparticles used consist of an inorganic core covered with an organic shell. The atomic structure of the inorganic core is crystalline and shows an inverse spinel structure with $a = b = c = 8.36\,\text{Å}$ and a $Fd\bar{3}m$ space group having 8 formula units, which was confirmed by x-ray diffraction [52, 103]. The distinction between magnetite (Fe_3O_4) and maghemite (γ-Fe_2O_3) could be made using the occupancy of the iron sites, deduced by Mössbauer spectroscopy and the atomic pair distribution function. From this analysis predominantly maghemite was found [52], suggesting a core shell structure consisting of a magnetite core (less than 5-10%) and a maghemite shell [103].

Morphological characterization

The extraction of the particle size distribution and the average radius of the nanoparticles is an important pre-characterization for the self-assembly and all further investigations. This study was done in this work with small angle X-ray scattering at an in-house lab source (**section**

Solution ID	model	radius r_{NP}	edge length a_{NP}	size distribution σ	degree of truncation τ
$S_S^{0.1}$:	spherical FF	5.01 ± 0.02 nm	/	$6.3 \pm 0.5\%$	/
	truncated cube FF	/	10.02 ± 0.04 nm	$5.6 \pm 0.6\%$	0.94 ± 0.05
$S_C^{0.1}$:	rounded cube FF	/	10.90 ± 0.04 nm	$5.8 \pm 0.5\%$	0.80 ± 0.05
	spherical FF	6.04 ± 0.02 nm	/	5.6 ± 0.4 %	/

Table 4.2: Results of the SAXS analysis for the morphological characterization of spherical and cubic γ-Fe_2O_3 particles. The data for the cubes were fitted with different form factor (FF) models as comparison. The description of the models can be found in **section 5.1.1**. The errors are estimated from the fitting procedure.

3.6). SAXS investigations give only structural information about the inorganic nanoparticle core due to the small contrast between the nanoparticle shell and the organic solvent. X-rays mainly probe differences in electron density, which is very similar for the oleic acid ligand and the matrix of toluene. The determination of the organic shell thickness is only possible with a SANS measurement, which was done by S. Disch [103]. With neutrons, a strong nuclear contrast between non-deuterated oleic acid and deuterated toluene can be used to be able to determine the shell thickness.

The nanoparticle dispersions $S_S^{0.1}$ and $S_C^{0.1}$ were diluted from higher concentration for this experiment to have enough scattering centers, but not to be too dense to produce too much absorption or to create a structure factor. The solution was poured into Hilgenberg borosilicate glass capillaries with an outside diameter of 1.5 mm and a wall thickness of 0.01 mm. The capillaries were sealed by melting the glass with a torch. The raw datasets were time-normalized and corrected for the detector sensitivity, empty cell scattering and dark current. The I(Q) scattering curves were determined by radially averaging over the corrected data. In addition, the dataset was normalized to absolute units by the use of a reference material. The resulting S(Q) plots are shown in **figure 4.1** and **figure 4.2** .

The results listed in **table 4.2** were extracted by fitting the data with the corresponding form factor (FF). The instrumental resolution is taken into account to achieve a good refinement of the model to the data and to avoid a masking of the narrow size distribution due to limited instrument resolution. The small structure factor contribution for the $S_C^{0.1}$ solution in the lower Q-range is negligible, as the data above 0.05 Å can be perfectly fitted with a pure form factor. Small agglomerations and/or a too large density in the solution can generate such a structure factor. In this case the refinement was done in the Q-range where the structure factor contribution could be neglected.

The depth of the minima already indicate a very narrow particle size distribution. In this case the log-norm size distribution of the model ($\sigma_{a_{NP}}$, $\sigma_{r_{NP}}$) certifies a narrow distribution around 6 $\pm$ 0.5% for both solutions, which is in agreement with earlier studies [34, 103]. These monodisperse nanoparticle solutions are an important pre-condition to achieve a well ordered assembly of particles [99] and to have magnetic characteristics homogeneously over the solution, due to the size dependent blocking temperature [107, 108].

The information about the average size of the inorganic nanoparticle cores in the solution is contained in the position of the minima of the oscillations. Larger particles will lead to a shift of the minima positions to lower Q values. The refinement of the $S_S^{0.1}$ solution with a spherical FF shows a perfect agreement (**figure 4.1**) and yields an average radius r_{NP} of 5.01 ± 0.02 nm

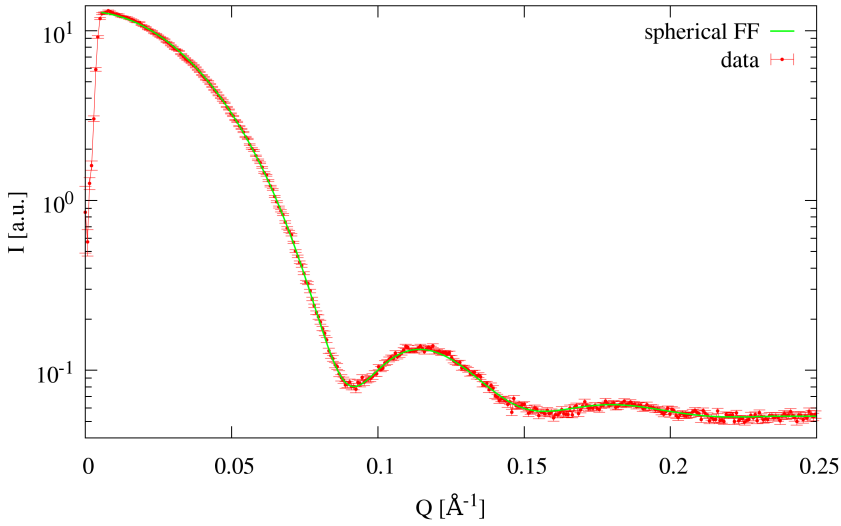

Figure 4.1: SAXS from spherical particles $S_S^{0.1}$ fitted with a spherical FF. The fit parameters are shown in **table 4.2**.

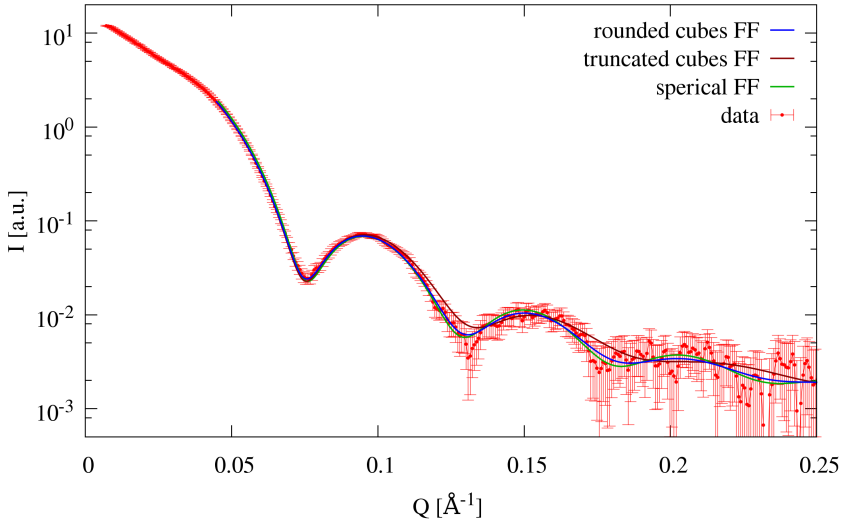

Figure 4.2: SAXS from cubic nanoparticles $S_C^{0.1}$ fitted with a spherical, truncated cubes and rounded cubes form factor. The fit parameters are shown in **table 4.2**.

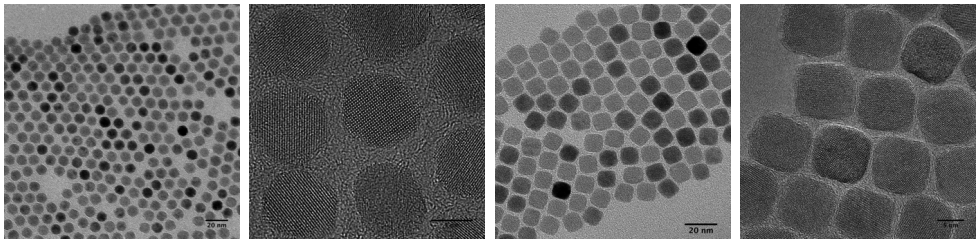

(a) Spherical particles **(b)** Spherical particles with high resolution **(c)** Cubic particles **(d)** Cubic particles with high resolution

Figure 4.3: TEM pictures of the used particles, deposited on a TEM grid.

of the particles. TEM pictures of single spherical particles with different magnifications are presented in **figures 4.3a, 4.3b** and confirm the spherical shape and narrow size distribution. The determination of the organic shell by S.Disch shows a shell thickness of 1-2 nm [33, 35, 103] and has to be considered for the distance between two nanoparticles in the assemblies described later.

The SAXS data from the cubic nanoparticles $S_C^{0.1}$ were fitted with a truncated cubical [33], a spherical [71] and the newly developed rounded cubical FF (**equation 5.5**, **figure 5.1**). All are shown in **figure 4.2**. The best refinement of the truncated cube model does not fit the data at all minima and shows that this morphological model with flat facets is not describing these particles very well. The model of highly truncated rounded cubes and the spherical FF fit the scattering curve much better, but the data is insufficient to distinguish between the two models. Small differences in the shape could be visible with a larger Q-range, which could ,however, not be accessed with the lab-source instrument due to the low intensity. The TEM pictures with high resolution show clearly a cubic shape characteristic with rounded edges (**figure 4.3d**). The result of the form factor modeling yields a non-spherical nanoparticle with an edge length a_{NP} of 10.90 ± 0.04 nm and an degree of truncation τ_{Round} of 0.8 ± 0.05. It should be noted that these results are an average over all particles in the solution.

4.2 Self-assembly of 3D ordered nanoparticles

This section will focus on the preparation and characterization of highly ordered 3D nanoparticle assemblies of iron oxide nanospheres and nanocubes. The nanoparticle superstructures developed are single crystals consisting of nanoparticles and are called supercrystals or (in this thesis) mainly mesocrystals. A further step of understanding and optimizing the process of mesocrystal growth is one main goal.

4.2.1 Sample preparation

For the preparation of highly ordered 3D supercrystals of different nanoparticle shapes, a drop casting method is used to generate a drying-induced self-assembly. A substrate is covered with the nanoparticle suspension, and during the evaporation of the solvent in a controlled

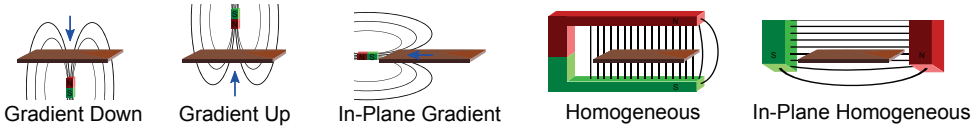

Figure 4.4: Schematics of the various applied magnetic fields.

atmosphere and under an applied magnetic field the nanoparticles arrange in ordered structures. The physical process itself is complex, including several interactions between nanoparticles, solvent and substrate. A more detailed description of the self-assembly mechanism is given in **chapter 6**. The drop casting method allows us to produce an ensemble of mesocrystals over a 2" substrate homogeneously. Details about the exact preparation technique are summarized in the following paragraphs.

Substrate and substrate cleaning
As substrates, silicon wafers with a thickness of 525 $\pm$ 25 µm, N/Phosphor doping and a $\langle 100 \rangle$ orientation from the Si-Mat company are used. Depending on the requirements of the experiments, samples from 5x5 mm^2 to 2" size were produced. Before the drop casting, the substrates are cleaned by sonication in ethyl acetate and ethanol for 30 min each. Afterwards they were stored in an ethanol bath until use. Before the usage the substrates were dried with compressed N_2 to prevent from dust trapping.

Evaporation chamber
The self assembly takes place in a closed petri dish or the customized in-situ cell (**section 6.1**). Both chambers have the possibility to control the evaporation rate with a well-defined amount of toluene in a dedicated reservoir inside the evaporation chamber. The in-situ cell has additional outlets to control the gas exchange between the chamber and the surrounding atmosphere. The setups allow a time for complete evaporation of the solvent between a few minutes and several days, which could be reached using the open chamber with no reservoir, or the closed chamber by saturating the atmosphere before the drop casting and using 400 µl toluene as reservoir. To produce a well ordered assembly of mesocrystals with a defined shape, longer evaporation times are needed (see **section 4.2.4.3**).

Deposition
The substrate surface is aligned horizontally using an adjustable table and a spirit level. The Si-substrates are then covered with a nanoparticle solution in toluene with a concentration of $8.4{\cdot}10^{14}$ NP/ml ($S_S^{8.4}$ and $S_C^{8.4}$) for mesocrystal growth and $1.0{\cdot}10^{14}$ NP/ml ($S_S^{1.0}$ and $S_C^{1.0}$) as base suspension to produce dilute solutions for monolayer growth. A typical deposition is made by applying a 20 µl droplet per cm^2 on the cleaned wafer.

Magnetic field
For most samples a defined magnetic field was applied during the process of self assembly. For the optimization of this process, the influence of the magnetic field direction and strength on the mesocrystal growth was investigated (see **section 4.2.4.2**). For this study, magnetic fields with field gradient pointing away from the sample surface $H_{\underline{\curlywedge}}$ (gradient up), pointing towards the sample surface $H_{\underline{\curlyvee}}$ (gradient down) and pointing along the substrate $H_{\underline{\succ}}$ (gradient in-plane), as well as a homogeneous field in the in-plane $H_{\underline{\rightrightarrows}}$ (in-plane homogeneous), the out-of-plane direction $H_{\underline{\uparrow\uparrow}}$ (homogeneous) and with zero field were applied (see **figure 4.4**). The strength of the magnetic fields reached from a few mT to 100 mT at the sample position with a

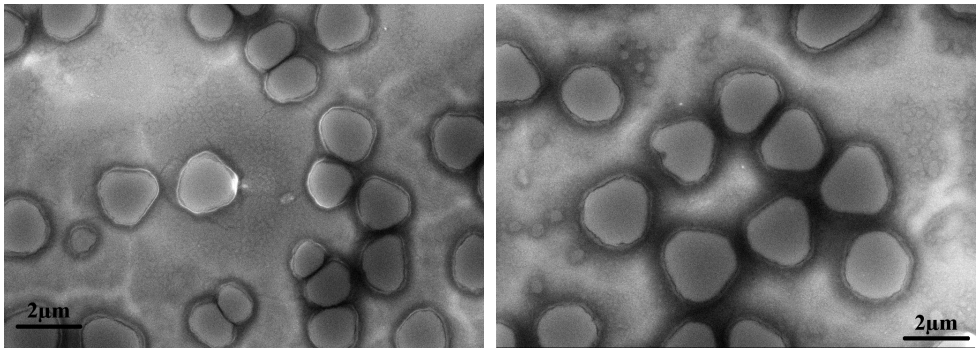

(a) sample 1 **(b)** sample 2

Figure 4.5: Samples produced under the same conditions.

gradient between 10^{-1} and 10^2 mT/cm. The magnetic fields were accomplished either by a coil especially for the 2 inch samples or a permanent magnet with a smaller area but higher field strength and gradient. The fields were applied during the entire drying processes.

Sample IDs
The self-assembled samples will be referred in the following by:

$$\mathrm{D}^{\text{time, particle surface density, gradient direction and field strength}}_{\text{shape, size, degree of truncation}}$$

at which D denotes a drop-casted sample. The shape denotes one of S for spherical and C for cubic particles. The size of the particle is given in nm, at which the number indicates a radius for spherical and an edge length for cubic nanoparticles. The degree of truncation is only given for the cubes. The time was varied between short (SH), which was a few minutes, medium (MD), meaning a few hours and long (LG), where the droplet evaporation needs days. The particle surface density deposited on the substrate is given in $\cdot 10^6$ NP/ mm^2 and was calculated from the particle density in the solution, the deposited amount and the substrate surface area (e.g. $1.86 \cdot 10^6$ NP/ mm^2 $\widehat{=}$ a concentration of $8.4 \cdot 10^{14}$NP/ml, an amount of 20 µl solution and 1 cm^2 surface area). The symbols for the gradient directions are used as defined in the paragraph above and the value of the field strength is given in mT. The used sample ID gives all necessary information about the parameters of the self-assembly and will be used in the subsequent chapters.

Reproducibility
In this PhD work, all $\approx$ 300 samples showed formation of mesocrystals. The reproducibility of the mesocrystal growth could be guaranteed by continued use of the same process and the respective parameters. The same solutions with constant concentration, equivalently treated substrates and precisely defined amounts of solution per surface were used. Thus it was possible to reach the same number of particles per cm^2. The same conditions on the substrate surface lead to the same droplet wetting behavior, which again can influence the self-assembly process. The reproducible order of magnitude of evaporation speed is an important factor for the self-assembly due to the time available for the ordering and could be verified using the light-band micrometer (**section 6.1**). Especially the in-situ cell enables perfectly reproducible conditions for the control of the growth parameters.

Mesocrystal samples produced with the same parameters show similar characteristics (compare **figure 4.5a** and **figure 4.5b**). Nearly the same surface coverage, equivalent mesocrystal shapes and sizes are observed.

4.2.2 Model for the mesocrystal growth

The 3D supercrystals are produced by an evaporation induced self-assembly on a substrate. In general, self-assembly is understood as autonomous ordering of preexisting components into more complex structures without external intervention [94]. Autonomous ordering means an organization induced by specific interactions between the components themself. Model concepts of the mesocrystal growth will be discussed in this section to explain the process and its outcome.

The substrates are covered with nanoparticle dispersions consisting of γ-Fe_2O_3 nanoparticles with oleic acid as ligand dissolved in toluene. The entire substrate surface is wetted with a droplet (see **figure 4.6a**), even for 2" wafers. The nanoparticles are freely movable in the solution by Brownian motion. During the controlled evaporation of the toluene the droplet shrinks, the contact line between the substrate and the end of the droplet stays pinned (see **section 6.3** stage 1) and the particle density of the solution increases, yielding less free space for the nanoparticle motion. The process of self-assembly is not induced before a critical concentration is reached which is defined by the length scale and magnitude of the required interactions [24]. The short mean free path of the particles increases the probability of the formation of stable clusters [24] (**section 2.1.5**) which act as nucleation centers for the growth of mesocrystals. The necessity of a critical concentration is experimentally shown in **section 6.3**.

The process of self-assembly is governed by the interaction of different attractive and repulsive forces. As described by Bishop et al. [24], van der Waals, electrostatic, magnetic and entropic forces are the fundamental interactions between nanoparticles and can be used to tune the nanoscale self-assembly. For our system the van der Waals and dipole-dipole attraction, as well as a steric repulsion make up the total interaction potential.

The self-assembly of sufficiently small particles into ordered states is mainly induced by the attractive van der Waals force [24, 33, 58, 99]. The electrostatic repulsive interaction forces, due to overlap of electron orbitals of the outer atomic shell, provide the balancing force to create stable structures [14, 24, 99]. The application of a medium strength magnetic field during the self-assembly induces a stronger dipole-dipole attraction in super paramagnetic particles, but has minor influence on the self-assembly itself. This could be shown experimentally in **section 4.2.4.2**, where in absence of an external magnetic field equally highly ordered mesocrystals have been fabricated. Furthermore the dipolar interaction is direction dependent, which renders it improbable to be the guiding force of a 3 dimensional crystal growth. The magnetic interparticle forces get relevant for the self-organization process if a strong magnetic field, for example 0.6 T for 10 nm γ-Fe_2O_3 nanoparticles, is applied during the drying. It then dominates the self-assembly [24, 58]. An additional influence on the ordering can originate from entropic effects at higher densities, where a high nanoparticle concentration generates a driving force to order the system to minimize its free energy [24]. In our system it is difficult to decide between the contribution of the van der Waals force and the entropy driven self-assembly (non-interacting), as similar behavior is observed in both systems at the critical density[24], but the selective

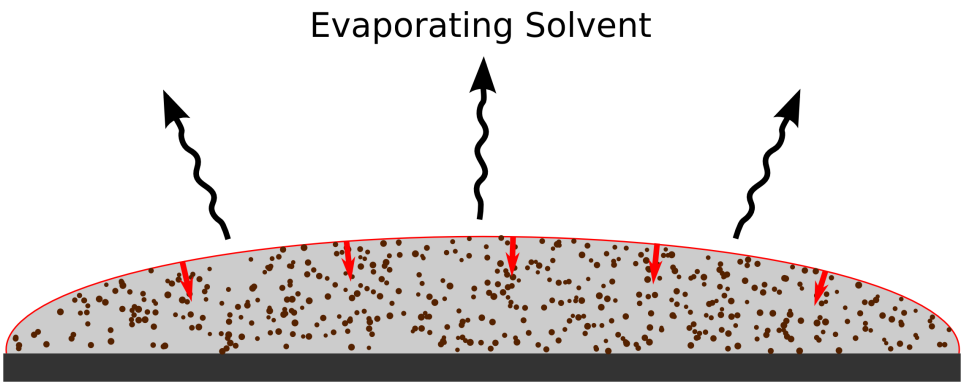

(a) Droplet evaporation

(b) Dense solution to reach the critical concentration for nucleation.

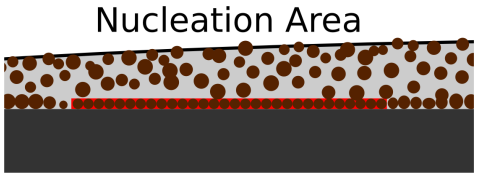

(c) Nucleation area where the shape and size selective 3D growth can take place.

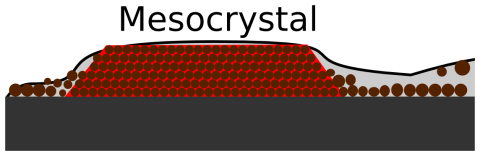

(d) Grown mesocrystal consists of one kind of particle size and shape. The residual particles are deposited on the ground only with a very short range ordering.

Figure 4.6: Schematic illustration of the model of the self-assembly of an ensemble of mesocrystals. The red box illustrates one nucleation area, which is magnified in the last two pictures.

ordering process described in the next paragraph strongly points to a sizable van der Waals interaction, as it is needed to explain this effect.

The droplet is very thin when reaching the concentration threshold for the self-assembly. This critical value is given, when the droplet reaches the stage of the horizontal drying front (see **section 6.3**, stage 3), where a circular inward movement of the contact line between the substrate and the end of the droplet is observed. The contact line area fulfills the conditions for the self-assembly and this area is marked with the red box (see **figure 4.6b**). In this region the mesocrystal growth takes place (see **section 6.3**) and leaves behind the drying front a coffee-stain-like ring of dense material agglomeration [22, 31, 32] at the edge of the substrate and in the inner region well separated mesocrystals. The nucleation starts at the substrate, which could be experimentally shown in **section 6.3**. Separated particles accumulate on the substrate when reaching a sufficiently small distance to get attracted by the van der Waals force between substrate and particles. It is possible that the attachment of single particles also happens before the threshold is reached, but with a low density only single particles are captured, which can be separated again easily. The particles assemble in a size- and shape selective ordering, as the

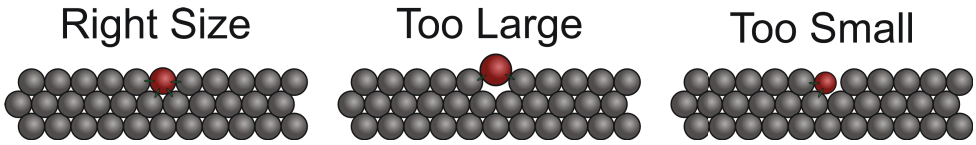

Figure 4.7: Schematics of the size dependent bonding formation in a vacancy of a regular nanoparticle superlattice.

growth with the same particles leads to minimization of the surface energy. In other words, differently sized or shaped particles will lead to lattice defects in the crystal structure inside one mesocrystal, which creates a lower packing density and thus an energetically unfavorable state. It is imaginable that a particle, which is much smaller than a regular lattice vacancy can bond only to maximum 3 out of 8 possible neighbors (see **figure 4.7**). It thus exhibits less bonding and can more easily be removed from the lattice. A too large particle for the existing vacancy does not fit into the vacancy and is therefore weakly bound as well. Thus the nanoparticles prefer to self-assemble with particles of the same size and shape. In other experiments it has been observed that for a two-dimensional assembly the largest particles order in the center, while the smallest particles accumulate at the periphery [24, 60, 64, 67]. The explanation of Bishop et al, Murthy et al. and Ohara et al. is that the size-dependent magnitude of the van der Waals interactions between the particles lead to a size- and shape selective ordering of the particles [24, 64, 67]. Such an effect has been observed at the ground layers of the investigated systems as well (see **figure 4.9a**), where no mesocrystals have grown. Crystal defects or strain occurs when the evaporation was fast and no more suitable particles are available to fill the existing gaps. Dislocations can arise by mechanical pressure on the growing crystal. It is possible only in certain cases, e.g. in binary superlattices, that the nanoparticles order with multiple components inside one superstructure, as the solution has a selected size and concentration ratio and allows an ordering in an energetically favorable high packing density structure [36, 74, 81].

In our case with highly monodisperse nanoparticle solutions, areas with highly ordered 2D nanoparticle assemblies of the same size and shape connected by areas with less ordered particles grow on the substrate. The highly ordered regions are nucleation areas for the 3D mesocrystal growth. The nucleation starts when reaching the critical concentration as described above. Nanoparticles are movable in the solution near to the substrate surface to find an energetically favorable position. It can be imagined that the layers grow similar to the epitaxial growth of thin films. In this situation atoms move on the surface and attach to adatoms, steps or step edges, where they loose their mobility due to the additional bond formation, which in the nanoparticle case is the van der Waals attraction. Ganapathy et al. could show for colloids with diameters of 1.0 or 1.3 µm that colloidal epitaxy obeys the same two-dimensional island nucleation and growth laws that govern atomic epitaxy [45]. Layer-by-layer growth can be assumed in **figure 4.8**, where the layers are not closed due to an interrupted mesocrystal growth after drying because of the low concentration used. Differences to the atomic crystal growth are the distribution of size and shape of the particles and the forces involved. The size and shape selective self-assembly leads to a growth of similar particles on the nucleation areas, continuing the growth with the existing structure. Such a shape and size self-segregation could be observed for 3D growth in previous publications [86], as well as in this PhD work for the corresponding system not only in microscopy, but using depth resolved GISAXS (**section 4.2.4.4**) and single crystal diffraction, as well (**section 7.3**). The particles start to order in the confined 3D arrange-

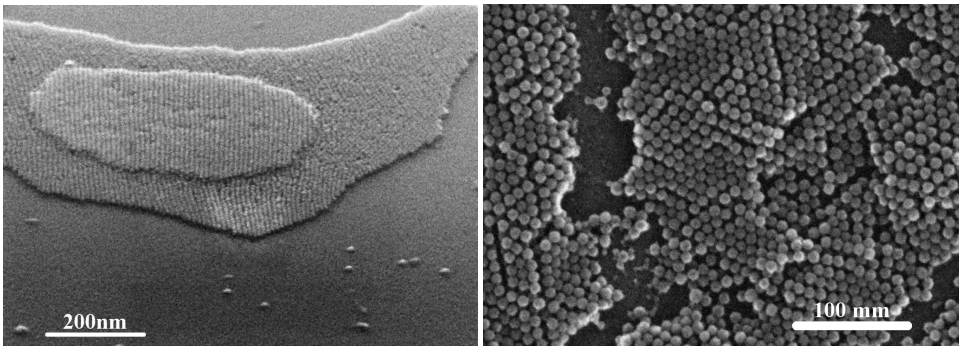

(a) Layer-by-layer growth

Figure 4.8: Illustration of characteristics of the mesocrystal self-assembly: Layer-by-layer growth can be assumed in these SEM pictures, where the layers are not closed because of an interrupted mesocrystal growth after drying due to low solution concentration.

ment, due to the finite area of nucleation centers, which result from a finite diffusion length. Nanocrystals which do not match continue to move around to find a vacancy in a mesocrystal or sediment on the ground as residual particles (see **figure 4.9a** and **appendix figure A.1**). The base layer is short-range ordered in a 2D assembly. For the areas with extremely different particles and hence more disorder, a good template to provide a crystalline growth is missing. It has to be mentioned that the surface of the substrate has not to be fully covered with a monolayer before the 3D ordering starts (see **figure 4.9b**, where a the first layer is not closed after drying). At the end of the self-assembly an ensemble of separated mesocrystals is generated (see **section 4.2.3**), covering all of the former nucleation areas. The 3D growth scheme is schematically shown in **figure 4.6d**. A comparison with the growth modes of atomic films shows remarkable similarities to the island or so called Volmer-Weber growth [19].

The substrate plays an important role for the self-assembly of the ensemble of mesocrystals, as the van der Waals interaction attracts the particles to the surface and thus provides a plane for the crystallization. It defines one crystal axis in the growth direction. The important condition of the coherence between the crystal structure of the substrate and the growing material for thin films for example is negligible in the nanoparticle case, as the particles are much larger than atomic distances and the atomic roughness or mismatch to the lattice has no influence on the binding energy.

The shape and quality of the mesocrystals is governed by various factors. Beside the basic requirements like uniform particles in size, shape and sufficient time for the particles to find a good vacancy in the growing crystals is an important condition to form long range ordered supercrystals (see **section 4.2.4.3**). The width of the mesocrystals is mainly defined by the region of well ordered nucleation areas. Furthermore the width is always larger than the height of the crystals, which can be explained by the way that the superstructure is growing from the predefined area on the substrate with a given size and a finite diffusion distance combined with a finite number of suitable particles. It is imaginable that a larger time window, a higher solution quality and a higher concentration can produce higher mesocrystals, unless the droplet height needed for the critical concentration is too low. The top of the mesocrystal is mainly flat which is a result of the layer-by-layer growth starting at the substrate plane. Additionally,

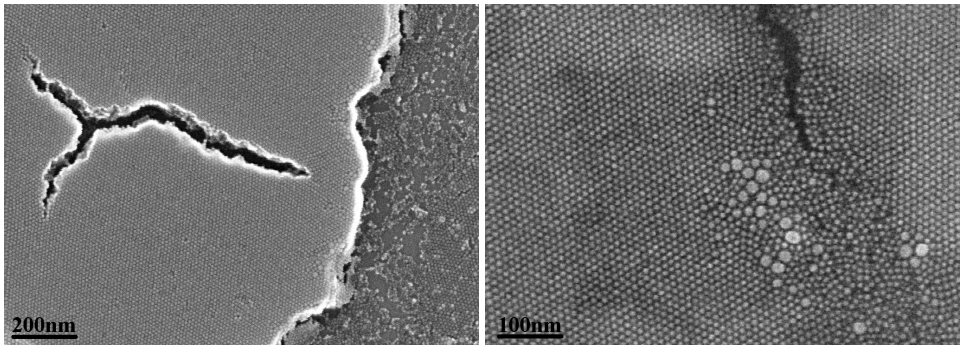

(a) Residual nanoparticles mainly sediment on the ground.

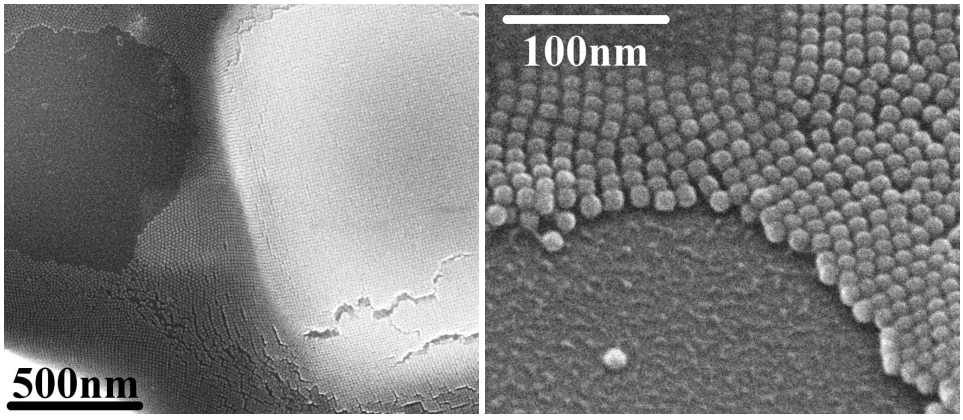

(b) Not fully closed base layer.

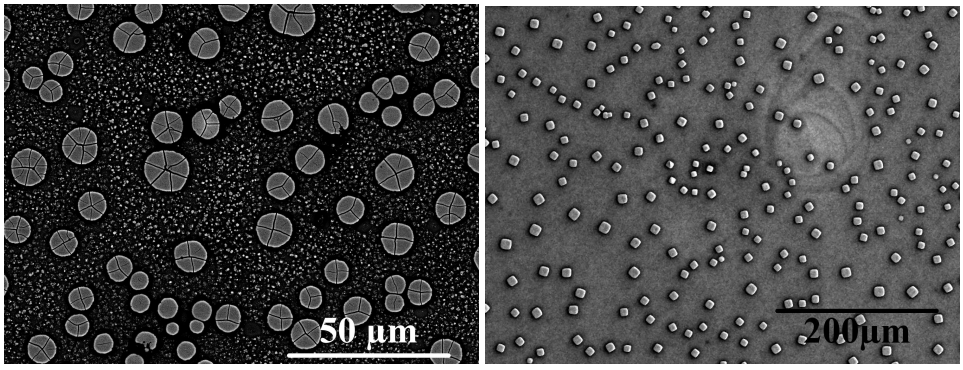

(c) Cylindrical/hexagonal shape for spheres **(d)** Quadratic shape for cubes

Figure 4.9: Illustration of characteristics of the mesocrystal self-assembly measured by SEM: The residual particles are shown on the base layer (**figure 4.9a**). The size dependent self-assembling is also observed in **figure 4.9a**, despite the small number of particles. Gaps in the base layer can be seen in **figure 4.9b**. **Figure 4.9c**, **figure 4.9d** illustrate the dependence of the shape of the mesocrystal on the geometry of the unit cell from the nanoparticle superstructure. A more cylindrical/hexagonal shape is grown for spheres and quadratic shape for cubes with small degree of truncation. **Figure 4.9d** shows also cracks inside the mesocrystal by higher magnification like the crystal consisting of spheres.

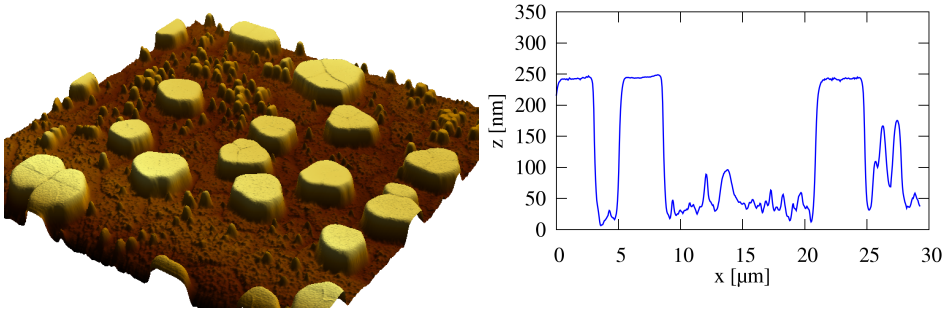

(a) Mesocrystals with perpendicular edges.

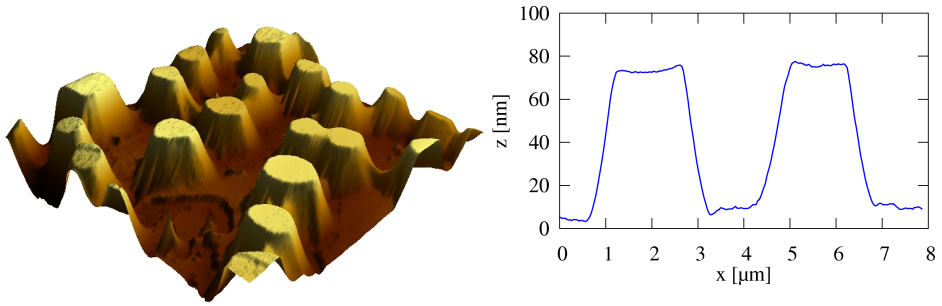

(b) Mesocrystals with trailing edges.

Figure 4.10: Illustration of characteristics of the mesocrystal self-assembly: A mesocrystal growth with and without inclined edges can be observed by AFM. The insets in the AFM pictures show a cross section for better illustration.

it is observed that the planes are almost always closed on the top of mesocrystals. This growth mode can be understood similarly as for thin films, where it is easily possible to move bound atoms on top of a surface and down an edge, as the number of bonds is low, but not up an edge as it costs too much energy. Additionally, it is imaginable that the surface of the droplet (nucleation starts at the substrate-liquid-air interface) can influence the surface as a plane boundary. Dependent on the geometry of the unit cell of the nanoparticle superstructure, the mesocrystals grow in different geometrical bodies like a cylindrical/hexagonal shape for spherical and more quadratic shape for cubic nanoparticles (see **figure 4.9c and 4.9d**). It can be assumed that mesocrystals form facets along their lattice planes as is found in atomic crystals. In addition it has been observed that some mesocrystals have inclined edges (**figure 4.6d** and in reality measured by AFM **figure 4.10b**), while others show straight edges to the substrate (see **figure 4.10a** and **appendix figure A.2**). Based on the model of the self-assembly, it is conceivable that a nucleation area which is not completely grown before the 3D ordering starts[1] leads to inclined edges, while the middle part of the mesocrystal is already growing in height, the nucleation area is still growing outwards. The middle part can grow higher than the outer one and so inclined

[1]The first layer of the nucleation area can only grow laterally until it is confined by disordered particles.

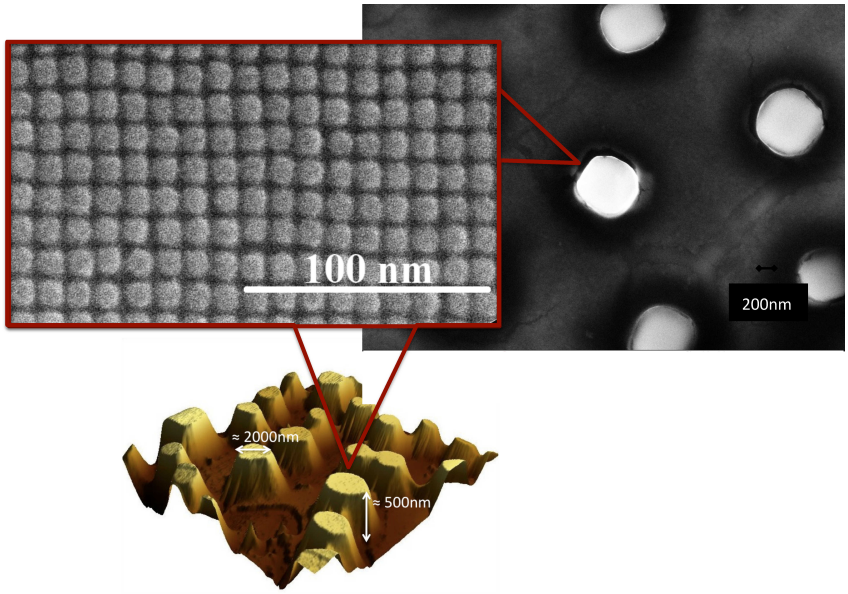

Figure 4.11: Ensemble of mesocrystals measured with AFM for its topography (bottom). The right SEM image shows a view from the top and the left picture shows the nanoparticle order on top of one mesocrystal with higher magnification.

edges are developed. For a terminated nucleation area the particles grow layer-by-layer and the mesocrystal has straight edges. Comparing the results of a self assembly with (medium) and without magnetic field points to the van der Waals interaction as the major driving force for building well ordered mesocrystals, as the ordering pattern is not changed by the magnetic field and the structural coherence length is already very high without it (see **section 4.2.4.2**). Applying a medium strength magnetic field for different gradient orientation during the process of self-assembly supports the process of building a mesocrystal or works as a source of irritation. The additional influence does not destroy mesocrystal assembly, but shows changes in the mesocrystal's shape, size and degree of ordering. Only extreme magnetic fields change this result dramatically, distorting or even destroying the resulting mesocrystals (see **section 4.2.4.4**).

4.2.3 Ensemble of mesocrystals

The self-assembly procedure as described in **section 4.2.1** for depositing the γ-Fe_2O_3 nanoparticles introduced in **section 4.1** yields pillars or islands of nanoparticles on top of a thin ground layer of particles (see **figure 4.11**). These islands are called mesocrystals and the complete sample is therefore an ensemble of about 10^6 mesocrystals.

The term mesocrystal is defined as a three dimensional highly ordered assembly of nanoparticles. The particles are arranged like atoms in a crystal and scattering experiments reveal properties of a single crystal (see **chapter 7**). The size of the building blocks leads to the term "mesocrystal", which is an abbreviation for "mesoscopically structured crystal" [61]. The

mesocrystals have a size of 0.5-10 µm in diameter and extend up to 700 nm in height. To give an idea about the number of particles inside one mesocrystal, the sample shown in **figure 4.11** with crystals of 2000 nm diameter and 500 nm height incorporate about 5 million nanoparticles in each mesocrystal. The top of the mesocrystal is obviously flat, which is shown in the AFM topography picture (**figure 4.11 bottom**) and can be estimated from the SEM picture (**figure 4.11 top, right**). The higher magnification from the top of a mesocrystal shows how nicely the particle are ordered, in this case cubes arranged in a square lattice (**figure 4.11 top, left**).

The AFM picture (**figure 4.11 bottom**) illustrates the distribution of mesocrystals on the substrate for a typical sample. The single crystals are arbitrarily orientated in the plane, but with a preferred c-axis orientation defined by the substrate's surface normal. A sample with arbitrary in-plane rotation of crystals is called a 2D powder. In this case a scattering experiment can access different lattice planes at once as they are realized in different mesocrystals on the same substrate and the pattern shows a lot of reflections without rotating the sample, as would be required for a single crystal. The arrangement of the mesocrystals on the substrate is mostly random without a fixed distance, special order or texture.

4.2.4 Influence of deposition parameters on the mesocrystal characteristics

A knowledge of the influences of different external parameters on the process of self-organization and the final characteristics of the mesocrystals is an important step to optimize the method. An in-situ study of the self-organization can be found in **chapter 6**. This section provides an overview on how the nanoparticle shape, the magnetic field strength, gradient direction and the evaporation time can affect the mesocrystals in their end characteristics like space group, shape, size, surface coverage or degree of order.

4.2.4.1 Nanoparticle shape

A variation of the shape of the nanoparticles for a drying-induced self-assembly process leads to different crystal structures. The spherical particles arrange themselves in a rhombohedral lattice, while the cubic nanoparticles with high degree of truncation self-assemble in a tetragonal structure [33, 35]. This effect can be seen globally in the GISAXS pattern (3D) and locally in microscopy pictures (2D) of the respective systems **figure 4.12** and **figure 4.13**. In both cases the scattering pattern shows sharp reflections, which is an indication for a good crystalline order.

The analysis of the space group is done according to well established crystallographic methods [7, 11]. In the special case of highly ordered mesocrystals, all reflections (hkl) from different directions arise in one single GISAXS pattern without rotation of the sample. The flat Ewald sphere in small angle scattering, as well as the 2D powder property with the in-plane orientation average allow this simultaneous observation. The Bragg peaks resulting from scattering of the reflected beam are weak under the angle of incidence used here and are not indexed. These arise from a scattering process with a reflection at the substrate and are thus dependent on the angle of incidence. The intensity of these Bragg peaks is much lower than the one of Bragg

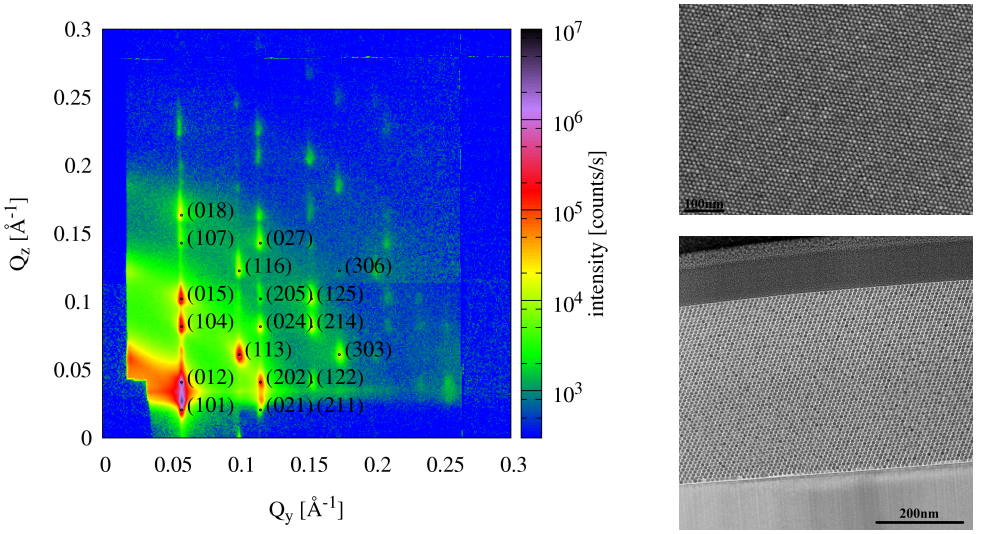

(a) GISAXS pattern (SWING/Soleil)

(b) SEM (top) and TEM (bottom)

Figure 4.12: Structural analysis of an ensemble of mesocrystals formed with long waiting time from spherical building blocks of radius 5.01 nm self-assembled under a magnetic field of 80 mT and gradient up ($D^{Lg1.68\perp 80}_{S,\,5.01}$). The measurement was done under an angle of 0.4 ° and with a wavelength of 1.77 Å. Reflections of the GISAXS pattern are indexed according to the rhombohedral structure discussed in the text. The Bragg peaks resulting from scattering of the reflected beams are weak under this angle and not indexed. The SEM picture is made from the top of a mesocrystal, the TEM picture shows a vertical cut through a mesocrystal and therefore a plane perpendicular to the substrate.

peaks from direct scattering as the reflection at substrate strongly reduces the beam intensity, especially at larger angles of incidence.

The spherical nanoparticles self assembled in an ensemble of mesocrystals, in which the average lattice constant of single mesocrystals are $c = 31.3 \pm 0.1$ nm for the crystal direction perpendicular to the substrate and $a = 12.7 \pm 0.1$ nm in-plane. These parameters are extracted from all well visible reflection positions in **figure 4.12a**. Indexing of the GISAXS reflections yields an extinction rule of $-h+k+l = 3n$, which is consistent with a rhombohedral space group R$\bar{3}$m (No. 166), a distorted form of a closed packed structure with face centered cubic (ABCABC) stacking. The unit cell of the rhombohedral lattice is shown in **figure 4.14**. Due to the 2D powder characteristics, the indices h and k cannot be distinguished, so the reflections could be indexed with the reverse lattice with the corresponding extinction rules $h-k+l = 3n$, too. The alternative possibility for the expected closed packed spheres with an hexagonal lateral symmetry is a hcp (ABAB) stacking type, which corresponds to the space group P 6_3/mmc (No. 194). This case can be excluded, because the extinction rule of $l = 2n$ could not be observed. The present fcc stacking confirms the preference of the face centered cubic structure over a hexagonally closed packed crystal. [26, 50, 95]. Heitkam et al. showed with model experiments that a mechanical instability in the self-assembly of the fourth layer for the hcp stacking leads to a rearrangement of the hcp into fcc packing [50]. Bolhuis and Frenkel showed

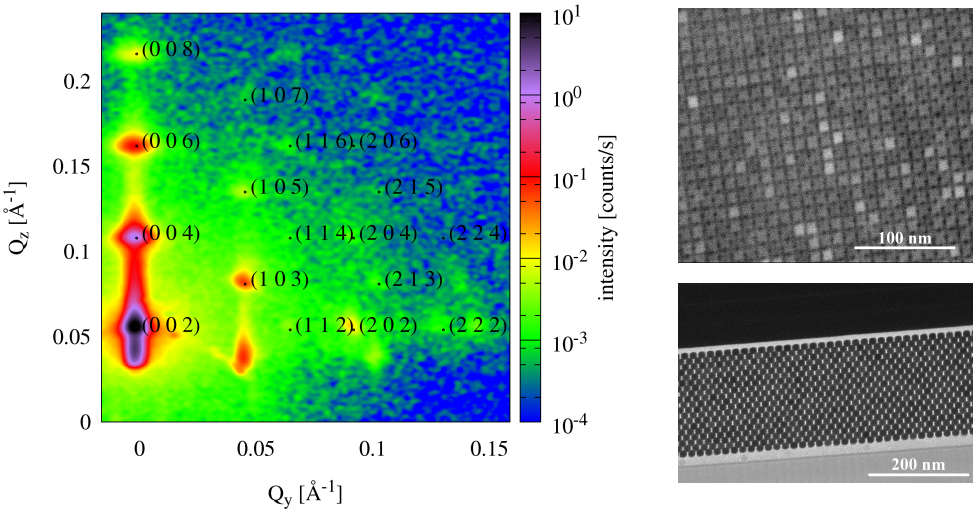

(a) GISAXS pattern (lab source/Risø)

(b) SEM (top) and TEM (bottom)

Figure 4.13: Structural analysis of an ensemble of mesocrystals formed with extra long waiting time from cubic building blocks of edge length 10.9 nm and degree of truncation of 0.8 self-assembled without a magnetic field ($D^{XLg1.68X}_{C,\ 10.9,\ 0.8}$). The measurement was done under an angle of 0.4 ° and with a wavelength of 1.54 Å. Reflections of the GISAXS pattern are indexed according to the tetragonal structure discussed in the text. The Bragg peaks resulting from scattering of the reflected beam are weak at this angle and not indexed. The SEM picture is made from the top of a mesocrystal, the TEM picture shows a vertical cut through a mesocrystal and therefore a plane perpendicular to the substrate.

that the free energy of the fcc stacking is smaller than for the hcp one, following a theoretically more stable fcc stacking [26]. The microscopy pictures confirm the results of the structural GISAXS analysis. Hexagonal layers are observed on top of the mesocrystals by SEM (**figure 4.12b top**) and the TEM picture with a vertical cut through a mesocrystal shows the (ABCABC) stacking (**figure 4.12b bottom**). The lattice constant determined as $a = 12.7 \pm 0.1$ nm corresponds to a face centered cubic array of spherical nanoparticles with a diameter of 10.02 nm and 1.34 nm shell thickness. The shell thickness lies in the range of the shell thicknesses measured by SANS between 1.1 and 1.6 nm [33, 103]. The extracted value for the c lattice constant with $c = 31.3 \pm 0.1$ nm is slightly higher than the one expected for a perfect fcc stacking of 31.1 nm for this type of structure. The expansion of only 0.6% in the [001] direction of the rhombroedral cell shows a nearly perfect fcc structure.

The cubes self-assemble in an ensemble of mesocrystals, where the average lattice constant of single mesocrystals are $c = 23.9 \pm 0.1$ nm and $a = 14.2 \pm 0.1$ nm. Indexing of the GISAXS reflections in **figure 4.13a** yields an extinction rule of $h+k+l = 2n$, which is consistent with a I4/mmm (No. 139) space group with a body centered tetragonal (bct) unit cell. The unit cell of the bct lattice is shown in **figure 4.14**. For the cubic particles, the local microscopy images confirm the results of the structural GISAXS analysis too, which give the average over the sample. The square symmetry is observed on top of the mesocrystals by SEM (**figure 4.13b top**) and the TEM picture with a vertical cut through a mesocrystal shows the tetragonal

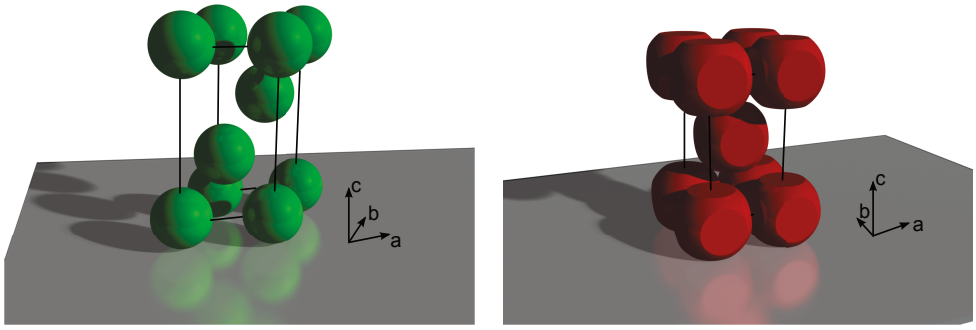

Figure 4.14: Schematic unit cell of the rhombohedral structure of the nanospheres (left) and the body centered tetragonal (right) structure of nanocubes mesocrystal.

lattice (**figure 4.12b bottom**). The simple cubic symmetry can be excluded from TEM and the selection rules, which clearly show a bct lattice. The crystal structure observed originates from the anisotropic shape of the nanoparticle.

In general, anisotropic particles favor a face-to-face packing to maximize the van der Walls interaction energy [86]. In this case, the (100) facets of the nanocubes touch each other in one layer. The preference of bct against simple cubic in the 3 dimensional direction can be explained by the truncated shape of the cubes. Each square layer offers a gap between neighboring particles in the plane, within which the particles of the next layer can arrange themselves. The gaps are generated by the high degree of truncation of the cubes. A higher degree of truncation favors the bct structure until the particles get too spherical, favoring the fcc structure. A lower degree of truncation would favor a simple cubic arrangement [33]. In detail, the energy of attractive van der Waals interactions for face to face stacking is inversely proportional to the square of the distance between two faces ($\sim \frac{1}{r^2}$) , while for the edge-to-edge stacking the interaction energy is inversely proportional to the separation distance ($\sim \frac{1}{r}$) [86]. The statement of Song et al. leads to the consequence that the van der Waals interaction is stronger for the face to face configuration than for edge to edge or corner-to-corner configuration for short distances between the particles. Consequently, the perfect cubes prefer the face-to-face stacking, arranging in simple cubic stacking as in this configuration all surfaces have the smallest distance between each other and the maximum van der Waals energy is reached. For the truncated particles a new surface is formed at the corners of the cubes and yields additional coupling areas. Increasing the degree of truncation within simple cubic stacking leads to corners with much more distance to each other

sample ID	selection rule	space group	a [nm]	c [nm]
$D_{S,\,5.01}^{Lg1.68\triangleq 80}$:	$-h+k+l=3n$	$R\bar{3}m$	12.7 ±0.1	31.3 ±0.1
$D_{C,\,10.9,\,0.8}^{XLg1.68X}$:	$h+k+l=2n$	$I4/mmm$	14.2 ±0.1	23.9 ±0.1

Table 4.3: Results of the structural analysis of the ensemble of mesocrystals formed with long/extra long waiting time from spherical/cubic building blocks of radius 5.01 nm/edge length 10.9 nm and degree of truncation of 0.8 self-assembled under an magnetic field of 80 mT and gradient up/without a magnetic field ($D_{S,\,5.01}^{Lg1.68\triangleq 80}$/$D_{C,\,10.9,\,0.8}^{XLg1.68X}$). These outcomes are an average over the ensemble of mesocrystals.

while the distance of the faces stays constant. The simple cubic case gets less and less favorable as the interaction energy between the corners get much smaller. A transition to the bct structure is given when the interaction energy is too low compared to the face-to-face arrangement, so that the particles start to order in bct structure [33]. Whereas the distance between the faces gets a little bit bigger, the corners get much closer, so that the competing interactions are in balance. An extreme increase of the degree of truncation leads to order the particles in an hexagonal lattice, which is shown in the high resolution TEM images in **figure 4.3c**. These examples give an impression of the importance of the relation between cubic ordering and degree of truncation.

4.2.4.2 Magnetic field

To optimize the self-assembly, a systematic variation of the magnetic field influence has been studied which is presented in this section. For this purpose a variety of magnetic field and field gradient strengths (80 mT magnet with 18 mT/ cm, 2 mT with 0.3 mT/ cm, homogeneous field of 4 mT and no field) and different directions of the gradient were applied during the self-organization of the nanoparticles. The gradient direction is always aligned with the field direction. Gradient directions away from the sample surface $H_{\underline{\perp}}$ (gradient up), towards the sample surface $H_{\underline{\curlyvee}}$ (gradient down) and along the substrate's surface $H_{\underline{\succ}}$ (gradient in-plane) have been investigated. The other drop casting parameters were kept fixed. The characterization was performed locally by SEM and AFM on different positions and in average over a large sample area by GISAXS measured at SWING, Soleil. The GISAXS patterns were analyzed by fitting selected peaks with the fitting routine described in **section 5.3.2**. The modeling of scattering patterns of an ensemble of mesocrystals will be explicitly discussed in **chapter 5**. The systematic investigation of the field dependence is demonstrated here with spherical particles of the solutions $S_S^{8.4}$ and $S_S^{4.7}$, respectively. The GISAXS results for different external field parameters are presented in **figure 4.15** and **figure 4.16**. The quantitative parameters extracted for these samples are listed in **table 4.4** and **figures 4.17 - 4.23**. Additional experimental images can be found in the **appendix section A.1**.

A good overview over the influences of various parameters for the $S_S^{8.4}$ solution can be obtained from the GISAXS patterns (**figure 4.15**). The seven pictures show the GISAXS patterns from the mesocrystal assemblies deposited at different field configurations: The symbol at the upper right corner indicates either the direction of the field gradient ($\underline{\perp}$, $\underline{\curlyvee}$, $\underline{\succ}$), homogeneous field ($\underline{\uparrow\uparrow}$) or zero field conditions (X). The colour of the symbol represents the strength of the field: $\underline{\perp}$ means a low field configuration with gradient up, while $\underline{\perp}$ is the analogon for a strong magnetic field. These field configuration symbols are also part of the sample ID, e.g. $D_{S,\,5.01}^{Lg1.68\underline{\perp}2}$ describes a sample deposited in a low field (2 mT) perpendicular to the substrate with gradient up.

The pictures in the left column show the GISAXS patterns of all mesocrystal assemblies prepared at small magnetic fields. The pictures to the right compare with their neighbour on the left by a different field strength and the same orientation of field and field gradient. The application of different field settings during the self-assembly (**figure 4.15**) shows influences on some characteristics of the sample while others stay unaffected. The gradient up fields ($\underline{\perp}$,$\underline{\perp}$) support the self-assembly, the gradient down configurations ($\underline{\curlyvee}$,$\underline{\curlyvee}$) have a negative impact on the mesocrystal growth. The peaks are found broader in the $\underline{\curlyvee}$ pictures compared to the $\underline{\perp}$ pictures at the same field strength. Furthermore the self-assembly in higher fields ($\underline{\perp}$, $\underline{\curlyvee}$) shows a better superstructure quality than the low field configurations ($\underline{\perp}$, $\underline{\curlyvee}$, $\underline{\succ}$). The low homogeneous field

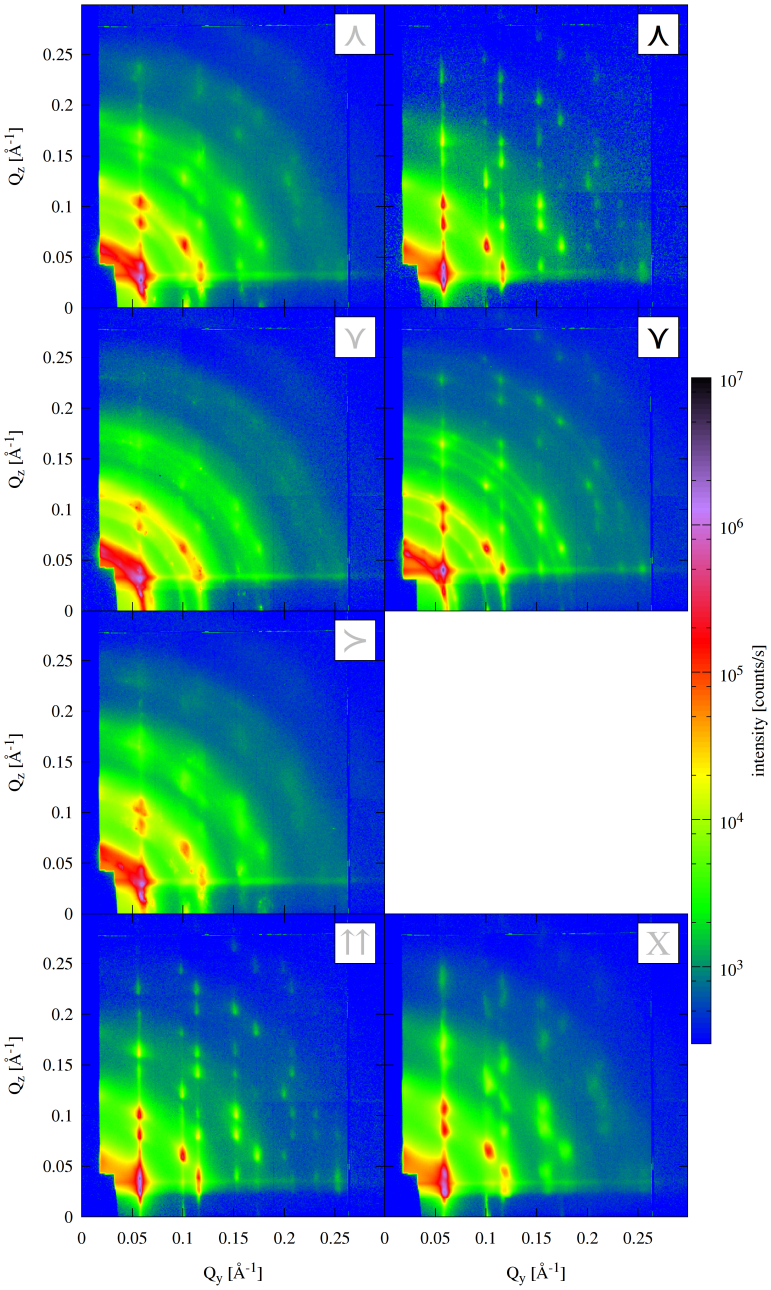

Figure 4.15: Ensembles of mesocrystals self-assembled with long waiting time from spherical building blocks of radius 5.01 nm and concentration $8.4{\cdot}10^{14}$ NP/ml ($S_S^{8.4}$) at different field conditions (low field: gray; strong field: black, $\underline{\curlywedge}$: gradient up, $\underline{\succ}$: gradient in-plane, $\underline{\curlyvee}$: gradient down, $\underline{X}$: without field, $\underline{\uparrow\uparrow}$: homogenous field perpendicular to the sample surface). The measurements were performed at an angle of incidence of 0.4 ° and with a wavelength of 1.77 Å at SWING, Soleil.

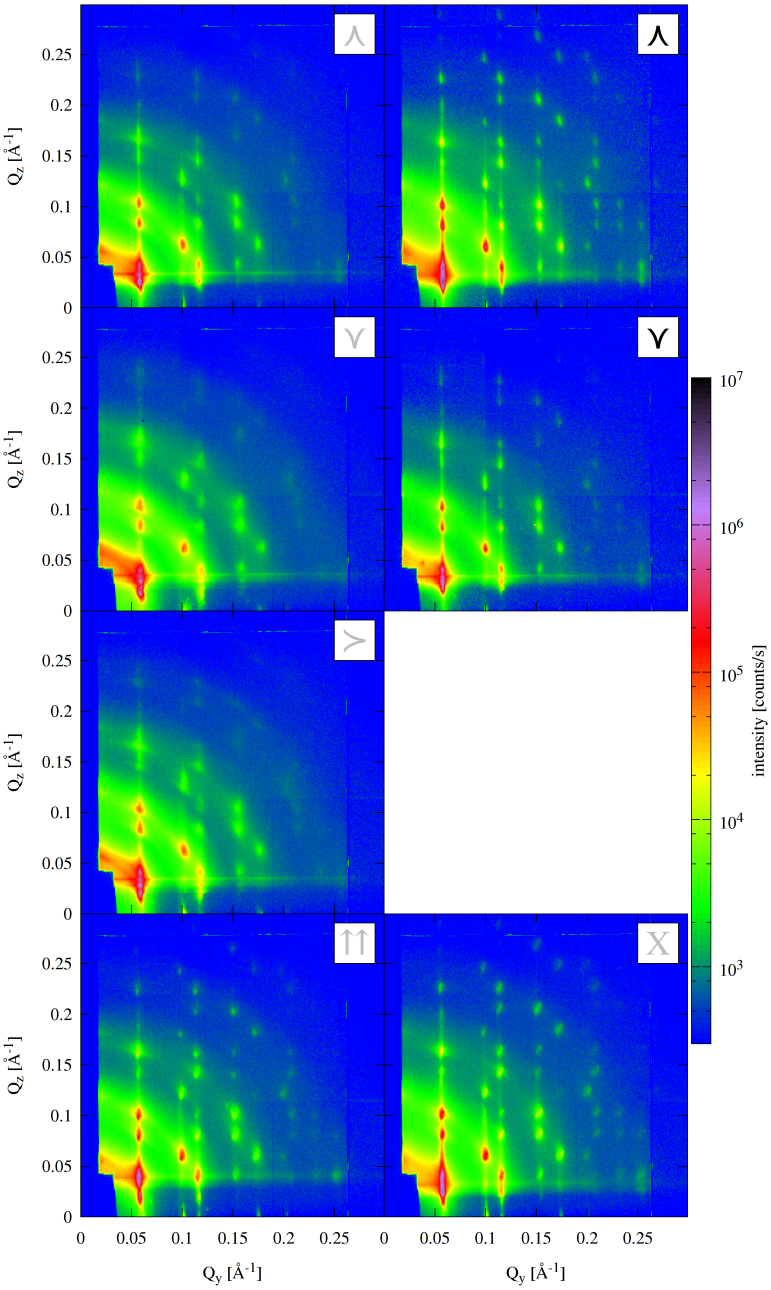

Figure 4.16: Ensembles of mesocrystals self-assembled with long waiting time from spherical building blocks of radius 5.01 nm and concentration $4.7{\cdot}10^{14}$ NP/ml ($S_S^{8.4}$) at different field conditions (low field: gray; strong field: black, $\underline{\curlywedge}$: gradient up, $\underline{\succ}$: gradient in-plane, $\underline{\curlyvee}$: gradient down, $\underline{X}$: without field, $\underline{\Uparrow}$: homogenous field perpendicular to the sample surface). The measurements were performed at an angle of incidence of 0.4 ° and with a wavelength of 1.77 Å at SWING, Soleil.

($\underline{\uparrow\uparrow}$) and the zero field setup (X) show an intermediate quality between the low and high fields. These results have been reproduced for samples grown from a solution with lower concentration of the same nanoparticles $S_S^{4.7}$ (**figure 4.16**).

It is remarkable that the magnetic field configurations have no influence on the resulting mesocrystal structure. All samples show the known $R\bar{3}m$ space group for the assemblies with spheres with minimal lattice constant variations of a few %. The major influence on the crystal structure of the mesocrystals is given by the morphology of the nanoparticles, which produces a close packed structure to minimize the energy for spherical particles (see **section 4.2.4.1**).

The quality of the ordering shows differences between high field/gradient and the low field/gradient configurations. The first two (**figure 4.17**, **figure 4.18**) yield long rang ordered assemblies, at which the quality of the $D_{S,\,5.01}^{Lg1.68\underline{\perp}80}$ sample is slightly better, mainly expressed as larger and higher mesocrystals. The homogeneous field (**figure 4.21**) as well as the zero filed setup (**figure 4.22**) produced well ordered superstructures nearly as good as with the strong field configuration. The correlation lengths are comparable to the locally measured sizes from the microscopy. The good order with low surface defects is verified by SEM pictures on top of a mesocrystal. The $H_{\underline{\perp}}$ configuration showed, in average, the largest mesocrystals with a correlation length of around 1200 nm in-plane and 430 nm in the height. The tilting of the mesocrystals is negligibly small, while a random variation of the lattice constant of 0.1% is observed only for the zero field configuration. This can be noticed in the scattering picture features as a modified peak shape getting broader with higher Q values. In the case of this sample the distribution seems to be non-isotropic, e.g. with different lattice constant distributions for the in-plane and out-of-plane directions. As the underlying directional distribution is not known, the measurement contains a 2D powder average and many additional parameters with similar impact on the peak shapes would be needed, a fit of this anisotropic broadening could not be performed. The $D_{S,\,5.01}^{Lg1.68\underline{\curlyvee}80}$ configuration (**figure 4.18**) exhibits further structural features in addition to the main structure. Preferred directions of the mesocrystal/crystallites tilting are present indicated by sharp peaks lying on the Debye-Scherrer-rings. For example the (104) and (006) are both found duplicated rotated 22 ° with respect to their main peak. Apparently, these crystallites have a c-axis rotated by this value using from the substrate surface normal.

In contrast, the samples with low gradient configuration (**figure 4.19**, **figure 4.20**, **figure 4.23**) have many visible surface defects and imperfections which can be observed in SEM and which are slightly reflected in the lower in-plane correlation length averaged over the ensemble. Additionally, the mesocrystal surfaces are bent, which is also confirmed by the GISAXS fit in the titling angle of 2 ° for the sample $D_{S,\,5.01}^{Lg1.68\underline{\perp}2}$. All three samples show Debye-Scherrer rings, where the in-plane gradient sample produces weaker and broader ones demonstrating a not so high number of 3D disordered objects with smaller sizes than the mesocrystals. Based on the sharpness of the rings for gradient down it is assumed that this scattering pattern is produced by small mesocrystals or crystallites, which are arbitrarily rotated against each other. For the $D_{S,\,5.01}^{Lg1.68\underline{\succ}2}$ and $D_{S,\,5.01}^{Lg1.68\underline{\curlyvee}2}$ sample a superposition of extreme broad peaks with very sharp peaks can be observed. This indicates that besides a broad distribution of lattice constants for most of the ensemble, there exists a fraction of mesocrystals with a well defined lattice constant. These peaks are extremely sharp which indicates the high quality of some mesocrystals.

The Yoneda lines observed for the $D_{S,\,5.01}^{Lg1.68X}$/$D_{S,\,5.01}^{Lg1.68\underline{\perp}80}$ samples are weak and narrow, while other samples like $D_{S,\,5.01}^{Lg1.68\underline{\curlyvee}2}$ have a more intense and broader Yoneda line. The position of the

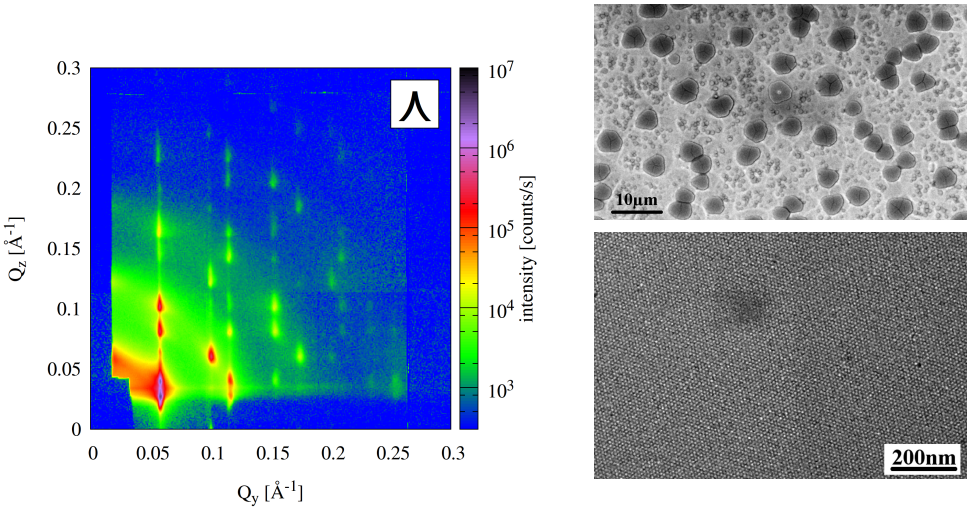

(a) GISAXS pattern (SWING/Soleil) **(b)** SEM

Figure 4.17: Ensemble of mesocrystals self-assembled with long waiting time from spherical building blocks of radius 5.01 nm and concentration $8.4{\cdot}10^{14}$ NP/ml in a magnetic field of 80 mT and gradient up ($D^{Lg1.68\perp 80}_{S,\,5.01}$). The GISAXS measurement was performed at an angle of incidence of 0.4 ° and with a wavelength of 1.77 Å at SWING, Soleil.

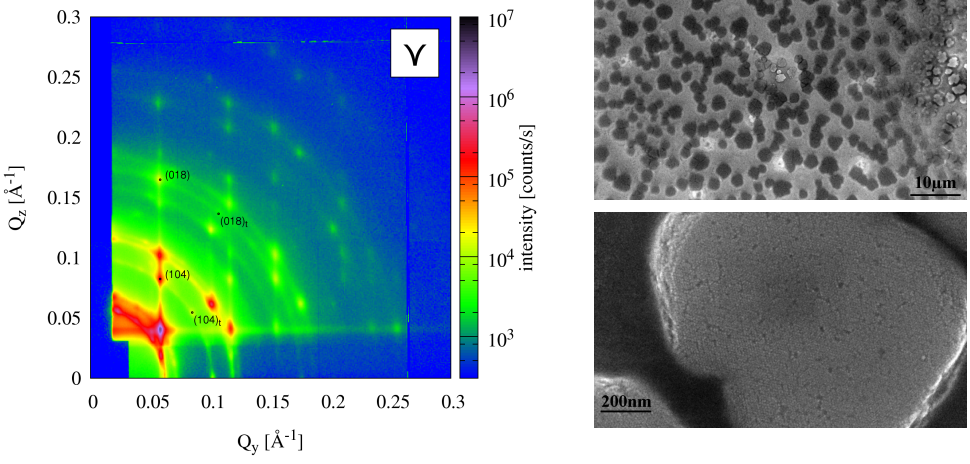

(a) GISAXS pattern (SWING/Soleil) **(b)** SEM

Figure 4.18: Ensemble of mesocrystals self-assembled with long waiting time from spherical building blocks of radius 5.01 nm and concentration $8.4{\cdot}10^{14}$ NP/ml in a magnetic field of 80 mT and gradient down ($D^{Lg1.68\gamma 80}_{S,\,5.01}$). The GISAXS measurement was performed at an angle of incidence of 0.4 ° and with a wavelength of 1.77 Å at SWING, Soleil. Peaks originating from a rotation of the main structure and their original positions are marked.

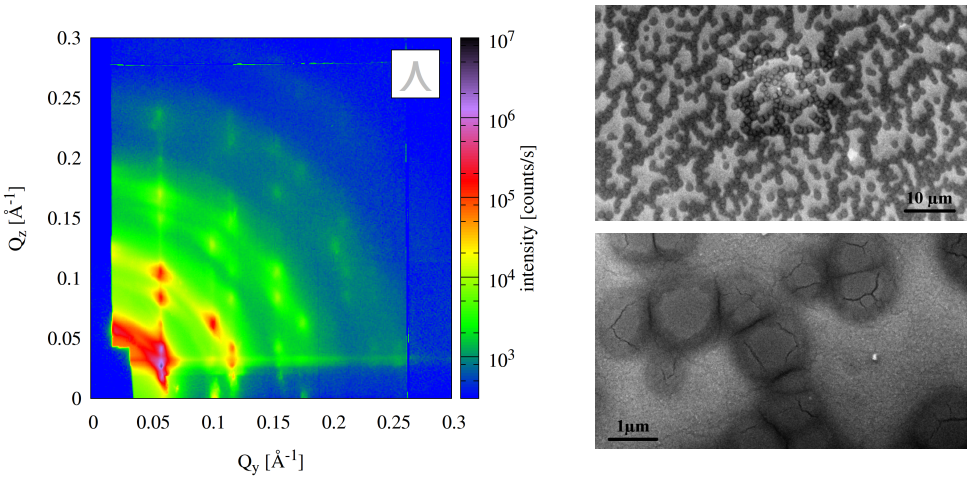

(a) GISAXS pattern (SWING/Soleil) **(b)** SEM

Figure 4.19: Ensemble of mesocrystals self-assembled with long waiting time from spherical building blocks of radius 5.01 nm and concentration $8.4{\cdot}10^{14}$ NP/ml in a magnetic field of 2 mT and gradient up ($D^{Lg1.68\_2}_{S,\,5.01}$). The GISAXS measurement was performed at an angle of incidence of 0.4 ° and with a wavelength of 1.77 Å at SWING, Soleil.

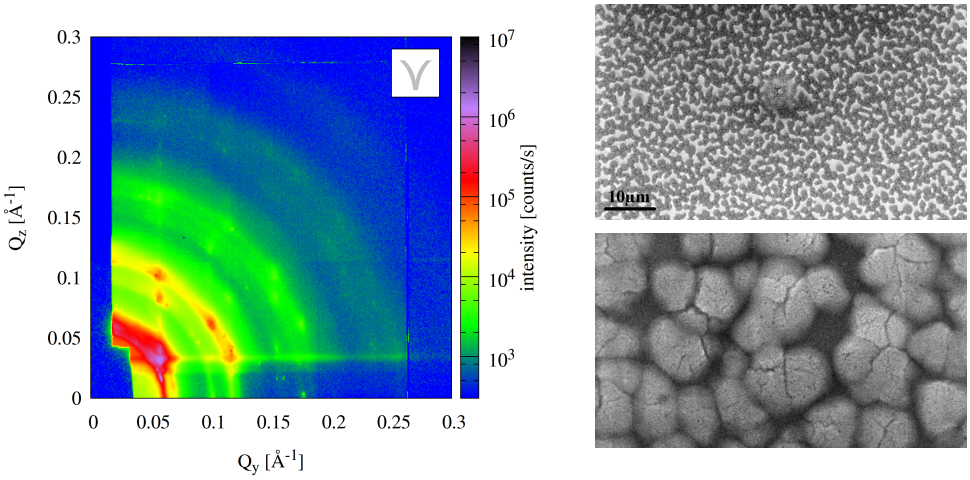

(a) GISAXS pattern (SWING/Soleil) **(b)** SEM

Figure 4.20: Ensemble of mesocrystals self-assembled with long waiting time from spherical building blocks of radius 5.01 nm and concentration $8.4{\cdot}10^{14}$ NP/ml in a magnetic field of 2 mT and gradient down ($D^{Lg1.68\_2}_{S,\,5.01}$).The GISAXS measurement was performed at an angle of incidence of 0.4 ° and with a wavelength of 1.77 Å at SWING, Soleil.

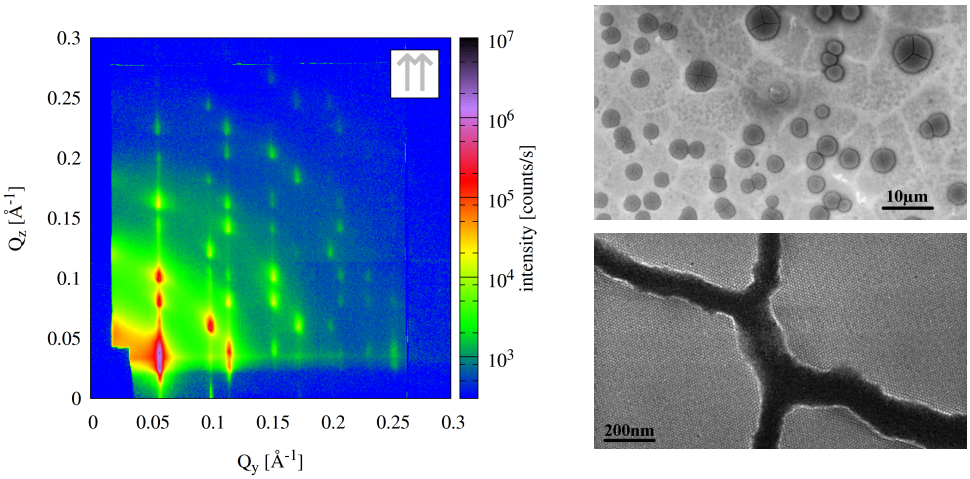

(a) GISAXS pattern (SWING/Soleil) **(b)** SEM

Figure 4.21: Ensemble of mesocrystals self-assembled with long waiting time from spherical building blocks of radius 5.01 nm and concentration $8.4{\cdot}10^{14}$ NP/ml in a homogeneous magnetic field of 4 mT perpendicular to the sample surface ($D^{Lg1.68\uparrow\uparrow 4}_{S,\,5.01}$). The GISAXS measurement was performed at an angle of incidence of 0.4 ° and with a wavelength of 1.77 Å at SWING, Soleil.

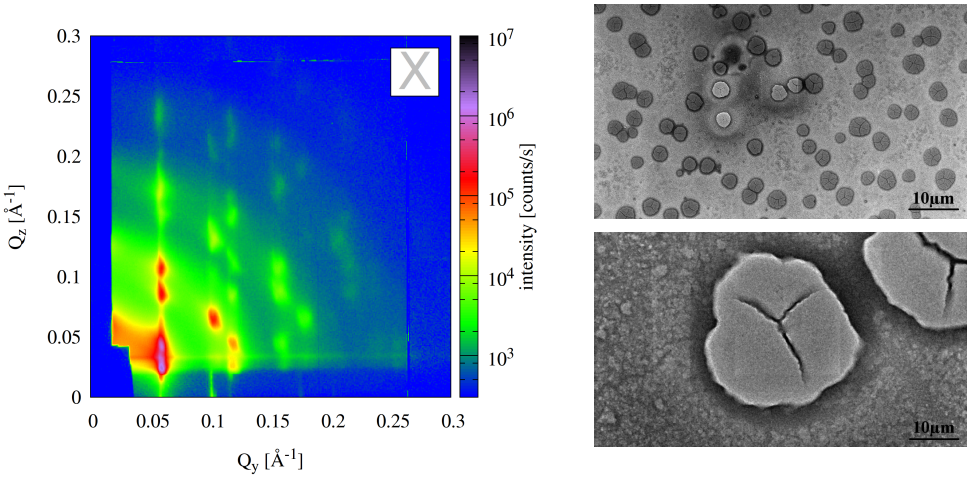

(a) GISAXS pattern (SWING/Soleil) **(b)** SEM

Figure 4.22: Ensemble of mesocrystals self-assembled with long waiting time from spherical building blocks of radius 5.01 nm and concentration $8.4{\cdot}10^{14}$ NP/ml ($S^{8.4}_{S}$) without applied magnetic field ($D^{Lg1.68X}_{S,\,5.01}$). The GISAXS measurement was performed at an angle of incidence of 0.4 ° and with a wavelength of 1.77 Å at SWING, Soleil.

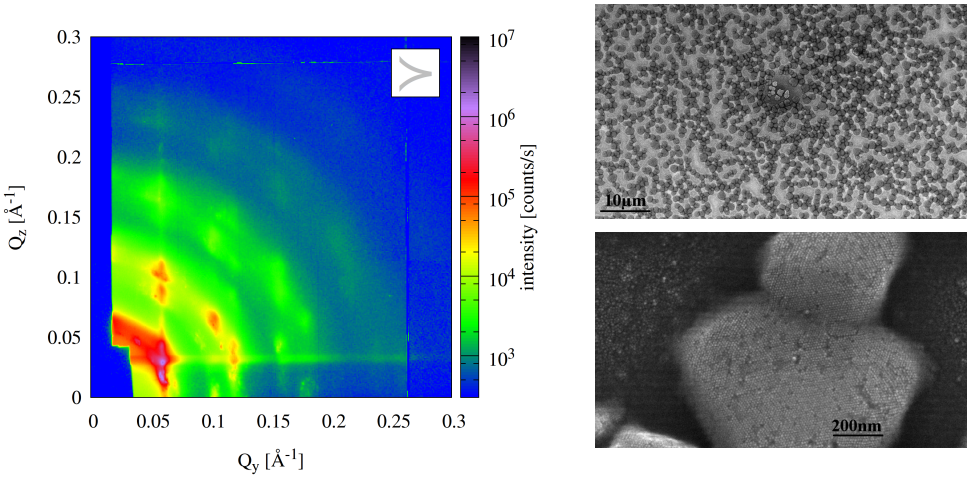

(a) GISAXS pattern (SWING/Soleil) **(b)** SEM

Figure 4.23: Ensemble of mesocrystals self-assembled with long waiting time from spherical building blocks of radius 5.01 nm and concentration $8.4{\cdot}10^{14}$ NP/ml in a magnetic field of 2 mT and and gradient in-plane ($D_{S,\,5.01}^{Lg1.68\succeq 2}$).The GISAXS measurement was performed at an angle of incidence of 0.4 ° and with a wavelength of 1.77 Å at SWING, Soleil.

Yoneda line depends on the critical angle α_c and its intensity on the substrate-layer-air contrast, which both depend on the laterally averaged scattering length density (SLD) (**section 2.2.5**). The shape and intensity of the Yoneda line depends on the relation of the coherence length of the experiment to the size and shape of the mesocrystals. For example, a sharp line can be observed for a coherence length smaller than the mesocrystal size when perpendicular edges are present. A broad Yoneda line can be induced by smaller coherence length than mesocrystal size with inclined edges or by a long coherence length compared to the mesocrystal and many mesocrystals of different heights. Generally speaking, the higher the uniformity of the SLD inside the coherence volume, the sharper the Yoneda line. The SEM observations show huge mesocrystals with straight edges for $D_{S,\,5.01}^{Lg1.68X}$ with sizes between 1 and 4 µm and for $D_{S,\,5.01}^{Lg1.68\perp 80}$ between 3 and 7 µm, which have big distances between the crystals, while the other samples show smaller mesocrystals with inclined edges separated with a lower distance and sizes of around 0.2-2 µm. From this complementary investigation it can be concluded that the narrow Yoneda lines in the GISAXS patterns arise from the scattering of individual mesocrystals, as the correlation length ($\leq$10 µm) is too small to scatter coherently between mesocrystals at these large distances. The perpendicular edges lead to no SLD distribution inside the coherence length and thus to no different critical angles. The other sample $D_{S,\,5.01}^{Lg1.68\succeq 2}$ has height differences measured by AFM (see appendix) so that it can be assumed that in this case the SLD profile induced by the inclined edges inside the coherence volume is the important factor which induces a depth dependent α_c distribution and thus the broader Yoneda line, while for $D_{S,\,5.01}^{Lg1.68\curlyvee 80}$ the height distribution of different mesocrystals inside the coherence volume can be the major cause.

Further features could be observed by microscopy investigations. The SEM showed that the zero field/homogeneous and gradient up field configurations produce cylindrical mesocrystals with a

Characteristics	$D_{S,5.01}^{Lg1.68\perp 80}$	$D_{S,5.01}^{Lg1.68\gamma 80}$	$D_{S,5.01}^{Lg1.68\perp 2}$	$D_{S,5.01}^{Lg1.68\gamma 2}$	$D_{S,5.01}^{Lg1.68\succ 2}$	$D_{S,5.01}^{Lg0.94\uparrow\uparrow 4}$	$D_{S,5.01}^{Lg1.68X}$
a [nm] :	12.7 ± 0.1	12.5 ± 0.1	12.4 ± 0.1	/	/	12.5 ± 0.1	12.2 ± 0.1
c [nm] :	31.3 ± 0.1	30.7 ± 0.1	29.2 ± 0.1	/	/	30.5 ± 0.1	29.8 ± 0.1
ε_y [nm] :	1188 ± 594	513 ± 257	606 ± 303	/	/	889 ± 444	606 ± 303
ε_z [nm] :	429 ± 43	337 ± 34	244 ± 24	/	/	365 ± 37	244 ± 24
σ_{tilt} [°] :	0.007 ± 0.004	0.013 ± 0.007	2 ± 1	/	/	0.007 ± 0.003	0.07 ± 0.04
σ_{rad} [%] :	0.07 ± 0.05	0.2 ± 0.005	2 ± 0.005	/	/	0.06 ± 0.056	0.1 ± 0.005
space group :	$R\bar{3}m$	$R\bar{3}m$	$R\bar{3}m$	$R\bar{3}m$	$R\bar{3}m$	$R\bar{3}m$	$R\bar{3}m$
Yoneda :	weak, narrow	weak	/	strong, broad	strong, broad	weak, narrow	weak, narrow
Debye-Scherrer-rings :	/	sharp rings	very weak	strong, broad	weak, broad	/	/
other preferred crystal directions :	/	3D tilted mesocrystals with preferred directions	indication of weak peaks	weak extra peaks	weak extra peaks	/	/
special remarks :				no fit possible[a], single peaks of mesocrystals inside one peak of the ensemble of mesocrystals, multiple peak structure		/	unsymmetrical lattice constant distribution
height(AFM) [nm]:	250-500	250-300	/	/	≈ 200	/	100-200*
surface coverage(AFM) [%] :	23 ± 2	35 ± 2	/	/	35 ± 2	/	comparable with $D_{S,5.01}^{Lg1.68\perp 80}$
$shape_{Meso}$ (SEM) :	cylindrical, flat $surface_{Meso}$, no inclined edges	no well defined shape, tilted $surface_{Meso}$, inclined edges**			**	cylindrical, flat $surface_{Meso}$, no inclined edges	cylindrical, flat $surface_{Meso}$, no inclined edges
$size_{Meso}$ (SEM) [µm] :	3-7	0.5-2	1-2	1-2	0.2-2	3-6	1-4
$order_{Meso_{top}}$ (SEM) :	very good, low surface defects	many surface defects (bigger or missing particles), imperfections***			***	very good, low surface defects	very good, low surface defects
special remarks (SEM/AFM) :	small mesocrystals between the big ones	mesocrystals start to form chains	mesocrystals form chains or clusters	mesocrystals form chains or clusters	mesocrystals form chains or clusters	/	rarely small mesocrystals between the big ones

Table 4.4: Results from the systematic investigation of the field influence on the outcome of the mesocrystals growth. Microscopy as well as depth resolved GISAXS experiments reveal different characteristics and the combination leads to a good description of the quality of the sample. The parameters $\varepsilon_{y/z}$ are the the average mesocrystal in-plane/out-of-plane correlation length and $\sigma_{rad/tilt}$ the radial/tangential standard deviations describing a random variation of the mesocrystal lattice parameters and tilting of the c-axis away from the substrate surface. The large error values for the in-plane correlation lengths result from approaching the instrumental resolution limit. (*: Measurement from a comparable sample.)

[a] Due to the multiple peak structure, these parameters could not be determined from the fitting routine.

flat surface, which cover around 23% (determined by AFM) of the substrate area. Additionally, small mesocrystals between the large ones are observed with a height of 100 nm and 100-800 nm in diameter only for $D_{S,\,5.01}^{Lg1.68\perp 80}$ (see **appendix figure A.3**). The $D_{S,\,5.01}^{Lg1.68\curlyvee 80}$ and the low field self-assembled mesocrystals have a less defined shape with tilted surfaces and inclined edges and cover 35% of the surface . These mesocrystals are much smaller.

In summary the applied magnetic field and field gradient influences the ensemble of mesocrystals grown in shape, size and quality of ordering. The conclusion that the self-assembly in an applied field can improve the long range order of the resulting structure [14, 24, 33, 84] is supported here, but in more detail it turns out to be strongly dependent on the direction and strength of the field and the field gradient. A field applied in the growth direction supports the self-assembly and improves the quality of the ensemble of mesocrystals, while the obverse hinders the mesocrystal growth and worsen the result. Furthermore, a stronger gradient lets grow more cylindrical, flat and higher mesocrystals compared to lower gradients. The gradient is in this case the important factor, as a homogeneous low field produces nearly comparable good mesocrystals as a field applied in the growth direction. The self-assembly process itself is not dominated by the magnetic interaction as the configuration with and without field result in the same structural characteristics.

The application of the field and the field gradient in the growth direction has a positive effect on the growing mechanism. The force in the growing direction can assist the 3D growth pulling the nanoparticles up, compensating the gravity force, acting in the opposite direction. It is a lot easier for the particles to detach from the surface and move around to find an energetically favorable site. This higher mobility can produce larger nucleation centers to achieve larger crystals as well as the possibility to grow higher. Cylindrical mesocrystals with a flat surfaces and sharp edges can be produced with a layer-by-layer growth, which is favoured if the nucleation area is nearly fully grown before the 3D ordering starts.

The samples produced with a field gradient opposite/perpendicular to the growth direction have an additional force which disturbs the process of self-assembly. In addition to the gravity it pulls the particles towards the substrate, so that the mobility of the particles is reduced. The dipole-dipole attraction introduces another disturbance in the in-plane field case, as it acts in a direction perpendicular to the growth. The shape and size selective self-assembly develops smaller nucleation areas due to insufficient time and the lower ability of the particles to move on the surface. It is also imaginable that the volume growth is preferred over the layer-by-layer growth. The additional force to the substrate can favor a 3D growth before the nucleation area is fully developed, which can explain the inclined edges. The missing mobility can cause many imperfections on the surface like lattice vacancies, tilted mesocrystals in preferred directions and the 3D powder characteristic.

4.2.4.3 Evaporation time

The evaporation time of the solution droplet is an additional factor of great importance for the process of self-assembly. It can influence the size, shape and quality of the resulting mesocrystals. First characterizations were performed by SEM and GISAXS measured at ID01, ESRF or in Risø. The samples measured at ESRF were self-assembled during an in-situ GISAXS experiment. In this case a time dependant recording was possible (**section 6.1** and **section 6.2**). The investigation of the time dependence is demonstrated with cubes of the solution $S_C^{8.4}$ and

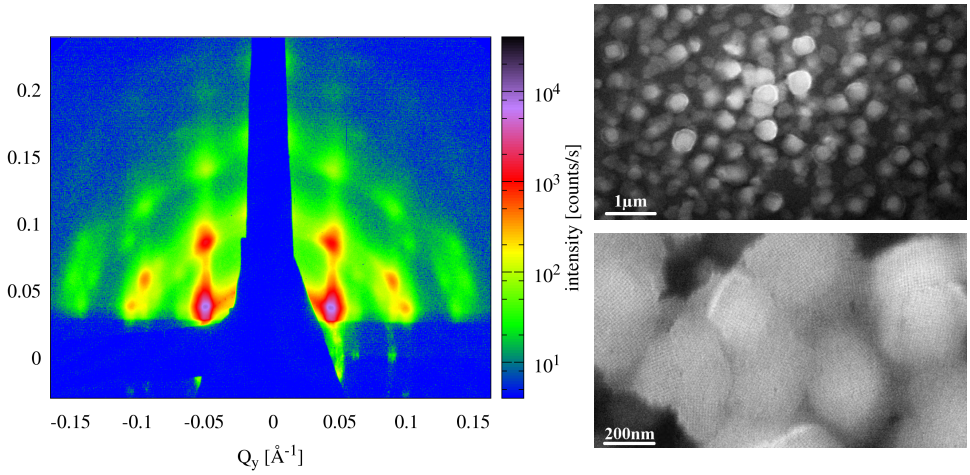

(a) GISAXS pattern (ID01/ESRF) **(b)** SEM

Figure 4.24: Ensemble of mesocrystals built up by cubic building blocks of edge length 10.9 nm and degree of truncation of 0.8 self-assembled within 12 min ($D^{Sh1.68\perp 36}_{C,\ 10.9,\ 0.8}$). The measurement was performed at an angle of 0.3 ° and with a wavelength of 1.27 Å.

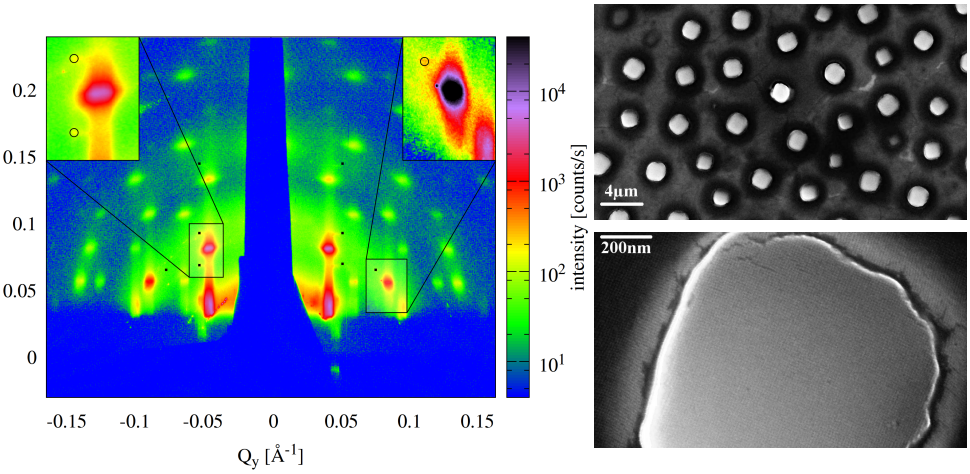

(a) GISAXS pattern (ID01/ESRF) **(b)** SEM

Figure 4.25: Ensemble of mesocrystals built up by cubic building blocks of edge length 10.9 nm and degree of truncation of 0.8 self-assembled within 250 min ($D^{Lg1.68\perp 36}_{C,\ 10.9,\ 0.8}$). The measurement was performed at an angle of 0.3 ° and with a wavelength of 1.27 Å. Some reflexes of the second structure are marked with black points.

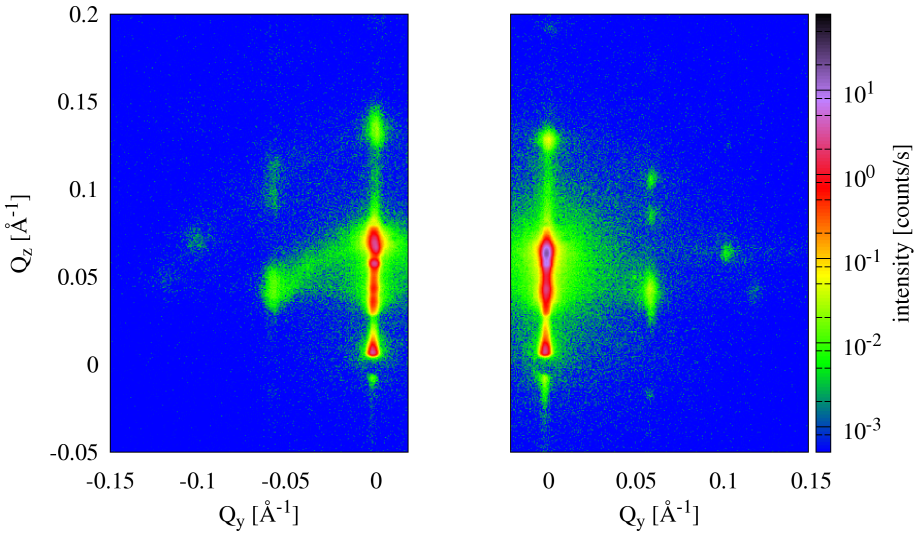

(a) shorter time (lab source/Risø)

(b) longer time (lab source/Risø)

Figure 4.26: Ensemble of mesocrystals built up by spherical building blocks self-assembled with shorter and longer evaporation time for a gradient down configuration. The measurement was performed at an angle of 0.4 ° and with a wavelength of 1.54 Å.

spherical particles of the solution $S_S^{8.4}$. Parameters other than the evaporation time were fixed as well as possible.

The sample self-assembled with a short evaporation time of 12 min produces a GISAXS pattern with relatively broad and low intensity peaks, which have a fast decay in intensity to higher Q's (**figure 4.24a**). This indicates a system with a low coherence of the scattering planes, either because the correlations decay with distance or because a low number of scattering planes exists. The fast decay to higher Q values can be caused by a lattice constant (peak broadening for higher Q) and the local disorder (Debye-Waller factor) caused by e.g. nanoparticle size distribution. For an interpretation of the low coherence of the scattering planes the SEM pictures are consulted (**figure 4.24b**). One finds small mesocrystals with an average size of 200 nm and a low height showing a high surface coverage with less gaps between the crystals. The small mesocrystals can be the reason for the low coherence. This statement is backed up by the fact that the structure on top of every single mesocrystal looks coherent. Additional crystal defects for example in the bulk cannot be ruled out as additional contribution. The SEM shows also that the mesocrystals have no well defined shape.

Extending the evaporation time leads to sharper and stronger peaks persisting up to higher order (**figure 4.25a**). These features of the scattering pattern suggest a higher correlation length in contrast to the sample produced with short evaporation time. The SEM pictures (**figure 4.25b**) confirm these, showing large mesocrystals up to 2 µm in edge length and a larger height. The crystals grown are more separated and have a cubic shape.

Both cases with cubic nanoparticles indicate a weak second structure in the scattering pattern, which has not been determined in the analysis. For the quickly evaporated sample it is smeared out, while the other sample shows small sharp reflexes (see **figure 4.25**). The extended time expectedly affects the second structure as well. A fitting of the datasets as done in **section 4.2.4.2** was not possible, due to the unknown structure and the overlap of reflections from both structures.

The effect of extending the evaporation time for other field configurations which - as shown above - produces less well ordered mesocrystals is shown in **figure 4.26**. For these sample preparations the in-situ setup was not available to define an exact time measurement, so the description here is just shorter and longer time. It is obvious that the residual Debye-Scherrer ring, crossing the point -0.05 Å, 0.06 Å, vanishes with longer evaporation time. A higher peak intensity is observed, too. A second example with an in-plane filed configuration is shown in **appendix figure A.11** and confirms the present observation.

It has to be emphasized that sufficient time for each particle to find a good place in the growing crystals is essential to form long range ordered supercrystals. More time can lead to growth of larger nucleation areas, as the time allows a diffusion of fitting particles to the growing areas and larger nucleation areas enable a growth of wider mesocrystals. Furthermore increasing the time allows the possibility to grow higher mesocrystals for the same reasons. In addition, the increased evaporation time can reduce the number of defects and thus increase the correlation length. Obviously, the improvement of the structural quality is limited as the diffusion radius of the particles scales with the square root of time (**section 2.1.1**) and an extension of the timescale has experimental limitations. Furthermore the growth of the nucleation areas will be limited, when a closed layer has been formed. The appearance of the different surface coverage can be explained by the short time of the high concentrated nucleation stage where mesocrystals are growing on every small nucleation area, while a longer nucleation stage allows development of well separated and ordered nucleation areas where the particles have time to find a energetic optimal position. Whether a longer time is only necessary in the nucleation stage or already before this stage in the dense solution as well, cannot be answered from these investigations and **chapter 6** will go more into detail about the stages.

4.2.4.4 Extraordinary Conditions

This section deals with the influence of self-assembly parameters behind the typical magnitude. New conditions can lead to complete changes of the outcome of the self-assembly. As has been done for the moderate parameter variations, the outcome of these different extraordinary parameters will be described in separate paragraphs split by the different extraordinary parameters.

Nanoparticle shape
The influence of a shape distribution dependent self-assembling can be investigated with a multicomponent nanoparticle solution, drying under typical conditions. A shape selective self-segregation for spherical, as well as for anisotropic nanoparticles was observed by microscopy investigations and explained by the size-dependent magnitude of the van der Waals interactions between the particles [24, 60, 64, 67, 86]. In this work the shape dependent self-assembly between spherical ($S_S^{8.4}$: r=5.01 nm, $8.4 \cdot 10^{14}$ NP/ml) and cubic particles ($S_C^{8.4}$: a=10.9 nm, τ_{Trunc} =0.8, $8.4 \cdot 10^{14}$ NP/ml) in 3 dimensional systems is investigated. Both components have been

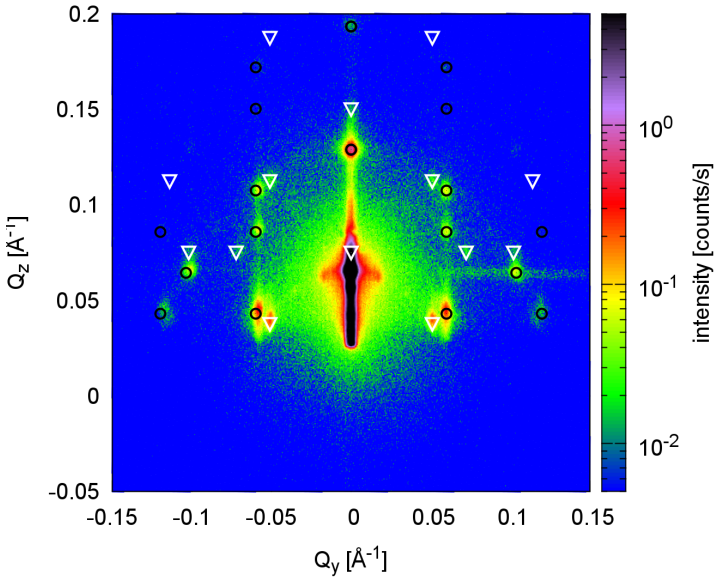

(a) GISAXS - Indicated by white triangles is the bct and by black circles the rhombohedral structure (lab source/Risø). The measurement was performed at an angle of 0.4 ° and with a wavelength of 1.54 Å. The line at $Q_z = 0.06$ Å^{-1} is a detector saturation effect.

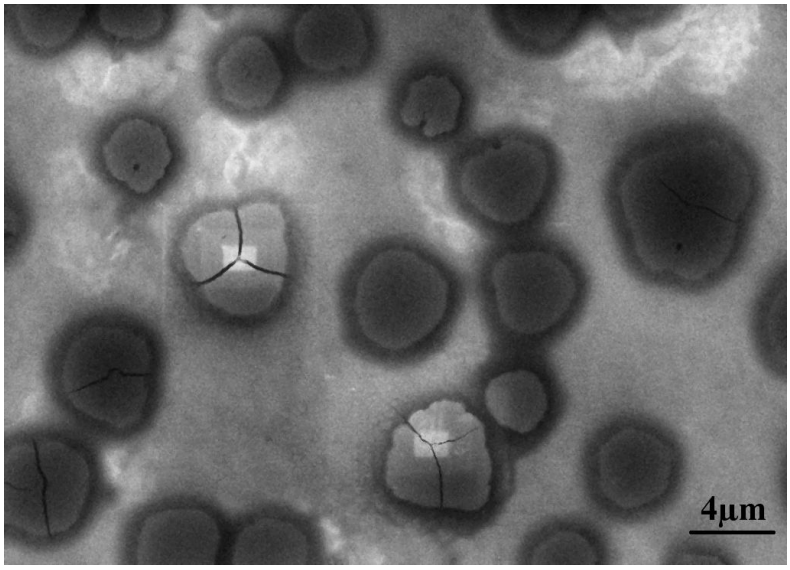

(b) SEM - The lighter areas are the results of a charging effect from higher resolutions scans, done before, see **figure 4.28a** and **figure 4.28b**.

Figure 4.27: Ensemble of mesocrystals self-assembled from spherical and cubic building blocks at once self-separated into mesocrystals. The result of the shape induced self-segregation is shown in the SEM pictures with obvious structural diversity on top of different mesocrystals (the overview at lower magnification is shown here), as well as in the existence of sharp mesocrystals GISAXS peaks of two different space groups.

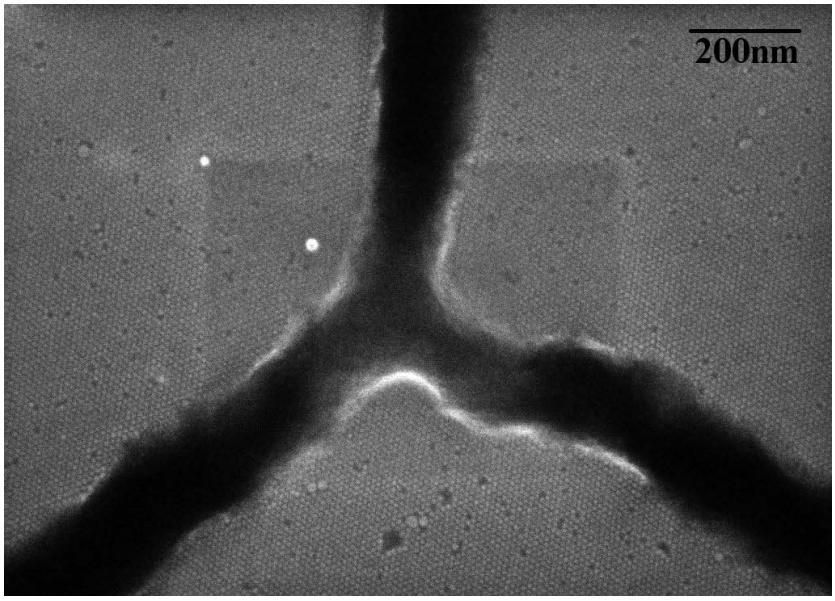

(a) SEM - mesocrystal with hexagonal top layer

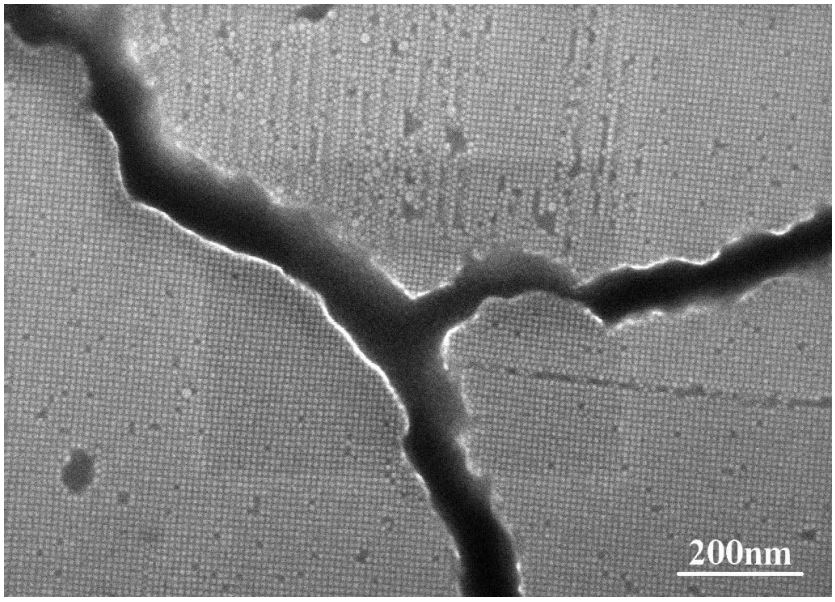

(b) SEM - mesocrystal with square lattice top layer

Figure 4.28: Ensemble of mesocrystals self-assembled from spherical and cubic building blocks at once self-separated into mesocrystals. The result of the shape induced self-segregation is shown in the SEM pictures with obvious structural diversity on top of different mesocrystals. The darker areas are the results of a charging effect from previous higher resolutions scans.

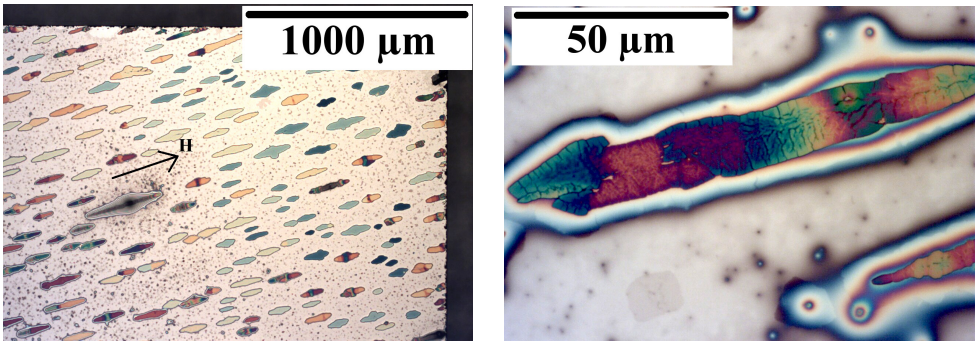

(a) overview **(b)** mesocrystal

Figure 4.29: Light microscopy images of an ensemble of mesocrystals self-assembled under an in-plane magnetic field of 30 mT and gradient of 70 mT/cm. The arrow shows the direction of the field lines.

mixed deliberately together in one solution and studied with microscopy and GISAXS. This is the first in depth observation of well separated 3D ordered structures within one sample.

The sample prepared with the multicomponent solution shows two separated well grown mesocrystal types in the SEM image **figure 4.27b**, which shows, from the top, different structures in higher magnification. One mesocrystal has a hexagonal layer on top **figure 4.28a**, while the other shows a quadratic structure **figure 4.28b**. To get the 3D structures and a hint about the overall structural distribution in the sample, the GISAXS pattern has to be analyzed. The diffractogram exhibits sharp mesocrystal peaks of two different 3D structures. This means that highly ordered mesocrystals are grown in one sample differing in their nanoparticle superstructure. The major part of the intensity, and therefore larger number of mesocrystals, comes from the known rhombohedral structure $R\bar{3}m$ (black) with a=12.11 nm and c=29.22 nm, the rest has the tetragonal structure $I4/mmm$ (white) with a=12.32 nm and c=16.76 nm found in deposited cubes. The small c-axis lattice parameter is the result of the small cube size of 8.9 nm and a truncation of 0.88 [35], of the solution which was used in this case. The high truncation can lead to a compression in the direction of the c-axis, which expands the a-axis. The observed extra peaks at $Q_z = 0.063\,\text{Å}^{-1}$ and $Q_y = 0.016\,\text{Å}^{-1}$ and its mirror position can be an indication of a similar superstructure as was observed by Disch et al. for the same particles [35] and the SEM picture shows a similar superstructure on the surface. A precise superstructure determination is not possible due to the low intensity of the lab source.

This experiment shows that the shape dependent self-segregation holds not only for different sizes, but for shape mixtures as well, and supports the statements in the model of the mesocrystals growth from **section 4.2.2**. The size and shape selective van-der-Waals force as well as shape selective vacancies lead to a selective ordering of the different particles. Mesocrystals form from similar kinds of particles, each highly ordered, while the ensemble contains diverse mesocrystals of different kinds of building blocks and structures. This is the first observation of two well separated 3D structures within one sample.

Magnetic field

Applying a very strong magnetic field with a gradient during the self-assembly of γ-Fe_2O_3

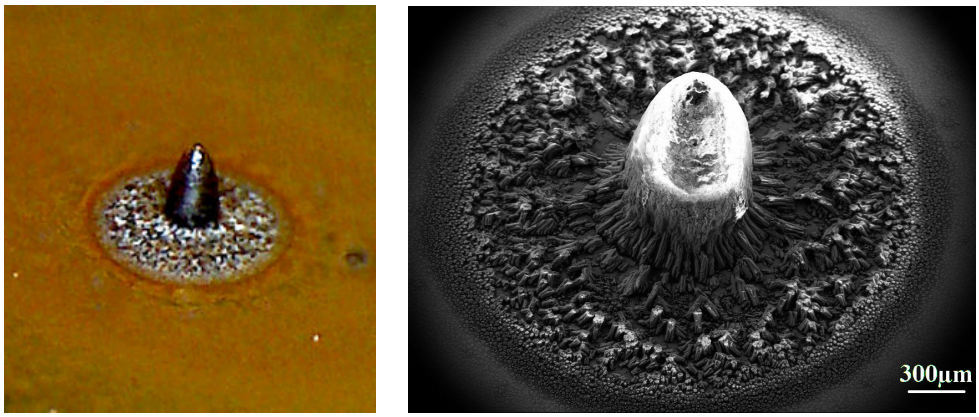

(a) camera **(b)** SEM

Figure 4.30: Images of a macroscopic poly-mesocrystal self-assembled from γ-Fe_2O_3 nanoparticles.

nanoparticles leads to a completely different crystalization behaviour as the one reported in **section 4.2.4.2** for smaller fields. A field of 30 mT and gradient of 70 mT/ cm applied parallel to the substrate induces elongated mesocrystals oriented along the H-field lines (see **figure 4.29**). The average mesocrystal size is in the order of 20 µm in width and $\approx$ hundred µm in length. The large gradient of the external magnetic field is the most likely cause of this growth pattern.

The asymmetric mesocrystal shape can be explained by the interplay of the van der Waals and the directional field induced dipole-dipole interaction between the magnetic nanoparticles enhanced in this special case to allow the formation of chain like structures. The additional directional force changes not only the shape of the mesocrystals, but allows the growth of much larger mesocrystals. Further details of this sample for example, the mesocrystal structure, have yet to be determined.

In another extreme magnetic field configuration with out-of-plane gradients during the drying of the droplet, a huge 3D nanoparticle assembly, visible to the naked eye, has been produced (see **figure 4.30a** made with a camera). The formation has a size in the mm-range, therefore referred to as macro-polycrystal, and is the first observed nanoparticle assembly in this dimension. The assembly looks like a droplet of a ferrofluid in a strong magnetic field as e.g. shown by Timonen et al. [91]. The macro-polycrystal as well as the ring around it has a metallic glossiness and a bluish black color as expected from maghemite material.

For a more detailed surface investigation normal SEM microscopy was consulted. The lowest possible magnification is shown in **figure 4.30b** and the huge object is barely visible. In this configuration the details of the pillar structure are not visible, but the mesoscopic surface structure inside the ring can be resolved. Densely arranged mesocrystals are visible at the edge of the ring. The size of the structures increases with decreasing radius and looks more like filaments with an inner structure. At the border of the macro-polycrystal filaments of nanoparticle assemblies appear as if pulled up to the pillar. In **figure 4.31a** a higher magnification is chosen and it is visible that the whole pillar consists of further branched formations, a dendrite like structure, already observed in other nanoparticle systems [37, 88].

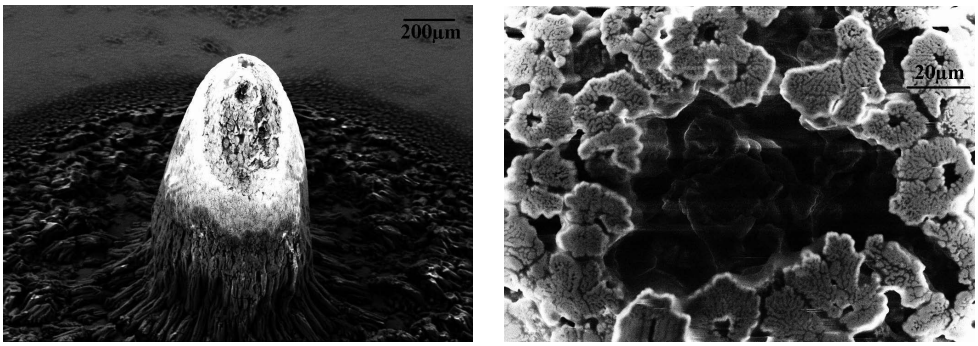

(a) overview **(b)** close-up view of the surface of the pillar

Figure 4.31: SEM images of a macro-polycrystal self-assembled with γ-Fe_2O_3 nanoparticles with different magnifications.

GISAXS measurements were performed at the lab source in Risø. **Figure 4.32a** shows the scattering pattern of the macro-polycrystal. The beam is scattered from the middle of the pillar without hitting the substrate in a typical SAXS geometry. Rings are visible as indication of a 3D powder. The sharpness of these rings proves a relatively large correlation length and thus an existing order in the system. To define the average correlation length a Voigt function is fitted to the peaks from the radially integrated intensities. A value of 550 nm for the average correlation length is received, which indicates an existing long range order inside the macro-polycrystal consisting of many well ordered mesocrystals rotated against each other. This order belongs to the $R\bar{3}m$ structure, known from the corresponding mesocrystals. Furthermore a texture can be observed on the Debye-Scherrer-rings, which indicates an inhomogeneously distributed 3D powder of mesocrystals. A measurement on the ground next to the macro-polycrystal (**figure 4.32b**) shows a mixture of 3D powder and partly oriented mesocrystals. Sharp peaks in Q_y direction indicate a well ordered in-plane structure and the broad peak in Q_z direction suggests the presence of a thin film of nanoparticles.

The sharp peaks on the rings can be explained by a few mesocrystals with larger correlation lenght. Additionally, the pillar height is much larger than the maximal measured droplet height in the in-situ experiments ($< 500\,\mu m$), which makes it even more fascinating, as no obvious differences were observed during the drop casting. Similar to the previous in-plane gradient study, the mesocrystal growth follows the field lines, moving to the sample center and even piling up above the liquid surface. The strong directional force of the field and field gradient align the magnetic moments of the nanoparticles and let them order as long mesocrystals chains mainly through the dipole-dipole interaction. The single chains are packed closely to each other, whereas the lower crystal can be assumed as a new basis for a new chain formation and the macro-polycrystal growth. If this formation happens in a fluid layer or outside the droplet can not be clarified until now. Furthermore with this experiment it is shown that a substrate is not necessary for the formation of good mesocrystals inside a dipole-dipole formation dominated system, although these are rotated against each other while a growth on a substrate leads to a preferred orientation of one crystal axis.

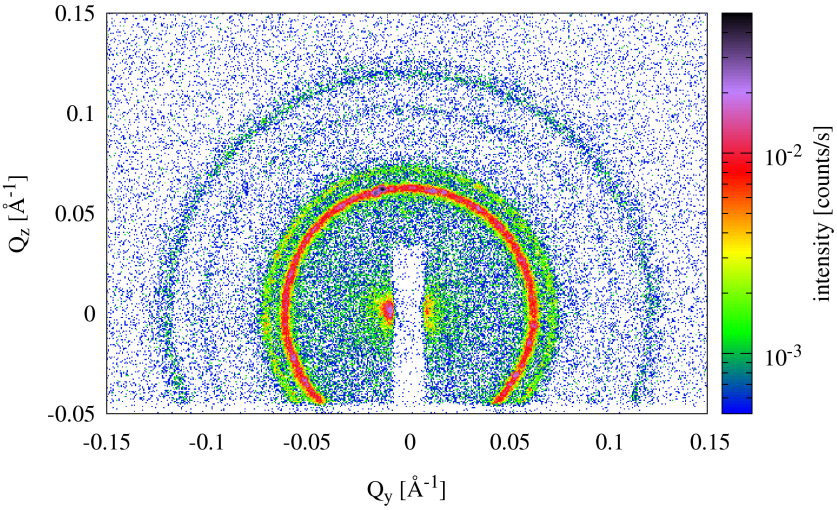

(a) macro-polycrystal without substrate

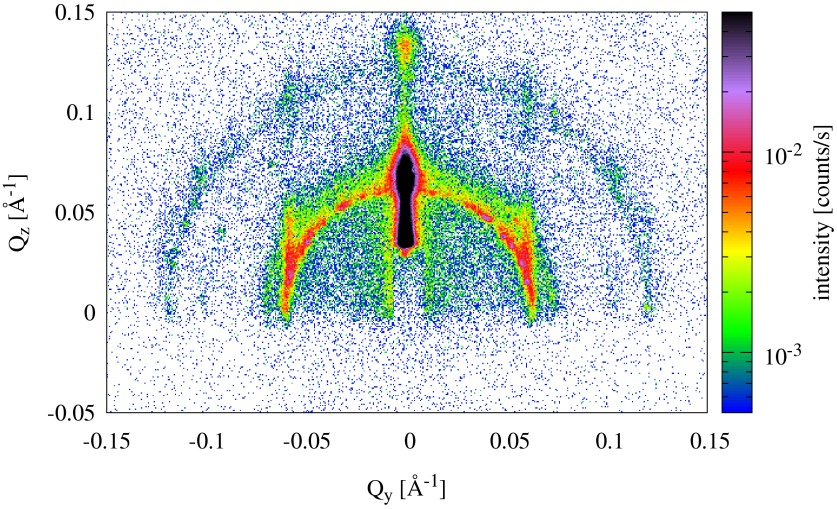

(b) next to the macro-polycrystal

Figure 4.32: GISAXS/SAXS measurements of a macro-polycrystal self-assembled with γ-Fe_2O_3 nanoparticles at the lab source in Risø. The measurement was done in transmission geometry (a) and under an angle of 0.4 ° (b) with a wavelength of 1.54 Å.

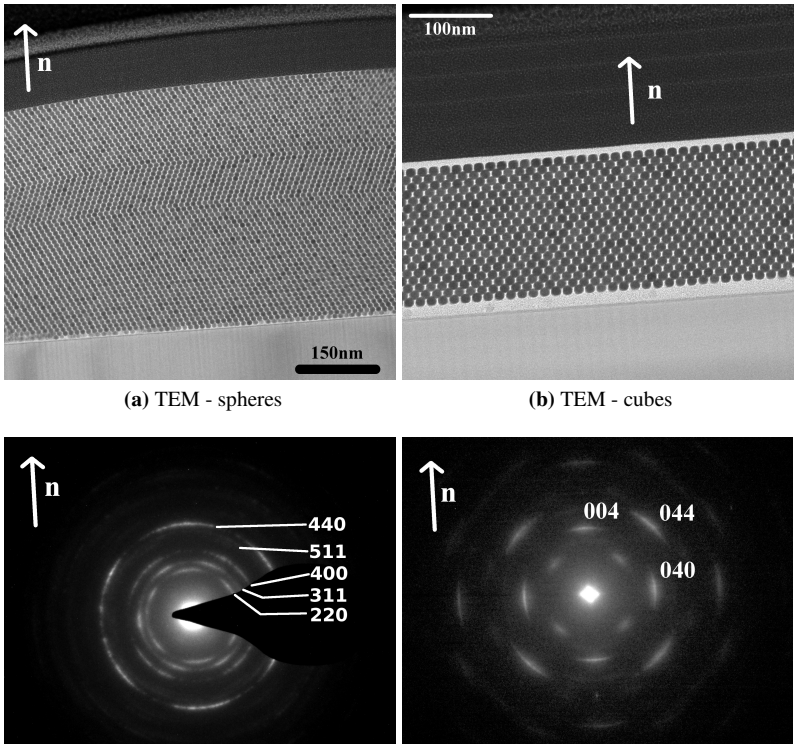

(a) TEM - spheres **(b)** TEM - cubes

(c) SEAD - spheres **(d)** SEAD - cubes

Figure 4.33: SEAD pattern of one mesocrystal with its corresponding real space TEM image for spherical and for cubic building blocks. The SEAD images are taken from around a 10x10 nanoparticle cluster from the mesocrystal mapped. The white arrow with the letter n defines the growth direction of the mesocrytsal.

4.2.5 Crystalline orientation of the nanoparticles

So far I have considered the individual nanoparticles as the elementary building blocks forming the mesocrystals when they arrange in a periodic manner. Now I go one step further and consider in addition the atomic structure of these nanoparticle building blocks. We can ask the question, how the atomic lattice planes of different nanoparticles are oriented with respect to each other. Can we achieve an orientational alignment of the atomic lattice planes within the entire mesocrystal? How we can achieve such an order and to which degree? What is the effect on the magnetic properties of the mesocrystal? As has been reported in [41, 73], single domain magnetic nanoparticles inside a solvent can align their easy axis in the magnetic field direction and allow a partial orientation by the application of an external field during the deposition process. It is expected that this formation stays stable in this preferred orientation after deposition. The question arises how this effect can be observed in an ensemble of mesocrystals of such particles. The influence of different shapes, like isotropic spherical and anisotropic cubic nanocrystals, is investigated, too. For this study space resolved selected area electron diffraction (SEAD), as well as depth resolved x-ray wide angle diffraction experiments, which

average over a large volume, are used to allow an estimate of any preferred orientation present in the sample. The possibility of manipulating the system during the process of self-assembly and thus a better control of the resulting structure is a desired goal of these experiments.

The influence of spherical and cubic shaped nanoparticles on preferred orientations of the nanoparticle atomic structure during the growth inside the 3D assemblies can be investigated by SEAD on a local area in the superstructure. The sample consists of one mesocrystal, which is cut perpendicular to the substrate surface to a lamella with a film thickness of around 1-2 nanoparticle layers (see real space images **figure 4.33a** and **figure 4.33b**). The SEAD images are taken from about a 10x10 nanoparticle cluster of the mapped mesocrystal. The white arrow with the letter n indicates the growth direction of the mesocrytsal and is the normal to the substrate's surface.

The mesocrystal, built up by spherical nanocrystals and self-assembled in an out-of-plane oriented field of 2mT, shows a SEAD pattern with a weak ring structure and clearly visible texture. All reflexes are visible indicating that the single particles are randomly oriented inside the mesocrystal. The intensity on the rings is not equal as the number of illuminated particles is limited. An influence of a weak magnetic field on the orientation of the crystallites during the self-assembly of isotropic spherical nanoparticles is not visible. In contrast, the mesocrystal built up by cubic nanoparticles and self-assembled without any field, shows a SEAD pattern with clearly visible reflections. The electron diffraction pattern shows a 4-fold axis indicating an alignment of the nanoparticles inside the mesocrystal in [100] direction with respect to the beam and for the growth direction an equivalent [001].

For an investigation of existing preferred directions of the nanoparticles inside the mesocrystals with larger statistical relevance, x-ray diffraction measurements with a geometry as shown in **figure 2.5** are used. With this method it is possible to average over a wide area and depth of an ensemble of mesocrystals, which allows the observation of out-of-plane aligned lattice planes. The $\omega - 2\theta$ scans from 0° to 100° scattering angle for formations with spherical and cubic building blocks are plotted in **figure 4.34**. The small angle region, which is shown as inset on the left side, is used to characterize the nanoparticle superstructure and looks very well for both samples. The insets on the right side show the zoom of the interesting wide angle part for the investigation of the preferred crystalline structure orientation.

The scan for the spherical nanoparticles shows all allowed reflections, which have enough intensity to be above the instrument and substrate background, with $\approx$ the ratios expected (**figure 4.34a**). This result demonstrates that the crystalline orientations inside the mesocrystals of the ensemble are powder like and nothing indicates a preferred orientation, confirming the observation of the SEAD investigation by TEM on an equivalent sample. Both, the local view on one mesocrystal and the averaged investigation on an ensemble of mesocrystals show no favored crystalline orientation. Independently, the observed peaks exhibit a small shift against the expected positions from bulk, which increase with higher Q values and thus indicate a slightly different crystal lattice in the nanoparticle. In this case a lattice constant which is 0.09% bigger than in bulk maghemite, published with 8.356 Å [72], is found. A lattice strain is a typical observation in nanometer sized particles, specifically the increase of the lattice constant was already observed for small nanoparticles in [103].

The system with cubic nanoparticles exhibits a larger lattice constant of the nanoparticle structure than the maghemite bulk material as well, in this case of 0.2% . In contrast to the spherical

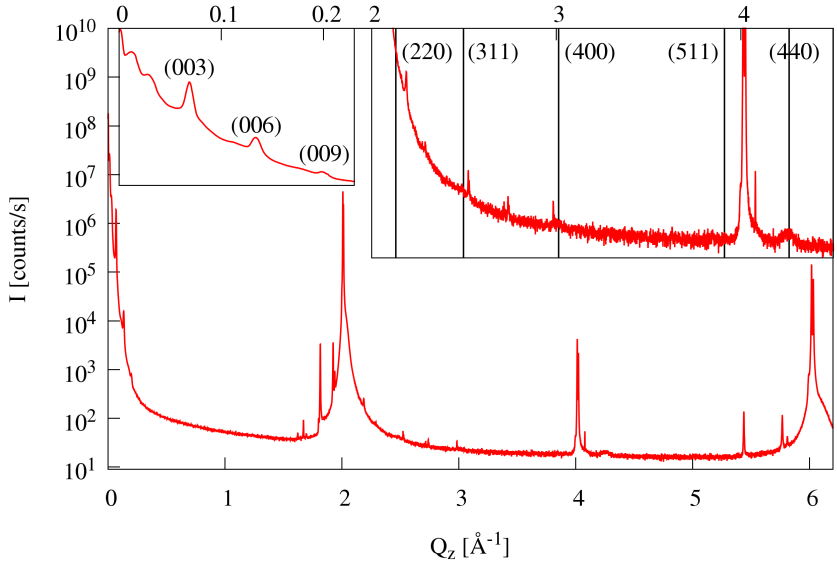

(a) spheres

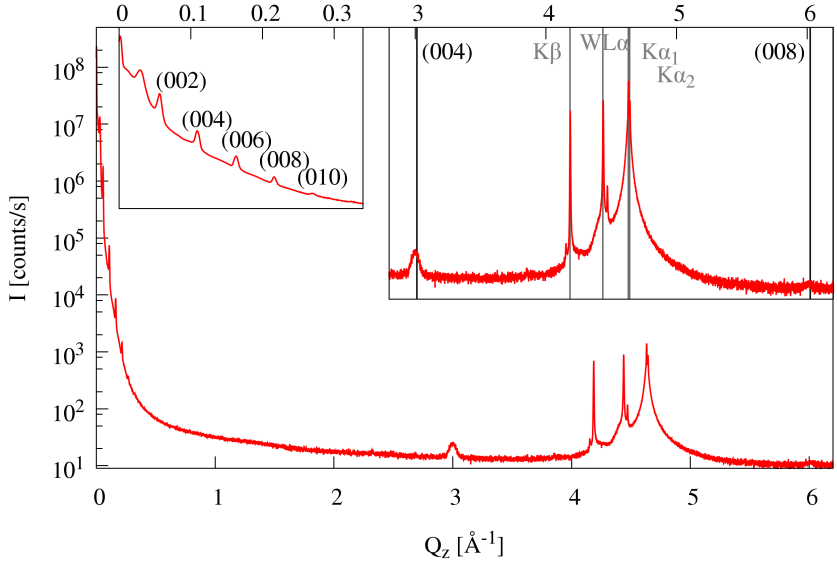

(b) cubes

Figure 4.34: X-ray diffraction measurements of an ensemble of mesocrystals with different building blocks. The $\omega - 2\theta$ scans run from 0° to 100° scattering angle and are shown in the overview plot. The small angle part (inset on the left side) shows the good structure of the nanoparticle superstructure, while the wide angle part (inset on the right side) is sensitive to the atomic structure of the particles inside the mesocrystals and illustrates the alignment of the crystalline orientation inside the mesocrystals averaged over the ensemble. The black indices correspond to the γ-Fe_2O_3 crystal lattice, the gray one for silicon reflexes from the substrate (spheres: (400) Si reflex; cubes: (111), (222) and (333) Si reflexes; all reflexes produce multiple peaks due to other wavelength contamination in the X-ray beam).

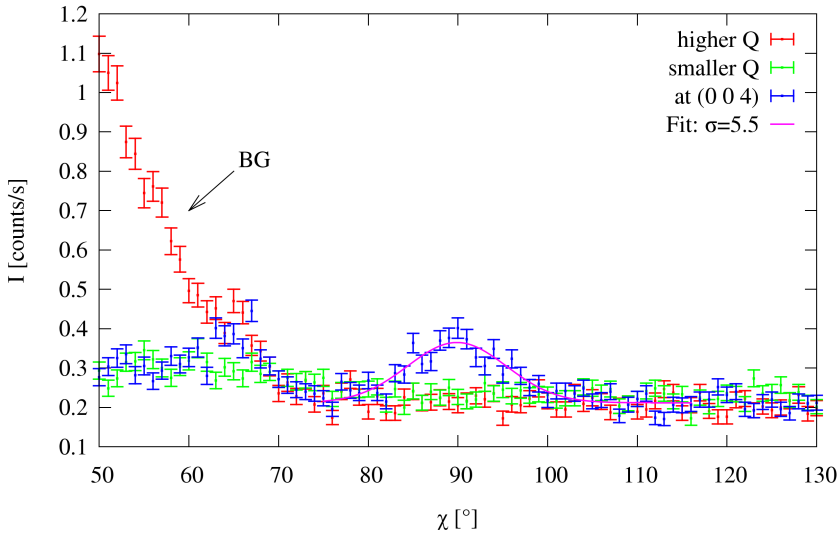

Figure 4.35: χ-scan on the (004) peak found in the $\omega - 2\theta$ scan (blue) and symmetric positions around the peak (red and green) are shown. In this configuration the scan is done in tangential direction, which is lying parallel to Q_y without changing of $|\vec{Q}|$. The Gauß-fit (pink) results in a peak width σ of 5.5 °.

system it features two clearly visible peaks in the wide angle range. These reflexes are indexed as (004) and (008) of the γ-Fe_2O_3 structure and show together with the absence of any other reflection (even stronger ones) definitively the presence of a preferred alignment of the nanoparticle structure [001] to the [001] direction inside the mesocrystals, which is parallel to the substrate normal. This observation is consistent with the SEAD experiment. Oriented and randomly aligned crystals have the same peak width in a $\omega/2\Theta$ -scan, but the parallel aligned particles all contribute to the same reflections and thus lead to higher intensities.

To quantify the degree of alignment in this sample, a 4-circle X-ray diffractometer was used with more degrees of freedom for the sample positioning (**section 3.8**). In the configuration used a χ-scan, which is a Q - scan in tangential direction ($\parallel$ to Q_y without changing of $|\vec{Q}|$), is measurable. Scans are performed on the (004) peak, which was found with the reflectometer, and symmetric positions close to the expected peak positions for comparison (see **figure 4.35**). The χ-scan on the (004) reflex shows a clear peak, while the other scans have no features at this position. Certainly a preferred crystalline orientation in the [001] direction of the nanocrystals inside the mesocrystals with cubic building blocks is confirmed.Although the particles obviously tend to orient themselves within the mesocrystal lattice, it is impossible to prove the orientation in-plane due to the arbitrary orientation of the mesocrystals. The increased intensity of the scan around (0 0 4.14) to lower χ values is no reflex of γ-Fe_2O_3 structure, but background from the substrate. A Gaussian fit on the (004) peak at $\chi_0 = 89.89$ yields a peak width σ, which describes a random variation of the tilting of the crystalline preferred orientation of the nanoparticles away from the substrate surface normal, of 5.5 °. The instrumental resolution of this setup is better than 0.1 ° and therefore can be neglected for the analysis. Noticeable is that the in-situ

GISAXS experiments show a random variation of the tilting of the c-axis of the nanoparticle superstructure away from the substrate surface of up to 5 ° (see **section 6.3.3**). This comparison shows how strongly the particle orientation is defined by the mesocrystal crystal lattice as there seems to be no measurable misalignment of the crystalline to the MC lattice, which would lead to a broadening of the diffraction peak with respect to the GISAXS results.

This series of experiments shows a dependence of the preferential orientation of the nanoparticle structure on the morphology of the building blocks. The system with spheres show no preferred orientation, as expected from their isotropic shape and as only a small field of 2 mT was applied during the process of self-assembly. The field is too low to overcome the thermally activated Brownian motion to align the easy axis in field direction. Applying a much stronger field can actually orient spherical particles, as has been shown in [55, 73]. The van der Waals dominated self-assembly of the spheres has no anisotropy or additional force which could lead to an energetically favorable alignment of the crystalline structure. The anisotropic cubes, on the other hand, exhibit a shape anisotropy which leads by the van der Waals dominated self-assembly to a face-to-face configuration (see **section 4.2.4.1**), and thus to an alignment of the cubic nanoparticles to the mesocrystal lattice, as one would expected from the structure given. The experiment shows further that the particle facets are always aligned in the [100] directions.

4.3 Conclusions

The process of self- assembly, where the nanocrystals spontaneously order in a superstructure, is a promising way for the fabrication of 3D highly ordered nanoparticle assemblies, so called mesocrystals. In this chapter the post deposition properties of the self-assembly have been investigated for different experimental conditions during the self-assembly. The gathered expertise can be used to develop a better self-organization procedure and tune the resulting parameters of the samples.

The good quality of the γ-Fe_2O_3 particles used, which is an important prerequisite for further experiments, is demonstrated and the newly developed rounded cubes form factor is successfully applied to the measured SAXS pattern. The results from this model of the particle shape have been verified by real space TEM images.

The feasibility of tuning the ensemble of mesocrystals grown by external preparation parameters such as shape, field and evaporation time is proven. For this investigation the combination of complementary microscopy and scattering methods is used to get a full overview over this complex system.

The mesocrystal structure is mainly influenced by the shape of the nanoparticles. No other preparation parameter varied in this work leads to changes in the space group. The determination of the nanoparticle superstructure is consistent with previous experiments [35, 103]: Cubes form a bct structure resulting from the maximization of the van-der-Waals interaction between facets and truncated edges of surrounding particles [86], while the spheres organize in a slightly deformed fcc superstructure due to an interplay of steric repulsion and van-der-Waals interaction, leading to an energetically more favorable fcc than hcp stacking [26, 50, 95]. Additionally, the nanoparticle shape influences the preferred crystalline orientation of the nanoparticles inside the mesocrystals. The anisotropic cubes order with a preferential crystalline orientation of the nanoparticles in the [001] direction parallel to the substrate normal, while isotropic spheres lead

to no preference under the used preparation conditions. An influence of the weak applied field is not visible.

The dependence of the long range order of the nanoparticle superstructure on an applied field during the self-assembly [14, 24, 33, 84] was confirmed in this chapter and examined in dependence on the strength and direction of the field and field gradient. An external field of medium strength (80 mT, 18 mT/ cm) applied in the growth direction supports the self-assembly and improves the quality of the ensemble of mesocrystals, while other orientations worsen the result. A good growth of the mesocrystal without any field has to be mentioned, which is in contrats to previous studies by Pileni et. al. [73]. With a field of medium strength the process of self-assembly is still dominated by the van der Waals force and not by the dipole-dipole interaction. For shorter evaporation times the field influence becomes stronger. In general, a longer drying time has a positive influence on the mesocrystal growth as has been reported earlier [33, 38].

Extraordinary conditions for the self-assembly parameters lead to strong alterations of the resulting structures. A multicomponent nanoparticle solution consisting of spheres and cubes self-assembles shape selective in perfectly separated 3D ordered mesocrystal systems. In contrast to previous experiments of the study of shape selective self-segregation [24, 60, 64, 67, 86], the depth resolved GISAXS method is used in addition to microscopy methods, allowing the differentiation between a 2D and 3D ordered structure averaged over the sample and thus a more precise classification of different structures. This is the first detailed investigation of well separated 3D ordered structures within one sample. Using a magnetic field configuration with higher field strength/gradient during the drying of the droplet, a macro-polycrystal (a "bullet"-shaped solid assembly) with a size in the mm-range has been grown, which is visible by the naked eye and consists of clusters of ordered nanoparticles. In this case the dipole-dipole interaction is the driving force to form structures along the field lines.

From the combination of the different results, it has been found that the mesocrystal growth within a broad range of deposition conditions is a size and shape selective ordering process dominated by the van der Waals force taking place in a dense solution at a defined nucleation area. Comparison to the atomic crystal growth of thin films shows many similarities, but mesocrystals feature some new aspects due to the distribution of size and shape of nanoparticles. The experiments realized and their interpretation with respect to the mechanisms of self-organization provide the first components for a model of the mesocrystal growth, which was refined by the results of the following chapters.

Chapter 5

Modeling of scattering intensities of 3D nanoparticle assemblies

In this chapter the quantitative analysis of the different scattering experiments will be discussed in detail. Although it was not possible to simulate most scattering patterns precisely, many of the core features could be reproduced and explained. Besides the experiment dependent difficulties (as e.g. refraction and reflection in GISAS experiments) the principle inhomogeneity of the mesocrystal 2D powder, forming on the substrate during the self assembly, introduces additional complexity to the model and leads to e.g. peak broadening, which masks the "true" physical characteristics of the structural order.

5.1 General considerations

5.1.1 Single mesocrystal structure factor in Born Approximation

Independent on the scattering method, the Born Approximation (BA) is a good starting point to analyze the scattering pattern, as it gives good results even for grazing incidence experiments, when one does not get too close to the critical angle of total reflection. Secondly, the DWBA used in the later case needs a BA structure factor for its calculations.

A single mesocrystal itself is approximately a cylinder shaped crystal of equal particles and the scattering potential $V_{Meso}(\vec{R})$ can thus be decomposed into the product of a function describing the cylinder shape P_{MC} and the regular, infinite lattice convoluted with the nanoparticle scattering potential V_{NP} (see **section 2.2.3**). The Fourier transform of this function (structure factor) can be derived using the convolution theorem (**eqn. 2.30**) as the product of the nanoparticle form factor F_{NP} with the convolution of the reciprocal lattice and a cylinder form factor $F_{MC}(\vec{Q})$:

$$V_{Meso}(\vec{R}) = V_{NP} \otimes \left(P_{MC}(\vec{R}) \cdot \sum_{uvw} \sum_{i=1}^{N} \delta(\vec{R} - \vec{R}_{uvw} - \vec{r}_i) \right) \tag{5.1}$$

$$S(\vec{Q}) = F_{NP}(\vec{Q}) \cdot \left(F_{MC}(\vec{Q}) \otimes \sum_{hkl} \sum_{i=1}^{N} \delta(\vec{Q} - \vec{Q}_{hkl}) \cdot e^{i\vec{Q}\vec{r}_i} \right) \tag{5.2}$$

where the real space and reciprocal lattice points are defined as $\vec{R}_{uvw} = u\vec{a} + v\vec{b} + w\vec{c}$ and $\vec{Q}_{hkl} = h\vec{a}^* + k\vec{b}^* + l\vec{c}^*$, respectively. N denotes the number of particles in the unit cell with a position of $\vec{r}_i$. The particle form factor for perfectly mono disperse spheres with radius r_S [71] and truncated cubes width edge length a_{NP} and truncation length t [33] as derived by Fourier transform of the real space scattering potential (constant scattering strength density ρ inside and 0 outside the particle) are:

$$F_{NP}^{\text{Spheres}}(\vec{Q}) = \frac{1}{\sqrt{V}} \left(\frac{3V\rho(\sin(Qr_S) - Qr_S\cos(Qr_S)}{(Qr_S)^3} \right) \tag{5.3}$$

$$F_{NP}^{\text{T-Cubes}}(\vec{Q}) = \frac{1}{\sqrt{V}} \left(\frac{\sin(\frac{a_{NP}}{2}Q_x)}{\frac{a_{NP}}{2}Q_x} \frac{\sin(\frac{a_{NP}}{2}Q_y)}{\frac{a_{NP}}{2}Q_y} \frac{\sin(\frac{a_{NP}}{2}Q_z)}{\frac{a_{NP}}{2}Q_z} - \sum_{i=1}^{8} F_i^E(\vec{Q}) \right) \tag{5.4}$$

$$\text{with } F_i^E(\vec{Q}) = (A_x + A_y + A_z - D) \cdot e^{-i\frac{a_{NP}}{2}(\pm Q_x \pm Q_y \pm Q_z)} \text{ (for all 8 sign permutations)}$$

$$A_m = \frac{e^{itQ_m}}{Q_m(Q_m - Q_n)(Q_m - Q_o)} \quad (m,n,o \in (x,y,z))$$

$$D = \frac{1}{Q_x Q_y Q_z}$$

$$\tau_{Trunc} = \frac{2t}{a_{NP}} \quad : 0 \leq \tau_{Trunc} \leq 1$$

Additionally, we introduce a form factor with a different kind of truncation for the nanocubes using the intersection of a cube with a sphere, which is better suited to describe the actual experiments in **section 4.1** and **section 7.3.2**. The FT for the rounded cubes is calculated numerically on a three dimensional grid, as no analytic solution for this case is known.

$$\begin{aligned}
F_{NP}^{\text{R-Cubes}}(\vec{Q}) &= \mathfrak{F}(\rho_{R-Cubes}(\vec{r}, a_{NP}, \tau)) \\
\text{with } \rho_{R-Cubes}(\vec{r}, a_{NP}, \tau) &= \rho_{Cube}(\vec{r}, a_{NP}) \bigcap \rho_{Sphere}(\vec{r}, R) \\
\rho_{Cube}(\vec{r}, a_{NP}) &= \begin{cases} \rho_0 \text{ for } |r_x| \leq \frac{a_{NP}}{2} \wedge |r_y| \leq \frac{a_{NP}}{2} \wedge |r_z| \leq \frac{a_{NP}}{2} \\ 0 \text{ else} \end{cases} \\
, \ \rho_{Sphere}(\vec{r}, R) &= \begin{cases} \rho_0 \text{ for } |\vec{r}| \leq R \\ 0 \text{ else} \end{cases} \\
\text{and } \tau_{Round} &= 1 - \frac{2R/a_{NP} - 1}{\sqrt{3} - 1} \quad : 0 \leq \tau_{Round} \leq 1
\end{aligned} \tag{5.5}$$

For the numeric calculation of the rounded cubes form factor, the density described by **equation 5.5** is calculated for a 200^3 points cubic space region, Fourier transformed using FFT and than interpolated (implementation in appendix **section B.1**). The flat truncation has the analytic solution **equation 5.4**, which is not defined for zero or equal Q_i components and thus needs to be calculated at slightly different Q positions numerically (see appendix **section B.1**). The new model can reproduce a perfect spherical and cubic system equivalent to the analytic models showing the applicability of the numeric approximation (see **figure 7.16**).

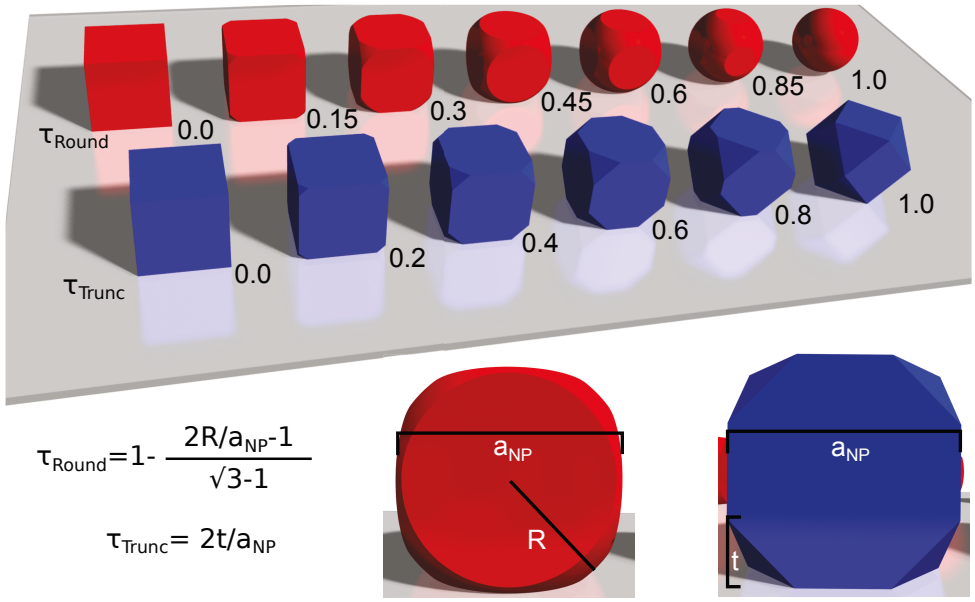

Figure 5.1: The geometric representation of the two different kinds of cubic form factors in real space. The definition and some example values for the degree of truncation τ is shown.

The real space representation of the two kinds of truncated form factors (truncated (flat) and rounded) are sketched in **figure 5.1**. The truncation parameter τ is chosen relative to the edge length a_{np} such that 1 corresponds to maximum and 0 to no truncation. The extreme case $\tau = 0$ matches for both cases an ideal cube, while $\tau = 1$ corresponds to a perfect spherical particle for the rounded cube model and a cubeoctahedron for the truncated cube model.

Equally, one can derive the mesocrystal shape form factor as the FT of a cylinder of radius r_{MC} and height h_{MC}, with J_1 as the Bessel function, aligned with the cylinder axis parallel to z as [71]:

$$F_{MC}(\vec{Q}) = 2\frac{\sin(h_{MC}Q_z)}{h_{MC}Q_z}\left(\frac{J_1(r_{MC}\sqrt{Q_x^2+Q_y^2})}{r_{MC}\sqrt{Q_x^2+Q_y^2}}\right) \tag{5.6}$$

The scattering intensity is the absolute square of the structure factor and as the particle form factor is a multiplicative factor it can be separated in the intensity equation as well:

$$I(\vec{Q}) = |S(\vec{Q})|^2 = |F_{NP}(\vec{Q})|^2 \cdot \left| F_{MC}(\vec{Q}) \otimes \sum_{HKL} \sum_{i=1}^{N} \delta(\vec{Q} - \vec{Q}_{HKL}) \cdot e^{i\vec{Q}\vec{r}_i} \right|^2 \tag{5.7}$$

Equation 5.7 shows clearly, that the individual measured peak intensity is given by the form factor and the sum in the structure factor term [1] while the peak shape is described by the mesocrys-

[1] The structure factor term can only be the square of an integer number between 0 and the number of particles in the unit cell N. For the simple systems investigates here, the structure sum is either zero or one/four, so each peak intensity is given by the FF only.

tal shape form factor, which is placed at every allowed reciprocal lattice position. This holds true for a mesocrystal of perfectly equal particles situated exactly at the lattice positions. In a real mesocrystal there will always be a deviation in particle size and position. The positional offset can be treated similarly as in the derivation of the Debye-Waller factor described in **section 2.2.4** with the only difference that the positional offset is not averaged over time but over particle positions. This leads to a Debye-Waller term $e^{-\frac{1}{3}|Q|^2|<a>|^2}$ in the intensities and an additional incoherent contribution to the single particle form factor.

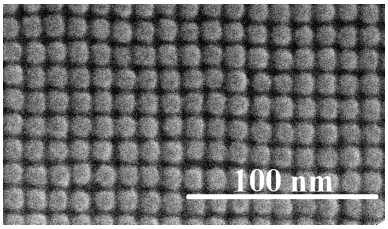

Figure 5.2: Cubic particles ordered in on a mesocrystal with deviation of the particle position (SEM picture on top of a mesocrystal).

The positional deviation can be seen in **figure 5.2**, where some cubic particles are not on the regular grid positions. Describing a variation of particle size is everything but trivial, as these variations will most definitely lead to a local change in lattice constants which introduces additional changes to peak shapes, intensity and incoherent contribution.

If the correlation of the mesocrystal structure is limited, and much smaller than the mesocrystal size, the peak shape described by $F_{MC}(\vec{Q})$ approaches a Lorentzian with a HWHM which is related to the correlation length as $\xi = \frac{2\pi}{HWHM}$.

5.1.2 Influence of 2D powder and mesocrystal ensemble statistics

In general, the samples under investigation consist not only of one single mesocrystal, but also of an ensemble of mesocrystals which grow independently. The ensemble delivers a variety of new properties, which influence the scattering pattern and the probability weighted sum of many individual simulations over the entire parameter range needs to be calculated. These new influences will be discussed in this subsection and are needed to describe the scattering pattern of complex 3D nanoparticle systems.

In-plane rotation For all but the single mesocrystal samples, the substrate only provides the surface plane, which defines the direction of the $\vec{c}$-axis, so that there is no preferred orientation of the $\vec{a}$ direction in the plane. The mesocrystals are arbitrarily oriented to each other, a so-called 2D powder. This means that each reciprocal lattice point is associated with a circle in reciprocal space around the z-axis. This makes it possible to measure all scattering planes in one orientation of the sample as it was used in all over GISAXS experiments, but it makes the individual lattice directions indistinguishable. As the mesocrystal areal density is in the order of $\frac{1}{(10\mu m)^2}$ compared to a beam size of 0.1-1 mm^2 there are 10^4-10^5 mesocrystals in the scattering volume, so one can expect no influence of texture on the peak intensities. This means that peaks originating from completely different scattering planes can still be compared in a GISAS experiment.

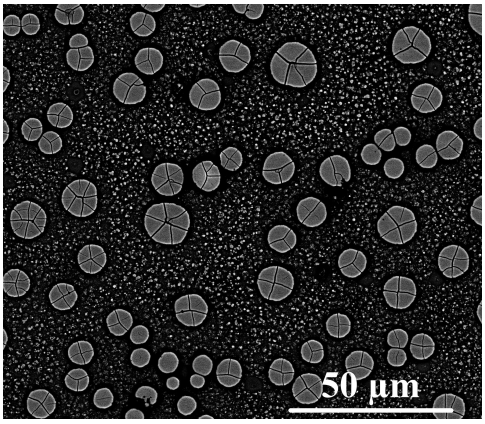

(a) SEM picture of an ensemble of mesocrystals. The small points between the huge mesocrystals are crystals in the nanometer range.

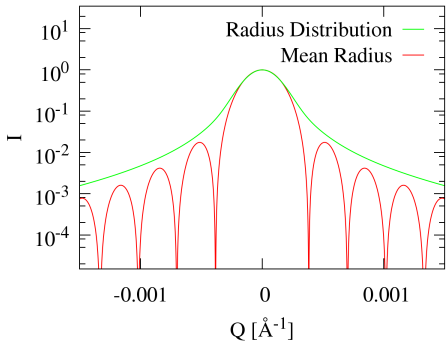

(b) An incoherent average of an ensemble of Gaussian size distributed mesocrystals compared to the pure peak shape of a mesocrystal of average size.

Figure 5.3: Influence of size distributed ensemble of mesocrystals on the peak shape.

Independence of mesocrystals Due to the effect described above there is a very low probability that two neighboring mesocrystals in an average distance of 10 µm are aligned equal enough to produce the same peaks (except for the (00L) type reflections) and thus the mesocrystals, which contribute to the same reflections, will have a distance much larger than the coherence area ($\leq 10\,\mu m \cdot 100$ nm) of the scattering experiment. Here we assume due to random variations in orientation and position of the mesocrystals coherent scattering between different mesocrystals can be neglected. Thus we calculated the incoherent superposition of scattering from the mesocrystals by adding intensities, not amplitudes. These components were to be add incoherent together as intensities.

Mesocrystal size distribution As can be seen in the SEM **figure 5.3a**, the mesocrystals grown have a large size variation between ≈500 nm and ≈20 μm. The incoherent average of an ensemble of Gaussian size distributed mesocrystals is shown in **figure 5.3b**, compared to the pure peak shape of the mesocrystal of average size. One can see that the shape of the central peak is distorted and the oscillation minima are smeared out. Although this variation is easily introduced into a model it requires recalculation of the complete model several times.

Deviation in shape The description of the in-plane shape of the mesocrystals as circles is a simplification as is obvious from many SEM images from nanocube samples (see **figure 5.4a, 5.4b**). Often the mesocrystals are less symmetric, building octagons, rectangles or diamond shapes. For the nanospheres samples the cylindrical model is very close to reality (**figure 5.3a**, **5.4c**) . A shape changing over one single sample is observed, too. Although this could change the peak shapes for single mesocrystal experiments (where the preparation automatically leads to cylindric shape) the impact on GISAS measurements is expected to be negligible due to several reasons. The limited resolution of the instrument (e.g. ID01: 0.0054 $Å^{-1}$) leads to much broader peaks than the theoretical width of the large in-plane size of the mesocrystals (0.00013 $Å^{-1}$), so any change in fine features would not be detectable. Additionally, the influence of

the nanoparticle size distribution on the peak shapes of the mesocrystal is expected to be much larger.

Out-of-plane rotation Samples produced with shorter solvent evaporation times often show radial smearing of peaks in the GISAXS patterns. Microscopy investigations have shown that some mesocrystals have tilted $\vec{c}$-axes with respect to the substrate surface normal (**figure 5.4d**). In contrast to the equally distributed rotational average of the in-plane component, this is a Gaussian distributed orientational misalignment, which needs to be considered by averaging the model for different rotations. The effect of such a rotational average is shown in (**figure 5.5c**) as σ_{tilt}.

Lattice constant deviations There can be a distribution of the mesocrystal unit cell geometry in the sample, which leads to different reciprocal lattice vectors and thus peak positions for the different mesocrystals. The simplest form of this distribution is an equal Gaussian variation of all lattice parameters, which leads to a radial smearing of the peaks as shown in (**figure 5.5c**) as σ_r. This is not always sufficient to describe the peak shape if the in-plane lattice constant variation is different from the out-of-plane one. In this case the directions need to be treated independently.

Computational challenges Unfortunately all of the situations above can be found combined in one sample, which requires the computational average over 3-5 variables. Even for an extremely low sampling of 10 points per variable this would lead to thousands of model evaluations. For a full modeling of a GISAXS pattern with about $(1024\ \text{pix})^2$ and a peak function which takes only 100 CPU operations (it is a high level function of complex variables) this leads to $10^4 \cdot 1024^2 \cdot 100 = 10^{12}$ operations taking about 5 minutes on a modern system. When the model function gets more complex this can increase drastically, making the model impractical or even useless. Some of the averages can also be described as a convolution of two simple functions which makes it possible in special cases to use a fast Fourier algorithm to compute the peak shapes, which reduces the evaluation times by several orders of magnitude (fast Fourier transform (FFT) convolution is $O(n \cdot \log(n))$ compared to $O(n^2)$ of a summation).

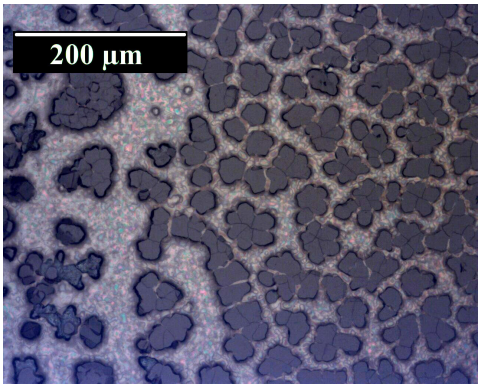

(a) Mesocrystals with cubic building blocks observed close to the edge of the sample (LM picture).

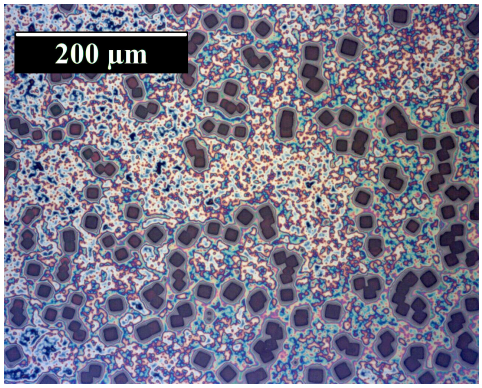

(b) Mesocrystals with cubic building blocks observed more in the center of the sample (LM picture).

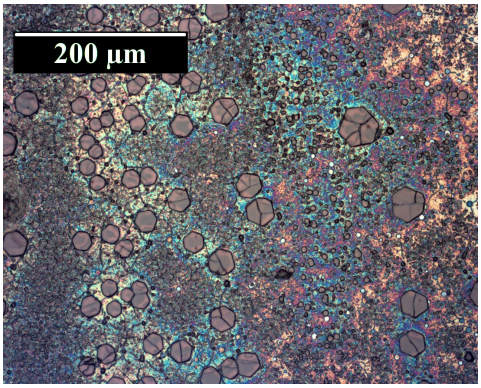

(c) Mesocrystals with spherical building blocks (LM picture).

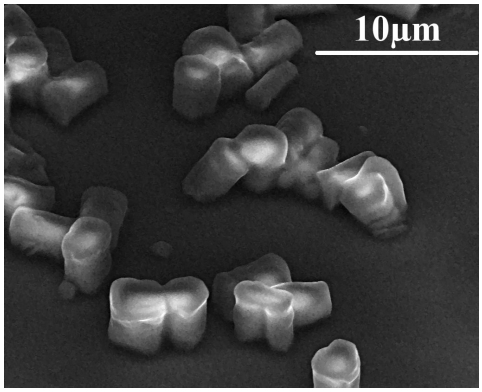

(d) Mesocrystals with cubic building blocks, which are tilted (SEM picture under 45°).

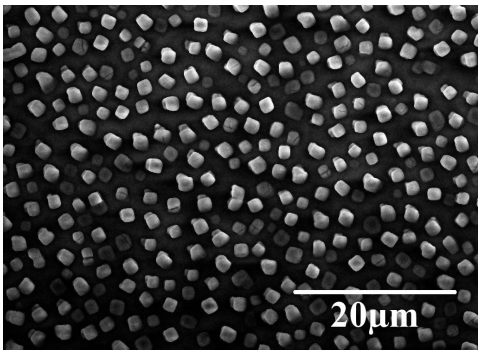

(e) Mesocrystals with cubic building blocks and high density (SEM picture).

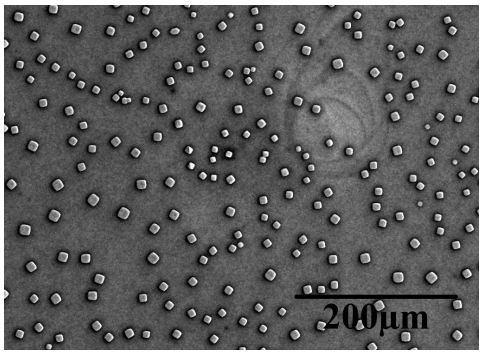

(f) Mesocrystals with cubic building blocks with large distance (SEM picture).

Figure 5.4: The complexity of the mesocrystal ensemble is shown as examples in these SEM and LM pictures. The shape deviation is illustrated in **figure 5.4a, 5.4b and 5.4c**, in which **figure 5.4a and 5.4b** exist in one sample. **Figure 5.4d** is an example for the out-of-plane rotation which is observed. The variation of the mesocrystal distances is shown in **figure 5.4e and 5.4f**.

5.2 Grazing incidence specific considerations

In scattering experiments at grazing incidence, the incoming or outgoing beam approaches the critical angle of total reflection of the substrate (and mesocrystal film). Close to this angle the beam is refracted when penetrating the material and partly reflected at the surface. The simple BA is no longer valid as the approximation of weak scattering no longer holds. When considering only the specular reflected beam intensity this can be described by an optical approach based on Parratt's formalism (see **section 2.2.5**). When other scattering geometries (in-plane GISAS, off-specular scattering) are considered, the distorted wave Born approximation combines the refraction and reflection effects of the optical approach with the Born approximation to describe scattering from structures in the surface plane (see **section 2.2.5**).

5.2.1 Substrate reflection

As most GISAXS experiments are performed close to the critical angle of the substrate there is a considerable part of the beam reflected from the surface. This reflected beam can also be scattered from the nanoparticles above the substrate surface which leads to additional "reflected" peaks. Although these peaks have been observed in some experiments they are in our case ($\alpha_i > \alpha_c$) much weaker than the directly scattered ones and thus do not impact most quantitative studies. Anyway, this effect is introduced in the DWBA based models.

5.2.2 Refraction

The ordered nanoparticles themselves can be seen as a separate layer on top of the substrate. When the beam penetrates this layer (or leaves the layer after scattering) it is refracted, is slightly changed the incident (or outgoing) beam direction. This effect leads to a slight Q_z shift of reflections. Considering Snell's law when calculating the scattering vector inside the material this shift can be deduced [27] to:

$$Q_{z_{\text{observed}}} = k_0(\pm sin(\alpha_i) \pm \sqrt{\{sin(\alpha_{c_{\text{Meso}}})^2 + [\frac{\mathrm{Q_z} \cdot \lambda}{2 \cdot \pi} \pm \sqrt{(sin(\alpha_i)^2 - sin(\alpha_{c_{\text{Meso}}})^2)}]^2\}}) \quad (5.8)$$

In this formula $\alpha_{c_{\text{Meso}}}$ is the critical angle of the mesocrystal layer and $\mathrm{Q_z}$ the momentum transfer component in the layer perpendicular to the surface. This shift is considered when fitting the peak positions to deduce the correct mesocrystal lattice parameters from the experimental data.

5.2.3 Inhomogeneity

The considerations above are usually applied to layered systems or continuous films of particles/polymers. In the case of the mesocrystal samples one faces additional obstacles as there are no closed layers of ordered particles (see **figure 4.10**). At the center of a mesocrystal there is a

thick layer of large density leading to strong refraction effects, at the edge the density is lower and between mesocrystals there are no particles or a thin layer of one or two particles, where the reflection from the substrate becomes more important. If the distance between the mesocrystals would be much smaller than the in-plane coherence length, these effects would lead to an average density profile, while a mesocrystal distance much larger than the coherence length could be modeled by incoherent summation of these three regions. The mesocrystal sizes/distances vary widely from 100/500 nm to 10/100 μm for different samples (see **figure 5.4e, 5.4f**) and even on different regions of the same sample. Unfortunately the intermediate situation is found for most samples and it is not clear prior to modeling how much incoherent summation is needed.

In addition to the lateral inhomogeneities, vertical ones are present in the ensemble of mesocrystals as well. A variation of heights of different mesocrystals leads to an $\alpha_{c_{\mathrm{Meso}}}$ distribution and thus a distribution at Q_z shift's, which results in smeared out peaks, especially in the low Q_z region. A broad Yoneda line is an other consequence of this inhomogeneity. Additionally a gradient of lattice constants increasing with height has to be assumed to accurately describe the Bragg-peak positions.

5.3 Model implementation

5.3.1 Single mesocrystal modeling

For the single mesocrystal diffraction measurement in **chapter 7** the data is described with the simple model given in **eqn. 5.7** with an additional Debye-Waller factor term representing the lattice position deviation. The peak shape and the Laue oscillations are introduced well by the mesocrystal shape, wherein the preparation automatically leads to a cylindric shape of the isolated mesocrystal. Variations of the particle size are not considered. The good agreement of this simple model with the measuered data can be seen in **figure 7.9** and in appendix **chapter B**. The python script is attached in **appendix section B.3**.

5.3.2 Peak shape computation for in-situ experiments

In these experiments there was no sign of oscillations between the main peaks, due to an average over different mesocrystals of the ensemble. The experimental intensities were divided by the single particle form factor before fitting selected peaks. Thus in this model, the mesocrystals diffraction pattern is analyzed without consideration of grazing incidence. The DWBA T_i R_f, R_i T_f and R_i R_f terms are negligible as there is no sign of reflected peaks and because the peak positions lie well above the Yoneda line. Additionally an averaged background correction was done for every picture before the fit. These two corrections make stable fits possible, not altered by the slopes of the FF.

The peak shapes were created by FFT convolution of a 2D Lorentzian (mesocrystal correlation) with 2D Gaussian (orientation and radial (a^*, c^*) average) and an experimental shape function.

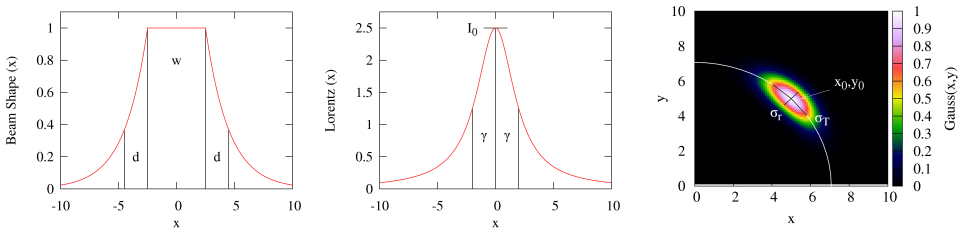

(a) Beam-shape **(b)** 2D Lorentzian **(c)** Radial Gaussian

Figure 5.5: The three components used to compute the peak shape with FFT.

The beam shape function (**eqn. 5.9** and **figure 5.5a**) consisting of a step with exponentially decaying edges was used to model the finite beam size and the crosstalk of neighboring pixels.

$$B(x) = \begin{cases} e^{(x-\frac{w}{2})/d}, & \text{if } x < -\frac{w}{2} \\ e^{(\frac{w}{2}-x)/d}, & \text{if } x > \frac{w}{2} \\ 1, & \text{else} \end{cases} \tag{5.9}$$

The beam shape function parameters were obtained by fitting to a specular reflection of the clean silicon substrate. To model the mesocrystal correlation length (γ_x, γ_y) a 2D Lorentzian function (**eqn. 5.10** and **figure 5.5b**) was used.

$$L(\vec{\mathrm{Q}}) = \frac{I_0}{1 + (\frac{\mathrm{Q_y}}{\gamma_y})^2 + (\frac{\mathrm{Q_z}}{\gamma_z})^2} \tag{5.10}$$

Finally, a random variation of the mesocrystal lattice parameters and tilting of the c-axis away from the substrate surface can be described by a 2D Gaussian function in polar coordinates of the radial σ_r and tangential σ_t position (**eqn. 5.11** and **figure 5.5c**).

$$G(\vec{\mathrm{Q}}) = e^{-\frac{1}{2}\frac{(\mathrm{Q_r}-r_o)^2}{r_o \cdot \sigma_r^2}} \cdot e^{-\frac{1}{2}\frac{(\phi-\phi_o)^2}{\sigma_t^2}}, \text{with} \quad \mathrm{Q_r} = \sqrt{\mathrm{Q_y^2} + \mathrm{Q_z^2}},\ \phi = \arctan(\frac{\mathrm{Q_z}}{\mathrm{Q_y}}) \tag{5.11}$$

The refraction formula **eqn. 5.8** was used to correct the measured peak positions in consideration of the DWBA. Fits of 6 different peaks and their -$\mathrm{Q_y}$ mirror pairs with coupled parameters were performed yielding the reciprocal lattice parameters, in-plane and out-of-plane correlation length and distribution widths. This simple model was sufficient to describe most of the measured peak shapes and was still applicable to fit several hundred of GISAXS images automatically. The good agreement of the fit functions to the measured data is exemplified in **figure 6.7**. A multicore implementation of this function can be found in **appendix section B.4**.

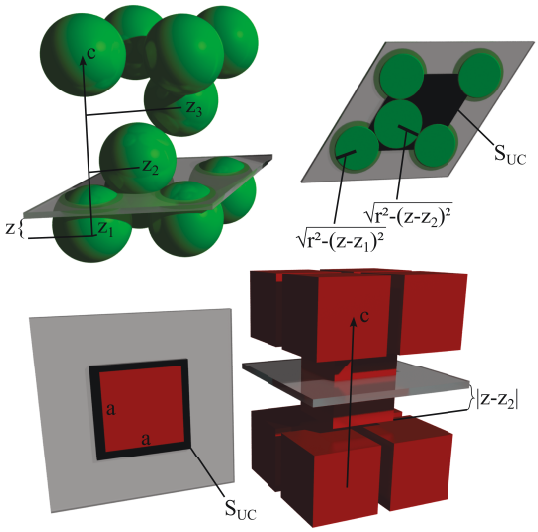

Figure 5.6: Sketch of the model for the particle density at a given position and the different parameters used in eqn. 5.12-5.14. For the case of closed packed spheres and body centered tetragonal cubes the model parameters indicated are: Position of the model slice z, individual particles z_i, spheres radius r, cubes edge length a and unit cell cross section S_{UC}.

5.3.3 Reflectivity modeling

For reflectivity the largest difficulty is to describe the scattering length density well enough to reproduce the unusual peak shapes. Simple layer models trying to implement all influences of the mesocrystal ensemble statistic described above get very complex, easily introduce 20 or more free parameters and still are not able to explain the full reflectivity curve including the total reflection region. The lateral inhomogeneity described above must be considered as well to describe the underlying long oscillations properly as they originate from the single particle layer between the mesocrystals.

A modified version of the GenX program [25] was used to include the incoherent averaging procedure, as most reflectivity programs do not consider this possibility. A new approach was tried, calculating density profiles from the particle shapes and positions while in a second step creating a fine layered model for the reflectivity simulation.

$$\rho_{UC}(z) = (\rho_{Fe_2O_3} - \rho_{Matrix}) \frac{\pi \sum_i r^2 - (z - z_i)^2}{S_{UC}} \tag{5.12}$$

$$\rho_{UC}(z) = (\rho_{Fe_2O_3} - \rho_{Matrix}) \frac{\sum_i a^2 \text{ for } |(z - z_i)| \leq a/2}{S_{UC}} \tag{5.13}$$

$$\rho_N(z) = \rho_{Matrix} + \sum_{j=0}^{N} \rho_{UC}(z - c \cdot j) \tag{5.14}$$

$$N = \text{repetitions of unit cell}$$

This method typically uses 20-40 layers to calculate the reflectivity with the Parratt's formalism (see **section 2.2.5**) for each mesocrystal unit cell while keeping the number of parameters to only 5 to 8 for the whole mesocrystal. This model is than calculated for different lateral particle densities to describe the center of a mesocrystal, the edges and the region in between the mesocrystals, summing up the intensities afterwards as described in equation 5.15.

$$I_R = S_{free} \cdot I(\rho_1(z)) + S_{edge} \cdot I(\rho_1(z) + 0.5 \cdot \rho_N(z)) + S_{center} \cdot I(\rho_N(z)) \tag{5.15}$$

$$S_{edge} = (1 - S_{free}) \frac{((R_{Meso}+R_{Coherence}/2)^2 - (R_{Meso}-R_{Coherence}/2)^2)}{(R_{Meso}+R_{Coherence}/2)^2} \tag{5.16}$$

$$S_{center} = (1 - S_{free}) \frac{(R_{Meso}-R_{Coherence}/2)^2}{(R_{Meso}+R_{Coherence}/2)^2} \tag{5.17}$$

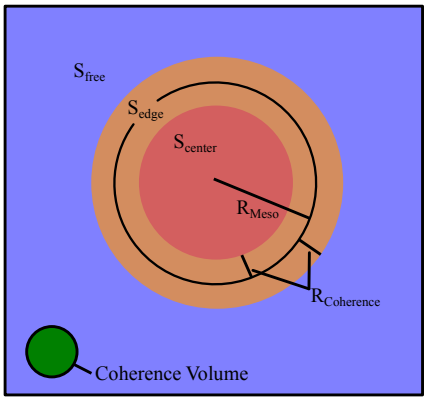

Figure 5.7: Sketch of the surfaces simulated in the reflectivity model

using the symbols: UC-Unit Cell, ρ-Scattering power density, S_{UC}-Unit cell cross section area, $I(\rho(z))$-Simulated intensity for a given scattering power density profile, S-Relative surface occupation, R-Cylinder radii as sketched in **figure 5.7**. To account for mesocrystals with reduced radius from bottom to top the segmentation of the outer region is increased and the particle density from bottom to top is decreased for the edge regions. To simplify the formulation of the relative size calculation of the coherence and mesocrystal areas, both are taken to be circles in this model. In the experiment the coherence volume is strongly elongated in the beam direction, but has an area that is smaller than most mesocrystals ($\approx$100 nm x 10 µm).

The different parts of this model are exemplified in **figure 5.8** together with the combined intensity. The center part describes a perfect mesocrystal with full density and thus showing strong maxima and low minima. The edge zone has a lower averaged density and produces a lower contrast. The mono layer between the mesocrystals (free) creates an underlaying long oscillation. The combination of all three components in addition with a deviation of lattice constant in one mesocrystals produce the resulting pattern.

Although this model fits the experimental x-ray and neutron data at higher Q values quite well the total reflection region below 0.04 $Å^{-1}$ in the x-ray case is not reproduced perfectly, most likely due to too much simplification of the inhomogeneity over the sample surface and missing interference terms from the different surface areas. In this routine an average mesocrystal size in height and diameter, as well as an average model for the coverage of the sample with the different density regions is used. An additional integration of a lattice constant variation for the substrate to the surface of the MC was introduced to properly fit the shape of the Bragg peaks. Although the model uses some generalizations and does not include size, height and shape deviations it is already very complex, especially from the implementation and calculation point of view (see code in appendix **section B.5**.). For example the influence of different mesocrystal sizes can lead to different densities (α_c's) and thus to a smeared out total reflection edge . This

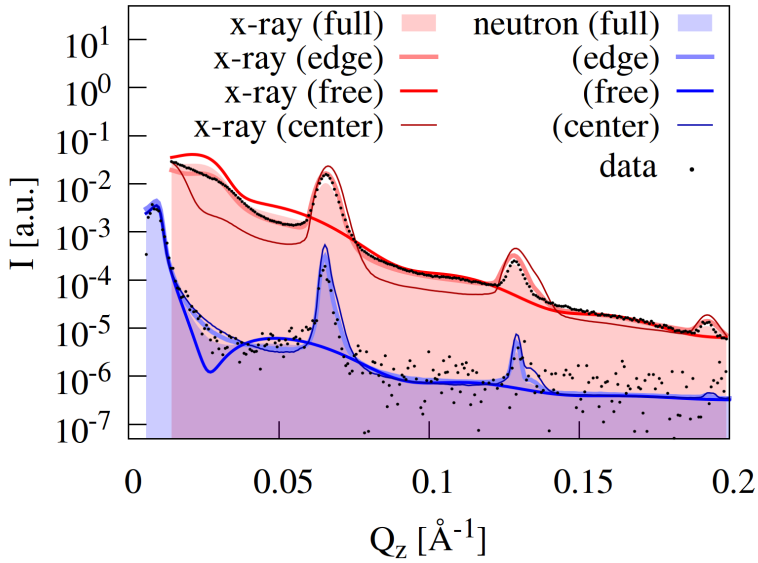

Figure 5.8: Example of simulated reflectivity with each sub-model. The red labels describes the X-ray data and the blue one correspond to the neutron data. The black points are the measured data. Edge, free and center correspond to the parts referred to as S_{edge}, S_{free}, S_{center} in eqn. 5.15-5.17, the contribution of the different regions of the mesocrystal. Full is the weighted sum of all components I_R from eqn. 5.15. The sample is an ensemble of mesocrystals formed with extra long waiting time from spherical building blocks of radius 5.01 nm self-assembled under an magnetic field of 2 mT and gradient up. The measurement was done with a wavelength of 4.73 Å for neutrons and 1.54 Å for X-rays.

parameter	value	error
c_{bottom} [nm] :	9.8	2
c_{top} [nm] :	9.2	7
r_{NP} [nm] :	4.9	7
N :	40	/
$R_{Meso_{bottom}}$ [nm] :	3630	500
$R_{Meso_{top}}$ [nm] :	670	500
$R_{\text{coherence length}}$ [nm] :	1500	/
surface filling ratio [%] :	47	7
magnetic moment per formula unit $[\mu_{Bohr}]$:	0.98	2

Table 5.1: Fit parameters used for the simulation shown in **figure 5.8**.

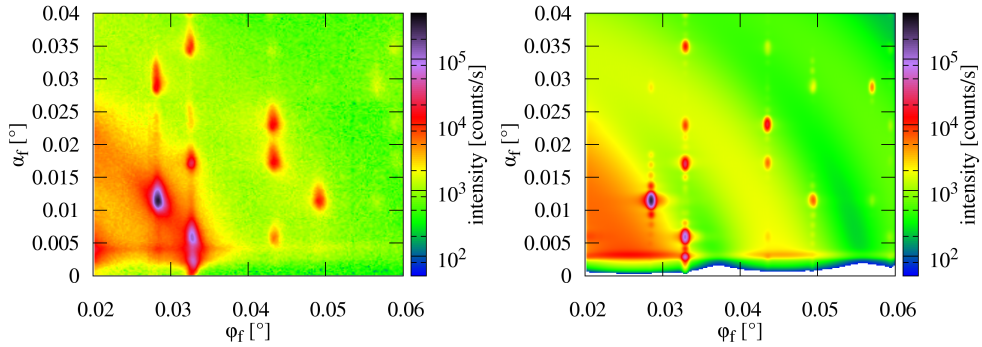

(a) GISAXS measurement

(b) GISAXS simulation

Figure 5.9: BornAgain simulation of the GISAXS scattering intensity of an ensemble of mesocrystals formed with long waiting time from spherical building blocks of radius 5.01 nm self-assembled under a magnetic field of 80 mT and gradient up. The measurement was done under an angle of 0.4 ° and with a wavelength of 1.77 Å at SWING/Soleil.

is not so prominent in the neutron case as the absorption can be neglected and the total reflection is dominated by the substrate.

5.3.4 Lógos and BornAgain (work in progress)

In the GISAS case the problem gets more complex as in addition to the layer density, the in-plane structure needs to be taken into account in the DWBA formalism. For both directions the influence of the mesocrystal ensemble statistics and their averages have to be considered. The DWBA implementations Lógos and BornAgain (developed together with the scientific computing group in the JCNS outstation at MLZ and Artur Glavic) of the model up to now does not incorporate surface inhomogeneity (explained in the reflectivity part) and thus only describes one homogeneous layer of average particle density. The model includes via **eqn. 5.7** the mesocrystal structure and shape ($F_{MC}(\vec{Q})$), the in-plane rotation (2D powder), distribution of mesocrystal size, Debye-Waller factor (deviation of lattice positions), refraction and reflection as well as the nanoparticle form factor. An example simulation is shown in **figure 5.9b** and the fit results in comparison to experimental determined parameters match well (**table 5.2**).

The mesocrystal structure provides the peak positions, the mesocrystal shape FF together the peak shape and the particle FF with the structure factor the peak intensity. The 2D powder allows one to see different scattering planes at once. The size distribution of the mesocrystals leads to a smearing out of the Laue-oscillations and the Debye-Waller factor to a decay of intensity for larger |Q|. Although this model already describes some datasets quite well, the Yoneda region and peak broadening are not well reproduced. As the reflectivity model shows, it is important to include several aspects of the surface inhomogeneity to describe the total reflection and thus the Yoneda region correctly. The incorporation of all regions and different sizes will give a distribution of critical angles and thus a broadening of the Yoneda line. The integration of out-of-plane rotations and lattice constant deviations would induce the tangential and radial broadening of the peaks.

parameters	fit parameters	experimental parameters
a [nm] :	12.4	12.7 $\pm$ 0.1 (GISAXS)
c [nm] :	30.2	31.3 $\pm$ 0.1 (GISAXS)
r_{NP} [nm] :	4.7	5.01 $\pm$ 0.02 (SAXS)
$\sigma_{r_{NP}}$ [%] :	8	6.3 $\pm$ 0.5 (SAXS)
$height_{Meso}$ [nm] :	112	250-500 (AFM)
$radius_{Meso}$ [µm] :	0.9	1.5-3.5 (SEM)
surface filling ratio [%] :	17	23 $\pm$2 (AFM)
roughness :	2.87	
beam intensity :	$5.01 \cdot 10^{12}$	

Table 5.2: Fit parameter used for the simulation shown in **figure 5.9b**.

The influence of e.g. out-of-plane rotation could be implemented, although at the cost of longer computation time, which already is in the order of minutes for a single scattering pattern.

5.4 Conclusions

Modeling of scattering intensities of an ensemble of 3D nanoparticles is introduced in this chapter and shows the good understanding of the system under investigation. The complexity of the mesocrystal samples represents a challenge for the simulation from physical and numeric perspectives. Simplifications in experimental or theoretical conditions, like investigation of a single 3D mesocrystal or an approximation by consideration of a special case, yields good agreement with experiments. If we consider the complete ensemble of mesocrystals and the full scattering pattern, the number of features increase and with them the free parameters and elements in the model. Although the simulations and fitting were not carried out until perfect agreement, the successful understanding of the underlying physics is evidenced. The possibility to deduce the influences of the 2D powder and the mesocrystal ensemble statistics, like in-plane rotation, mesocrystal size distribution, shape deviation, out-of-plane rotation, lattice constant deviation, lateral and vertical inhomogeneities and the space group, gives a new aspect of interpreting reflectometry and GISAS data. A new form factor model complements the study to allow a more precise fitting of different scattering experiment datasets.

Chapter 6

Time evolution of mesocrystal growth

The self-assembly of magnetic nanoparticles has a high potential for future applications [63], as it allows mass production processes of very small structures without the use of expensive equipment. The process itself is complex, including several interactions between nanoparticles, solvent and substrate. A deeper understanding is the key for a better control of the self-organization, which subsequently can be used to develop better self organization procedures and tune the resulting parameters of the sample. Previous studies investigated the self-assembly of non-magnetic particle systems [21, 22, 28, 53, 65, 76, 92, 93], spherical superparamagnetic nanoparticle monolayers [82, 83] or nonspherical particle systems like cubic [29] or nanooctahedra [98]. Most of the observed self-assembling process can be classified into the following groups: The ordering takes place at the liquid-air interface [22, 28, 53, 65, 92, 93] or at the triple phase contact line (substrate-liquid-air) [76, 82, 83]. The in-situ GISAXS technique has been established as a good choice for real time investigations of the ordering at the nanometer scale [49, 75].

In this chapter, an in-situ GISAXS study of highly ordered 3D nanoparticle assemblies is discussed. In contrast to earlier studies we have focused our investigation on the evaporation-induced 3D growth of spherical and cubic magnetic particles, which form a highly correlated system. Our main focus was to observe the influence of different evaporation times on the growth mechanism and to measure the very early assembly stages. To achieve a better insight into the self-organization process compared to earlier experiments, an additional apparatus was installed which recorded different parameters simultaneously with the GISAXS information and a more quantitative time dependent analysis of the GISAXS patterns was carried out. The main scientific question addressed with this study is where, when and how the assembly does take place. The following pages treat these questions and give a new insight into the evolution of mesocrystal growth from magnetic nanoparticles.

6.1 Development of the in-situ cell

For our in-situ SAXS and GISAXS experiment we designed a new evaporation cell with several features for the control of the self assembling parameters. The dimension was restricted by the available space at the ID01 beamline at ESRF (see **section 3.7**) to less than 10 cm in beam direction. The setup was designed to be similar to the conventional drop casting, as done in a Petri dish. The cell (**figure 6.1**) consists of a glass body with gas inlet/outlet valves (a) and a glass cover plate (b). Two Kapton windows (c) allow transmission of the x-ray beam and two

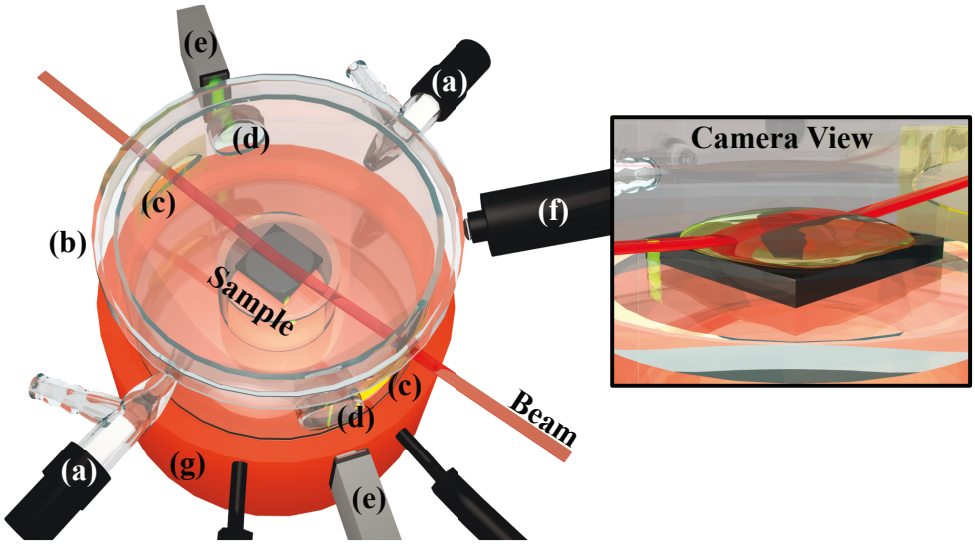

Figure 6.1: In situ cell used in the experiment. Different components are marked with letters, which are explained in the text. The inset shows the view from the microscope camera (f) on the substrate.

flat windows (d) offset by 30° against the x-ray beam axis transmit light from the attached light band micrometer (e) to measure the droplet height. Additionally a microscope camera (f) observes the sample surface under an angle. The magnetic field is produced by permanent magnets that can be inserted into the body holder (g) or on top of the cover plate (b). The evaporation rate is controlled by the air inlet/outlet through the valves and by an additional symmetric toluene reservoir inside the cell.

In the following the former features are described in more detail:

- Kapton windows, allowing x-rays to enter/exit the cell without too much intensity loss (85% transmission). The size of these windows are 30 x 17 mm^2. They enable a large scattering angle in forward scattering of up to 16°, which corresponds to a Q value of 2.74 $Å^{-1}$ at the used wavelength. This is more than adequate for our scattering experiment.
- A light-band micrometer from Keyence® was used to measure the height of the droplet during the experiment. The system consist of a strong diode with a line shaped green ray that shines on the sample horizontally and the shadow cast by the droplet is detected with a high resolution camera. It was tested with several solvents to be able to measure the height through the glass setup with a precision of 0.1 µm. This precision in combination with the scattering makes an identification of the position of the mesocrystal growth possible. Additionally an exact starting time for the experiment could be defined. An advantage of this method is the independence from the solvent (for example the refractive index which influences a fill metric sensor). The Light-band micrometer system was connected with a computer outside the measurement hutch and recorded with a time code to correlate it to the x-ray images taken. The micrometer was tilted to the beam, as well, to fit inside the residual space.

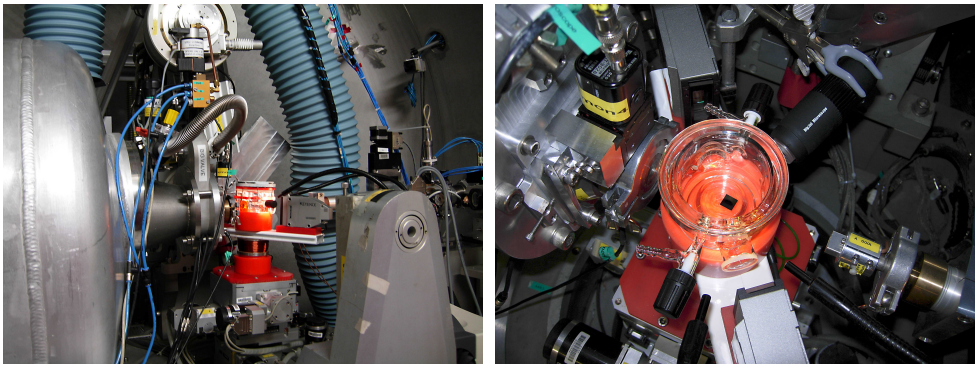

(a) Side view **(b)** Top view

Figure 6.2: Experimental setup at the ID01 beamline (see **section 3.7**) including the new developed in-situ cell. The features of the cell are described in **section 6.1**.

- The microscope camera was used to monitor the droplet size from an angle to be able not only to see the height of the droplet but also its in-plane coverage. It was also connected to the computer outside the measurement hutch and the images were saved with a time code.
- Applying a magnetic filed is important for the deposition process (see **chapter 4**). The influence of the magnetic field (strength and direction) on the self assembling process can be controlled in this setup, as well. A permanent magnet with a steel plate on the back was placed on top of the in-situ cell, producing a field gradient pointing away from the substrate $\underline{H_{\perp}}$ with 36 mT field strength at the sample position. For a field gradient pointing to the substrate $\underline{H_{\curlyvee}}$, a permanent magnet was included inside the holder body (g) and reached a field of 65 mT. A homogeneous magnetic field in out-of-plane direction $\underline{H_{\Uparrow}}$ with a field strength of 100 mT could be reached with both magnets at once. An in-plane filed $\underline{H_{\succ}}$ of 30 mT can be applied using two magnets on opposite sides on top on the toluene vessel, too.
- For a better control of the evaporation, small symmetric openings allow gas exchange (solvent<->air), which can be controlled with valves. Varying openings change the evaporation rate of the toluene and allow a precise control. Additionally a symmetric solvent reservoir can be used to slow down the evaporation rate. It is surrounding the sample stage and can be filled with different amounts of toluene. This way the reservoir could be used to control the evaporation rate as well as saturate the atmospheres already before adding the solution and gave us the possibility to leave the hutch and start the measurement without missing important stages.

6.2 Experimental details

The cell was mounted at the sample position of the ID01 beamline (**figure 6.2**) and aligned with a silicon wafer using the reflected beam. The flight path was evacuated up to a few cm before

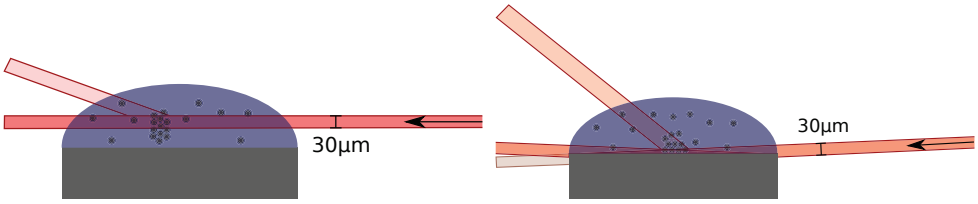

(a) SAXS geometry **(b)** GISAXS geometry

Figure 6.3: Different geometries used at ID01 beamline

and after the cell to minimize air scattering. The best available focus of 30x1000 µm^2 was set to achieve a small footprint on the sample, which is necessary to define the observed region. Two different geometries have been used, a transmission SAXS geometry (**figure 6.3a**) with the substrate parallel to the incident beam as long as the droplet was larger than the beam height and a standard GISAXS geometry (**figure 6.3b**) with 0.3 ° and 0.6 ° angle of incidence. The 0.6 ° setting was not used for a short evaporation time experiment. The SAXS geometry allows the detection of ordered clusters within the solvent and at the solvent surface. As the transmission geometry was measured with a fine vertical focus it allowed us to scan the beam through the liquid during evaporation (not possible for short evaporation time). Nucleation at the bottom could be detected in this configuration, too. The GISAXS geometry is mostly sensitive to particles ordered at the substrate surface and is applied after the droplet has a minimal height between 20-50 µm measured by the light-band micrometer. So we could assure not to miss the beginning of the nucleation on the substrate.

The sample handling and preparation for the in-situ experiment was done with the conventional preparation process as described in **section 4.2.1**. For all deposited samples the standard solutions $S_S^{8.4}$ and $S_C^{8.4}$ were used. The preprocessed wafer was inserted into the cell, covered with a cap and every substrate was aligned with the silicon reflection for its position and angle. The zero position of the micrometer was set with the substrate shadow afterwards. Depending on the required evaporation speed, a defined amount of toluene was put in the reservoir to achieve the desired degree of saturation of toluene in the atmosphere and the valves were opened completely or partially. The light- band micrometer and the camera was started to record the droplet behavior. Afterwards, 20 µl of the solution was drop casted with a needle on the substrate. The cell was closed with the cap and ,if necessary, the magnet was put on top of it. The time for closing the hutch, drop casting and starting of the measurement was between 3 and 5 minutes. The different parameters and the produced samples are listed in **table 6.1**.

Sample ID	Solution	Amount	Magnetic field	Reservoir	Valve
$D_{S,\,5.01}^{Sh1.68\perp 36}$:	$S_S^{8.4}$	20 µl	$H_\perp$ 36 mT	no toluene	completely opened
$D_{S,\,5.01}^{Md1.68\perp 36}$:	$S_S^{8.4}$	20 µl	$H_\perp$ 36 mT	100 µl	3turns opened
$D_{C,\,10.9,\,0.8}^{Sh1.68\perp 36}$:	$S_C^{8.4}$	20 µl	$H_\perp$ 36 mT	no toluene	completely opened
$D_{C,\,10.9,\,0.8}^{Md1.68\perp 36}$:	$S_C^{8.4}$	20 µl	$H_\perp$ 36 mT	100 µl	3turns opened
$D_{C,\,10.9,\,0.8}^{Sh1.68X}$:	$S_C^{8.4}$	20 µl	no field	no toluene	completely opened

Table 6.1: Sample parameters which were used for the ESRF in-situ experiment

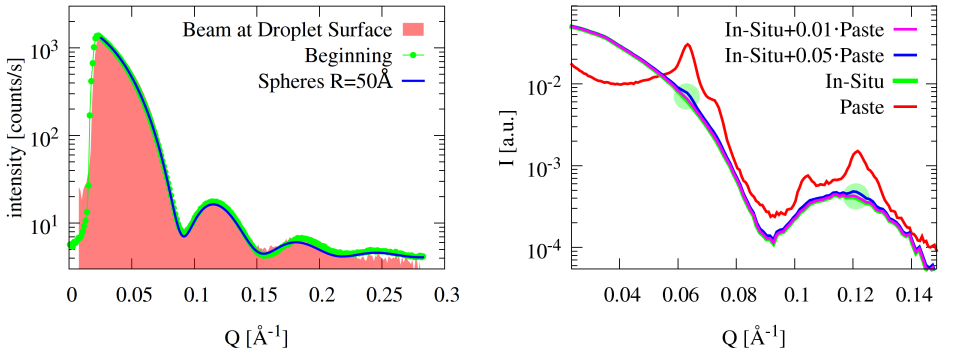

(a) Form factor from SAXS measurement at different points in time for a sample with short evaporation time. A spherical form factor is found at the beginning of the experiment (data: green; fit: blue solid line), which does not show a large change during evaporation until the droplet surface passes the beam (red area).

(b) Estimation of measurably of clusters. In comparison to the in-situ SAXS measurements we can see that 5% of all particles in clusters are enough to get a measurable signal (indicated by the round labels).

Figure 6.4: Results from SAXS measurements

6.3 Results and discussion

In this section we consider the time dependent behavior of a self-organizing system of spherical or cubic particles and compare them with measurements under different deposition conditions (see **table 6.1**). The determination of the position of the nucleation is a further challenge to solve.

6.3.1 Qualitative analysis of the data

After drop casting the particles onto a silicon substrate the droplet was measured repeatedly in transmission geometry at different heights above the silicon surface for the middle evaporation time and for the short one only at the lowest position to improve the time resolution. Grazing incidence measurements at 0.3 ° incident angle were started after the light-band micrometer displayed a value smaller than 50 µm. The acquisition time of 1 s and a readout time of 7 s defined our time resolution.

From the transmission experiments no sign of cluster formation in the fluid could be found. As can be seen in **figure 6.4a** as an example for a sample with spherical particles and short evaporation time, there is only a spherical form factor present at the beginning of the experiment (green), which does not show any significant change during evaporation until the droplet surface reaches the beam at its lowest position, where the total reflection makes further SAXS observation impossible (red area). An estimation for the possible measurable structure factor of clustered particles in a solution shows that $\approx 5\%$ of all particles need to be bound in clusters to get a measurable signal (see **figure 6.4b**). A clustered paste of the same particles measured at

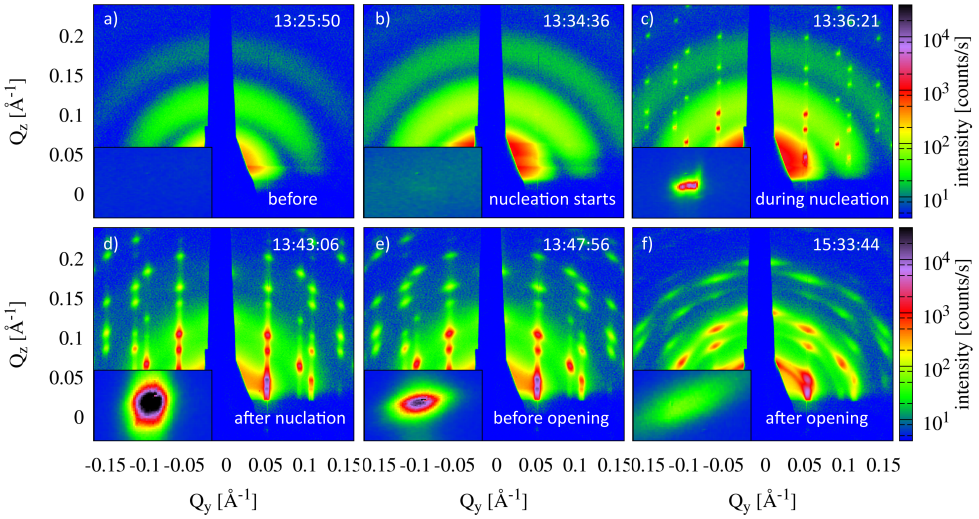

Figure 6.5: Time evolution of the GISAXS pattern during a middle evaporation time for spherical particles. The insets show the $(0\bar{1}5)$ reflex enlarged in in a linear scale. The text insets on the right side indicates the time.

an in-house lab source in SAXS geometry and normalized to the total scattering of the in-situ transmission measurement was used to get this estimation.

After in-situ SAXS measurements on the drying droplet, GISAXS images have been taken continuously until the experiment was finished. This geometry is mainly sensitive to the substrate but records clustering in the rest of the droplet film of a few µm as well. For the longer evaporation times the cover glass was removed after a given time when the nucleation was finished to speed up the final drying process. An excerpt of the GISAXS data taken for one experiment with a middle evaporation time for a spherical particle system is shown in **figure 6.5**. The insets show the $(0\bar{1}5)$ reflex magnified in a linear scale. The time evolution is nicely shown in these pictures. At the beginning, there is no sign of ordering, but the increasing intensity on the FF rings at the starting point of the nucleation shows an increasing of the density in the film of disordered nanoparticles. Suddenly, the self organization starts and sharp peaks with the beam profile develop (see **figure 6.5c** during nucleation). A closer look shows a shape with splitted peaks not mirror symmetrical around the Q_z- axis, which clearly shows that this effect is not the result of the structure itself. As the size of the splitted parts at the beginning is even smaller than the measured instrumental resolution, this behavior can be explained by the drying front approaching the region covered by the beam footprint, so only a part of the 1mm beam is scattered, which improves the apparent resolution until the whole beam contributes to the peaks. Different peak regions are coming from different surface areas from the curved droplet front. Peaks sharper than the resolution result from a highly ordered system with nearly the same lattices constants in all areas and no tilting angle. The tilting angle describes the inclination between the mesocrystal c-axis and the substrate surface normal. The combined scattering of mesocrystals with different tilting angle leads to rotational broadening of all reflections up to the most extreme case of closed Debye-Scherrer rings for a 3D powder. This increased width, however, is no sign for a decreased structural coherence in each mesocrystal.

For this evaporation rate, most of the ordering takes place within 9 minutes. In this time the amount of scattering centers grows, which causes the increase of the peak intensity (compare **figure 6.5** during (c) to after nucleation (d)). During the nucleation time of the GISAXS pattern, we could observe an horizontal drying front with the microscope camera. The droplet is uniformly drying from the outer to the inner part. With the motion of this front more and more area of grown mesocrystals is accumulated, with a distribution of lattice constants and mesocrystal sizes indicated by the broadening of the peaks in Q_z and Q_y direction. During the nucleation the incoherent background reduced, due to the reduction of the number of free particles.

During the subsequent drying process (compare **figure 6.5** after nucleation (d) to before opening (e)) the mesocrystal lattice parameters shrink, a distribution of lattice constants broadens and the crystals develop a random tilt around the surface normal, which leads to smeared reflections in tangential and radial direction around the position of the primary beam. The peak intensity decreases as no more mesocrystals are formed while the peak width gets larger. The opening of the cell due to time limitation of the beamtime induces a fast drying of the system and increases the tilting of the mesocrystals. While during the growth of the mesocrystals the lattice constants are similar, the drying of the grown crystals generates the tilting and different lattice constant. The measured GISAXS peaks are the result of a distribution of mesocrystals with different lattice constants and orientations.

After the experiments all samples exhibited order with the same known space group $R\bar{3}m$ for the sperical system and $I4/mmm$ for the cubic one. Although the degree of order (peak width) in the resulting assemblies vary with the given evaporation time the overall process was found to be similar for all samples. No structural transition is observed during the growth process. For a more quantitative analysis of the GISAXS pattern we developed a routine, which can fit the GISAXS peaks in dependence of the time. This procedure is described in the next chapter, where we analyze the drying properties in more detail.

6.3.2 Data evaluation

The time evolution of the ordering process was analyzed by fitting selected peaks for all recorded patterns. To obtain the correct peak shape a Fast Fourier Transform convolution of a beam shape function, a 2D Lorentzian function to model the mesocrystal correlation length (γ_y, γ_z) and a 2D Gaussian function with the radial σ_r and tangential σ_t standard deviations describing a random variation of the mesocrystal lattice parameters and tilting of the c-axis away from the substrate surface was used. The distorted-wave Born approximation was considered for the peak positions, a constant background, determined far away from the scattered intensity, was subtracted and the data was divided by the single particle form factor, leaving only the structure factor part of the scattering for better comparison and fitting of the peaks. More details about the fitting routine can be found in **section 5.3.2**.

For the spherical system as an example, 12 peaks were selected for fitting, (108), (104), (105), (113), (204), (116) and their mirror reflections with negative Q_y values, as they exhibited enough intensity, don't have too low Q_z and are not very close to intense background regions. All peaks have been fitted together with coupled lattice constants (a, c), γ and σ parameters as well as Q_z and Q_y offsets to keep the number of free parameters as low as possible. The peak positions are no free parameter as they are defined by the reciprocal lattice. The intensities I are only coupled for each mirror pairs. The good agreement of the fit functions to the measured data

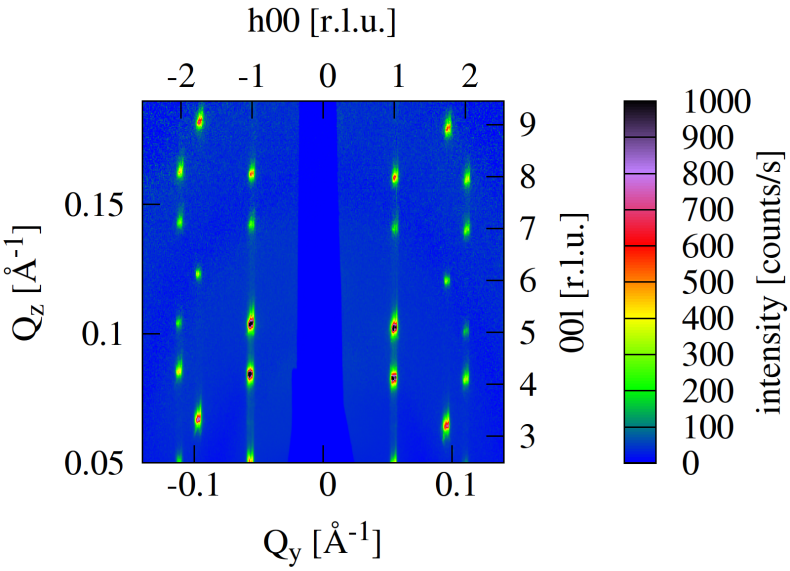

(a) measurement (13:37:04)

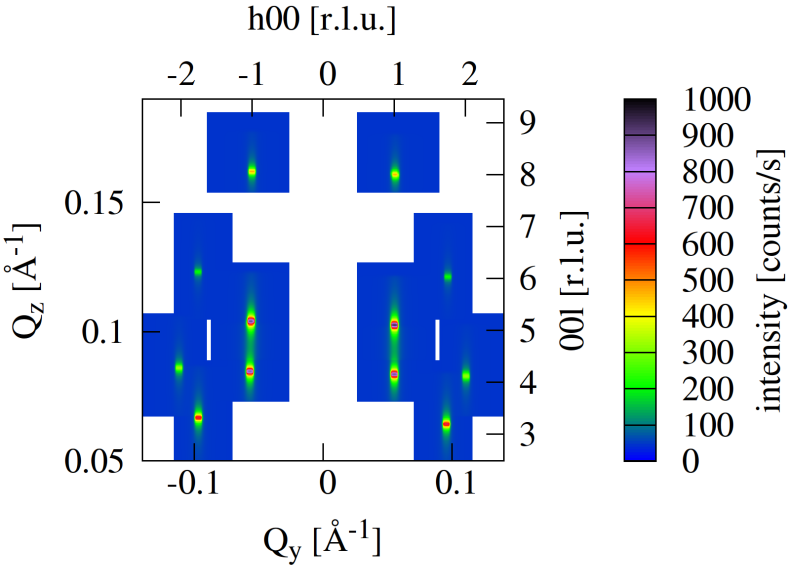

(b) simulation (13:37:04)

Figure 6.6: Example datasets from fits of the time dependent data analysis. For every single dataset, all peaks have the same σ_r, σ_t,γ_x and γ_y parameters. The fit model describes the shape nicely in dependence of the time with only 9 free parameters.

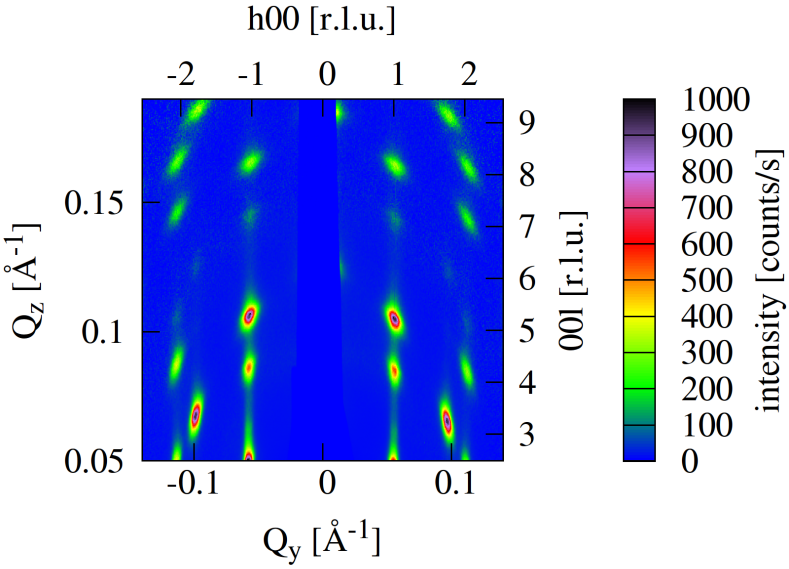

(a) measurement (13:53:30)

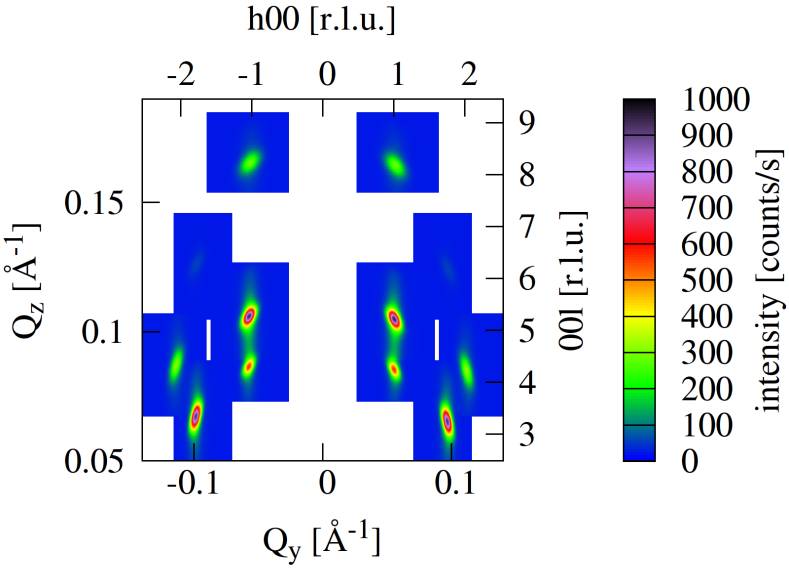

(b) simulation (13:53:30)

Figure 6.7: Example datasets from fits of the time dependent data analysis. For every single dataset, all peaks have the same σ_r, σ_t,γ_x and γ_y parameters. The fit model describes the shape nicely in dependence of the time with only 9 free parameters.

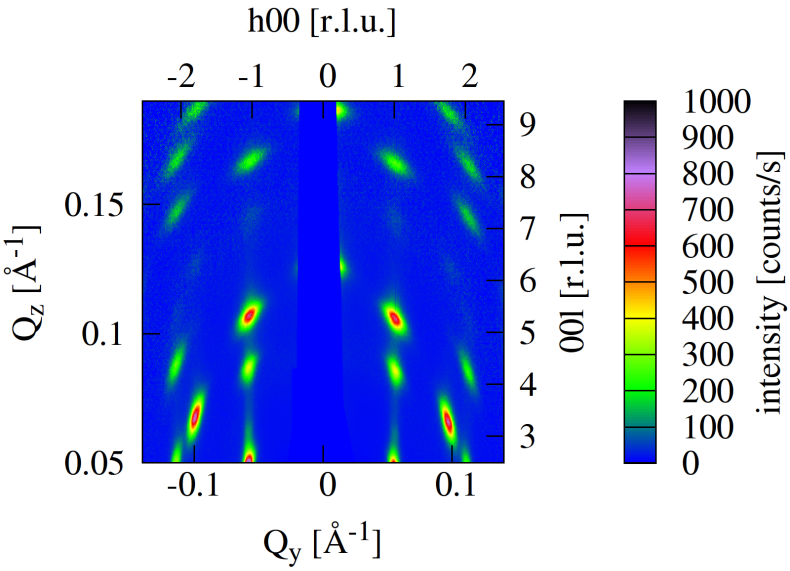

(a) measurement (14:08:10)

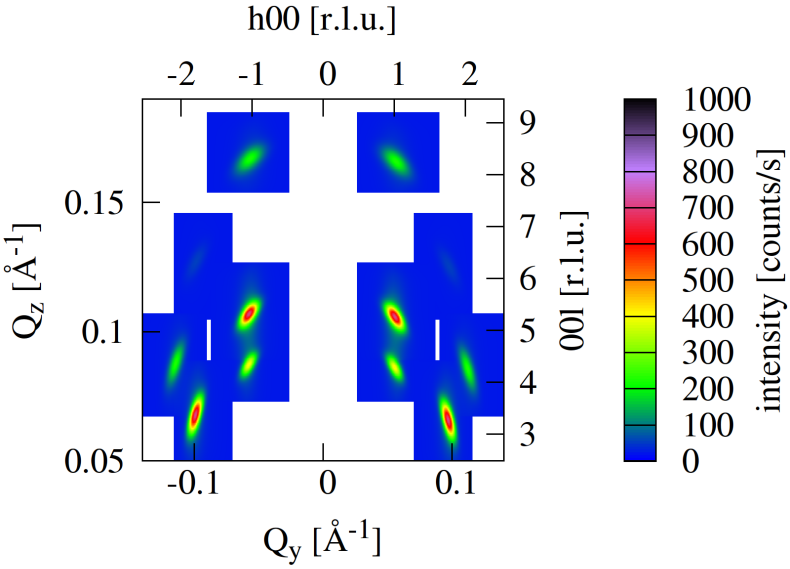

(b) simulation (14:08:10)

Figure 6.8: Example datasets from fits of the time dependent data analysis. For every single dataset, all peaks have the same σ_r, σ_t,γ_x and γ_y parameters. The fit model describes the shape nicely in dependence of the time with only 9 free parameters.

is exemplified in **figure 6.6-6.8**. The **table A.1** in the appendix shows the fit results of theses three example pictures, the results of all fits for important parameters are shown in **figure 6.10**, **figure 6.11a** and **figure 6.11b**.

6.3.3 Four stages of the mesocrystal growth

The combination of the GISAXS fit results, the light-band micrometer data and the microscope images yield new details of the self-assembling and drying process. The resulting parameters are combined in **table 6.2** and show the relationship between the used methods. The new insights will be explained on the next pages with the spherical samples. The cubic system behaves equivalent. In general the experiments can be divided into four stages (see **figure 6.10**):

Stage 1: After drop casting the solution on the silicon substrate, the surface is completely wetted, the droplet forms a meniscus (see **figure 6.9a**) and is slowly shrinking in height. The decreasing height of the droplet is recorded by the light-band micrometer (green), which shows that during this first stage almost the full height of the droplet vanishes. Only a few μm are left at the end of the first part. The wetting angle gets smaller and a thin film of nanoparticle solution is generated. It is possible to perform SAXS measurements only in this stage as long as the beam is smaller than the residual droplet height. The incoherent form factor, which indicates the density of disordered particles, shows only a slower increase for the middle evaporation time and a faster one for the short experiment. No sign of ordering could be observed. This phase is observed in all measurements, equally for different evaporation times. The main difference observed is the time the samples stays in this stage. A short evaporation needs only a few minutes, in contrast to long evaporation times where the droplet stays hours in the saturated atmosphere. This stage is referred to as **vertical droplet reduction**.

Stage 2: In the next stage, so called **highly concentrated film**, a flat film of highly concentrated colloidal solution is observed as constant in the camera (**figure 6.9b**), while the LBM shows a small decay to zero (or a constant offset) . The integrated intensity of the incoherent background shows a nonlinear increase of the density of the nanoparticle solution (**figure 6.10**). The meniscus collapses and the evaporation of the toluene is ongoing. This behavior is only observed in the medium and long evaporation times, at which the saturated atmosphere inhibits

	microscope camera			LBM			GISAXS
Sample ID	1st stage	2nd stage	3rd stage	Duration_{zero}	height_{start}	speed	Duration_{nuc}
$D^{Sh1.68\perp 36}_{S,\,5.01}$:	6-7 min	/	3-4 min	6-7 min	245 µm	-0.604 $\frac{\mu m}{s}$	2.5 min
$D^{Md1.68\perp 36}_{S,\,5.01}$:	38 min	26 min	11 min	44 min	300 µm	-0.066 $\frac{\mu m}{s}$	9 min
$D^{Sh1.68\perp 36}_{C,\,10.9,\,0.8}$:	7 min	/	4 min	9 min	315 µm	-0.580 $\frac{\mu m}{s}$	4 min
$D^{Md1.68\perp 36}_{C,\,10.9,\,0.8}$:	41 min	35 min	10 min	77 min	335 µm	-0.073 $\frac{\mu m}{s}$	7 min
$D^{Sh1.68X}_{C,\,10.9,\,0.8}$:	11 min	/	3-4 min	12 min	400 µm	-0.58 $\frac{\mu m}{s}$	2 min

Table 6.2: Recieved values from the LBM, camera and 3D GISAXS pattern. Duration_{zero} shows the time untile the LBM value is zero. Duration_{nuc} is the value for the nucleation, which is read out the 3D GISAXS pattern. The errors for the time values read out from the camera is 0.5 min, for the LBM 0.1 min and from the GISAXS pattern 0.5 min.

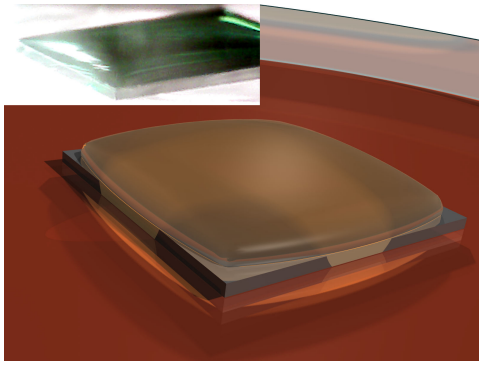

(a) Stage 1: vertical droplet reduction

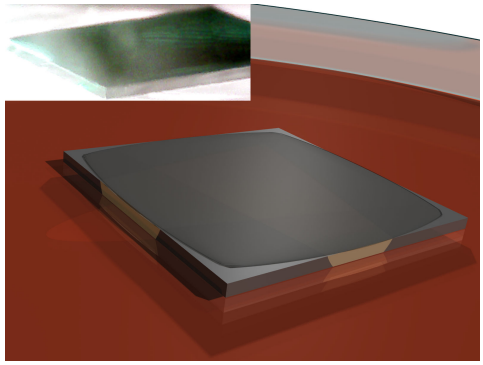

(b) Stage 2: high concentrated film

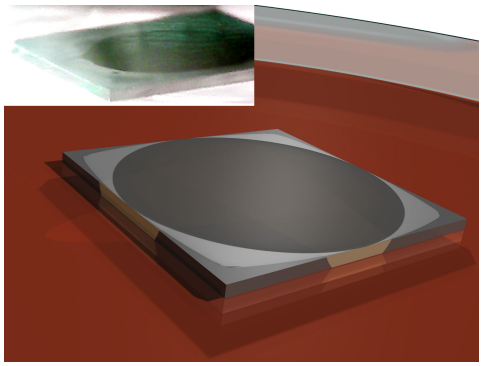

(c) Stage 3: horizontal drying front and nucleation

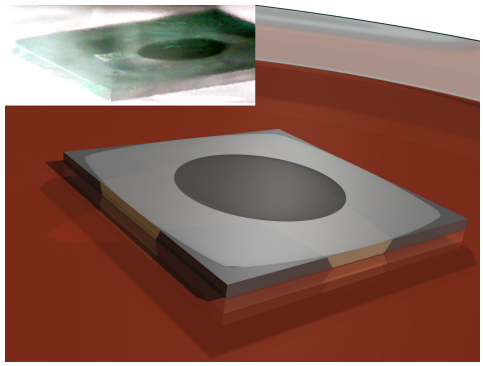

(d) Stage 3: horizontal drying front and nucleation

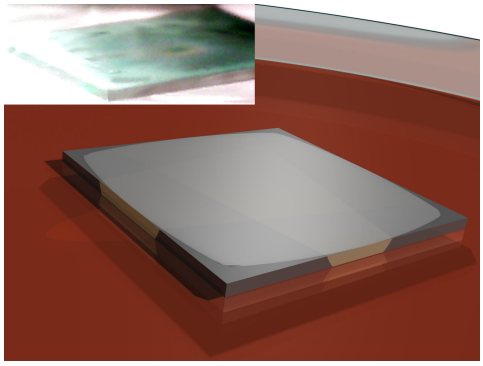

(e) Stage 4 - drying stage

Figure 6.9: Sketch of the four stages of the droplet drying. The insets show the corresponding pictures of the microscope camera, which are in good agreement.

too fast evaporation. In GISAXS ,no sign of order is found in this stage. Obviously a critical concentration is needed for the nucleation of the 3D systems .

Stage 3: The next period, which is called **horizontal drying front** or **nucleation**, is recorded with the camera for every sample. A circular inward movement of the contact line[1] is observed (**figure 6.9c** and **figure 6.9d**). When the drying front approaches the beam footprint and the necessary concentration is reached, a sudden nucleation starts and sharp peaks from the mesocrystal order appear. The peaks get stronger as more and more mesocrystals form in the area illuminated by the x-ray beam. This phenomenon is directly measurable by the integrated intensity of the peaks from the fitting routine (**figure 6.10**). Simultaneously the amount of disordered particles decreases as is indicated by a rapid decay of incoherent scattering intensity. The time between the start and the end of the nucleation (the main mesocrystal growth) is approximately 3 minutes for the short measurement and 9 minutes for the long ones. This time frame corresponds to the time the pinning line needs to move from the outer to the inner part and the droplet is fully dried. As the beam footprint ranges from the sample center to about 2/3 of the sample surface, the contact line is only observed a bit later. Thus the measured nucleation period from GISAXS is often shorter compared to the microscope. This effect is an indication that the self-organization happens at the drying front of the droplet in the 3rd stage. The position of the nucleation and the growth process is therefore identified as the substrate-liquid-air interface (so called triple phase contact line TPCL [76]).

The peak shape does not change significantly during this first growth step (see **figure 6.11a**). The jump at the beginning is a numeric artefact, as the radial σ part has no influence when it is much smaller than the intrinsic beam width. During the nucleation, mesocrystals with a low lattice constant deviation and tilting exist. The behavior of c and a shows a quick decay in the nucleation stage (**figure 6.11b**), which slows down afterwards. This effect shows the nonlinear behavior in this part, it is much less pronounced for the longer evaporation times, because we average over a lot more different drying times of the mesocrystal growth in contrast to the short experiments.

A better degree of order can be observed for the medium evaporation time sample, because the particles have more time to order during the nucleation stage (see **section 4.2.4.3**), as well for the first and the additionally second stage.

Stage 4: The last stage is the **drying stage**, where no significant mesocrystal formation is taking place. This is easily seen in **figure 6.10**, where the integrated intensity stays constant. No new scattering centers appear inside the observation area. The mesocrystals are drying and the toluene between the ordered particles evaporates, so that the distance between the individual nanoparticles decreases. This leads to a movement of the peaks towards higher Q values, which is shown in **figure 6.11b**. The extracted lattice constants c and a contract simultaneously and the ratio between c and a drifts as well, showing that the shrinking is neither isotropic nor in a single direction. Comparing the c/a value with 2.45 expected for a perfectly closed packed structure shows, that the unit cell is extended in c direction when nucleated, approaching the fcc packing and even slightly compressing at the end of the short experiments. In all cases the observation time was not long enough to reach a stable state, so the finally approached values can only be guessed to be close to the perfect fcc structure. The starting and end values of the relation are higher for the longer evaporation time.

[1] The connection between the substrate and the end of the droplet.

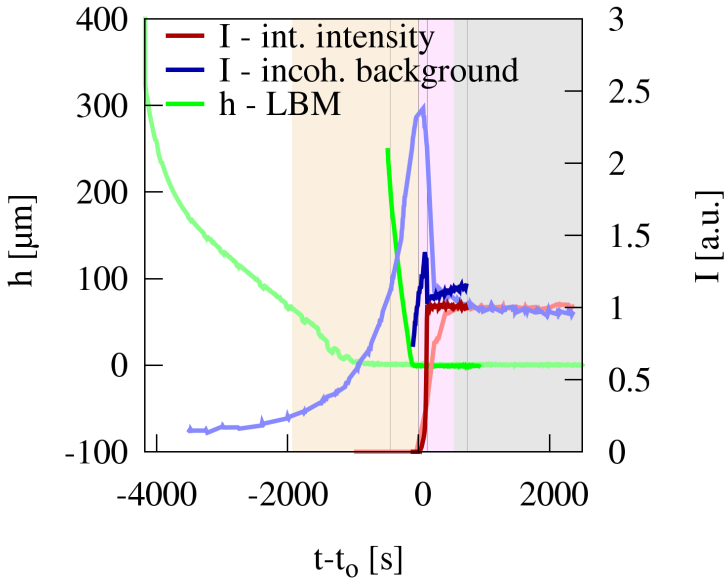

Figure 6.10: Integrated intensity of the peak and incoherent background versus time in comparison to the height of the droplet measured by the LBM. The four stages of the mesocrystal growth independently observed with the LBM are indicated by the colored regions for the measurement with medium evaporation time (pale colors) and by the gray lines for the short evaporation time (strong colors). The value t_0 describes the starting time of the nucleation. Each intensity point is the result of the GISAXS data treatment of one measurement described in **section 5.3.2**.

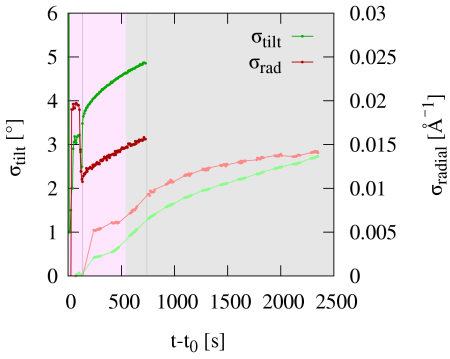

(a) Tangential and radial width of the peaks versus time.

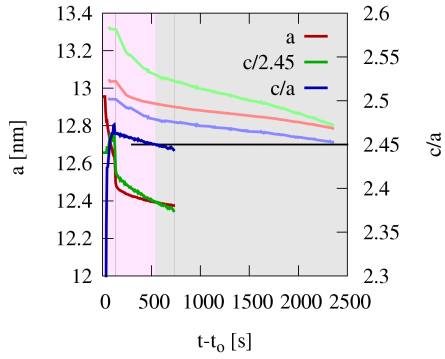

(b) Lattice constants versus time

Figure 6.11: Comparison of structural parameters versus time. Due to necessary available ordered system for this investigation, only the last two stages are indicated by the colored rectangular in the background for the medium measurement (pale colors) and by the gray lines for the short evaporation time (strong colors). The value t_0 describes the starting time of the nucleation. The black line indicates a perfect closed packed lattice, which will be crossed for every sample.

In addition to the integrated intensities, the fit yields structural quality parameters, which are shown in **figure 6.11a**. Both sigmas have the same qualitative behavior, they increase with time, so the peaks get broader. The tilting of the mesocrystal, as well as the distribution of the lattice constants increase with the longer drying time. For shorter evaporation time and less toluene reservoir both effects are stronger. At least the evaporation of solvent in the center of the mesocrystal during the final drying stage will lead to the large observed spread of lattice constants, so that the observed GISAXS peaks are an integration over mesocrystals with different lattice constants. In the average a tilting angle of 3° for the longer and 5° for the short evaporation time is observed.

6.4 Conclusions

An in-situ GISAXS study of highly ordered nanoparticle assemblies was carried out, to get a deeper understanding of the self-assembling process of the 3D system. A specialized in-situ cell was build to measure the crystal growth of nanoparticles in real time. Simultaneous measurements of high spatial resolution GISAXS, light band micrometer and microscope measurements could yield a new insight in the droplet evaporation and nanoparticle ordering. Precise control of the system and accurate identification of key features was possible. The highly ordered system, as well as a new fit function enabled new observations and a more quantitative understanding of the process.

In general the evaporation induced mesocrystal growth could be divided into four stages:

- Stage 1 - vertical droplet reduction: The droplet is cast on the silicon, forms a meniscus and slowly evaporates in the experiment with strongly saturated atmosphere, while a faster decay is observed for the short measurements. No sign of order can be found in this stage. The incoherent form factor, which indicates the density of disordered particles, shows only a slower increase for the middle evaporation time and a faster one for the short experiment.

- Stage 2 - highly concentrated film: The meniscus collapses and a constant, highly concentrated flat film is visible. No sign of ordering is found in this stage as well. The incoherent background shows a nonlinear increase of the density of the nanoparticle solution, which indicates that the evaporation of the toluene is ongoing. This stage is only observed for the samples with longer evaporation time.

- Stage 3 - nucleation: Suddenly, the contact line of the droplet moves circularly inward, the nucleation starts and sharp peaks from the mesocrystal order appear in the GISAXS pattern. Peaks get stronger as more and more mesocrystals form in the area illuminated by the x-ray beam. The nucleation period is longer for longer evaporation time.

- Stage 4 - drying stage: In the last stage no significant new mesocrystal formation is taking place. The mesocrystals are drying and the toluene between the ordered particles evaporates, so that the distance between the individual nanoparticles decreases.

The position of the nucleation and the growth process is identified as the substrate-liquid-air interface (so called triple phase contact line TPCL). While previous publications stated that the

evaporation kinetics and the amount of excess dodecanethiol ligand molecules affected monolayer formation at the liquid–air interface [22, 65], the iron oxide particles by Roth and Siffalovic et.all. [76, 82, 83] formed a monolayer at the TPCL. In this case the monolayer formation is similar to the 3D growth of spherical nanoparticles. SAXS measurements at different heights of the drop volume during evaporation show neither cluster formation at the drop surface, nor nucleation in the drop volume until a droplet height of a few µm. This result supports a process as described by Siffalovic et.all. [83] for the mesocrystal formation at the TPCL. The concurring explanation in [28] does not hold in our case as it should be possible to measure a monolayer formation inside the drying droplet at the liquid–air interface. The agreement of the time between the start and the end of the nucleation observed by GISAXS and the time the pinning line needs to move from the outer to the inner part is a further indication.

A critical concentration is necessary to start the mesocrystal growth, so the nucleation starts when the drying front of the droplet moves over a given position on the sample. Gonuguntla et.al. [47] report an existing increased evaporation near the contact line, which leads to an advection current that transports material in the drop toward the periphery. The high concentration, as well as the possible interaction with the substrate create ideal conditions for mesocrystal growth at the contact line. When the front reaches the illuminated area, the formation happens very quickly, so that the first visible peaks are already very narrow. As a consequence the only dynamic process observable in our experiment is the aggregation of more mesocrystals creating a statistical distribution on the sample surface and the much slower drying of already formed mesocrystals, changing their lattice parameters.

Unfortunately the nucleation process is not visible due to the limited time resolution in the order of seconds, disordering of the perhaps existing clusters or the low signal of these precursors. We can rule out a coherent nuclation process over the whole sample area, as small clusters formed by at least 5% of the particles inside the solution would have been visible as was shown by comparison to the SAXS measurement on particles clustering in solution.

Our main focus was to observe the influence of different evaporation times on the growth mechanism. A higher evaporation time allows the sample to stay longer in each stage, additionally a second stage is observed. A better degree of order can be found, as well, because the particles have more time to order in the final nucleation stage. Although the time particles spend in the free solution seems to have no influence for the self organization, the slower evaporation leads to a decreased movement of the TPCL, where the ordering is supposed to take place. As the movement of the TPCL is slower, more time is available during the final nucleation stage, allowing a better degree of order, too. In addition, the reduced drying rate can lead to a reduction of crack formation and similar effects, that reduce the structural quality of mesocrystals after the growth is finished. Furthermore it can be explained by a larger diffusion radius for the particles allowed by the slower evaporation, which can lead to accumulation of particles with similar size and shape, allowing better long range order. This theory is supported by the observation of self separation of cubic and spherical particles in a mixed solution as described in **chapter 4**.

The time dependent fit of multiple peaks yielded additional quantitative information about the drying of the mesocrystal. While the mesocrystal is shrinking the lattice constants c and a contract simultaneously and the ratio between c and a drifts as well, showing that the shrinking is neither isotropic nor in a single direction. Comparing the c/a value with 2.45 expected for a perfect closed packed structure shows that the unit cell in c direction is extended when nuclated, approaching the fcc packing and even slightly compressing at the end of the short experiments.

In all cases the observation time was not long enough to reach a stable state, so the finally approached values can only be guessed to be close to the perfect fcc structure. It was found that the starting and end values of these lattice constants are higher for the longer evaporation time. This could be explained by the fact that particles with a bigger radius have a slower movement inside the solution and could order in a mesocrystal only when given enough time. A too short evaporation time avoid the growth of mesocrystals with bigger particle, which leads to lower averaged lattice constant values. Although the degree of order (peak width) in the resulting assemblies varies with the given evaporation time, the overall process was found to be similar for all samples.

In summary, a deep insight into the 3D self-assembly process for spherical particles was obtained. Unfortunately, some aspects could not be clarified conclusively with the performed experiment. For example the measurement of the nucleation stage would profit from a much higher time resolution and smaller beam size.

Chapter 7

Diffraction from a single mesocrystal

Another aspect of this PhD work is to understand the exact 3D structure of one single mesocrystal formed from magnetic nanoparticles using the already established deposition methods. The basis of this study was a completely new approach: Performing a diffraction experiment on a single, isolated mesocrystal with a micro-focus x-ray beam. This experiment makes it possible to measure the mesocrystal peaks without the in-plane orientational average and without background from disordered regions. In previous GISAXS experiments, the peak shape has been broadened due to the average over the ensemble of mesocrystals with a statistical variation of lattice constants or tilting angle to the substrate (**chapter 5**). These effects are not present when considering only a single mesocrystal.

Separation of a single mesocrystal of nanoparticles from an ensemble of mesocrystals as-grown is a completely novel process as well. This experiment is not only interesting from a scientific point of view, but enters a new level of crystallography. Diffraction experiments to investigate the atomic structure of solids and crystals in the Å-range is a well established method [39, 57, 78, 79]. Larger building blocks of crystals in the nm-range were studied on self-assembled crystals of fullerenes [62, 97] or proteins [56, 77] already. In this work we increased the challenge by performing diffraction experiments on 3D self assembled nanoparticle crystals with building blocks in the 10 nm -range and forming small crystals of a few 100 nm height with a sample volume in the range of 1 μm^3. So far small crystals investigated for the atomic structure are reported with a volume in the 100 μm^3 range [16, 17, 48]. In contrast to the former crystals built of large molecules, the nanoparticle building blocks are not exactly equal in their atomic structure and surrounded by a soft organic shell. Therefore the resulting crystalline order is slightly different.

7.1 Separation of a single mesocrystal

For the single mesocrystal preparation one crystal is isolated from a standard sample with an ensemble of mesocrystals using Focused Ion Beam preparation (FIB). The 2D powder samples were produced with the best parameters known to achieve a well ordered structure, which was investigated for this kind of samples by GISAXS analysis (see **section 4.2.4**). The FIB preparation was done with a FEI Dual Beam System Helios NanoLab 400S. A dual beam system combines the advantage of a scanning electron microscope (SEM) and a focused ion beam instrument. In the SEM, secondary electrons (SE) are generated through the low-mass electrons interacting with the sample surface non-destructively. Collected SE offer an image resolution

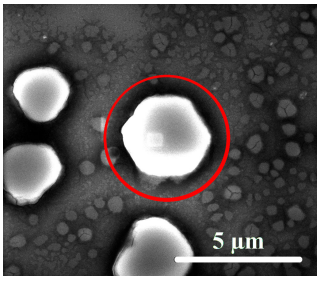

(a) Searching for a free standing and good ordered mesocrystal.

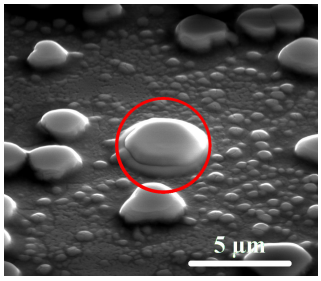

(b) Covering a mesocrystal with a Pt layer.

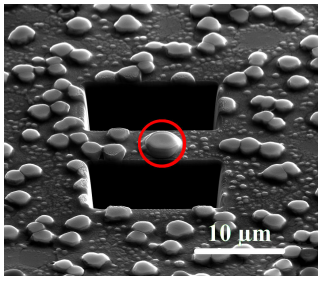

(c) Cutting of the two trenches.

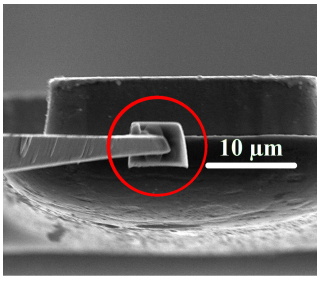

(d) Transferring the block to a copper Omniprobe® grid

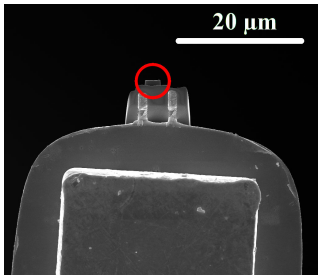

(e) Fixing the block with platinum.

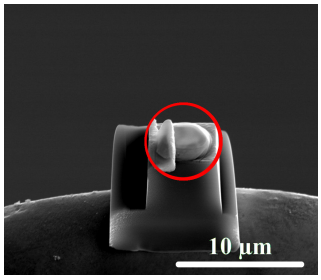

(f) Clearance cutting of a mesocrystal.

Figure 7.1: Description of the extraction process of a single mesocrystal (highlighted in color).

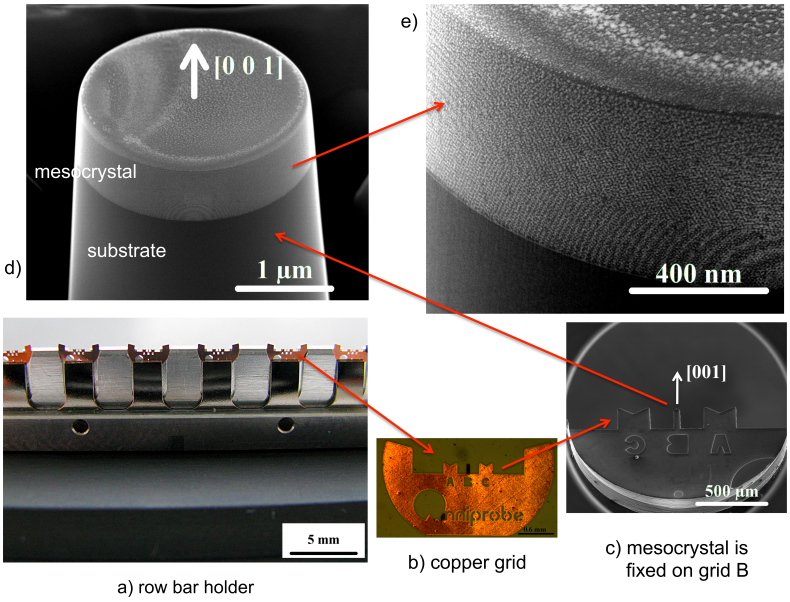

Figure 7.2: Single mesocrystal sample as used.

Sample ID	2D powder sample ID	2D powder structure	diameter	height
M_S^I :	$D_{S,\,5.01}^{XLg1.68\perp 80}$	$R\bar{3}m$	3.45± 0.1 µm	361± 80 nm
M_S^{II} :	$D_{S,\,5.01}^{XLg1.68\perp 80}$	$R\bar{3}m$	2.45± 0.1 µm	570± 80 nm
M_C^I :	$D_{C,\,10.9,\,0.8}^{XLg1.68X}$	$I4/mmm$	4.50± 0.1 µm	215± 80 nm

Table 7.1: Produced mesocrystals which were used for the diffraction experiment and their main parameters.

down to sub-nanometer range. The FIB is similar to a SEM, but utilizes a beam of higher-mass Gallium ions, which induce a sputtering process that modifies the surface with nanometer precision. In this Dual Beam system the electron and the ion beams intersect at a 52° angle at a coincident point near the sample surface. This allows in-situ SEM imaging of the FIB milling process and allows one to precisely cut out a single mesocrystal from the 2D powder sample. The information about the FIB system presented here was taken from the manufacturers website [105]. The separation process was done in collaboration with Doris Meertens from the Ernst Ruska-Centre (ER-C) for Microscopy and Spectroscopy with Electrons. In this chapter a detailed description of the separation process is given and illustrated with some example images.

At the beginning a mesocrystal, which is well separated from others and shows a nice structure on top (**figure 7.1a**) has to be found with SEM. On top of the chosen mesocrystal a Pt-layer of 300-500 nm is deposited with an electron beam of 5 kV and 5.5 nA, exemplified in **figure 7.1b**. This Pt-layer protects the mesocrystal from the focused ion beam, which will be used for the detaching process of the chosen mesocrystal from the substrate. During the carving process the neighboring mesocrystals are destroyed by the high energetic ions.

For the extraction of a mesocrystal with an underlying Si block as bottom support, two trenches around the chosen crystal have to be cleaved with an ion beam of 30 kV and 6.5 nA using the parameter for milling Silicon (see **figure 7.1c**). Thereafter, one side block and the bottom area are cut free. The substrate block with the mesocrystal on top has to be large enough to allow the fixation with platinum at the tungsten manipulator needle with enough distance to the mesocrystal. The second side block is removed and the pieces with the mesocyrstal hangs freely on the tip of the tungsten needle.

The block is transferred to a copper Omniprobe® grid, which is a standard holder for mounting TEM lamellas milled out by FIB systems (**figure 7.2b**) and attached to the top of the middle grid position B, trying to keep the c axis orientation upwards (**figure 7.1d**, **figure 7.2c**). The block is fixed with platinum (ion beam 30 kV and 93 pA) to the Omnigrid® (see the stripes of Pt at the backside in **figure 7.1e**). Then the manipulator needle is detached from the specimen and the final preparation of the single mesocrystal can be started. Layer by layer everything around the single mesocrystal is dissipated (**figure 7.1f**). From the outside to the inside, one ring after the other is excavated with an ion beam of 30 kV and 93 pA. Slowly getting closer to the core of the mesocrystal, while constantly taking SEM images to control the process. Undesirable edges of the silicon around are removed to have a free path for the x-ray beam through the mesocrystal. The platinum protection layer on top has to persist to avoid damaging the mesocrystal. Finally a fully isolated mesocrystal is achieved (**figure 7.2d**), which is well oriented upwards with the [001] direction of the silicon substrate. This known orientation of the mesocrystal helps with the alignment for the scattering experiment. The crystalline order of the mesocrystal is

not destroyed by the procedure as indicated in **figure 7.2e**. For the diffraction measurement the copper grid was fixed on a row bar holder **figure 7.2a**, which could be transported in a special box and could be inserted into a dedicated sample holder at the beamline. The produced single isolated mesocrystals, that were subsequently investigated by x-ray diffraction, are listed in **table 7.1**.

7.2 Experimental details

To be able to investigate crystals of µm size some requirements are absolutely mandatory: The x-rays have to be focused down approximately to the size of the crystal to achieve high photon flux densities, the beam has to stable within a fraction of the beam diameter, the background has to be virtually zero and the motor resolution has to be significantly better than the sample size. These necessary conditions make this experiment an absolute challenge. The investigation was done with a focus spot size of 5 µm vertically and 10 µm horizontally to measure crystals with ≈300 nm height and a few µm width. The samples have a small scattering volume and thus provide weak intensities, so a focusing down to close to the sample size is required to increase the signal and even lower the background. This small spot size induces other challenges as to find the sample in the first place with such a small beam. For each crystal orientation the xyz-position needed to be realigned to bring the mesocrystal into the beam center as the sphere of confusion of the six-circle was in the order of the beam size. For a measurement with lower focusing (see M_S^{II}, which is the only sample measured with 50 µm vertically and 200 µm horizontally) more background from other regions around the sample and low peak intensities are visible. So the decision was clear to use the fully focused beam, although three days of sample alignment were necessary.

The diffraction experiment was performed at the high resolution diffractometer P08 at Petra III (**figure 7.3**, see **section 3.8** for the instrumental details). After alignment of the beamline and the exact determination of the beam position, the single mesocrystal was fixed on a special setup on the sample holder (**figure 7.2**a) and aligned optically with a microscope camera to the beam position. The copper grid B was clearly visible and could easily be aligned. The crystal itself was not optically visible, but could be guessed from a blue spot, which was produced by the Si block under the crystal by reflections from the illuminated silicon. For the rough positioning of the sample on grid part B, we used a NaJ point detector measuring the beam attenuation due to the Cu sample holder (attenuation due to the small mesocrystal or silicon substrate was too weak to be detected with a beamsize of 10 µm horizontally and 5 µm vertically). The next step was to find a Si peak and to carry out a precise adjustment of the goniometer angles with the Si (004) reflection to align Si (001) and thus the mesocrystal (001) direction parallel to the axis of the phi motor. This way the orientation could be found very precise to a few hundredths of a degree, in contrast to about 0.5 ° when using the mesocrystal structure reflections. With this orientation the phi motor could be used to rotate the sample around its (001) direction. To locate the small silicon substrate (5x10x10 μm^3) and its Si(004) reflection, the Roper Scientific detector was used. The detector has a high resolution and is optimized for the used energy of 12.4 keV. The same detector was used to search for the mesocrystal reflections, afterwards. After discovering the nanoparticle superstructure peaks, a fine adjustment was done to maximize the reflex intensities.

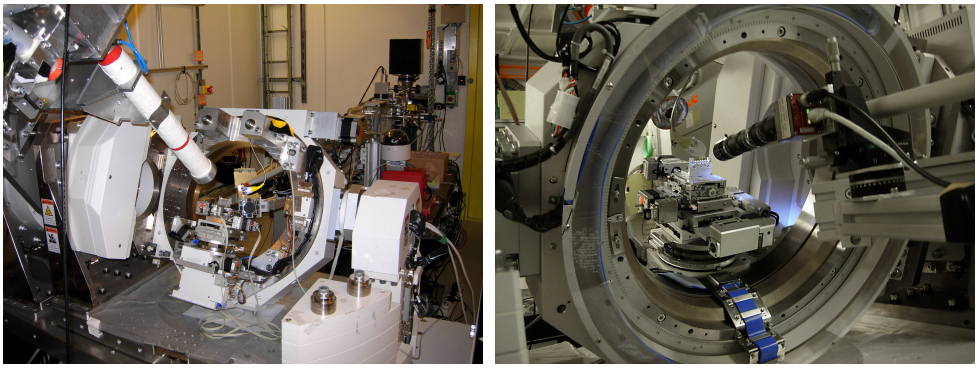

(a) (b)

Figure 7.3: High resolution diffractometer P08 at Petra III

For the scattering pattern measurements, different reciprocal lattice planes were selected by rotating the crystal around the φ-axis, optimized in the position and measured by rocking the crystal in both ω and φ. In detail, images were exposed while continuously moving φ for 5 separate ω positions ("cmesh"). A sketch of this cmesh procedure is shown in **figure 7.4**. The scans were measured for φ in the range of $\pm 3.5\,^\circ$ and for ω in the range of $\pm 1\,^\circ$ around the position where the left and the right as well as the bottom and top equivalent reflexes have about the same intensity on the detector. With the used wavelength all mesocrystal reflections with reasonable intensity have small diffraction angles $< 3\,^\circ$ and thus the Ewald sphere is very flat and several reflections can be observed simultaneously (as in the GISAXS case **section 4.2.3**). However, the high resolution of the synchrotron beam, which corresponds to a narrow " shell" of the Ewald sphere, inhibits the simultaneous observation of the full scattering plane and reflections at higher Q appear much weaker, as they are further away from the perfect diffraction condition (Bragg-condition). The optimal measurement range for ω and φ would reach from the Bragg angle of the lowest Q reflection to the highest Q reflection, which is about $1.5\,^\circ$ for the (004) reflection, which is still visible on the observed detector range. In our experiment the cmesh areas where chosen as as given above, so for the Q_y direction this optimal conditions are fully satisfied while the Q_z is a compromise between measurement time and covered area/step size. As the φ direction is scanned during exposure, it is possible to make very small steps over a large area without increasing the counting time (in our case 60 s for 70 steps) as the detector does not need to be read out between each step. ω, on the other hand, needs to be done in discrete steps and thus each additional step increases the counting time. As can be seen in the measured figures, this selected area is sufficient to access all peaks in the detector area. For comparing the images with simulated intensities, these experimental conditions needs to be considered as well, as they lead to e.g. lower observed intensities for all reflections with the Miller indices l>3.

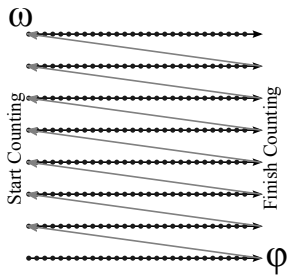

Figure 7.4: Sketch of the used cmesh.

To obtain integrated intensities of the reflections necessary for a quantitative structure analysis

of a single mesocrystal, rocking scans of peaks of the cubic system for all accessed planes were performed. To achieve a well defined and optimized rocking scan of a reflection, the mesocrystal was aligned using the chi angle to bring the reflections in vertical direction. This way the omega angle could be used to scan the peaks perpendicular to their $\vec{Q}$ direction, thus the ω-scan is equivalent to a scan in $\vec{Q}_x$direction. As the sphere of confusion of the six-circle was of the order of the beam size, it was necessary to realign the xyz-position for each χ orientation to bring the mesocrystal into the beam center.

A first attempt of wide-angle diffraction was tried for the (220) peak at 19.5°detector angle. The goal was to search for a preferred crystalline orientation of the nanoparticles inside one mesocrystal. Low intensity peaks were expected, but we could not detect anything within reasonable counting times. Additionally, we had to avoid a region of reciprocal space around a Bragg reflection from Cu. A later estimation based on the intensity ratio between the mesocrystal and γ-Fe_2O_3 (004) reflexes of $3 * 10^{-4}$ measured on the laboratory reflectometer with a $\theta 2\theta$-scan for a 2D powder samble resulted in an expected peak intensity of $1 * 10^{-3}$ c/s for the MC. This intensity would have been impossible to measure given our experimental conditions with an average background of 1-2 c/s.

7.3 Result and discussion

In this challenging experiment we succeeded to measure three single mesocrystals, two with spherical and one with cubic particles (see **table 7.1**). This section is split in two subsections. The first one shows a selection of different reciprocal lattices and a discussion about the crystal structure and their quality. In the second part an integrated Intensity analysis is done for the cubic sample to give a quantitative approach to the structure analysis. The description of the nomenclature used for the angles is given in **section 3.8**.

7.3.1 Analysis of the scattering pattern

Different reciprocal lattice planes were measured by rocking the crystal in both ω and φ. For each of the five recorded pictures at different ω positions a measurement period of 60 s and one additional background measurement with equal time was chosen. One c-mesh including background measurement needs more than 10 min and is repeated a number of times in dependence of the expected scattering intensity. Such a measurement was done for all selected planes. For the data treatment the different scans for ω are combined using the maximal pixel intensity of each individual image. This procedure is advantageous compared to summing up all images as it reduces the relative background (BG). The average BG for all images is comparable while the peak is only present in some images. Thus the BG sum is $\approx 5 \cdot BG_{max}$ while the peak sum is $\approx (1-2) \cdot peak_{max}$. The repeated cmesh's are combined by averaging. A selection of pictures, which were recorded from different planes, is represented in components of the scattering vector and reciprocal lattice units in **figure 7.6** and **figure 7.7**. For an complete overview, all images left out in this section are shown in **appendix table A.2** of the appendix. To prevent confusion of the parameter symbols retrieved from fits of the single mesocrystal data with the ensemble parameters the former are marked with MC subscript, which abbreviates single Meso

Crystal. MC is in a sense relate to the previous use in the form factor formulas in **chapter 5** as both symbols describe physical parameters of only one mesocrystal.

The non-uniform background scattering, spreading "beam like" from the center, is different but present in every scattering plane. It looks like a shadowing effect from something inside the beam path. Equivalent reflexes of for example (301) and (30$\bar{1}$) of the (h0l) plane from the M_C^I have not the same intensity. While the (301) reflex has a similar intensity as the other reflexes which are lying on the same $|\vec{Q}|$ of the form factor ring, the (30$\bar{1}$) is obviously weaker and lies on a shadowed cone. Due to the impact on the reflexes, it is possible to assume that the object or the reason for the shadowing effect is positioned behind the sample. Shadowing of silica pillars, which are a residue from the separation process of a single mesocrystal, can be excluded, because the beam path seems to be open (see **figure 7.5**). The reason could be situated inside the flight tube behind the sample. A low φ dependence of the non-uniform background supports this possibility, as the tube is fixed. Additionally a halo effect from the residual direct beam is visible. The absorption by the silicon substrate of the scattered beam creates a reduced BG in the lower hemisphere.

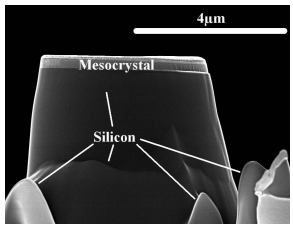

Figure 7.5: Mesocrystal view in the beam direction.

7.3.1.1 Structure

Reflections for four independent reciprocal lattice planes for M_C^I (**figure 7.6a (h0l), 7.6b (hhl), A.13a (h2hl), A.13b (h3hl)**) , three for M_S^I (**figure 7.7a (h0l), 7.7b (hhl), A.12b (0kl)**) and one for M_S^{II} (**figure 7.8 (hol)**) have been detected.

For the mesocrystal with cubic building blocks we found: Repetitions as a function of φ of selected planes have been verified, proving a fourfold rotation axis parallel to c_{MC} for the cubes crystal and together with $a_{MC} \neq c_{MC}$ (see **table 7.2**) and the identical 90°rotated crystal planes (hhl) and (h$\bar{h}$l) the mesocrystal system is confirmed to be tetragonal. For the tetragonal system the zonal selection rules are:

(h0l) h+l=2n (tetragonal $\Rightarrow$ (0kl) k+l=2n)

(hhl) l=2n

(h2hl) h+l=2n (tetragonal $\Rightarrow$ (2hhl) h+l=2n)

(h3hl) l=2n (tetragonal $\Rightarrow$ (3hhl) l=2n)

Combining all these planes leads to the general selection rule h+k+l=2n with no additional selection rules. Note that reflections extinguished by the form factor have not been taken into account, as e.g. (103), which is the main difference to crystal diffraction where the FF generally leads to no extinctions. This selection rule refines the system to a I-centered tetragonal lattice with one of the following space groups: I4, I4/m, I4mm, I$\bar{4}$m2, I4/mmm, I422, I$\bar{4}$2m and I$\bar{4}$. We expect to have the one with highest symmetry, I4/mmm, due to our simple unit cell containing only two particles (particle volume inhibits any higher number for this unit cell size). In addition to the selection rules there are three independent mirror planes visible, which in deed allow the refinement of the symmetry to I4/mmm. The (h0l) as well as the (0hl) plane

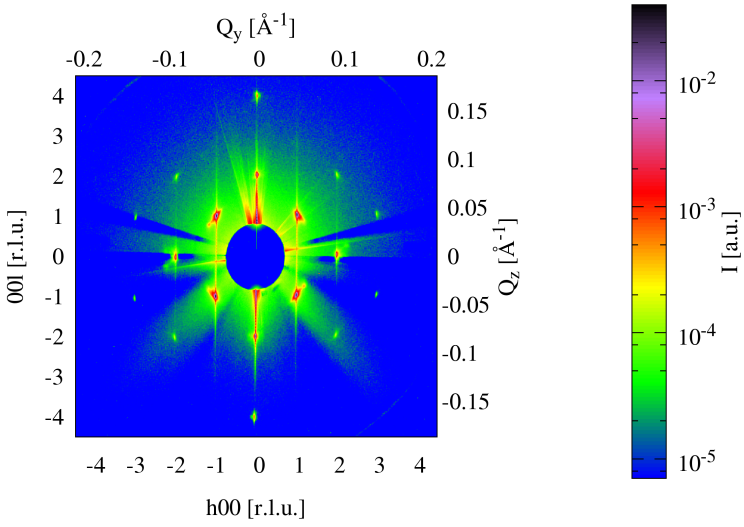

(a) Cubes M_C^I: measurement of the (h0l) plane

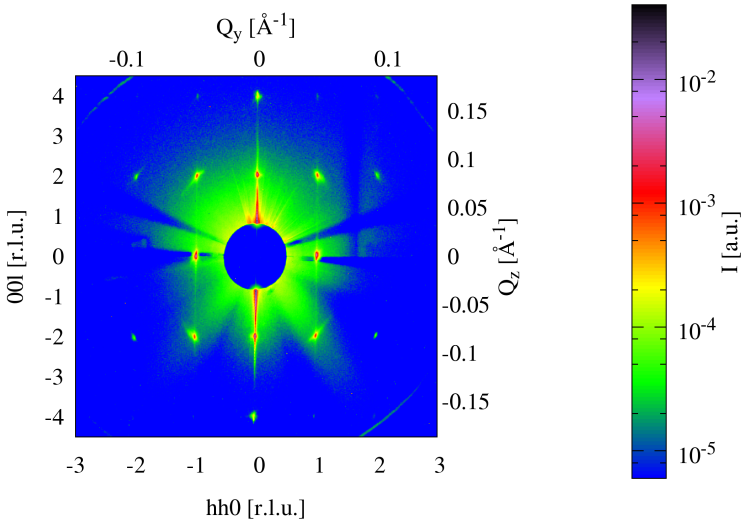

(b) Cubes M_C^I : measurement of the (hhl) plane

Figure 7.6: Diffraction pattern from a single mesocrystal with cubic building blocks for different reciprocal planes. A simulation of these patterns is shown in the appendix **section A.3.3**.

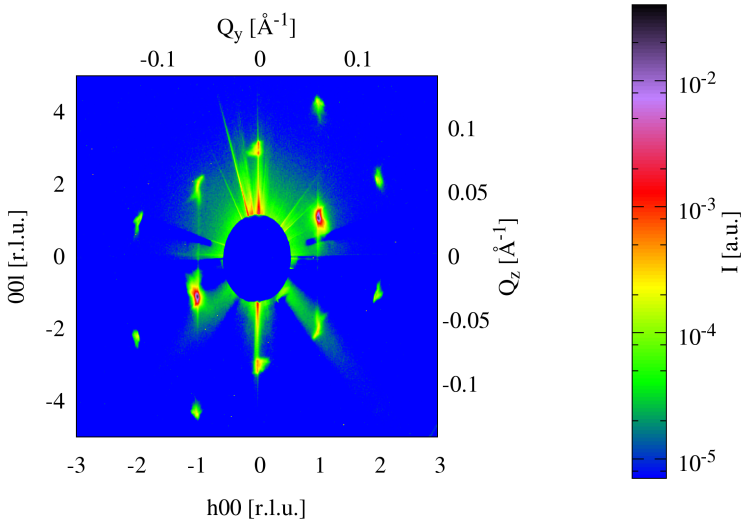

(a) Spheres M_S^I : measurement of the (h0l) plane

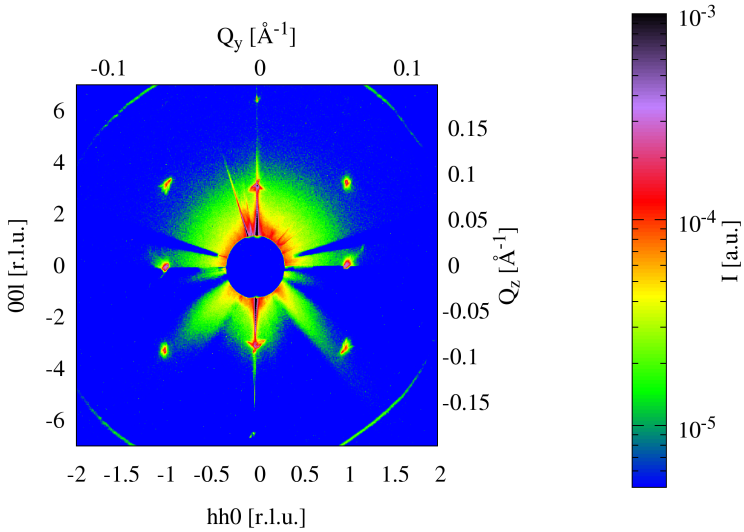

(b) Spheres M_S^I . measurement of the (hhl) plane

Figure 7.7: Diffraction pattern from a single mesocrystal with spherical building blocks for different reciprocal lattice planes.

show 2 mirror planes and due to the planes are perpendicular to each other the 3 mirror planes are necessary.

The crystal with spherical building blocks shows a three fold symmetry of the lattice from the repetitions as a function of φ of selected planes. The observed reflections clearly follow -h+k+l=3n with no additional selection rules. This selection rule refines the system to a R-centered lattice with one of the following space groups: R32, R$\bar{3}$, R3m, R3 and R$\bar{3}$m. We expect to have the one with highest symmetry, R$\bar{3}$m, due to our simple unit cell containing only three particles (particle volume inhibits any higher number for this unit cell size).

In contrast to an atomic crystal (when ignoring orbital arrangement as typically done in diffraction), the symmetry of the individual building blocks needs to be considered for the space group determination, as well. All symmetry elements from the mesocrystal unitcell heave to be applied to the single particle form to test this. For spherical particles this is trivial, as all symmetries will be present, when they are positioned at their center. For a cube (as well as for a truncated and rounded cube) the fourfold symmetry axes through the face centers, the three mirror planes and the inversion symmetry are all present, when it is aligned parallel to the unit cell (the same orientation as the unit cell). Different particle orientations (like placing the cube with the edge or corner upwards) would violate at least one fourfold axis or mirror plane.

M_C^I and M_S^I show a single crystalline structure, in contrast M_S^{II} has a twinned structure with multiple grains. The observation of both reflections e.g. (101) and (01$\bar{1}$) shows the presence of 180 ° twinning, either resulting in peaks following -h+k+l=3n or h-k+l=3n. This twinning structure is verified independently for these samples by TEM, made from a mesocrystal of the same sample (**figure 7.8**). Different colors inside the TEM as well as in the GISAXS picture indicate each twin orientation. The similar peak shapes of (0$\bar{1}$1) and (01$\bar{1}$), arising from the same twin, are consistent with this. The obversed rhombohedral R$\bar{3}$m structure, which is the standard setting, as well as the reversed rhombohedral structure, where the a_{MC} and b_{MC} axis are rotated by 60 ° around c_{MC}, is another way of describing the twin relation. Reflexes on the (00l) line are coincident for both crystal orientations.

The indexed peaks of a single mesocrystal are consistent with the suggested R$\bar{3}$m symmetry for spheres and I4/mmm space group for crystals made of cubes derived for an ensemble of mesocrystals. While the analysis of the GISAXS pattern deliver an average structure of all mesocrystals, in this experiment the structure of one crystal is determined uniquely.

7.3.1.2 Lattice constant and correlation length

The lattice constants and correlation lengths determined as an average over peaks of different planes in reciprocal space from every sample are shown in **table 7.2**. The individual values of the reflections are listed in **appendix table A.2**, where the parameters from two mirrored peaks ((hkl) and ($\overline{hkl}$)) were averaged to compensate potential shifts due to an imperfect zero position of the detector. In **table 7.2** the average is taken over all accessible peaks from the table in the appendix for each mesocrystal. To define the positions and half widths of the reflexes, a Gaussian fit was used. The parameters of M_S^{II} are taken directly from the picture, as the peaks were not fittable. The extraction of intensity along the horizontal and vertical detector directions corresponds to coupled Qy (horizontal) or Qz (vertical) and Qx scans, however the Qx variation is negligible in our scattering geometry (small angles at the used wavelength) and furthermore

Sample ID	$\langle a_{MC} \rangle$	$\langle c_{MC} \rangle$	$\langle \varepsilon_{y_{MC}} \rangle$	$\langle \varepsilon_{z_{MC}} \rangle$
M_S^I :	11.86 ± 0.15 nm	21.04 ± 0.7 nm	362 ± 163 nm	244 ±136 nm
M_S^{II} :	11.62 ± 0.2 nm	24.62 ± 0.4 nm	1.1 ±0.55 µm	172 ±86 nm
	12.17 ± 0.2 nm	25.44 ± 0.4 nm	741 ±371 nm	167 ±84 nm
	12.28 ± 0.2 nm	19.98 ± 0.4 nm	782 ±391 nm	207 ±104 nm
	12.05 ± 0.2 nm	21.26 ± 0.4 nm	650 ±325 nm	210 ±105 nm
M_C^I :	13.47 ± 0.03 nm	15.08 ± 0.07 nm	923 ± 350 nm	309 ±93 nm
$D_{S,\,5.01}^{Lg1.68\perp 80}$:	12.7 ± 0.1 nm	31.3 ± 0.1 nm		
$D_{C,\,10.9,\,0.8}^{XLg1.68X}$:	14.2 ± 0.1 nm	23.9 ± 0.1 nm		

Table 7.2: Lattice constant and correlations length taken from the average of reflexes from different planes of the single mesocrystal measurements. For M_S^{II} the (h0l) plane was used. Due to asymmetric peak shapes and unknown factors as e.g. influence of the measurement method on the peak shape, the width are expected to be increased. The different colors red and cyan belong each to one twin according to **figure 7.8**. The three grains with the same orientation, enumerated in the scattering image figure **figure 7.8**, have been treated separately to derive the data shown and are color coded here as 1, 2 and 3. For a comparison the lattice constant values for an average over an ensemble of mesocrystals are shown below the line.

would be dependent on the phi and omega orientations, which we combine in one single image. Therefore it is possible to extract the correlation length $\varepsilon_{y_{MC}}$ and $\varepsilon_{z_{MC}}$ from half width in y and z direction of the peaks in these images. The errors were calculated from the standard deviation of all peaks. The resolution of $3.1 \cdot 10^{-4}$ Å^{-1}, fitted with a Voigt function on the smallest, best defined peak $(00\bar{2})$ from M_C^I, has no influence on the peak width except for the calculation of $\varepsilon_{y_{MC}}$ for the cubic sample where it was considered.

A reduced $\langle c_{MC} \rangle$ lattice constant of about 37% for cubic and 33% for spherical particles is observed for the investigated single mesocrystals in comparison to the averaged values from GISAXS results of a 2D powder sample (see results in **section 4.2.4.1**) produced under the same conditions and from the same particle solution. The average in-plane lattice constants from all observed reciprocal lattice planes shows only a slightly reduced value of about 5% for the cubic and 7% for the spherical nanoparticles. The lattice constants depend on the sample age, providing the drying time. Gradual evaporation of rest toluene between the particles inside a mesocrystal can reduce the distance between the particles and the reflections move to higher Q values. Additionally the in-situ experiments show that a constant value of the c/a axes is not reached after a day and it can be assumed that the drying of crystals needs a long time. The smaller lattice constant in comparison to the ensemble of mesocrystals could be caused by the fact that the 2D powder sample is being dried in a vacuum system a few days before detaching the single mesocrystal. Furthermore the separated mesocrystal is free standing which could lead to an increased drying rate. Additional influences of the Pt cover layer as well as the selection of a mesocrystal formed from slightly smaller particles than the average is possible, as well. After **section 4.2.3** it is expected that similar particles will order together in one mesocrystal, so it is not surprising that the large crystals selected for the FIB extraction process are found by particles slightly smaller than the average. All these effects can lead to a few percent reduced lattice constant for the in - as well as for the out-of-plane direction. The huge reduction in the out-of-plane direction is dominant and most likely attributed to the platinum cover layer, which leads to a compression of the c_{MC}-axis. On the other hand the mesocrystals are not destroyed by the extraction process and the structure is completely intact as can be seen in the scattering pattern.

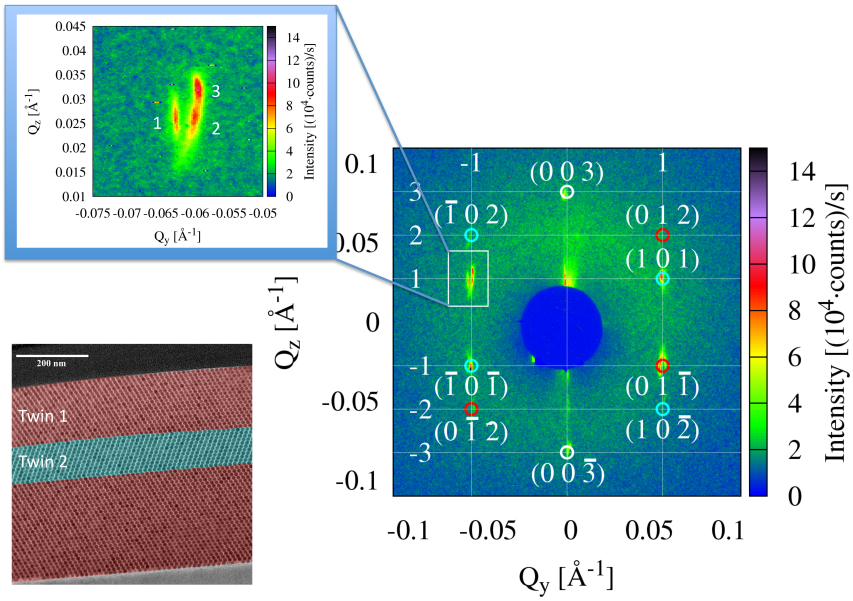

Figure 7.8: Measurement of the (h0l) plane from M_S^{II} shows the presence of twin domains. Each color indicates peaks, which belong to one twin. A TEM picture on the left side visualizes the existence of such twins in a single mesocrystal again colored in dependence of the orientation. This microscope picture was measured on a mesocrystal of the same sample. The zoom shows the splitting of one of the peaks suggesting several crystallites with slightly different lattice constants.

Looking at the lattice constant values extracted from the reflex position (see **appendix table A.2**), the values for the in-plane constants a_{MC} from M_C^I of the (hhl) and (hh$\bar{l}$) planes show that the difference of 0.04 nm is smaller than the error of 0.059 nm. The result of the same in-plane constant for 90° rotated planes proofs the tetragonal lattice. The difference in c_{MC} between (002) and (004) reflexes is a systematic error that can occur through a shift of the peak fit position of (002) due to the influence of the FF slope on the Laue oscillations. For the mesocrystal M_S^I single peaks are visible, which are smearing out in one huge reflection. The lattice constant difference between the multiple peaks vary a few percent. The pictures of M_S^I (**figure 7.7a, 7.7b**) show a single crystal with a continuous distribution of lattice constants, while the pictures of M_S^{II} (see **figure 7.8**) shows additional peaks. The observation of both e.g. (101) and (01$\bar{1}$) shows the presence of 180° twins, either resulting in peaks following -h+k+l=3n or h-k+l=3n. The colors red and cyan indicate peaks which belong to one twin with the corresponding parameters in **table 7.2**. This structure formation, which can be interpreted as stacking faults, is documented for these samples by TEM, made from a mesocrystal of the same sample (**figure 7.8**). The different colors inside the TEM picture mark twins with different orientations. The similar peak shapes of (0$\bar{1}$1) and (01$\bar{1}$), arising from the same twin, are consistent with this explanation. The peaks of one twin are split, suggesting that this twin is made up of three grains with different lattice constants, both out-of-plane and in-plane. These three peaks are separated from each other. The difference of the in-plane lattice constant is 5%, while the difference in c parameters is many times higher with 21%. This example shows

that there can be varying structural parameters within one single mesocrystal, not only in an ensemble as was expected from the GISAXS investigation.

The correlation length describes the average size of ordered domains. The peak width in Q_z- and Q_y-direction correspond to out-of-plane and in-plane correlations, respectively. In the case of the single mesocrystal, the measured correlation lengths are the value for one crystal and not an average over an ensemble. The crystal with cubic particles M_C^I shows a smaller in-plane correlation length $\langle \varepsilon_{y_{MC}} \rangle$ than the diameter measured with SEM (**table 7.1**), so the structure is not coherent through out the full diameter. A larger value for $\langle \varepsilon_{z_{MC}} \rangle$ than the height from the microscopy experiment indicates a correlation through the whole mesocrystal in the out-of-plane direction. The results of the single reflex rocking scan in **appendix table A.2** show an influence of a lattice constant deviation and mosaic spread on the peak width. The increased Q_y-width of (00l) reflections with large Q_z-position can be explained by mosaicity around the beam axis (χ) due to increased influences of the same tilting angle for a larger radius, while the broadening of the Q_z-width is influenced by the c_{MC} lattice constant distribution. The comparison of the (101) and (301) reflexes of the (h0l) plane show only a small influence of a a_{MC} lattice constant distribution. In contrast, the two single mesocrystals with spheres show broader peaks in comparison to the cubic one. A lesser degree of order is present, which is mainly manifested as a lattice constant distribution generating peaks which merge seamlessly indicating several grains. An influence from mosaic spread or a direction dependent lattice constant distribution is not clearly visible from the correlation length values. In contrast M_S^{II} shows distinct reflections which are more separated from each other indicating only a few grains with a large difference between their lattice constants.

7.3.1.3 Laue oscillation

The M_C^I crystal with cubic building blocks has sharp strong peaks (**figure 7.9a**) allowing a closer evaluation of the actual peak shape. The peak tails in Q_z direction visible in logarithmic color scale, are Laue oscillations (see **figure 7.9a inset**), which indicate a high degree of order in the cubic sample, a flat surface and a relatively small and equal height. Oscillations in Q_x and Q_y direction are not visible due to the much larger size of the crystal in these directions and the limited correlation length discussed in the last subsection. The factor 20 between the diameter of 4.5 µm in comparison to 215 nm height would lead to 20 times smaller oscillations, which are not resolvable any more. Due to the cylindrical mesocrystal shape, the in-plane peak shape is a modified Bessel function (see **equation 5.6** in **section 5.1.1**) instead of a Laue function. To proof that the shape actually resembles Laue oscillations and extract parameters like height and height distribution, a shifted Laue function in combination with a form factor, a particle size -, height - and lattice constant distribution and an incoherent background was used to fit the oscillations (see script in appendix **section B.2**). In the case of nanoparticles the form factor is important due to the relative size of the particles compared to the structure size and hence the influence of the oscillations on the scattering in comparison to atomic crystal. The atomic size distribution is not existing, while nanoparticles have typically a size distribution of a few percent. The used form factor with convoluted size distribution increases the Laue oscillations around $Q_z = 0$ in relation to the main peaks. The additional lattice constant distribution is required to describes the peak shape and oscillation amplitude. The result of the fit is shown in **figure 7.10a**. The model describe the scattering well and the present discrepancy is mainly introduced by the non-uniform background, which was described earlier and is not fit-able. The

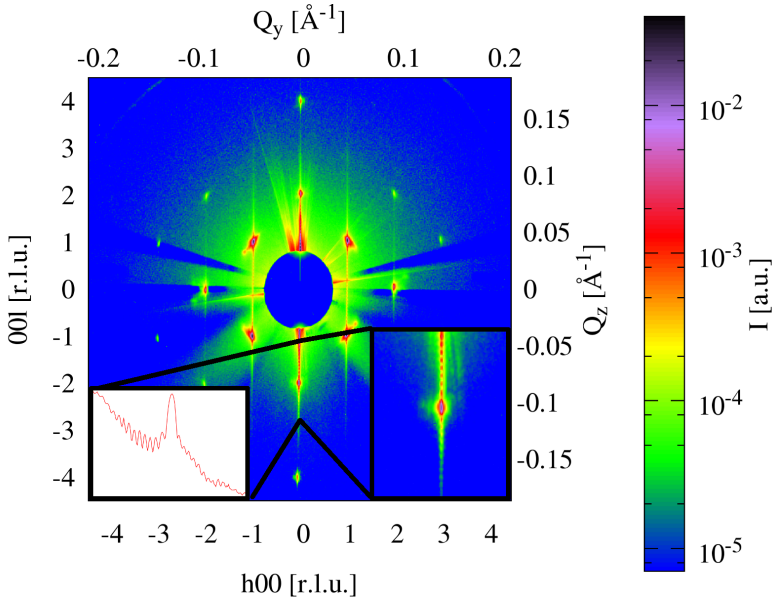

(a) Measurement from M_C^I

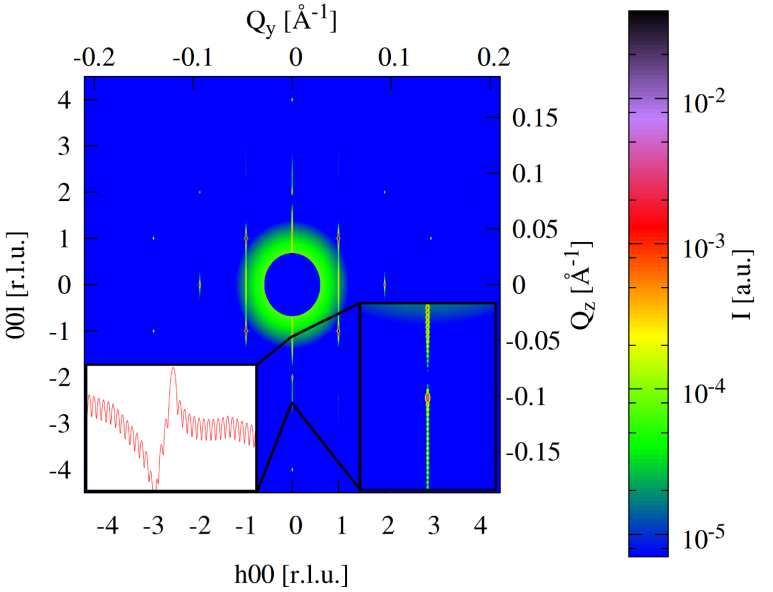

(b) Simulation

Figure 7.9: Measurement of the (h0l) plane of a single mesocrystal with cubic particles. The zoom around the $(00\bar{2})$ reflection shows nice Laue oscillations, which could be reproduced with a simulation. The left inset shows a vertical line scan through the reflection.

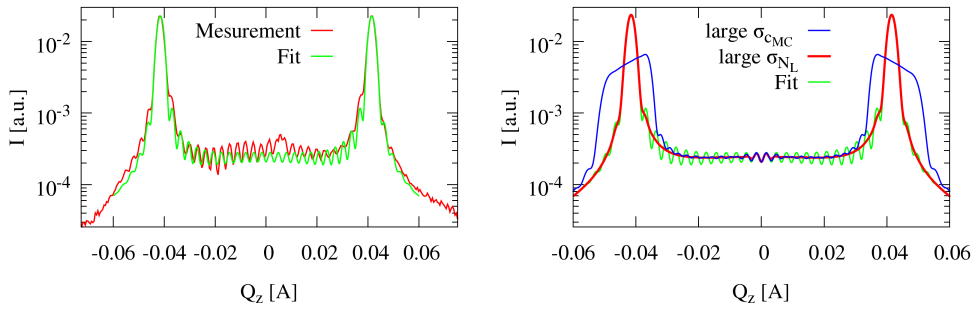

(a) Comparison of measurement and fit

(b) Influence of parameter variation on the fit function

Figure 7.10: Cross-section through the reflexes (101) and (10$\bar{1}$) in Q_z direction from **figure 7.9a**. The Laue oscillations are fitted with a Laue function in combination with a form factor, a particle size and lattice constant distribution and an incoherent background. The influence of a larger lattice constant distribution ($\sigma_{c_{MC}}$) and height distribution (σ_{N_L}) is shown in **figure 7.10b**

asymmetry of the oscillation amplitude around the peaks can be induced by a distribution of lattices constants, which is observed in the reflectometry dataset from an ensemble of mesocrystals as well (see **section 5.3.3**). The derived lattice constant in out-of-plane direction of c_{MC} =15.11 matches the result from **table 7.2** perfectly. The lattice constant distribution is with $\sigma_{c_{MC}}$=0.85% smaller than the in-situ GISAXS determined value from an ensemble of mesocrystals in an unfinished drying state of 1.5% . For the in-situ GISAXS case it is assumed that the value will increase with longer drying time, so that the single mesocrystal lattice constant deviation found here is much smaller than for the ensemble average. This indicates a variation of lattice constants from mesocrystal to mesocrystal as has been proposed in earlier chapters. The influence of a higher distribution of $\sigma_{c_{MC}}$=5.8% (particle size distribution[1]) is shown in **figure 7.10b**, where the peak shape gets broader and the oscillations smearing out to higher Q. Such an asymmetrical broadening of the peak shape could be observed in reflectometry from an ensemble of mesocrystals where a lattice constant between different mesocrystals is expected (**section 5.3.3**). The number of repetitions of the unit cell is $N_L = 13$, which result to a mesocrystal height of 196 nm. This value matches the result measured by the SEM (**table 7.1**) proving a fully coherent structure through out the whole mesocrystal. The distribution of the number of repetitions, which correspond to the height, is with σ_{N_L}=0.3 very small and confirms the observed flat mesocrystal from SEM (**figure 7.2d**). The influence of a higher height distribution is shown in **figure 7.10b** as red curve. A σ_{N_L}=3 suppresses nearly all oscillations, due to the different heights which are averaged. This is observed in an ensemble of mesocrystals, where the crystals have different heights and no oscillations between the GISAXS peaks are visible. The visible Laue oscillations makes this measurement unique, because normal crystals are too large to resolve such oscillations. In this experiment a perfect single crystal with a height in the 100 nm-range and 10 nm structure size is investigated, which allows the study of this peak shape. The results of the fit of the Laue oscillations are summarized in **table 7.3**.

[1] The particle size distribution in the precursor solution is the order of magnitude for the lattice constant distribution expected when a mesocrystal would be formed by a random selection of particles.

sample ID	c_{MC} [nm]	$\sigma_{c_{MC}}$ [%]	N_L [c_{MC}]	σ_{N_L} [c_{MC}]
M_C^I :	15.11	0.85	13	0.3

Table 7.3: Result of the Laue oscillation fit from the (101) reflection.

7.3.1.4 Simulation of the scattering pattern

The simulations in **figure 7.9b** for a perfectly ordered cubic system fit very well. A convolution of the cylinder form factor describing the mesocrystal shape with the reciprocal lattice including selection rules multiplied by the spherical form factor, the Lorentz factor and the Debye-Waller factor are considered. Additionally, an incoherent background is added. The resolution of $3.1 \cdot 10^{-4}$ Å^{-1} determined earlier is used in this simulation. The shape and oscillations of the peaks introduced by the mesocrystal shape as a cylinder are in good agreement with the experiment using the height and radius from **table 7.1**. The mesocrystal shape influences mainly the simulated peak shape in Q_z direction, while Q_y is defined by the resolution function due to a µm sized crystal. A lattice constant distribution induced for example by a variation of the particle size, as well as existing mosaic spread are not considered, which explains the remaining difference to the shape, intensity and width of the measured peaks, especially for peaks at lower Q. The measurement method has no influence on the peak shape, only the intensity. A spherical form factor is used in this model due to the prohibitive computing time for the new rounded cubes FF model for $4 \cdot 10^5$ grid points. The problem arising from the FF imperfections is shown in the **inset of figure 7.9b** , where a too deep minimum in comparison to the measurement exists. On the other hand the used FF describes for example the absence of the structure factor allowed ($10\bar{3}$) reflex in the (h0l) plane. The Lorentz-factor (see **section 2.2.4**) used for the modeling tries to mimic the experimental conditions by assuming a constant scan rate in φ (normal Lorentz-factor, Q_y) and taking the maximum for the 5 measuered positions in ω (Q_z direction). For example the (402) reflex which lies on a FF maximum with high intensity, is strongly suppressed by the scanning process. The effect is obvious when comparing a simulation with and without Lorentz correction (see **appendix figure A.14**). For the Debye-Waller factor an average displacement parameter a_{DW} = 0.5 nm is used. This simplified model describes the measured intensities quite well on the full Q-range. The simulation is described in **section 5.3.1** in more detail and the python script and all simulations are attached in appendix **section B.3** and **section A.3.3**.

7.3.2 Crystal structure analysis

7.3.2.1 Rocking scans

To obtain integrated intensities of the reflections necessary for a quantitative structure analysis of a single mesocrystal, rocking scans of peaks of the cubic system for all accessed planes were performed. To achieve a well defined and optimized rocking scan of a reflection, the mesocrystal was aligned using the chi angle to bring the reflections in vertical direction. This way the omega angle could be used to scan the peaks perpendicular to their $\vec{Q}$ direction, thus the ω-scan is equivalent to a scan in $\vec{Q}_x$ direction.

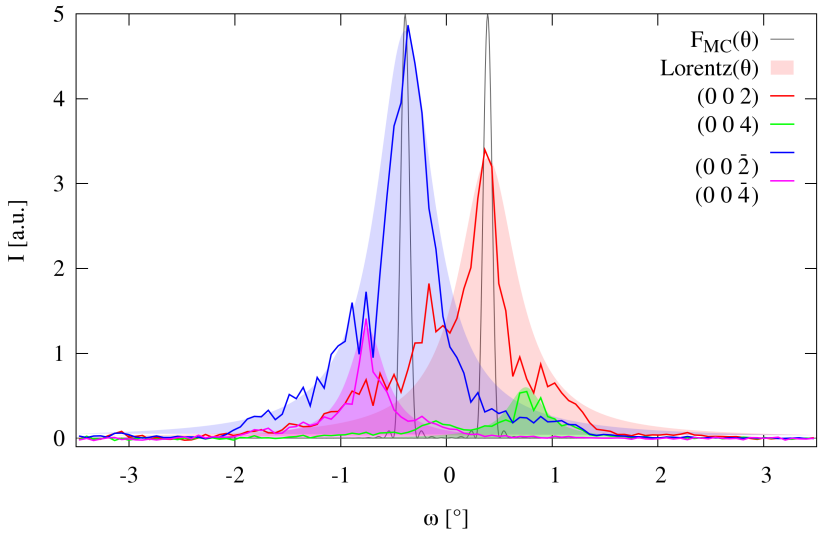

Figure 7.12: Rocking scans for different peaks of the (h0l) plane of M_C^I. The grey line is the form factor of a perfect mesocrystal with defined sizes by SEM and shows the natural line shape. The filled curves shows a Lorentz function with HWHM determined at the Q_y-Q_z plots, presenting the natural line shape of the present mesocrystal with limited correlation length. $F_{MC}(\theta)$ is the perfect mesocrystal form factor.

The integrated intensities are analyzed as follows: For each ω position two areas are chosen around one peak in the 2D-detector image (see **figure 7.11**). The smaller area defines the region, where a integration (sum) over the chosen area are taken and the large area excluding the integration region is used to extract the background by fitting a 2D parabola. The fitted background is then subtracted from the integration area prior to intensity extraction. With this method the integration works stable for all peaks, including those with low intensity. An example of the 2 dimensionally integrated intensity versus the incident angle ω for the (h0l) plane is shown in **figure 7.12**. These measurements are called rocking scans. The zero intensity far from the peak is an indication that the background subtraction works properly.

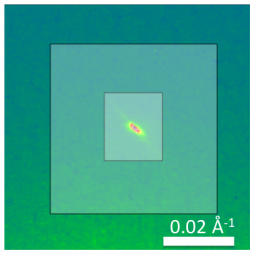

Figure 7.11: Definition of the regions for the integration and a background

The peak shape and width of a rocking scans are defined by the energy and wavelength resolution of the experiment, the size and correlation length of the mesocrystal and the mosaicity. Mocaicity or mosaic spread is a property of macroscopic crystals which describes the average degree of tilting of lattice planes of structurally coherent regions against each other. Atomic crystals normally contain imperfections producing mosaic domains inside the structure which are misaligned against each other. To extract the mosaicity parameter from the measurement the half-width at half-maximum (HWHM) of the peaks have to be determined. Due to the asymmetric shape the HWHM can not be fitted and is calculated with the root mean square deviation

plane	peak index	standard deviation [°]
(h0l) :	(002)	0.54632
	(00$\bar{2}$)	0.567285
	(004)	0.392597
	(00$\bar{4}$)	0.284569
	(10$\bar{1}$)	0.880231
	($\bar{1}$01)	0.998652
(hhl) :	(11$\bar{2}$)	0.949898
	($\bar{1}\bar{1}$2)	0.959914
	(110)	0.838374
	($\bar{1}\bar{1}$0)	0.869483

Table 7.4: Width of the rocking scan peaks measured on M_C^I determined by numeric calculation of the standard deviation.

(standard deviation SD). With this method the peak shape is not of importance. The results are shown in **table 7.4**. The good energy resolution of $\delta E/E = 0.5 * 10^{-4}$ and the small divergence of the beam of 400 µrad in the present experiment is negligible.

At first we confine the analysis to the (00l) reflexes, which were measured in the (h0l) plane. For the same χ and φ position for one plane, the width of the plotted (00l) reflections of one ω-scans should be constant by pure mosaic spread. The discrepancy of the (002) and (004) parameters indicate an other influence on the peak width beside pure mosaic spread. The natural width given by the finite size of the mesocrystal can affect the rocking curve as it provides a finit peak width, which is constant in Q-space for all peaks. As has been described above, every ω-scan is a transverse Q-scan perpendicular to the vertical and horizontal direction (for example for the (h0l) plane a scan in [0k0] direction). A finite broadening in [0k0] direction (e.g. Lorentz-function) yields a broadening of the ω-scan. A Q_x (ω, $Q_{\parallel\vec{\omega}}$, $Q_{\perp\vec{\omega}}$) scan is different for reflexes at different $\vec{Q}$ positions in the angle coordinate representation. In the case of small angles ($\widehat{=}$ a flat Ewald-sphere), the contribution of the natural line shape to the width of the rocking curve is antiproportional to the value of $Q_{\perp\vec{\omega}}$ ($\Delta\omega \propto \frac{\Delta Q}{Q_{\perp\vec{\omega}}}$). For the same step size in ω, the increments in Q are larger for peaks with higher Q value and consequently the width of the peaks in the ω scan are smaller for higher Q values. Exactly this behavior is observed, the width of (002) is broader than for (004) reflexes (see **figure 7.12**, **table 7.4**). A transformation of the rocking scans from angle coordinates to Q space shows that the width of the peaks have the same order of magnitude for different reflexes (see **appendix figure A.16**), which is expected for the natural line shape contribution. Small differences show an influence of the mosaic spread and probably experimental imperfections not accounted for. An influence of the relatively large ω step size has to be considered for reflexes with l>3, for example (004) reflexes, and could explain the different peak shapes. It can be concluded that the shape and width of the rocking curves are mainly governed by the natural line shape of the mesocrystal The influence of the mosaic spread is small. Additional structure next to the main peak suggests the presence of only a few big crystallites inside one mesocrystal. Plenty of small fragments would lead to a more Gaussian like peak shape and would have a smaller correlation length.

To indicate the influence of the natural line shape, the optimal mesocrystal form factor $F_{MC}(\theta)$ (see 5.6) is plotted in **figure 7.12**. The natural line shape is given by the perfect cylinder FF with size parameters extracted from SEM **table 7.1**. It is obvious that the natural line shape of a perfect mesocrystal is much smaller than the measured curve. Plotting a Lorentz function with the HWHM determined for Q$\parallel \vec{a}^*$ at the Q_y-Q_z plots (see **table 7.2**) shows that the determined

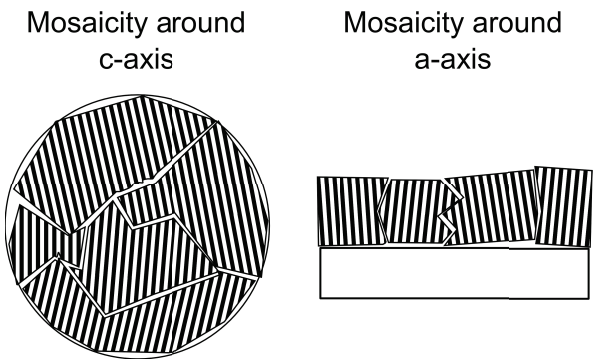

Figure 7.13: Sketch of different mosacity components. The rotation vector is in the viewing direction.

width from the other measurement geometry corresponds to the width of the rocking curve **figure 7.12**. This comparison confirms the statement that the natural line shape is the main determining factor. The deviation between theoretical line width of a perfect crystal and the measured curve of the present mesocrystal shows the existence of a limited in-plane correlation length, which is much smaller than the diameter of the mesocrystal. Discontinuities are present in the in-plane direction that limit the correlation of the mesocrystal structure.

The mosaic spread around the a-axis without the natural line shape can be calculated with the (00l) reflections for one crystal orientation. The influence of the natural width doubles from |l|=2 to |l|=4 reflexes and thus the difference between the mean square of (002) and (004) give the natural line shape part of 0.22 ° for the (004) reflex in $\vec{b}^*$ direction. The difference between the (004) and the calculated line shape value yields a mosaic spread of 0.12 ° in this direction, which rotates around the a-axis (horizontal axis) (see **figure 7.13**).

The c-axis mosaic spread can be estimated from the average value of the $(10\bar{1})$ and $(\bar{1}01)$ reflexes. Using the above approach, the natural line shape of the $(10\bar{1})$ is 0.58 ° calculated from the value of the (004) reflex. The mosaicity including an a- and c-axis component is 0.36 °, which leads to an estimated c-axis mosaic spread of 0.52 °. The other analyzed reflexes with an in-plane component (for example $(11\bar{2})$) show higher values for the HWHM, which is an additional indication for a higher mosaic spread around the c-axis (see **figure 7.13**). That means that the average tilting of the crystallites around the vertical axis is higher than around the horizontal one. This result makes sense in consideration of the self-assembly process. The substrate provides a preferred direction for the ordering of the cubic particles, so it is more energetic favorable to order the planes parallel to the substrate. An a-axis mosaic spread of 0.1 ° represents a tilting of crystallites to the substrate surface that corresponds to 1.7 nm distance to the substrate at one side of a 1 µm domain, which corresponds to the measured correlation length (see **table 7.2**). This distance matches the thickness of the organic shell (see **section 4.1.2**), which is reasonable, because the organic shell is soft and movable, while a higher tilting would not be energetically favorable due to the large gap.

In contrast, a higher mosaicity around the c-axis is not prohibited by the the self-assembly process. An in-plane tilting of crystallites against each other has no influence on the attachment to the substrate surface and needs less energy to be produced. Gaps, cracks and missing layers can produce such mosaics as shown in **figure 7.14a** obtained from an other mesocrystal. A shift

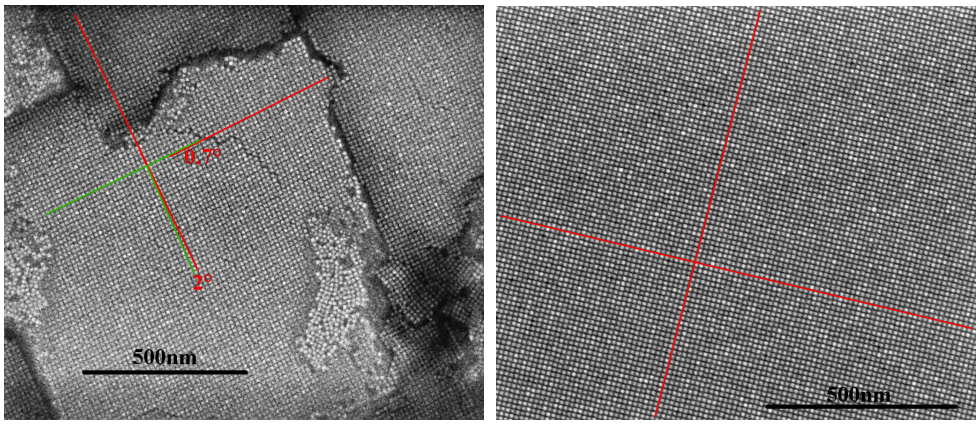

(a) Example for visible c-axis mosaicity **(b)** Investigated sample M_C^I

Figure 7.14: SEM pictures from top of mesocrystals of equivalent samples.

of 2 ° between two crystallites is visible, probably produced by the drying process. Crystallites inside one crystal can result from discontinuities like in an atomic crystal. In the case of a self-assembled nanoparticle superstructure the drying process as an additional factor is relevant for the formation of bent lattice planes and cracks leading to crystallites separation, which both produce mosaicity. In contrast to the tilting due to cracks as seen in **figure 7.14a** the weaker bending effects of nanoparticle rows inside one crystallite without a crack are not visible on this small length scale. The higher flexibility in the mesocrystal structure differs strongly from atomic crystals, where every crystallite has a rigid lattice. Due to soft bondings between the nanoparticles, lattice planes can be sheared or bent against each other caused by the stress during the drying process or other pressure effects. For a crystals composed of nanoparticles it is energetic favorable to build the special superstructure, but the energy cost for deformation is relatively low.

A comparison with a SEM picture taken before extraction from the top of the investigated single mesocrystal showed no measurable shears or crystallites inside the mapped area. **Figure 7.14b** illustrates this with the aid of red lines. The determined mosaic spread around the c-axis of 0.52 ° should be hardly measurable with SEM as it would be in the order of a pixel over the full length of the red lines. A shearing effect over a long range or a few crystallites with very low tilting against each other can lead to the measured c-axis mosaic spread. The quantitative results of the rocking scan analysis are summarized in **table 7.5** and overall the investigated mesocrystal shows an excellent structural coherence considering all possible influences described above. The existence of mosaicity cannot be established by GISAXS because an average over an ensemble of mesocrystals, rotated against each other, is present.

sample ID	a-axis mosaicity [°]	c-axis mosaicity [°]	natural line shape of (004) [°]	natural line shape of $(10\bar{1})$ [°]
M_C^I :	0.12	0.52	0.22	0.58

Table 7.5: Result of the rocking scan analysis for mosaicity. The a-axis component is determined from the (00l) reflexes and the c-axis component from the $(10\bar{1})$ reflexes, both from the (h0l) plane.

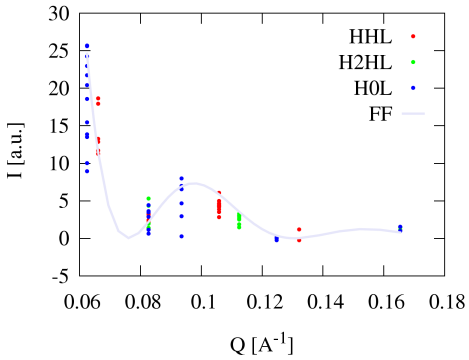

(a) Integrated intensities for different points in reciprocal space to show the high scattering of the intensities. The grey line is a spherical form factor with the values determined by SAXS.

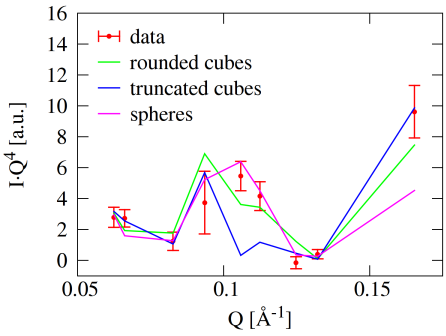

(b) Comparison of different FF models (solid lines) with the averaged integrated intensities (data points).

Figure 7.15: Integrated intensities of M_C^I.

7.3.2.2 Integrated intensities

For the previous analysis of the rocking scans (2 dimensionally integrated intensities) only vertical reflections were considered[2]. Due to the low statistics, other peaks from the same measurement are used for the integrated intensity analysis in addition. In this case $2\theta_h$ is not equal to zero ($2\theta_h$ is the scattering angle component perpendicular to $\vec{\omega}$). As an example, for $\chi = 0$ $2\theta_v$ corresponds to the Q_z direction and $2\theta_h$ to the Q_y direction. For the integration of the rocking curves the trapezoidal rule is applied. Simple summation as well as Simpson's rule integration have been tried as well, but did not yield much different results. A Lorentz factor (see **section 2.2.4**) correction is made in dependence on $2\theta_v$. Through this approach several redundant intensity values are collected for the same reflection. The integrated intensities versus $|\vec{Q}|$ for different reciprocal lattice planes are shown in **figure 7.15a** and in **table A.3**-**table A.11**, where a large variation of intensities is observed for every equivalent peak. This points out the challenge of measuring a µm-size crystal with a µ-focus beam. Due to the limited positional accuracy the translation motors needed to be realigned for each χ orientation[3]. This alignment, however, will never result in exactly the same photon density because of beam inhomogeneities in horizontal direction, which were measured in a translation scan (**appendix figure A.17**). To make a comparison with a possible model the average of the intensities of all equivalent peaks is used. For each set of symmetry equivalent reflections, the error is calculated as the standard deviation of all measured points.

The extracted structure factors allow a direct comparison with a model based on the $I4/mmm$ structure discussed in **section 7.3.1**. The body centered tetragonal (bct) structure with only one particle in its basis (2 per unit cell at (0,0,0) and $(\frac{1}{2},\frac{1}{2},\frac{1}{2})$) leads to no intensity variation (except for the selection rules) from the unit cell part of the structure factor, thus the peak

[2] Vertical means that the scattering plane normal is parallel to $\vec{\omega}$ and therefore the scattering angle 2θ has only a vertical component (called $2\theta_v$)

[3] The changes in χ can be as big as 180 °.

model	I_0	$a_{NP}/2r$ [nm]	$\sigma_{a_{NP}/r_{NP}}$ [%]	τ	$a_{DW_{MC}}$ [Å]	χ^2
rounded cubes:	$(13 \pm 2.3) \cdot 10^{-9}$	10.8 ± 1.4	0.45 ± 5	0.85	$0.001 \pm$ NaN	24.43
truncated cubes:	$(9.3 \pm 1.6) \cdot 10^{-10}$	8.6 ± 0.4	0.65 ± 52	0.6	7.44 ± 4.12	44.62
spheres:	$(28 \pm 3.9) \cdot 10^{-9}$	12.0 ± 0.1	0 ± 2	1	$0 \pm$ NaN	16.63
SAXS(rounded cubes):	$(430 \pm 2.8) \cdot 10^{-11}$	10.8 ± 0.02	5.9 ± 0.5	0.775	/	138.4
SAXS(spheres):	$(920 \pm 5) \cdot 10^{-11}$	12.22 ± 0.02	7.4 ± 0.3	1	/	299

Table 7.6: Fit parameters of the models shown in **figure 7.15b**. The parameters without error have not been fitted, errors with NaN denote numerical problems in the error calculation.

intensity must be described by the directional dependent form factor and possibly a Debye-Waller contribution.

Consequently the discussion in **section 4.1.2** needs to be resumed as the rounded cubes and the spherical form factor, indistinguishable in the directionally averaged SAXS measurements, lead to notably different structure factors in the ordered case. It is expected that the particles are aligned with respect to the mesocrystal lattice so the directional average is not the correct description any more. Therefore a spherical form factor (**equation 5.3**) is compared to the analytical directional truncated cubes form factor (**equation 5.4**) and the numerical directional rounded cubes form factor (**equation 5.5**). The truncated cubes FF with edge length a_{NP} and degree of truncation τ_{Trunc} describes a flat truncation and makes a cubeoctahedron for the highest degree of truncation. The rounded cubes FF on the other hand with edge length a_{NP} and degree of truncation τ_{Round} describes a spherical truncation and produces a perfect sphere for the highest degree of truncation. The real space representation of the two kinds of cubic form factors in real space and different degree of truncation are shown in **figure 5.1**. A distribution of the particle size and an isotropic Debye-Waller factor term which involves the information about the average displacement of the lattice position is included in all fit models. The python script is attached in **section B.1**.

The best fit result of all form factor fit functions including size distribution and Debye-Waller factor are shown in **figure 7.15b**, **table 7.6** and **table A.12**. Fitting parameters have been the edge length $a_{NP_{MC}}$, the Debye-Waller factor average displacement $a_{DW_{MC}}$ and the particle size distribution $\sigma_{a_{NP_{MC}}}$ (log normal - integral over different FF of different sizes). $\tau_{Trunc_{MC}}$ or $\tau_{Round_{MC}}$ were fixed for one fit but have been varied manually. For a better comparison, the intensity scale is plotted in $I \cdot \vec{Q}^4$. The rounded cube model describes nearly every measured point well for every direction within the error bars, while the truncated cube model shows strong discrepancies for some points. The spherical form factor describe the data well at low Q, but shows expected discrepancies at higher Q, as small changes in the shape mostly manifest themselves at higher Q values. Within the limit of the error bars, the rounded cube model describes the data best. Although the χ^2/R_1 value for the spherical form factor is slightly lower than for the rounded cubes case, the latter can still be considered the best suited FF as it better describes the SAXS data (**figure 4.2**) and still incorporates the cubic facets visible in e.g. TEM images. The flat truncated model does neither fit the single MC diffraction, nor the SAXS data very well.

To clarify the difference between theses models and the point where the model does not fit well, complete FF's in different crystallographic directions were calculated using the resulting fit parameters. This is done for the spherical, truncated and rounded cubes model. A selection of the results can be seen at **figure 7.16**, all pictures for different τ can be found in **appendix**

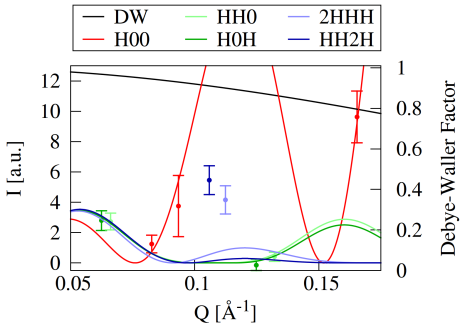

(a) Truncated cubes model with $\tau_{\mathrm{Trunc_{MC}}} = 0$
$a_{\mathrm{NP_{MC}}} = 8.27 \pm 0.0\%$, $a_{\mathrm{DW_{MC}}} = 0.50\,\mathrm{nm}$

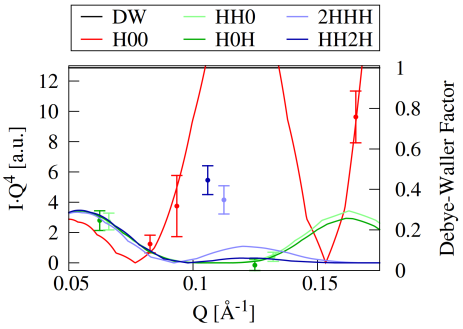

(b) Rounded cubes model with $\tau_{\mathrm{Round_{MC}}} = 0$
$a_{\mathrm{NP_{MC}}} = 8.20 \pm 0.0\%$, $a_{\mathrm{DW_{MC}}} = 0.007\,\mathrm{nm}$

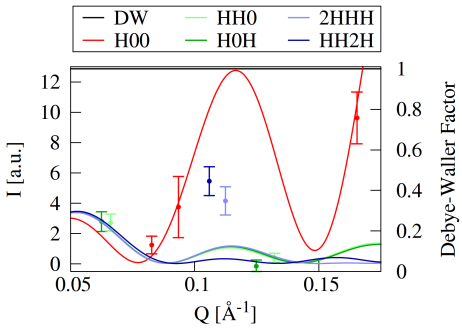

(c) Truncated cubes model with $\tau_{\mathrm{Trunc_{MC}}} = 0.8$
$a_{\mathrm{NP_{MC}}} = 8.69 \pm 3.8\%$, $a_{\mathrm{DW_{MC}}} = 0.00\,\mathrm{nm}$

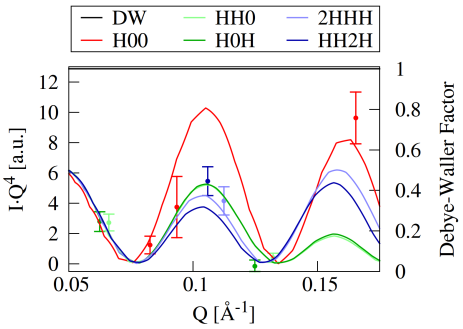

(d) Rounded cubes model with $\tau_{\mathrm{Round_{MC}}} = 0.85$
$a_{\mathrm{NP_{MC}}} = 10.78 \pm 0.4\%$, $a_{\mathrm{DW_{MC}}} = 0.00\,\mathrm{nm}$

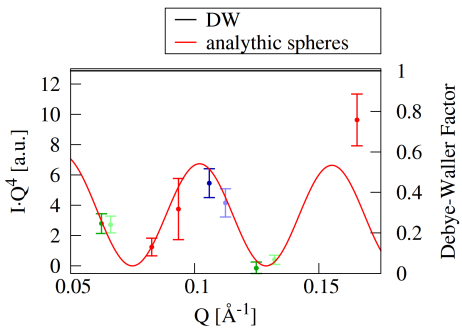

(e) Analytical spherical FF

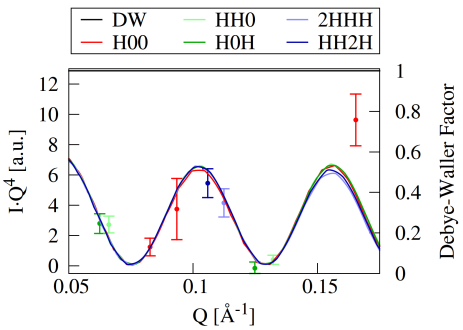

(f) Rounded cubes model with $\tau_{\mathrm{Round_{MC}}} = 1$
$a_{\mathrm{NP_{MC}}} = 12.01 \pm 0.0\%$, $a_{\mathrm{DW_{MC}}} = 0.00\,\mathrm{nm}$

Figure 7.16: Results of fits from the truncated cube and the rounded cube model. **Figure 7.16a and 7.16b** fitted for a perfect cube and **figure 7.16e and 7.16f** for a perfect spherical particle shows the correctness of the new rounded cube model. The best parameters for the respective models are shown in **figure 7.16c and 7.16d**.

A.18 and A.19. For a better comparison the intensity scale is plotted in $I \cdot \vec{Q}^4$. The scale of the Debye-Waller factor term, which is included in the fit, is plotted linearly on the right y-axis. Different colors present various Q-directions.

Figure 7.16c and 7.16d show the results for different τ's for both direction-dependent FF's. It is obvious that the model with the rounded cubes describes the data well for every direction within the error bars, while the truncated cubes model could not describe the scattering in the direction of the edges. The results from figure **figure 7.16** make it obvious, that it is important to use a direction dependent form factor to correctly describe the peak intensities for the 3D nanoparticle assemblies. In contrast to the perfectly isotropic scattering potential of spheric particles the cubes have a directional dependence in the form factor, which needs to be considered when the particles have a defined orientation in the mesocrystal unit cell[4]. A GISAXS pattern of an ensemble of mesocrystals contains the information about the direction dependent form factor as well, but the modeling of the intensities needs to be performed using DWBA which is far more complicated and requires additional information (see **section 5.3.4**).

The shape differences between the truncated and rounded cubes in the direction of the edges leads to sizable changes in the scattering for example for the [hh0] and [2hhh] directions. In the rounded case not only the corners get truncated, but the edges as well, creating an additional facet responsible for additional intensity in the diagonal [hh0] directions. The shape of the rounded cube model reproduces the HRTEM pictures well (see **figure 4.3** in **section 4.1.2**), The new fits confirm the results of the SAXS measurement, where the truncated cubes FF does not match the data and shows that the flat facets do not describe the present particles. The SAXS experiment cannot distinguish between shapes with small differences due to the integration over all directions. It is dominated by the most intense scattering of the [h00] direction, which has the smallest difference between all models.

The comparison between the analytical and the numerical form factor model with FFT shows no difference between the fits for a perfect cube ($\tau_{\mathrm{Round_{MC}}} = \tau_{\mathrm{Trunc_{MC}}} = 0$) (**figure 7.16a, 7.16b**). The other extreme case of the rounded cube model is shown in **figure 7.16f**, where a perfect spherical particle is simulated. All directions are similar and follow the analytic sphere (**figure 7.16e**). The new model can reproduce a perfect spherical and cubic system equivalent to the analytic models showing the applicability of the numeric approximation. The snatchy shape of the model is a result of the interpolation used to extract the intensity from the regular grid of the calculation.

The result of the fit with the rounded cube model has an edge length of the cubes $a_{\mathrm{NP_{MC}}}$ of 10.78 nm, a size distribution of 0.4%, a truncation $\tau_{\mathrm{Round_{MC}}}$ of 0.85 and no notable Debye-Waller factor (isotropic, a_{DW} =0 nm). The value of $\tau_{\mathrm{Round_{MC}}}$ confirms the results of the SAXS fit (see **chapter 4** in **table 4.2**). The used nanoparticles are not perfectly cubic but have strongly rounded edges and small flat facets in [100] directions (see **figure 7.17a**). With this experiment we could show that highly truncated nanocubes self-assembled in a body-centered tetragonal (bct) arrangement inside one mesocrystal.

The absence of a Debye-Waller term shows that the changes from the perfect lattice position are immeasurable small, although small differences in the form factor can lead to a similar influence

[4]Which we can assert with large confidence as it is present at the surface measured by SEM and is a prerequisite for self organization in non closed packed structures.

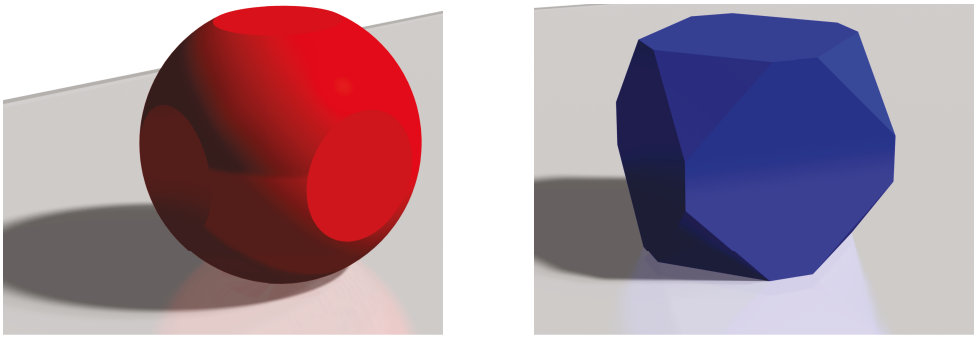

(a) $\tau_{\text{Round}_{\text{MC}}}$ =0.85 **(b)** $\tau_{\text{Trunc}_{\text{MC}}}$ =0.8

Figure 7.17: Real space representation of the rounded and truncated cube model with the best fitting truncation parameters.

on the intensity for higher |Q|, too. In any case, an $a_{\text{DW}_{\text{MC}}}$ parameter of >1 nm would lead to a sizable effect on the intensities.

The edge length of the cubic particles inside one mesocrystal is $\approx 1\%$ smaller than the measured average size in the solution from SAXS, but still within the particle size distribution of $\sigma_{a_{\text{NP}}}$ of 5.8% . The fitted size distribution in one single mesocrystal is with $\sigma_{a_{\text{NP}_{\text{MC}}}}$ =0.4% much smaller than the one of the solution. This is a fascinating outcome, which shows more quantitatively the results discussed in **section 4.2.2** and **section 4.2.4.4** that nanoparticles with similar shape and size favor to order in one mesocrystal. As a consequence each crystal will have an average particle size which differs from the mean value of the whole solution. During the self organization it is energetically much more favorable to grow crystals with very similar particle size to reduce defects like dislocations or stacking faults which reduce the binding energy. This information could not have been obtained by GISAXS on an ensemble of mesocrystals, as it is impossible to disdinguish between parameter distributions of an ensemble and of each mesocrystal.

7.4 Conclusions

This challenging experiment proved the feasibility of the investigation on single, small mesocrystals of nanoparticles to open a new field for further investigations of the mesocrystal properties. With the outstanding intensity and precision of state of the art synchrotron beamlines it is possible to push the already established limits in diffraction from Å-size [39, 57, 78, 79] and nm-size unit cells [62, 97] further to 10 nm large building blocks with samples of only 2.5 μm^3 scattering volume. So far the smallest crystals investigated for the atomic structure are reported with volume in the 10^3 μm^3 range [16, 17, 48]. The achievable data quality is, as expected, not yet comparable to conventional single crystal XRD, as is obvious for the integrated intensities. Nevertheless a lot of new information could be gained complementary to GISAXS on a 2D powder sample.

The space group analysis is consistent with the structure deduced from the ensemble of mesocrystals, $R\bar{3}m$ for spheres and $I4/mmm$ space group for crystals build from cubic nanoparticles. A

quantitative structure analysis of a single mesocrystal with GISAXS was not possible before as the Born approximation does not apply. Furthermore it was not clear if the GISAXS measurement from an ensemble of mesocrystals masks the real structure of a single one as the single crystals are rotated against each other (2D powder). A measurement of the related reciprocal lattice planes is only possible in this experimental configuration without averaging intensities from hundred thousand of probably different mesocrystals and without the need to apply the DWBA to the modeling.

The images from different planes show the high degree of order in these mesocrystals and that 2 out of 3 investigated samples are actually single crystals. The other closed packed mesocrystal shows a twin with reversed structure, as results of stacking faults in the nearly closed packed structure. The correlation length measured at one mesocrystal for the out-of-plane direction is the height of the crystal, while the in-plane value is smaller. This knowledge about the structural correlations of one crystal is not be measurable in the 2D powder. Additionally it is shown that these crystals differ in the lattice constants from the ensemble average, which is attributed to a tendency of similar particles to assemble in one mesocrystal.

All findings about the reflex shape can be fully explained with a Born approximation model of a single crystal with little in-plane mosaic of around 1 μm size. A micro-strain effect (variation of lattice parameters) as well as a small mosacity can be observed. The presence of different lattice constant in different grains of one mesocrystal can be seen nicely in the spherical mesocrystal, where a few distinct peaks are visible. A small lattice constant distribution in out-of-plane direction could be observed in the cubic crystal as a broadening effect and as influence on the Laue oscillations, as well. The rocking curve analysis shows the existence of a few big mosaics inside the mesocrystal and a different mosaicity for different directions. The a-axis mosaic spread of 0.1 ° and the c-axis mosaic spread of 0.5 ° are quite small for this new crystal system and have a comparable quality to atomic crystals. According to P. Jeffrey [109] crystals are considered good with a mosaicity of 0.2 ° or less and bad with a mosaic spread with 1.0 ° or more. The comparison to small crystals, which have been reported to have large mosaic spread of 0.5-1 ° or more [16], shows that the new crystal system has very good mosaicity values especially when one considers the soft bonding between the nanoparticles and the nanoparticle size distribution. The higher average tilting of the crystallites around the vertical compared to the horizontal axis makes sense in consideration of the gravity and van-der-Waals attraction to the silicon pulling towards the substrate during self-assembly. Tilting in the plane does not produce such a problem.

Crystals with nanoparticle building blocks have special properties, which influence the formation of crystallites and their nature. On the one hand crystallites can develop with stacking faults (closed packed structure), cracks or other defects like in atomic crystals, but the weak bond between the particles and the flexible distance due to the organic shell of the nanoparticles can lead to shearing and bending of lattice planes within one crystallite. The crack and stacking fault formation during the growth process could be observed in SEM, as well. The size distributed nanoparticles in contrast to perfectly equal atoms, can order together by size and lead to grains inside one mesocrystal with different lattice constants. A continuous lattice constant distribution in the c-direction can be produced by e.g. curved planes caused by the stress from the cutting process at the edges of the crystal.

The existence of Laue oscillations is another unique observation in this measurement, because normal crystals are too large to resolve oscillations and typically non uniformly shaped. In this

experiment a perfect single crystal with a height of 215 nm is investigated which makes this phenomenon observable. Averaging over a lot of heights from different mesocrystals in the GISAXS experiment destroys these oscillations. The complexity of a system of nanoparticles can be seen in the fit of the Laue oscillations, where the Laue function, a form factor, size- , height - and lattice constant distribution needs to be considered to fully describe the system. In contrast to the GISAXS case where only correlation lengths could be extracted, this fit allows us to deduce the real height of the mesocrystal which perfectly matches the SEM observation. In addition, this allowed us to fit a height and lattice constant distribution, which both are found to be small.

The results of the 2D simulations of the single crystal pattern confirms the developed model (**section 5.1.1**) and the understanding of the described features of the scattering pattern. The cylindrical form factor for the mesocrystal describes the observed Laue oscillations and shape of the peak and the used nanoparticle form factor together with a Lorentz factor explains the pattern well.

The new model of the direction dependent rounded cubes form factor describes the integrated intensity well. From the comparison of the observed intensities with radial symmetric and directional form factors it is clear that the structure factor can only be described with a directional dependence in the cubic case. This implies that the orientation of the nanocubes within the mesocrystal unit cell is aligned to the unit cell axes as excepted from the unit cell symmetry. This is supported by the TEM images in **chapter 4**, too. An analytical spheres FF, as well as the truncated cubes form factor do not describe the structure factor as good. The directional dependence of the FF non parallel to the [H00] directions is strongly dominated by the fine shape differences at the edges, which yields a strong difference between the truncated and rounded model. This sensitivity is lost in the orientational average of a SAXS experiment.

The good agreement of the form factor fit with a size distribution of 0.4% and the fact that the cube edge length a_{NP} is lower than the average value derived from SAXS shows quantitatively that particles with very similar shape and size tend to form one mesocrystal. A shape-selective self-separation process during the self-assembly of the superstructures was already indicated with microscopy analysis by Song et al. [86], but in this work additionally to the relatively coarse SEM analysis we have analyzed this effect more quantitatively and with full bulk sensitivity using scattering. During the crystal growth it is energetically favorable to grow crystal with the same size and shape to reduce defects like dislocations or stacking faults. This new information has not been obtained by GISAXS on an ensemble of mesocrystals, because every mesocrystal has its own small size distribution but the experiment yields an average over a lot of different average sizes from different mesocrystals, which mask the quality of a single one.

All together the single mesocrystal is an almost perfect crystal system with typical crystalline defects. The extraction of a single mesocrystal using focused ion beam techniques and the investigation with a microfocus x-ray beam shows the high stability of these mesocrystals. The investigation of a separated crystal gave a new quantitative insight into some structural parameters not accessible in a sample containing a mesocrystal ensemble.

A first attempt of wide angle-diffraction on a single mesocrystal was tried to search for preferred crystal orientations of the nanoparticles inside one mesocrystal. A subsequent estimation of the expected intensity shows that only $1 * 10^{-3}$ c/s can be expected, which is not feasible. A reduction of the background with for example a completely evacuated fly path could probably enable this type of experiment.

Chapter 8

Conclusion and outlook

In this PhD thesis, a very detailed and profound structural characterization of the 3D assemblies of magnetic nanoparticles is presented. The process of self-assembly and its properties have been analyzed with in-situ and post-deposition characterization. The combined results of these experiments have led to a possible explanation of the self-assembly process; a detailed model is also included.

Well-characterized γ-Fe_2O_3 nanoparticles were used as basic materials [14, 34, 52, 103], which self-assembled on silicon substrates under well-controlled preparation conditions resulting in an ensemble of mesocrystals distributed over the surface. Each mesocrystal is a three-dimensional, highly-ordered periodic arrangement of nanoparticles. It was possible with the combined effort of local microscopy and global diffraction experiments to find the optimal deposition conditions to produce high-quality nanoparticle superstructures. In this thesis, particular attention was given to the characteristics of the ensemble of mesocrystals and their self-assembly as well as of a single mesocrystal, which was investigated by a challenging diffraction experiment.

The microscopy methods applied yield important information, such as the height, shape and surface coverage of the mesocrystals (AFM). They visualize the nanoparticle superstructure, the existing material and larger structures in µm size on the surface (SEM) and inside the crystals (TEM). Additionally, selected area electron diffraction was performed to determine the atomic structure and the preferred crystalline orientation inside a small area of the assembly. For a depth-resolved structural characterization over a large sample area, scattering experiments were carried out. Basic information, such as the knowledge of the morphology of individual nanoparticles was obtained by SAXS and a new form factor model for the cubic particles was applied successfully. The nanoparticle superstructure in the ensemble was primarily investigated by GISAXS in-situ time-dependent or after deposition. These experiments shed light on the averaged structure of the ensemble of mesocrystals in terms of space group, lattice constant distribution, correlation length or crystal tiltings. Complementary to the SEAD experiments, the crystalline orientations in the assemblies averaged over the ensemble were analyzed by diffraction measurements at the x-ray reflectometer and the four circle diffractometer. To get an insight into parameters otherwise masked by the ensemble average, a diffraction experiment was performed on a single separated mesocrystal. In this configuration, a quantitative structure analysis could be made. Although this experiment alone yields interesting results concerning the structural quality and coherence of a single mesocrystal, it was found once again that the combination of different methods allows the development of a detailed structural and growth model.

The structure model describing all results coherently is an ensemble of mesocrystals with an arbitrary in-plane rotation and a preferred c-axis orientation parallel to the substrate's normal (2D powder). A single mesocrystal itself is an approximately cylindrically shaped crystal consisting of particles with extremely narrow size distribution. It is only possible for the particles to make small, local deviations from the perfect lattice position. The coherence of the structure in the best samples is limited only by the mesocrystal boundaries; stacking faults were found in the case of spheric particles. Crystals with nanoparticle building blocks have special properties which influence the formation of crystallites and their nature. On the one hand crystallites can develop with stacking faults (closed packed structure), cracks or other defects as in atomic crystals, but the weak bond between the particles and the flexible distances involved, due to the organic shell of the nanoparticles, can lead to the shearing and bending of lattice planes within one crystallite. A continuous lattice constant distribution in the c-direction can be produced e.g. by stress on the edges of the crystal or gravity pulling towards the substrate.

If we consider the complete ensemble of mesocrystals growing independently, a lot of inhomogeneity of the mesocrystal 2D powder has to be taken into account, which introduces additional complexity to the model and leads to peak broadening, for example, which masks the "true" physical characteristics of the structural order. One of the properties of the ensemble statistic is the out-of-plane rotation (c-axis tilted with respect to the substrate surface normal) of the individual mesocrystal, which could be observed in microscopy images and is connected to the radial smearing of the peaks in the GISAXS patterns. This phenomenon was often found in samples produced with a shorter solvent evaporation time. The quantitative space group analysis, which is only possible in the single mesocrystal configuration, is consistent with the analysis from the GISAXS pattern measured on the ensemble. The space groups determined are $R\bar{3}m$ for spheres and $I4/mmm$ for crystals consisting of cubes. In samples with very good mesocrystal structures, it is even observed that the mesocrystals have facets defined by the unit cell geometry (30/60° angles for the closed packed spheres and 45/90° for the cubic system). Diffraction measurements show that the anisotropic cubic shape aligns the individual particles to the mesocrystal lattice so that a preferred crystal orientation was found, which was absent in the case of spheres. The observed size distribution of the mesocrystals inside the ensemble has an obvious effect on the measured scattering pattern in comparison to the single mesocrystal diffraction patterns. The incoherent average of an ensemble of Gaussian-size distributed mesocrystals in a GISAXS pattern shows distorted peak shapes and blurred peak tails, while for the single mesocrystal, Laue oscillations are clearly visible.

The observations used to develop this structural model indicate a property of the mesocrystal ensemble which helps to understand the self-organization process itself. As single mesocrystals have been found to have a smaller particle size and lattice parameter distribution than free particles in solution and in 2D mesocrystal powder samples, the particles must form mesocrystals in a shape-selective process. This is visible in the GISAXS patterns as the lattice constant distribution between the individual mesocrystals broadens the peaks with respect to a single mesocrystal as they are the sum of several peaks with different positions. Also in the in-situ experiment at the beginning of the nucleation,it is clear that the peaks which grow broader over time are made up of narrow peaks. The size and shape-selective self-separation process during the self-assembly of the superstructures was already indicated in the microscopy analysis by Song et al. [86], but in this current work additional to the relatively coarse SEM analysis, we have analyzed this effect more quantitatively and with full depth resolution using scattering methods. Combining the results from our attempts at structure determination and in-situ obser-

vations during the growth phase, the model of the self-organization process was developed.

In general, evaporation-induced mesocrystal growth can be divided into four stages: vertical droplet reduction, the highly concentrated film, the nucleation and the drying stage, whereby only the third stage was found to be important for the structure formation and is described in the model. Whether the first two stages are relevant for good order, or whether only the nucleation stage itself was of importance, could not be revealed with the experiments performed. Mesocrystal growth occurs in the dense solution when a critical concentration is reached at the substrate-liquid-air interface, verified by the in-situ GISAXS measurement. SAXS measurements at different heights of the droplet during evaporation show neither cluster formation at the droplet surface, nor nucleation in the droplet volume. This result supports a process as described by Siffalovic et.al. [83] for nanoparticle ordering at the three-phase contact line (TPCL). When a critical concentration is reached at the drying front where separated particles, movable via Brownian motion, accumulate on the substrate and reach a sufficiently low distance to get attracted by the van der Walls force between substrate and particles, then cluster formation can occur. The particles assemble size- and shape-selective, as the growth of similar particles minimizes the surface energy. Nucleation areas develop as highly-ordered 2D nanoparticle assemblies on the substrate, which are connected by less ordered particles of different shapes. Three-dimensional mesocrystal growth takes place in these highly ordered regions with matching nanoparticles. The particles start to order in the confined 3D arrangement, due to the finite area of nucleation and a finite diffusion length. This selective growth pattern is the reason for the formation of separate mesocrystals. Nanocrystals which do not find a match continue to move around to find a vacancy in a mesocrystal or sediment on the ground as residual particles. When compared to the atomic thin film growth, a similarity to the Volmer-Weber growth is observable [19], but some new aspects, such as the distribution of the size and shape of nanoparticles must also be considered. For the areas with extremely different particles and hence more disorder, a good template to provide a crystalline growth is missing. At the end of the self-assembly process, an ensemble of separated mesocrystals is generated, covering all the nucleation areas.

In addition, the influence of different deposition parameters on this process has been investigated. As can be expected from the diffusion-dependent size separation, evaporation time was found to be very important for a good structural quality, as the particles need to be able to find suitable vacancies. Although the time particles spend in the free solution seems to have no influence in terms of self-organization, slower evaporation leads to decreased movement of the TPCL, where the ordering is supposed to take place. In addition, the reduced drying rate can lead to a reduction of crack formation and similar effects that reduce the structural quality of mesocrystals after growth has finished. Different magnetic field arrangements can either support or hinder this process depending on the field strength and direction as well as gradient. The best nanoparticle superstructure is obtained for an upwardly-pointing magnetic gradient configuration. No sizable effect of the dipole-dipole interaction between the particles on the formed mesocrystal structure was found unless very extreme conditions were applied (e.g. a field gradient of 70 mT/ cm). In a very strong gradient field a macroscopic polycrystalline particle assembly in the mm-range was formed, following the field lines. Similarly, a strong in-plane field leads to elongated mesocrystals ($\approx$ hundred µm in length) along the field lines. The systematic parameter variation allowed the selection of the best deposition conditions for the given system, which will be of great importance for future experiments.

Although many qualitative statements about structure and self-organization models can be made directly from experimental observations, many differences could only be quantified from the

modeling of scattering intensities. Different approaches to the intensity simulation from the structure model described here have been derived and optimized for the given application. The good agreement between measured and simulated peak shapes supports the confidence in the structure model.

In Summary, many new scientific findings have been gathered from observing the process of self-assembly and the structural properties of the ensemble of mesocrystals and of a separated single mesocrystal consisting of magnetic nanoparticles. New and challenging experiments were performed, allowing novel insights only possible using modern scattering techniques. A first model for the complex structure of the ensemble of the mesocrystal, as well as a model for the self-organization process has been developed.

This knowledge provides several basic requirements for the construction of new and almost perfect model systems for the subsequent investigation of the magnetic correlations inside a nanoparticle superstructure. The new magnetism reflectometer MARIA at MLZ in Garching, capable of measuring GISANS with polarized neutrons, as well as the new small-angle diffractometer D33 at ILL in Grenoble, will lead to new possibilities for the analysis of information on magnetic moments averaged over the entire nanoparticle arrangement and the correlations between adjacent particles, respectively. The first experiments studying the magnetic properties have been performed with scattering methods and will be published separately.

Appendix A

Additional Figures and Tables

In this chapter additional figures and tables are given. The context and descriptions can be found in the corresponding chapters.

A.1 Appendix for chapter 4

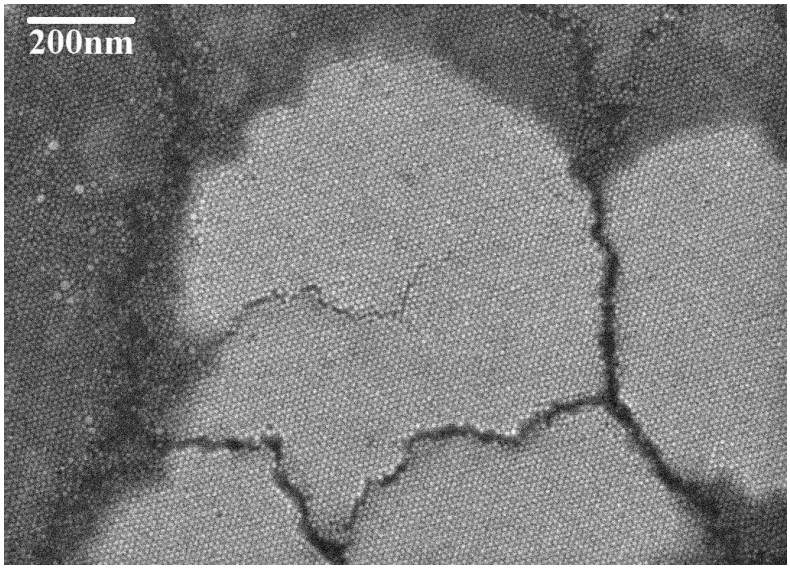

(a) The residual particles on the ground layer

Figure A.1: Illustration of characteristics of the mesocrystal self-assembling.

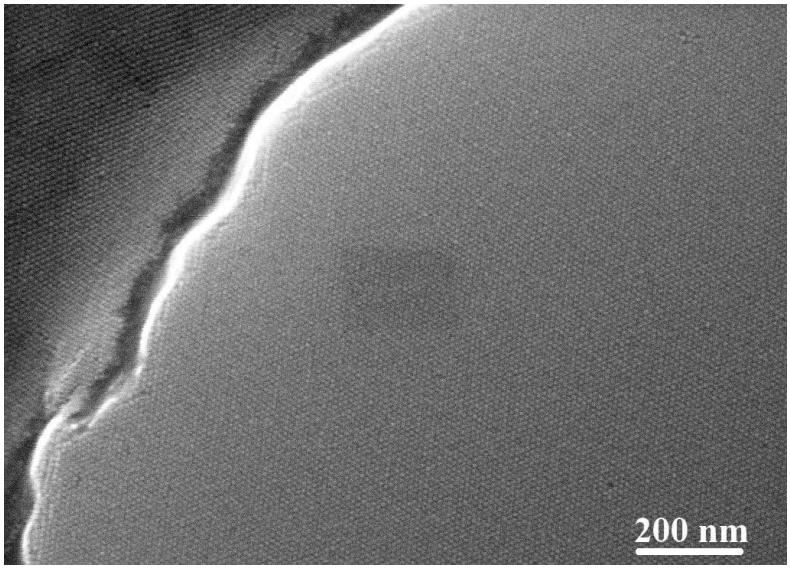

(a) Perpendicular edges of mesocrystals.

Figure A.2: Illustration of characteristics of the mesocrystal self-assembling.

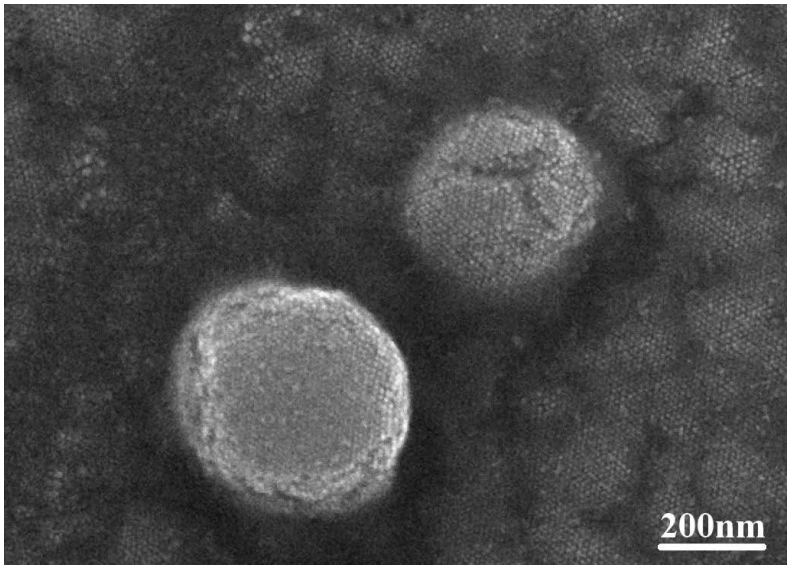

(a) Small mesocrystals and ground layer

Figure A.3: SEM characterization of an ensemble of mesocrystals formed from spherical building blocks self-assembled under a magnetic field of 80 mT and gradient up ($D_{S,\,5.01}^{Lg1.68\perp 80}$).

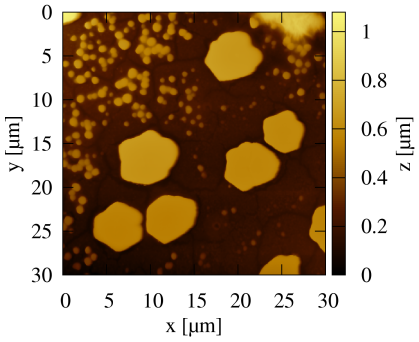

(a) Topography (position 1)

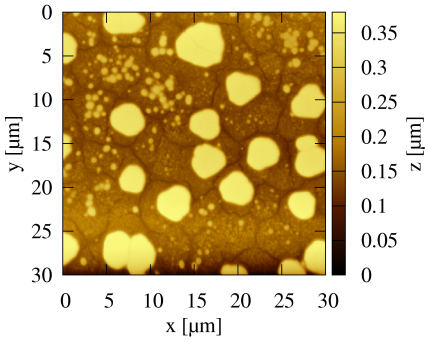

(b) Topography (position 2)

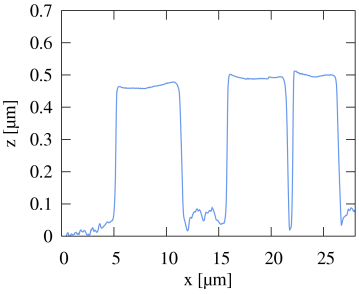

(c) Cross section (position 1)

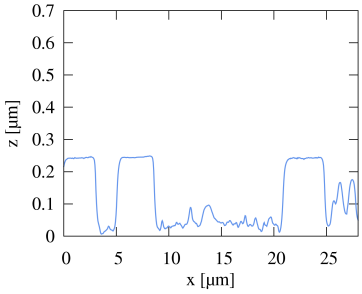

(d) Cross section (position 2)

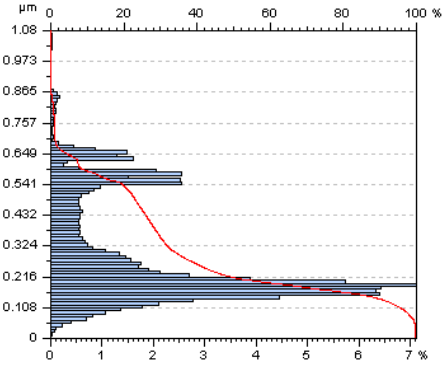

(e) Height distribution (position 1)

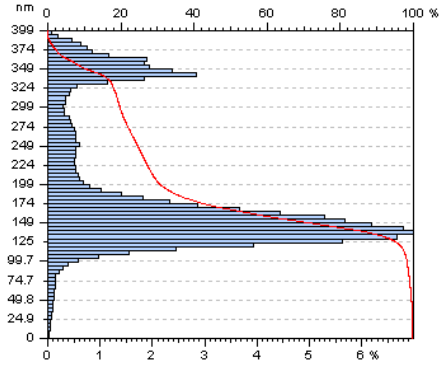

(f) Height distribution (position 2)

Figure A.4: AFM characterization of an ensemble of mesocrystals formed from spherical building blocks self-assembled under a magnetic field of 80 mT and gradient up ($D_{S,\,5.01}^{Lg1.68\perp 80}$).

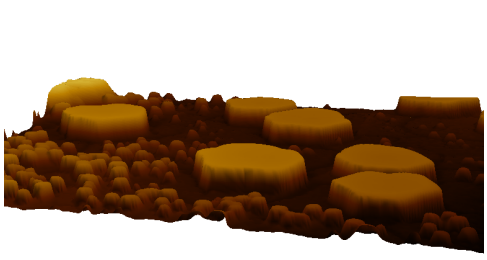

(a) 3D plot - position 1

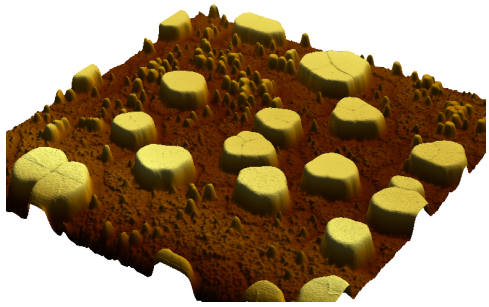

(b) 3D plot - position 2

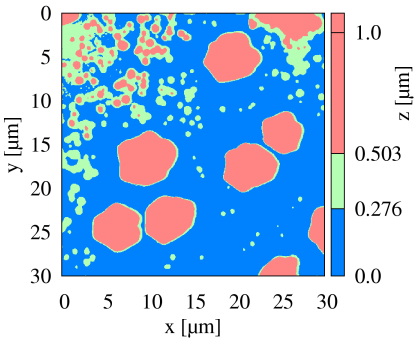

(c) Surface coverage (62.6%, 15.1%, 22.3%) - position 1

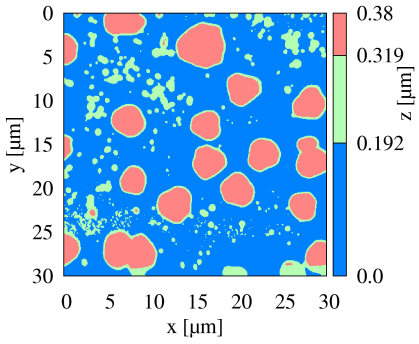

(d) Surface coverage (67.2%, 14.2%, 18.5%) - position 2

Figure A.5: AFM characterization of an ensemble of mesocrystals formed from spherical building blocks self-assembled under a magnetic field of 80 mT and gradient up ($D_{S,\,5.01}^{Lg1.68\perp 80}$).

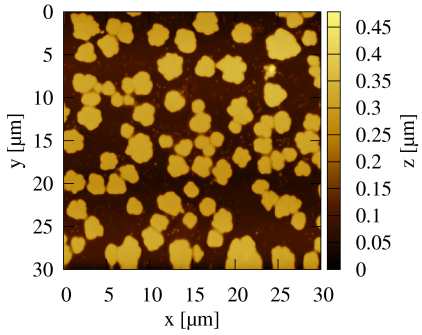

(a) Topography (position 1)

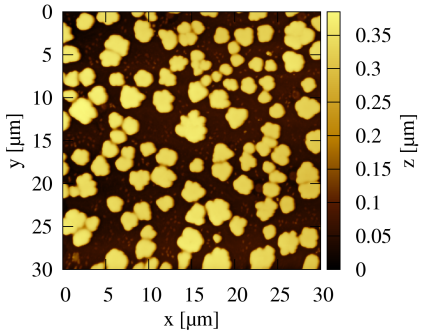

(b) Topography (position 2)

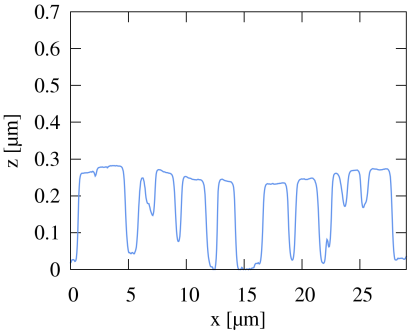

(c) Cross section (position 1)

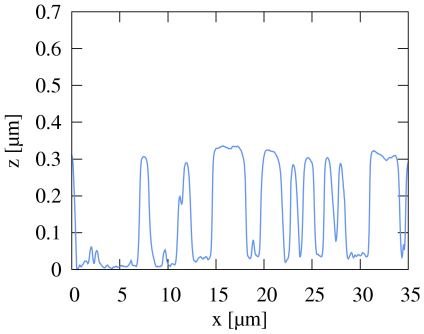

(d) Cross section (position 2)

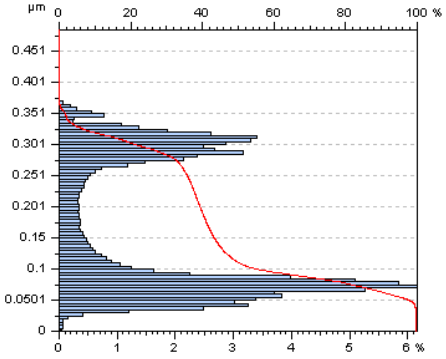

(e) Height distribution (position 1)

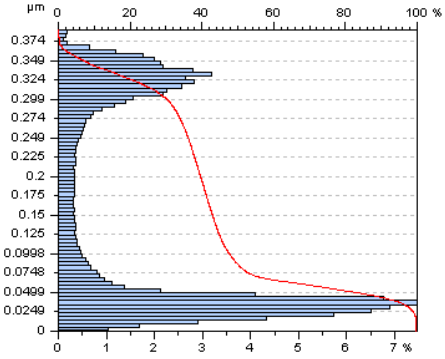

(f) Height distribution (position 2)

Figure A.6: AFM characterization of an ensemble of mesocrystals formed from spherical building blocks self-assembled under a magnetic field of 80 mT and gradient down ($D_{S,\,5.01}^{Lg1.68\underline{Y}80}$).

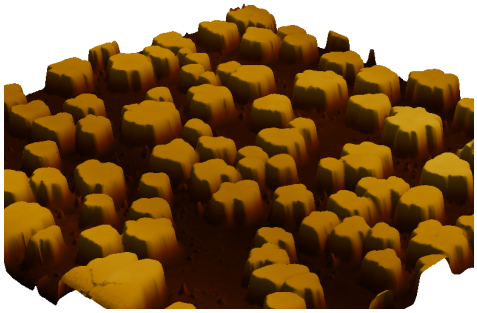

(a) 3D plot - position 1

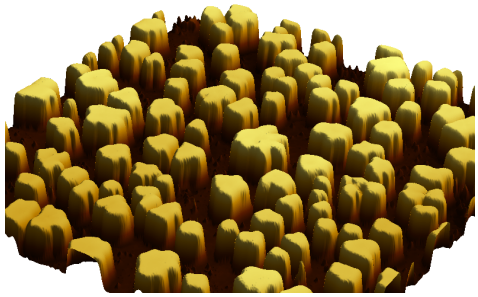

(b) 3D plot - position 2

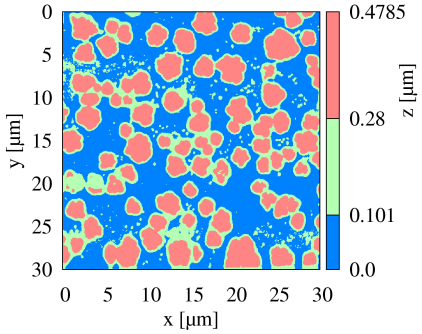

(c) Surface coverage (45.8%, 22.8%, 31.4%) - position 1

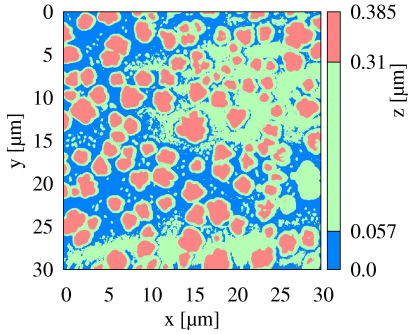

(d) Surface coverage (27.5%, 45.5%, 27.0%) - position 2

Figure A.7: AFM characterization of an ensemble of mesocrystals formed from spherical building blocks self-assembled under a magnetic field of 80 mT and gradient down ($D_{S,\,5.01}^{Lg1.68\curlyvee80}$).

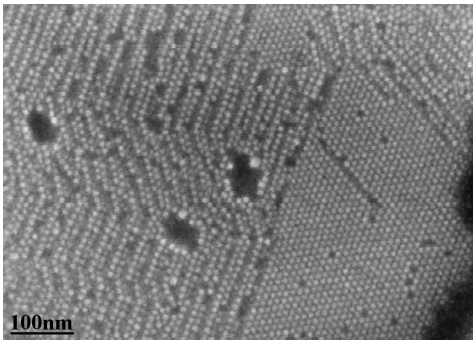

(a) $D_{S,\,5.01}^{Lg1.68\curlyvee 80}$ - top of mesocrystal

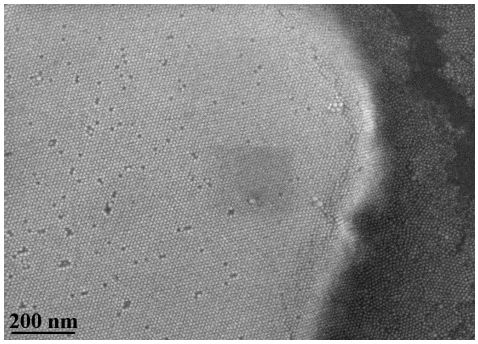

(b) $D_{S,\,5.01}^{Lg1.68\succeq 2}$ - top of mesocrystal

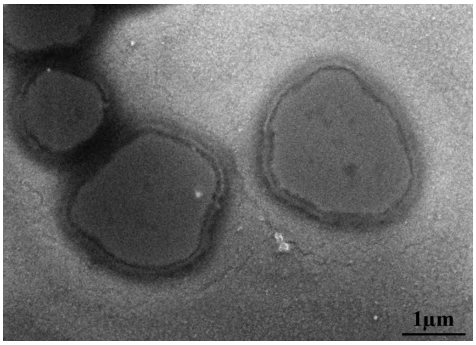

(c) $D_{S,\,5.01}^{Lg1.68\succeq 2}$ - overview

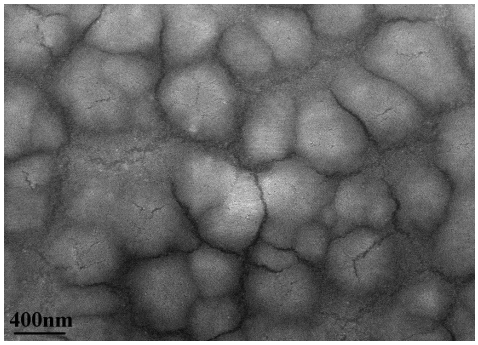

(d) $D_{S,\,5.01}^{Lg1.68\succeq 2}$ - overview

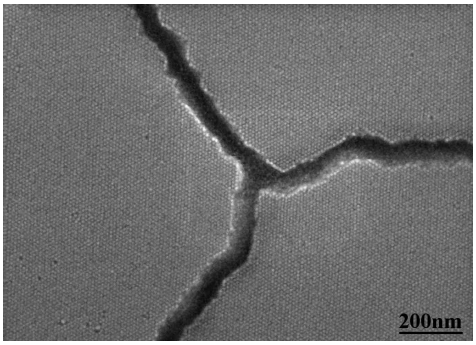

(e) $D_{S,\,5.01}^{Lg1.68X}$ - top of mesocrystal

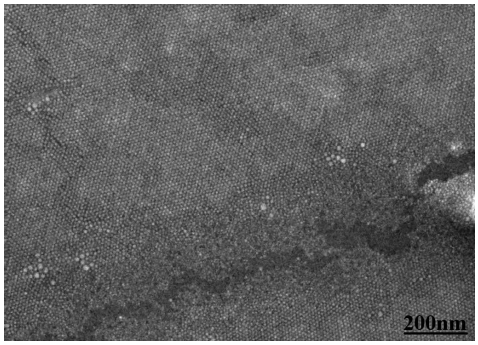

(f) $D_{S,\,5.01}^{Lg1.68X}$ - bottom layer

Figure A.8: SEM characterization of an ensemble of mesocrystals formed from spherical building blocks self-assembled under different field conditions.

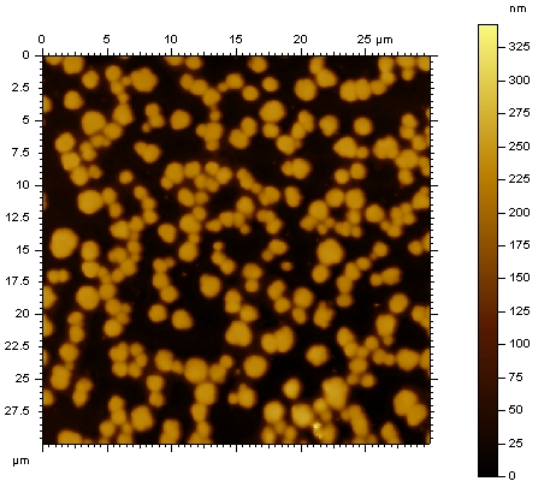

(a) Topography (position 1)

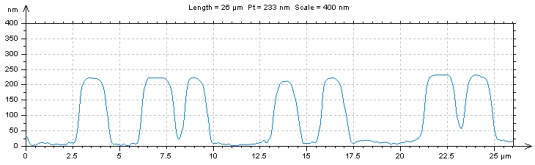

(b) Cross section (position 1)

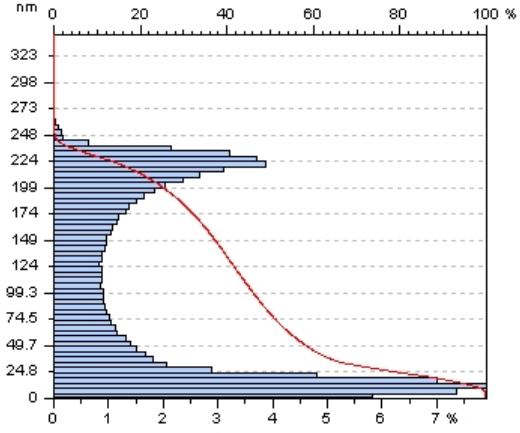

(c) Height distribution (position 1)

Figure A.9: AFM characterization of an ensemble of mesocrystals formed from spherical building blocks self-assembled under a magnetic field of 80 mT and gradient in-plane configuration ($D_{S,\,5.01}^{Lg1.68\geq 2}$).

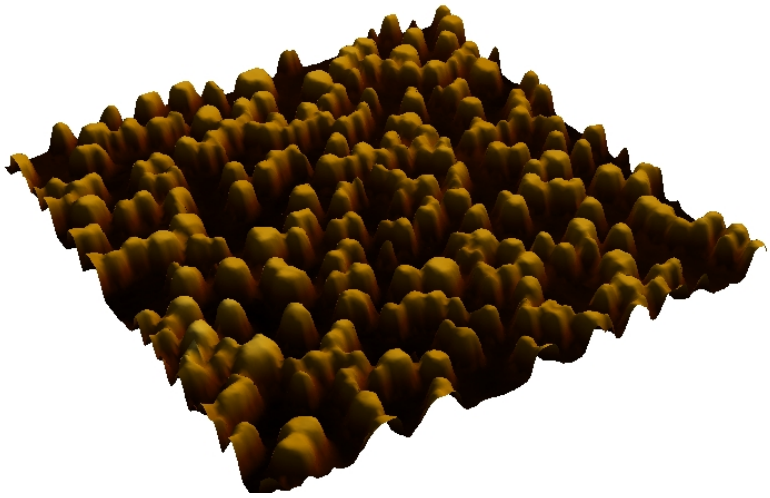

(a) 3D plot - position 1

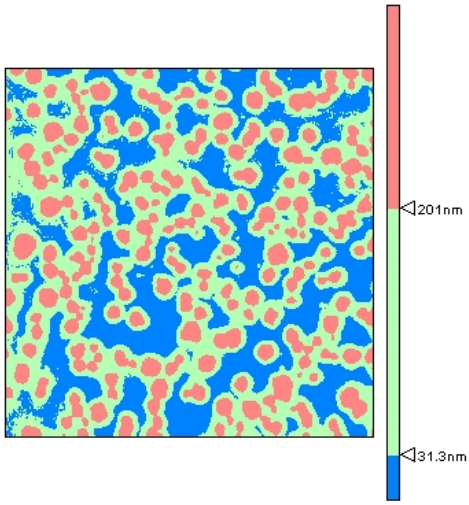

Projected Area (%)	31.2	44.5	24.3
Volume of void (%)	10.9	56.3	96.1
Volume of material (%)	89.1	43.7	3.91
Volume of void (nm.µm2/µm2)	3.4	95.7	136
Volume of material (nm.µm2/µm2)	27.9	74.2	5.53
Mean thickness of void (nm)	3.4	95.7	136
Mean thickness of material (nm)	27.9	74.2	5.53

(b) Surface coverage - position 1

Figure A.10: AFM characterization of an ensemble of mesocrystals formed from spherical building blocks self-assembled under a magnetic field of 80 mT and gradient in-plane configuration ($D_{S,\,5.01}^{Lg1.68\_2}$).

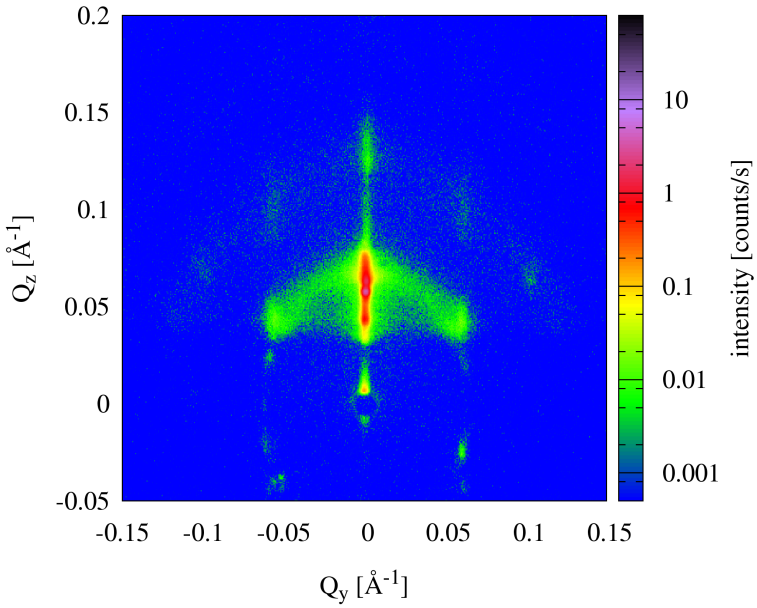

(a) shorter time (lab source/Risø)

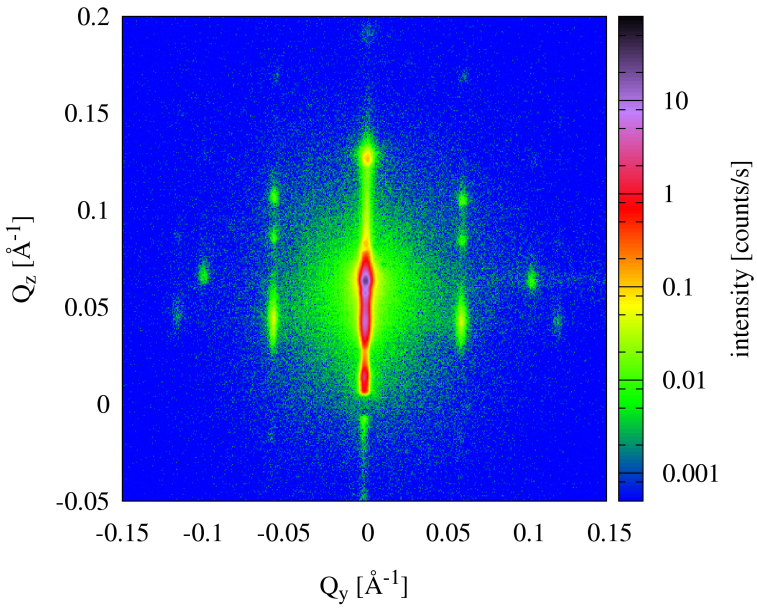

(b) longer time (lab source/Risø)

Figure A.11: Ensemble of mesocrystals formed from spherical building blocks self-assembled with different evaporation times for a gradient in-plane configuration.

A.2 Appendix of chapter 6: Time evolution of mesocrystal growth

parameters	(14:08:10)	(13:53:30)	(13:37:04)
number :	555	451	336
t-t_0 [s] :	1980	1100	114
a* [$Å^{-1}$] :	0.0565911	0.0563474	0.0556516
c* [$Å^{-1}$] :	0.019933	0.0197497	0.0192654
γ_y [$Å^{-1}$] :	8.86745e-05	7.9466e-05	0.000177023
γ_z [$Å^{-1}$] :	0.000294225	0.000583983	0.000755836
σ_{tilt} [°] :	2.47508	1.79049	0.0332648
σ_r [$Å^{-1}$] :	0.0136496	0.0115496	-1.71099e-05
Q_y-off [$Å^{-1}$] :	-0.00187479	-0.00178182	-0.00156154
Q_z-off [$Å^{-1}$] :	0.00692759	0.00693289	0.0072286
Q_{phi}-off [$Å^{-1}$] :	-0.564942	-0.564942	-0.564942
α_c [°] :	2.44498e-05	2.44498e-05	2.44498e-05
background [a.u] :	18.1987	18.8207	41.0732
I_0 [a.u] :	438987	404260	166918
h_0 :	1	1	1
k_0 :	8	8	8
I_1 [a.u] :	430735	479739	398159
h_1 :	1	1	1
k_1 :	4	4	4
I_2 [a.u] :	945243	976736	440244
h_2 :	1	1	1
k_2 :	5	5	5
I_3 [a.u] :	935130	935654	277927
h_3 :	1.73205	1.73205	1.73205
k_3 :	3	3	3
I_4 [a.u] :	372672	403068	144734
h_4 :	2	2	2
k_4 :	4	4	4
I_5 [a.u] :	64784.9	49652.6	75545.7
h_5 :	1.73205	1.73205	1.73205
k_5 :	6	6	6
I_6 [a.u] :	438987	404260	166918
h_6 :	-1	-1	-1
k_6 :	8	8	8
I_7 [a.u] :	430735	479739	398159
h_7 :	-1	-1	-1
k_7 :	4	4	4
I_8 [a.u] :	945243	976736	440244
h_8 :	-1	-1	-1
k_8 :	5	5	5
I_9 [a.u] :	935130	935654	277927
h_9 :	-1.73205	-1.73205	-1.73205
k_9 :	3	3	3
I_{10} [a.u] :	372672	403068	144734
h_{10} :	-2	-2	-2
k_{10} :	4	4	4
I_{11} [a.u] :	64784.9	49652.6	75545.7
h_{11} :	-1.73205	-1.73205	-1.73205
k_{11} :	6	6	6

Table A.1: Example fit parameters of the time-resolved in-situ GISAXS study. The errors are small as they are only numerical results from the fitting algorithm.

A.3 Appendix of chapter 7: Diffraction from a single mesocrystal

A.3.1 Scattering patterns

The scattering patterns on the following pages show additional measurements from different reciprocal lattice planes of the samples investigated.

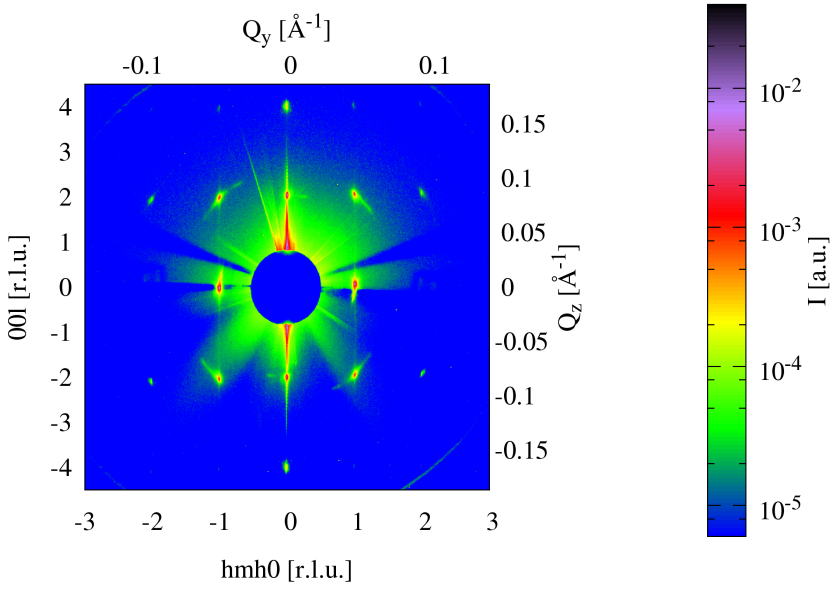

(a) Cubes M_C^I: measurement of the (h-hl) plane

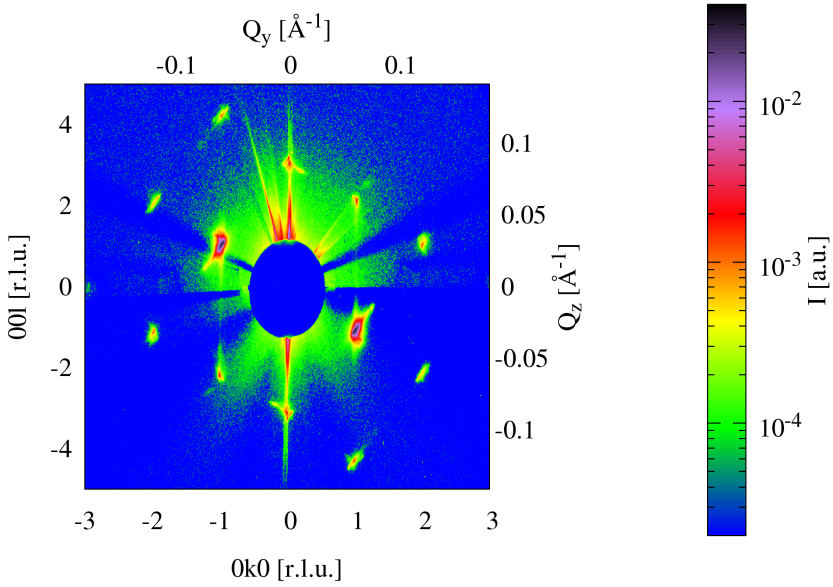

(b) Cubes M_S^I : measurement of the (0kl) plane

Figure A.12: Diffraction pattern from single mesocrystals with cubic or spherical building blocks for different crystalline planes.

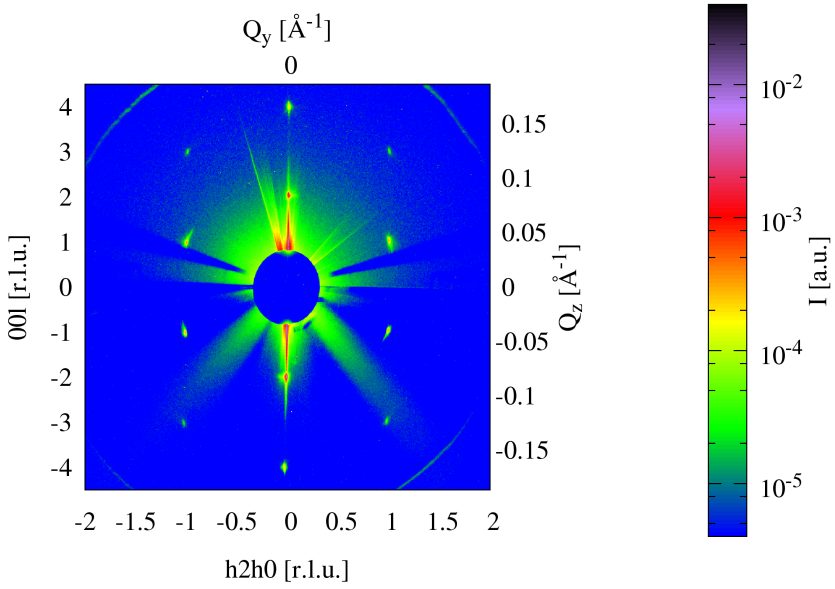

(a) Cubes M_C^I: measurement of the (h2hl) plane

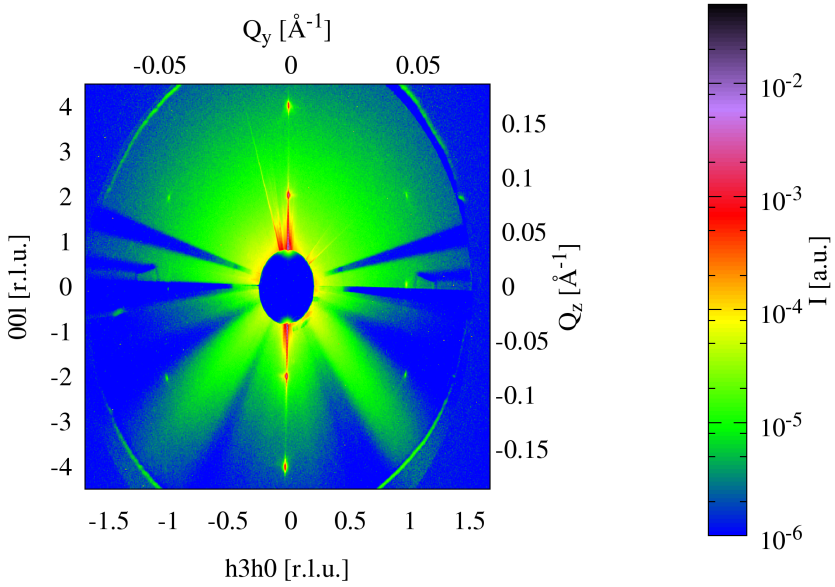

(b) Cubes M_C^I : measurement of the (h3hl) plane

Figure A.13: Diffraction pattern from single mesocrystals with cubic building blocks for different crystalline planes.

A.3.2 Lattice constant and correlation lengths

In the following table the individual values of lattice constants and correlation lengths from different reciprocal lattice planes are listed.

Sample ID	crystal plane	peak index	a_{MC} [nm]	c_{MC} [nm]	$\varepsilon_{y_{MC}}$ [nm]	$\varepsilon_{z_{MC}}$ [nm]
M_C^I :	(h0l)	(002)/(00$\bar{2}$)	/	15.05	1263	332
		(004)/(00$\bar{4}$)	/	15.16	1051	267
		(101)/($\bar{1}$01)	13.46	/	987	384
		(301)/($\bar{3}$01)	13.48	/	843	203
	(hhl)	(002)/(00$\bar{2}$)	/	15.02	1287	371
		(004)/(00$\bar{4}$)	/	15.15	717	203
		(11$\bar{2}$)/($\bar{1}\bar{1}$2)	13.49	/	671	333
		(110)/($\bar{1}\bar{1}$0)	13.47	/	1072	343
	(h2hl)	(002)/(00$\bar{2}$)	/	15.00	1134	402
		(004)/(00$\bar{4}$)	/	15.16	591	237
		(121/($\bar{1}\bar{2}$1)	13.48	/	789	226
		(123)/($\bar{1}\bar{2}$3)	13.53	/	731	324
	(h$\bar{h}$l)	(002)/(00$\bar{2}$)	/	14.98	1279	378
		(004)/(00$\bar{4}$)	/	15.14	683	239
		(1$\bar{1}$2/($\bar{1}$ 21)	13.46	/	645	335
		(1$\bar{1}$0/($\bar{1}$ 10)	13.42	/	1032	365
M_S^I :	(h0l)	(003)/(00$\bar{3}$)	/	22.48	248	179
		(101)/($\bar{1}$0$\bar{1}$)	11.75	19.94	220	126
		(202)/($\bar{2}$0$\bar{2}$)	11.87	20.61	426	208
	(hhl)	(003)/(00$\bar{3}$)	/	22.37	261	222
		(113)/($\bar{1}\bar{1}$3)	11.73	20.57	332	198
		($\bar{1}\bar{1}$3)/(11$\bar{3}$)	11.91|12.11	21.05|20.22	425|434	302|420
	(0kl)	(003)/(00$\bar{3}$)	/	21.77	364	225
		(01$\bar{1}$)/(0$\bar{1}$ 1)	11.74	20.64	201	111
		(012/(0$\bar{1}$ $\bar{2}$)	11.69	20.91	590	234
		(0$\bar{2}$2)/(12$\bar{2}$)	11.85|12.13	21.57|20.36	432|412	315|383

Table A.2: Lattice constants and correlation lengths taken from reflexes of different reciprocal lattice planes of the single mesocrystal measurements. The values are averages of two individual peaks at positions mirrored at the origin to remove any effect from an imperfect determined zero position. Reflexes with two well separated peaks have two values, one for each individual peak.

A.3.3 Simulations

The scattering patterns on the following pages show simulations of the single mesocrystal diffraction.

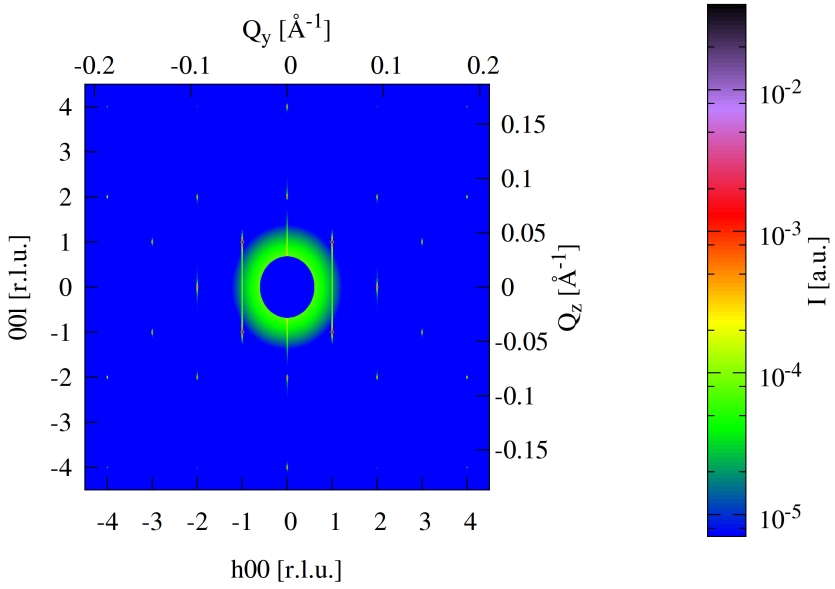

(a) without Lorentz factor

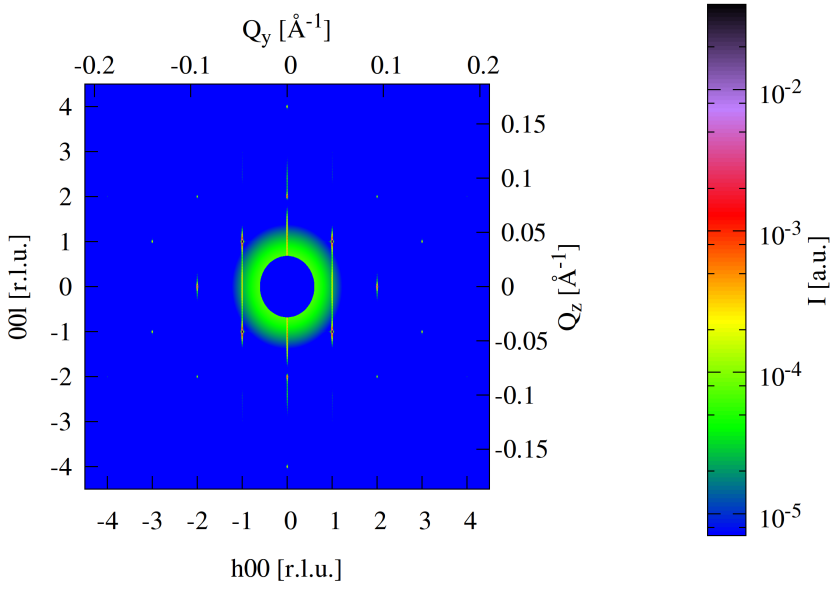

(b) with Lorentz factor

Figure A.14: Calculated diffraction pattern from single mesocrystals with cubic building blocks for the (h0l) plane. The influence of the Lorentz factor is shown by comparison of simulations with and without consideration.

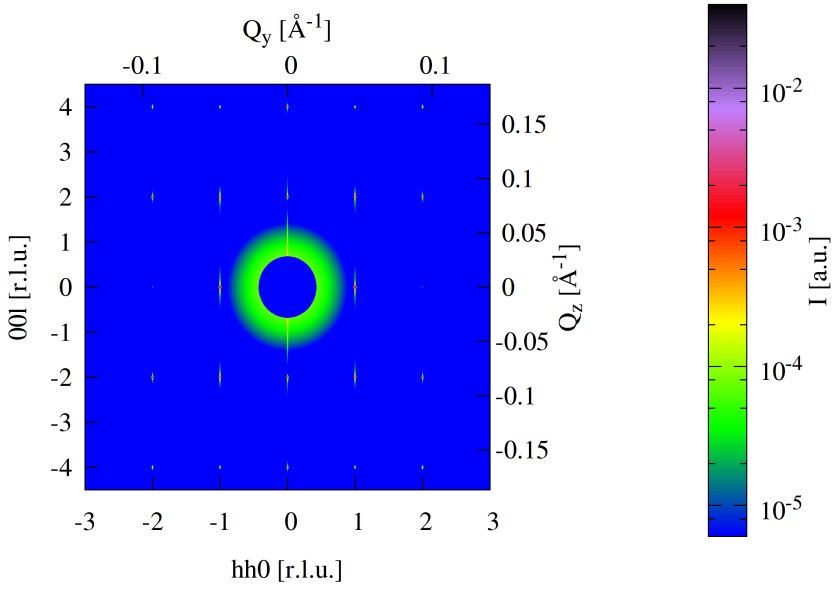

(a) without Lorentz factor

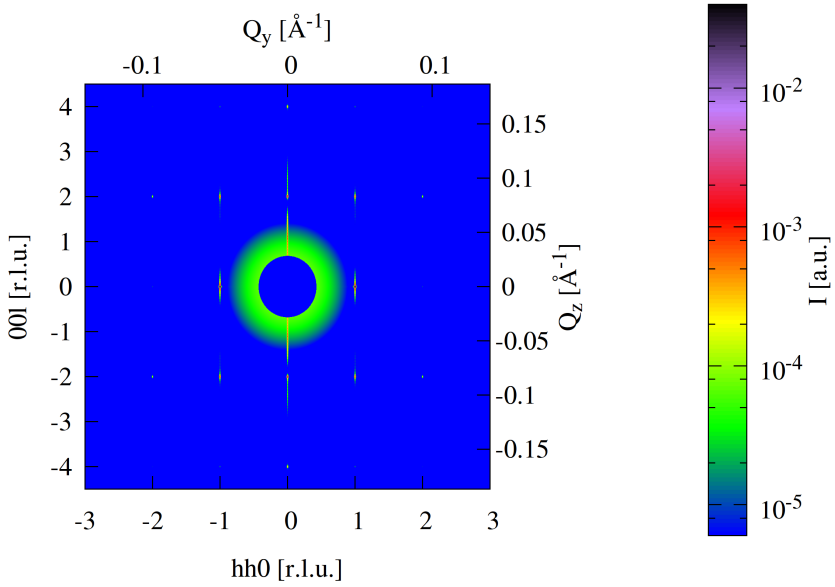

(b) with Lorentz factor

Figure A.15: Calculated diffraction pattern from single mesocrystals with cubic building blocks for the (hhl) plane. The influence of the Lorentz factor is shown by comparison of simulations with and without consideration.

A.3.4 Rocking scans and integrated intensities

The plots on the following pages show rocking scans in Q space, additional fits of the integrated intensities with different parameters and tables with integrated intensities.

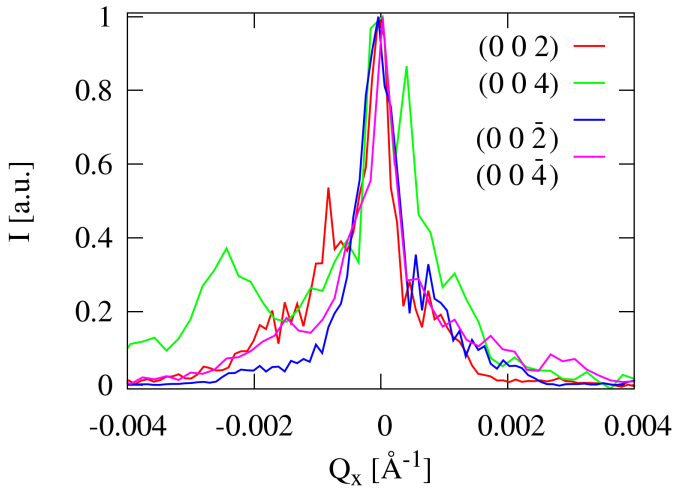

Figure A.16: Rocking scans for different peaks of the (HOL) plane of M_C^I in Q space. The peak width are obviously very similar, showing a small influence of the mosaicity on the measured shape.

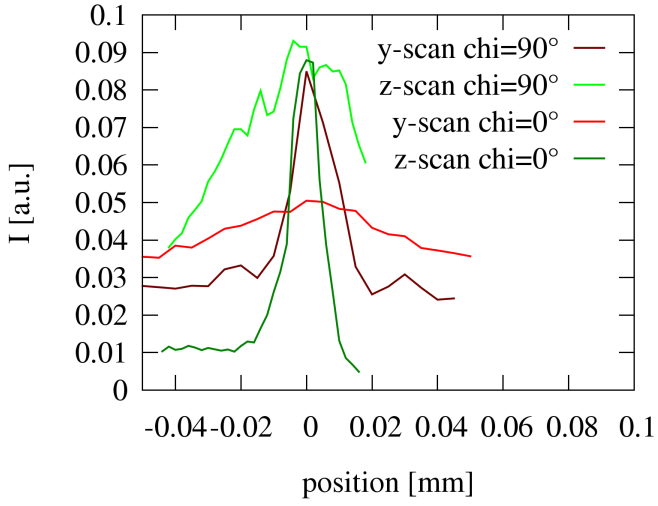

Figure A.17: Translation scans of the (100) and (001) reflections to measure the homogeneity/inhomogeneity of the beam. The curves with dark color are scans over the beam height and show sharp peaks which indicate a small beam. The lighter color plots are scans over the beam width, which show a large and inhomogeneous beam in this direction.

(hkl)	plain	χ [$^\circ$]	I [a.u.]	I_L [a.u.]
(002)	(h0l)	0	42.180000	3.487474
(00-2)	(h0l)	0	53.427399	4.417417
(002)	(h0l)	38	17.912201	1.164279
(00-2)	(h0l)	38	9.876070	0.641937
(002)	(h0l)	38	55.738800	3.622978
(00-2)	(h0l)	38	44.397499	2.885802
(002)	(hhl)	0	38.926601	3.218481
(00-2)	(hhl)	0	35.632301	2.946105
(002)	(hhl)	52	48.048801	2.442972
(00-2)	(hhl)	52	23.884800	1.214388
(002)	(hhl)	52	42.139301	2.142512
(00-2)	(hhl)	52	64.349297	3.271747
(002)	(h2hl)	0	52.649502	4.353100
(00-2)	(h2hl)	0	63.996601	5.291287
(002)	(h2hl)	70	67.876099	1.936964
(00-2)	(h2hl)	70	49.146801	1.402490
(002)	(h2hl)	70	49.046398	1.399625
(00-2)	(h2hl)	70	70.172203	2.002487

Table A.3: Integrated intensities of symmetry equivalent reflexes of (002) at a Q position of 0.083 from M_C^I. I are the uncorrected and I_L are the Lorentz corrected integrated intensities, which are shown in **figure 7.15a**.

(hkl)	plain	χ [$^\circ$]	I [a.u.]	I_L [a.u.]
(004)	(h0l)	0	6.081300	1.005613
(00-4)	(h0l)	0	9.412490	1.556463
(004)	(hhl)	0	9.038650	1.494645
(00-4)	(hhl)	0	6.464110	1.068915
(004)	(h2hl)	0	8.981660	1.485221
(00-4)	(h2hl)	0	6.726580	1.112317

Table A.4: Integrated intensities of symmetry equivalent reflexes of (004) at a Q position of 0.165 from M_C^I. I are the uncorrected and I_L are the Lorentz corrected integrated intensities, which are shown in **figure 7.15a**.

(hkl)	plain	χ [$^\circ$]	I [a.u.]	I_L [a.u.]
(-101)	(h0l)	49	216.313000	13.498137
(10-1)	(h0l)	49	248.050990	15.478618
(101)	(h0l)	49	160.414000	10.009986
(-10-1)	(h0l)	49	143.416000	8.949295
(10-1)	(h0l)	90	549.461000	25.605288
(101)	(h0l)	7	438.153020	20.418253
(-10-1)	(h0l)	90	297.129000	13.846430
(-101)	(h0l)	7	398.660000	18.577848
(101)	(h0l)	0	584.380980	24.252295
(10-1)	(h0l)	83	619.343990	25.703287
(-101)	(h0l)	0	524.030030	21.747679
(-10-1)	(h0l)	83	553.419010	22.967346

Table A.5: Integrated intensities of symmetry equivalent reflexes of (101) at a Q position of 0.062 from M_C^I. I are the uncorrected and I_L are the Lorentz corrected integrated intensities, which are shown in **figure 7.15a**.

(hkl)	plain	χ [$^\circ$]	I [a.u.]	I_L [a.u.]
(110)	(hhl)	90	282.514010	18.675230
(-1-10)	(hhl)	90	271.595000	17.953444
(110)	(hhl)	37	320.909000	12.848164
(-1-10)	(hhl)	37	281.700010	11.278361
(110)	(hhl)	37	331.531010	13.273435
(-1-10)	(hhl)	37	292.238010	11.700269

Table A.6: Integrated intensities of symmetry equivalent reflexes of (110) at a Q position of 0.066 from M_C^I. I are the uncorrected and I_L are the Lorentz corrected integrated intensities, which are shown in **figure 7.15a**.

(hkl)	plain	χ [$^\circ$]	I [a.u.]	I_L [a.u.]
(112)	(hhl)	39	40.708401	4.309290
(-1-1-2)	(hhl)	39	26.591999	2.814963
(11-2)	(hhl)	39	39.874802	4.221046
(-1-12)	(hhl)	39	47.053600	4.980977
(112)	(hhl)	0	54.132900	4.480233
(-1-12)	(hhl)	0	73.199600	6.058261
(11-2)	(hhl)	77	53.206799	4.403585
(-1-1-2)	(hhl)	77	56.057800	4.639545
(112)	(hhl)	13	62.961399	4.176178
(11-2)	(hhl)	90	70.618896	4.684094
(-1-12)	(hhl)	13	52.657799	3.492749
(-1-1-2)	(hhl)	90	58.328400	3.868875

Table A.7: Integrated intensities of symmetry equivalent reflexes of (112) at a Q position of 0.106 from M_C^I. I are the uncorrected and I_L are the Lorentz corrected integrated intensities, which are shown in **figure 7.15a**.

(hkl)	plain	χ [$^\circ$]	I [a.u.]	I_L [a.u.]
(121)	(h2hl)	68	16.629101	1.869076
(-1-2-1)	(h2hl)	68	13.183700	1.481820
(12-1)	(h2hl)	68	24.212200	2.721400
(-1-21)	(h2hl)	68	22.275900	2.503764
(121)	(h2hl)	0	77.709198	3.255261
(12-1)	(h2hl)	43	72.662102	3.043836
(-1-21)	(h2hl)	0	70.117500	2.937242
(-1-2-1)	(h2hl)	43	72.432899	3.034235

Table A.8: Integrated intensities of symmetry equivalent reflexes of (121) at a Q position of 0.112 from M_C^I. I are the uncorrected and I_L are the Lorentz corrected integrated intensities, which are shown in **figure 7.15a**.

(hkl)	plain	χ [$^\circ$]	I [a.u.]	I_L [a.u.]
(200)	(h0l)	90	74.667397	6.980267
(-200)	(h0l)	90	50.117699	4.685243
(200)	(h0l)	48	42.208900	2.934401
(-200)	(h0l)	48	3.742710	0.260197
(200)	(h0l)	48	114.821000	7.982461
(-200)	(h0l)	48	94.417503	6.563991

Table A.9: Integrated intensities of symmetry equivalent reflexes of (200) at a Q position of 0.093 from M_C^I. I are the uncorrected and I_L are the Lorentz corrected integrated intensities, which are shown in **figure 7.15a**.

(hkl)	plain	χ [$^\circ$]	I [a.u.]	I_L [a.u.]
(-202)	(h0l)	49	0.330552	0.041254
(20-2)	(h0l)	49	1.098830	0.137136
(202)	(h0l)	49	0.242135	0.030219
(-20-2)	(h0l)	49	-1.942690	-0.242451

Table A.10: Integrated intensities of symmetry equivalent reflexes of (202) at a Q position of 0.125 from M_C^I. I are the uncorrected and I_L are the Lorentz corrected integrated intensities, which are shown in **figure 7.15a**.

(hkl)	plain	χ [$^\circ$]	I [a.u.]	I_L [a.u.]
(220)	(hhl)	90	9.036520	1.194695
(-2-20)	(hhl)	90	-1.975710	-0.261204

Table A.11: Integrated intensities of symmetry equivalent reflexes of (220) at a Q position of 0.132 from M_C^I. I are the uncorrected and I_L are the Lorentz corrected integrated intensities, which are shown in **figure 7.15a**.

(hkl)	Q [Å^{-1}]	$\langle I_{L_{exp}} \rangle \cdot Q^4$ [a.u.]	R_1 [%]	$I_{calc_{rcubes}} \cdot Q^4$ [a.u.]
(101) :	0.062	2.79 ± 0.65	27	3.06
(110) :	0.066	2.73 ± 0.56	18	1.93
(002) :	0.083	1.24 ± 0.58	40	1.80
(200) :	0.093	3.74 ± 0.20	46	6.93
(112) :	0.106	5.45 ± 0.95	12	3.62
(121) :	0.112	4.16 ± 0.93	18	3.43
(202) :	0.125	-1.43 ± 0.39	1382	1.22
(220) :	0.132	4.04 ± 0.31	155	012
(004) :	0.165	9.62 ± 1.70	17	0.74

Table A.12: Average of the integrated intensities of symmetry equivalent reflexes from M_C^I. $\langle I_{L_{exp}} \rangle$ are the measured integrated intensities, Lorentz corrected and averaged and $I_{calc_{rcubes}}$ are the simulated intensities of the rounded cube model. Both are shown in **figure 7.15b**. R_{int} and R_1 are the R factors known from crystallography, which quantify the quality of the data and the goodness of the fit, respectively. (R_1-rounded cubes: 18%, R_1-truncated cubes: 21%, R_1-spheres: 13%)

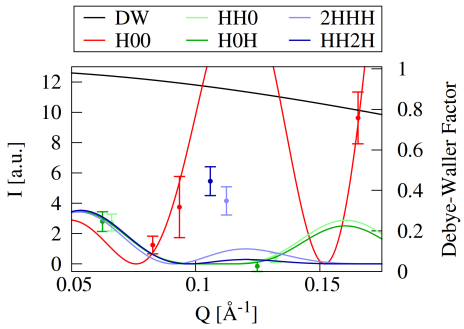

(a) Truncated cubes model with $\tau_{\text{Trunc}} = 0$
$a_{NP} = 8.27 \pm 0.0\%$, $a_{DW} = 0.501$ nm

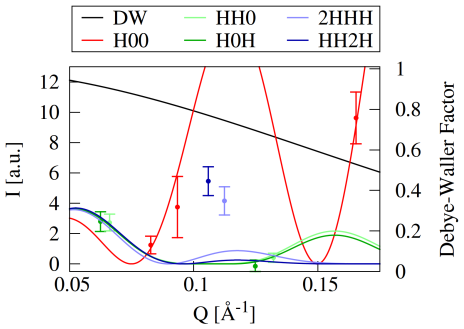

(b) Truncated cubes model with $\tau_{\text{Trunc}} = 0.2$
$a_{NP} = 8.4 \pm 0.0\%$, $a_{DW} = 0.84$ nm

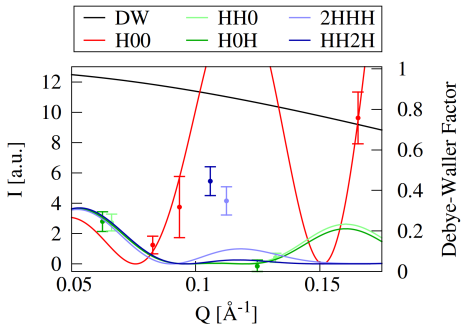

(c) Truncated cubes model with $\tau_{\text{Trunc}} = 0.4$
$a_{NP} = 8.38 \pm 0.1\%$, $a_{DW} = 0.594$ nm

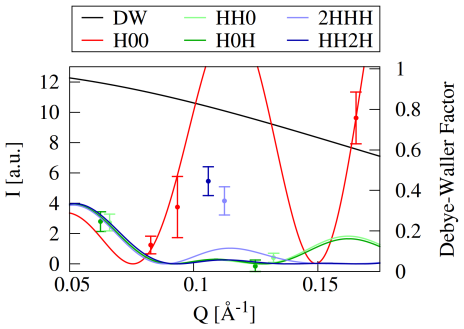

(d) Truncated cubes model with $\tau_{\text{Trunc}} = 0.6$
$a_{NP} = 8.59 \pm 0.6\%$, $a_{DW} = 0.744$ nm

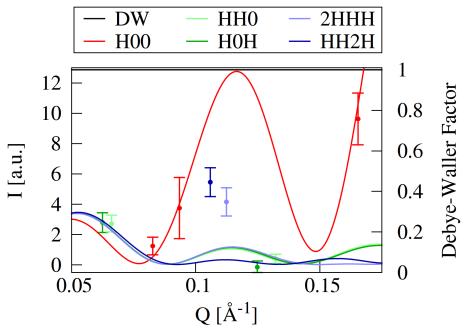

(e) Truncated cubes model with $\tau_{\text{Trunc}} = 0.8$
$a_{NP} = 8.69 \pm 3.8\%$, $a_{DW} = 0.00$ nm

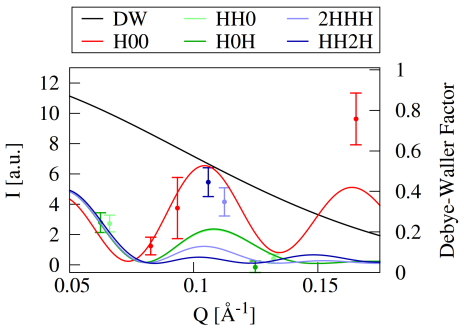

(f) Truncated cubes model with $\tau_{\text{Trunc}} = 1.0$
$a_{NP} = 9.64 \pm 6.1\%$, $a_{DW} = 1.29$ nm

Figure A.18: Results of fits from the truncated cube model. **Figure A.18a** fitted for a perfect cube and **figure A.18f** for a cubeoctaedron. The best parameters for the respective models are shown in **figure A.18e**.

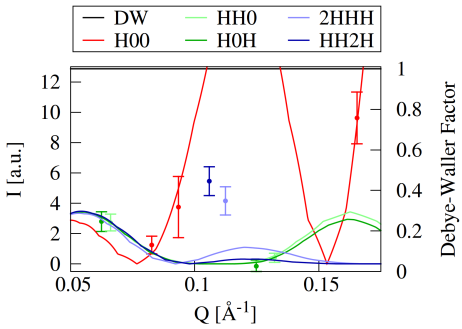

(a) Rounded cubes model with $\tau_{\text{Round}} = 0$
$a_{NP} = 8.197 \pm 0.0\%$, $a_{DW} = 0.007$ nm

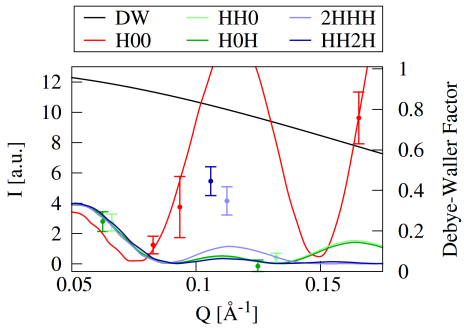

(b) Rounded cubes model with $\tau_{\text{Round}} = 0.5$
$a_{NP} = 8.714 \pm 1.2\%$, $a_{DW} = 0.730$ nm

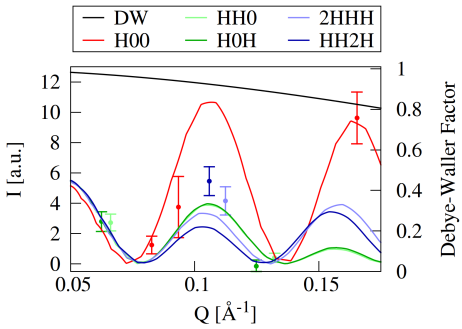

(c) Rounded cubes model with $\tau_{\text{Round}} = 0.8$
$a_{NP} = 10.42 \pm 0.0\%$, $a_{DW} = 0.460$ nm

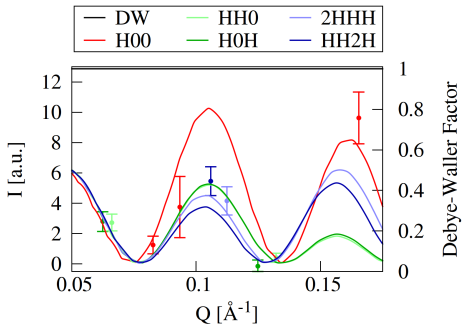

(d) Rounded cubes model with $\tau_{\text{Round}} = 0.85$
$a_{NP} = 10.78 \pm 0.4\%$, $a_{DW} = 0.00$ nm

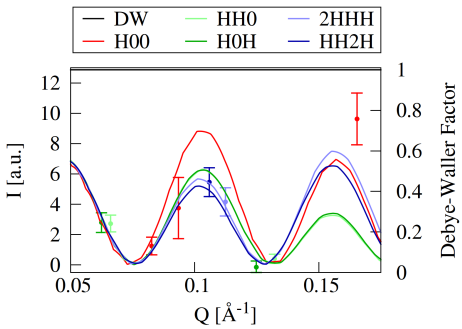

(e) Rounded cubes model with $\tau_{\text{Round}} = 0.9$
$a_{NP} = 11.21 \pm 0.0\%$, $a_{DW} = 0.00$ nm

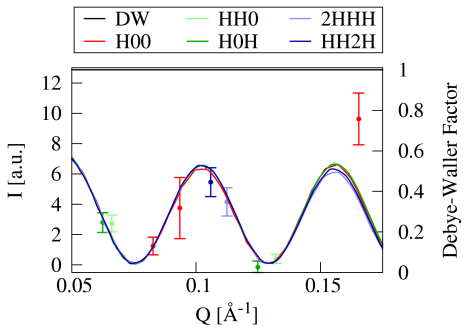

(f) Rounded cubes model with $\tau_{\text{Round}} = 1.0$
$a_{NP} = 12.01 \pm 0.0\%$, $a_{DW} = 0.00$ nm

Figure A.19: Results of fits from the rounded cube model. **Figure A.19a** fitted for a perfect cube and **figure A.19f** for a perfect spherical particle The best parameters for the respective models are shown in **figure A.19d** .

Appendix B

Used algorithms

The following pages list the programs developed for this dissertation. These scripts were programmed in close collaboration with Artur Glavic. The author would appreciate that any publication resulting from using these scripts as basis would cite this source appropriately. The GISAXS framework Lógos from Artur Glavic and BornAgain written by Gennady Pospelov, Walter Van Herck, based on the model of **chapter 5**, are still under development and the results shown here only display the current snapshot.

B.1 Form factor fit for integrated intensities

```
1
2  # <codecell>
3
4  from numpy import *
5  from pylab import *
6  from matplotlib.colors import LogNorm, LinearSegmentedColormap
7  cmap=LinearSegmentedColormap.from_list('default', ['#0000ff', '#00ff00', '#ffff00',
8                                                     '#ff0000', '#ff00ff', '#000000'],
                                                          N=256)
9  folder='/home/josten/mesotest_dr/'
10 seterr(all='ignore')
11
12 def export_gnuplot(fname, *columns):
13     output=open(fname, 'wb')
14     if columns[0].ndim==1:
15         data=array(columns)
16         savetxt(output, data.transpose())
17         output.close()
18     else:
19         data=array(columns)
20         for i in range(columns[0].shape[1]):
21             savetxt(output, data[:,:,i].transpose())
22             output.write('\n')
23         output.close()
24
25 def lognorm(x,x0,sigma):
26     return 1./(x*sigma*sqrt(2*pi))*exp(-0.5*(log(x)-log(x0))**2/sigma**2)
27
28 def ffc(Qx, Qy, Qz, a, tau):
29     # set high precision complex numbers
30     Qx=Qx.astype(complex128)
31     Qy=Qy.astype(complex128)
32     Qz=Qz.astype(complex128)
33     a2=a/2.
34     # truncated edge length is edge length times tau
35     b=tau*a
36     # Untruncated cubes form factor
37     FC=a**3 * sinc(Qx*a2/pi) * sinc(Qy*a2/pi) * sinc(Qz*a2/pi)
```

```
    if tau!=0:
        # For the truncation calculate the scattering from all 8 edges
        # this is done by moving and rotating a quarter of an octahedron
        # as given in By R. W. HENDRICKS, J. SCHELTEN and W. SCHMA, Philosophical Magazine (1974)
        F8 =F0( Qx,  Qy,  Qz,b) * exp(-1j * a2 * ( Qx + Qy + Qz))
        F8+=F0(-Qx, -Qy, -Qz,b) * exp(-1j * a2 * (-Qx - Qy - Qz))
        F8+=F0(-Qx,  Qy,  Qz,b) * exp(-1j * a2 * (-Qx + Qy + Qz))
        F8+=F0( Qx, -Qy, -Qz,b) * exp(-1j * a2 * ( Qx - Qy - Qz))
        F8+=F0( Qx, -Qy,  Qz,b) * exp(-1j * a2 * ( Qx - Qy + Qz))
        F8+=F0(-Qx,  Qy, -Qz,b) * exp(-1j * a2 * (-Qx + Qy - Qz))
        F8+=F0( Qx,  Qy, -Qz,b) * exp(-1j * a2 * ( Qx + Qy - Qz))
        F8+=F0(-Qx, -Qy,  Qz,b) * exp(-1j * a2 * (-Qx - Qy + Qz))
        return abs(FC-F8)**2
    else:
        return abs(FC)**2

def F0(Qx, Qy, Qz, b):
    A = exp(1j * b * Qx) / (Qx * (Qx - Qy) * (Qx - Qz))
    B = exp(1j * b * Qy) / (Qy * (Qy - Qx) * (Qy - Qz))
    C = exp(1j * b * Qz) / (Qz * (Qz - Qx) * (Qz - Qy))
    D = 1.0 / (Qx * Qy * Qz)
    A[isnan(A.real)|isinf(A.real)]=0j
    B[isnan(B.real)|isinf(B.real)]=0j
    C[isnan(C.real)|isinf(C.real)]=0j
    D[isnan(D.real)|isinf(D.real)]=0j
    return 1j * (A + B + C - D)

def ffc_d(Qx, Qy, Qz, a, da, tau, steps=5):
    oshape=Qx.shape
    Qx=Qx.astype(complex128).flatten()
    Qy=Qy.astype(complex128).flatten()
    Qz=Qz.astype(complex128).flatten()
    delta=linspace(max(0.,(1.-2*da)), (1.+2*da), steps)
    Pi=lognorm(delta, 1., da)
    Pi/=Pi.sum()
    a=a*delta[:, newaxis]
    Fd=ffc(Qx, Qy, Qz, a, tau)
    F=trapz(Pi[:,newaxis]*Fd, axis=0)
    return F.reshape(*oshape)


def ffs(Qr, r):
    QR=Qr*r
    return ((sin(QR)-QR*cos(QR))/QR**3)**2

Qr=linspace(0.,1,500).astype(complex128)
taus=linspace(0, 0.5, 100)

# <codecell>

figure(figsize=(13,12))
res=[]
for tau in taus:
    res.append(ffc(Qr, 0.0001*Qr, 0.0002*Qr, 50., tau))
res=array(res)
Q,T=meshgrid(Qr.real, taus)
pcolormesh(Q,T,res, norm=LogNorm(1e3, 1e10), cmap=cmap)
title('Truncation dependent cubes form factor in (H 0 0) direction for 5 nm cubes', fontsize=16)
xlabel('Q [$AA^{-1}$]', fontsize=16)
ylabel('tau', fontsize=16)
colorbar()
savefig(folder+"/single_meso_ff_H00.png", dpi=300)

# <codecell>

figure(figsize=(13,12))
res=[]
for tau in taus:
    res.append(ffc(sqrt(2)*Qr, sqrt(2.0001)*Qr, 0.0001*Qr, 50., tau))
res=array(res)
```

```
Q,T=meshgrid(Qr.real, taus)
pcolormesh(Q,T,res, norm=LogNorm(1e3,1e10), cmap=cmap)
title('Truncation dependent cubes form factor in (H H 0) direction for 5 nm cubes',
    fontsize=16)
xlabel('Q [AA^-1]', fontsize=16)
ylabel('tau', fontsize=16)
colorbar()
savefig(folder+"/single_meso_ff_HH0.png", dpi=300)

# <codecell>

figure(figsize=(13,12))
res=[]
for tau in taus:
    res.append(ffc(sqrt(3)*Qr, sqrt(3.0001)*Qr, sqrt(3.0002)*Qr, 50., tau))
res=array(res)
Q,T=meshgrid(Qr.real, taus)
pcolormesh(Q,T,res, norm=LogNorm(1e3,1e10), cmap=cmap)
title('Truncation dependent cubes form factor in (H H H) direction for 5 nm cubes',
    fontsize=16)
xlabel('Q [AA^-1]', fontsize=16)
ylabel('tau', fontsize=16)
colorbar();
savefig(folder+"/single_meso_ff_HHH.png", dpi=300)

# <codecell>

qx=linspace(0.00005,1.00005,200).astype(complex128)
qy=linspace(0.0001,1.0001,200).astype(complex128)
Qx,Qy=meshgrid(qx,qy)
Qz=Qx*1e-6
figure(figsize=(13,16))

for i,tau in enumerate([0, 0.1, 0.2, 0.3, 0.4, 0.5]):
    subplot('32'+str(1+i))
    I=ffc(Qx, Qy, Qz, 50., tau)
    xlim((-1,1.))
    ylim((-1,1.))
    pcolormesh(Qx.real,Qy.real,I, norm=LogNorm(1e3,1e10), cmap=cmap)
    pcolormesh(-Qx.real,Qy.real,I, norm=LogNorm(1e3,1e10), cmap=cmap)
    pcolormesh(Qx.real,-Qy.real,I, norm=LogNorm(1e3,1e10), cmap=cmap)
    pcolormesh(-Qx.real,-Qy.real,I, norm=LogNorm(1e3,1e10), cmap=cmap)
    title('tau=%g'%tau)
    xlabel('Qx [AA^-1]')
    ylabel('Qy [AA^-1]')
    colorbar();
    export_gnuplot(folder+'/single_meso_ff_taus_%.1f.dat'%tau, Qx.real, Qy.real, I)
savefig(folder+"/single_meso_ff_taus.png", dpi=300)

# <codecell>

# measured peaks as: H, K, L, |Q|, I, δI
data=array(
        [[1.0, 0.0, 1.0, 0.062400950016, 18.4212049128, 4.29199311658],
         [1.0, 1.0, 0.0, 0.0661037360179, 14.2881506228, 2.93087082572],
         [0.0, 0.0, 2.0, 0.08268075, 2.6578912882, 1.25053640925],
         [2.0, 0.0, 0.0, 0.0934848, 4.90109340758, 2.64686639613],
         [1.0, 1.0, 2.0, 0.105857500141, 4.34414952185, 0.758417415793],
         [2.0, 1.0, 1.0, 0.112397893192, 2.60582942009, 0.584909634579],
         [2.0, 0.0, 2.0, 0.124801900032, -0.0590093060426, 0.161877029074],
         [2.0, 2.0, 0.0, 0.132207472036, 0.132207472036, 0.1],
         [0.0, 0.0, 4.0, 0.1653615, 1.2871956886, 0.228134450133]]
           )
#astar=0.0467424
#cstar=0.041340375
astar=0.046611167
cstar=0.04147317
# calculate Q-positions, making sure there are no exactly equal or zero values
H,K,L,Q,I,dI=data.transpose()
Qx=H*astar+1e-6
Qy=K*astar+2e-6
```

```
Qz=L*cstar+3e-6

# <markdowncell>

# Below the model and model function is defined, which is used to simulate the data.
#
# Parameters are:
#
# <table>
#     <tr><td> I0  </td><td> Scaling intensity </td></tr>
#     <tr><td> a   </td><td>  Size of the cubes </td></tr>
#     <tr><td> tau  </td><td> truncation of the cubes </td></tr>
#     <tr><td> dw_a </td><td> Debye-Waller displacement factor a </td></tr>
# </table>

# <codecell>

from mpfit import mpfit

def f(p):
    I0=p[0]
    a=p[1]
    da=p[2]
    tau=abs(p[3])
    dw_a=p[4]
    DW=exp(-1./3.*dw_a**2*(Qx**2+Qy**2+Qz**2))
    return I0*ffc_d(Qx, Qy, Qz, a, da, tau)*DW

def residuals(p, fjac=None, use_error=True, use_log=False):
    if use_log:
        Iuse=maximum(I,0.1*I[I>0].min())
        res=log(Iuse)-log(f(p))
        err=dI/Iuse
    else:
        res=(I-f(p))
        err=dI
    if use_error:
        return 0, res/err
    else:
        return 0, res

# <codecell>

p0=[9e-10, 85., 0.025, 0.5, 0.1] #94., 0.05, 0.45, 5.]

# plot before fitting
errorbar(Q,I*Q**4,dI*Q**4)
plot(Q, f(p0)*Q**4)
plot(Q, 8e3*ffs(Q,59)*Q**4)
ylim((-1e-4,1.2e-3))
xlabel('Q [AA^-1]')
ylabel('IcdotQ^4');

# <codecell>

# fit parameters
result=mpfit(residuals, p0, iterfunct=None)
p1=result.params
result=mpfit(residuals, p0, functkw=dict(use_error=False), iterfunct=None)
p2=result.params
result=mpfit(residuals, p0, functkw=dict(use_log=True), iterfunct=None)
p3=result.params
# fit with different constant tau values
ptau=[]
p0i=list(p0)
for tau in [0.,0.1, 0.2, 0.3, 0.4, 0.5]:
    p0i=list(p0)
    p0i[3]=tau
    parinfo = [{'value': p0i[i], 'fixed':0, 'limited':[0,0], 'limits':[0.,0.]}
                   for i in range(5)]
    parinfo[2]['limited']=[True, True]
```

```
    parinfo[2]['limits']=[0., 0.1]
    parinfo[3]['fixed'] = True
    parinfo[4]['limited']=[True, True]
    parinfo[4]['limits']=[0.,20.]
    for i in range(5): parinfo[i]['value']=p0i[i]
    result=mpfit(residuals, p0i, functkw=dict(use_log=False), iterfunct=None,
        parinfo=parinfo)
    ptau.append(result.params)
    p0i=result.params
    print "I0=%.4g    a=%.4g    da=%.3g    tau=%.4g    dw_a=%.4g"%tuple(p0i)

# <codecell>

export_gnuplot(folder+"/single_meso_refinement_result.dat", Q, I*Q**4, dI*Q**4,
                               f(p1)*Q**4, f(p2)*Q**4, f(p3)*Q**4)

errorbar(Q,I*Q**4,dI*Q**4, label="Data")
plot(Q, f(p1)*Q**4, label="Linear w/o Error")
plot(Q, f(p2)*Q**4, label="Linear with Error")
plot(Q, f(p3)*Q**4, label="Logarithmic")
ylim((-1e-4,1.2e-3))
legend(loc=2)
xlabel('Q [$AA^{-1}$]')
ylabel('I$cdot Q^4$')
for pii in [p1,p2,p3]:
    print "I0=%.4g    a=%.4g    da=%.3g    tau=%.4g    dw_a=%.4g"%tuple(pii)
savefig(folder+"/single_meso_refinement_result.png", dpi=300)

# <codecell>

Qr=np.linspace(0.05,0.18, 400)
def fcc_dw_rad(p, H, K, L):
    I0=p[0]
    a=p[1]
    da=abs(p[2])
    tau=abs(p[3])
    dw_a=p[4]
    DW=exp(-1./3.*dw_a**2*(Qr**2))
    uv_scale=sqrt((H*astar)**2+(K*astar)**2+(L*cstar)**2) # length of the unit
        vector in HKL direction
    Qx=Qr*H*astar/uv_scale+1e-6
    Qy=Qr*K*astar/uv_scale+2e-6
    Qz=Qr*L*cstar/uv_scale+3e-6
    return I0*ffc_d(Qx, Qy, Qz, a, da, tau)*DW

def plot_all(ptaui, n, m, i, datfile=None):
    IH00=fcc_dw_rad(ptaui, 1,0,0)
    IHH0=fcc_dw_rad(ptaui, 1,1,0)
    IH0H=fcc_dw_rad(ptaui, 1,0,1)
    I2HHH=fcc_dw_rad(ptaui, 2,1,1)
    IHH2H=fcc_dw_rad(ptaui, 1,1,2)
    dw_a=ptaui[4]
    DW=exp(-1./3.*dw_a**2*(Qr**2))
    H00=[2,3,8]
    HH0=[1,7]
    H0H=[0,6]
    _2HHH=[5]
    HH2H=[4]

    IQ4=I*Q**4
    dIQ4=dI*Q**4
    Qr4=Qr**4
    if datfile is not None:
        export_gnuplot(datfile%ptaui[3], Qr, DW*0.001, IH00*Qr4, IHH0*Qr4, IH0H*Qr4,
            I2HHH*Qr4, IHH2H*Qr4)

    #figure(figsize=(8,6))
    subplot(n*100+m*10+i)
    errorbar(Q[H00],IQ4[H00],dIQ4[H00], fmt='.', color='red', label="Data",
        linewidth=2., markersize=10, capsize=5)
```

```
314     errorbar(Q[HH0],IQ4[HH0],dIQ4[HH0], fmt='.', color='green', label=None,
            linewidth=2., markersize=10, capsize=5)
315     errorbar(Q[HOH],IQ4[HOH],dIQ4[HOH], fmt='.', color='darkgreen', label=None,
            linewidth=2., markersize=10, capsize=5)
316     errorbar(Q[_2HHH],IQ4[_2HHH],dIQ4[_2HHH], fmt='.', color='blue', label=None,
            linewidth=2., markersize=10, capsize=5)
317     errorbar(Q[HH2H],IQ4[HH2H],dIQ4[HH2H], fmt='.', color='darkblue', label=None,
            linewidth=2., markersize=10, capsize=5)
318     plot(Qr, DW*0.001, '-', color='black', label="DWcdotfrac10^-3Q^4", linewidth=2.)
319     plot(Qr, IH00*Qr4, '-', color='red', label="H00", linewidth=2.)
320     plot(Qr, IHH0*Qr4, '-', color='green', label="HH0", linewidth=2.)
321     plot(Qr, IH0H*Qr4, '--', color='darkgreen', label="H0H", linewidth=2.)
322     plot(Qr, I2HHH*Qr4, '-', color='blue', label="2HHH", linewidth=2.)
323     plot(Qr, IHH2H*Qr4, '--', color='darkblue', label="HH2H", linewidth=2.)
324     xlim((0.05, 0.18))
325     ylim((-1e-4,1.2e-3))
326     legend(loc=2)
327     xlabel('Q [AA^-1]')
328     ylabel('IcdotQ^4')
329     title('a=%.3f nm +/-%.1f%%   tau=%.2f a_DW=%.3f nm'%(ptaui[1]/10., abs(ptaui[2])
            *100., ptaui[3], ptaui[4]/10.))
330
331 # export points with directional array
332 export_gnuplot(folder+'/single_meso_data.dat', Q, I, dI, I*Q**4, dI*Q**4, array
        ([3,2,1,1,5,4,3,2,1]))
333
334
335 # <codecell>
336
337 figure(figsize=(13,16))
338 for i, ptaui in enumerate(ptau):
339     plot_all(ptaui, 3, 2, i+1, datfile=folder+"/single_meso_refinement_tau_%.1f.dat"
            )
340 savefig(folder+"/single_meso_refinement.png", dpi=300)
341
342 # <markdowncell>
343
344 # Numeric form factor with FFT for rounded cubes
345
346 # <codecell>
347
348 def normed_round_cube_realspace(tau, points, resolution):
349     a=1.
350     r=(a/2.*sqrt(3)-a/2.)*(1.-tau)+a/2.
351     x,y,z=mgrid[-a*resolution:a*resolution:points*1j,
352                 -a*resolution:a*resolution:points*1j,
353                 -a*resolution:a*resolution:points*1j]
354     dens=zeros_like(x)
355     dens[(abs(x)<=a/2.)&(abs(y)<=a/2.)&(abs(z)<=a/2.)]=1.
356     dens[(x**2+y**2+z**2)>r**2]=0
357     return dens
358
359 Is_tau={}
360 resolution=5
361
362 def getFFrcubes(qx, qy, qz, a, tau):
363     if not tau in Is_tau:
364         dens=normed_round_cube_realspace(tau, 400, resolution)
365         A=rfftn(dens)[:201,:201,:]
366         I=abs(A**2)
367         Is_tau[tau]=I
368     else:
369         I=Is_tau[tau]
370     xsteps=2.*a*resolution/400.
371     qmax=pi/xsteps
372     qi=linspace(0., qmax, 201)
373
374     try:
375         x=where(qi>abs(qx))[0][0]-1
376         y=where(qi>abs(qy))[0][0]-1
377         z=where(qi>abs(qz))[0][0]-1
```

```
    except IndexError:
        # The Q value is out of the calculation range, return zero to prevent
            failure of fit
        return 1.e-300
    qidx=(x,y,z)
    Q=(qx,qy,qz)
    w=[[1.,0.],[1.,0.],[1.,0.]]
    Iout=0.
    for i in range(3):
        if Q[i]!=qidx[i]:
            w[i][0]=1./(Q[i]-qi[qidx[i]])
            w[i][1]=1./(qi[qidx[i]+1]-Q[i])
            ws=w[i][0]+w[i][1]
            w[i][0]/=ws
            w[i][1]/=ws
    for i in range(2):
        for j in range(2):
            for k in range(2):
                Iout+=w[0][i]*w[1][j]*w[2][k]*I[x+i,y+j,z+k]
    return Iout

def FFrcubes(Qx,Qy,Qz,a,da,tau, steps=11):
    Iout=zeros(*Qx.shape, dtype=float)
    delta=linspace(max(0.,(1.-2*da)), (1.+2*da), steps)
    P=lognorm(delta, 1., da)
    P/=P.sum()
    for di,Pi in zip(delta, P):
        ai=a*di
        for i in range(Qx.shape[0]):
            Iout[i]+=Pi*getFFrcubes(Qx[i],Qy[i],Qz[i],ai,tau)
    return Iout*30.


# <codecell>

def f(p):
    I0=p[0]
    a=p[1]
    da=p[2]
    tau=abs(p[3])
    dw_a=p[4]
    DW=exp(-1./3.*dw_a**2*(Qx**2+Qy**2+Qz**2))
    return I0*FFrcubes(Qx, Qy, Qz, a, da, tau)*DW

p0r=[p0[0], 105., 0.025, 0.5, 0.1]
ptaur=[]
for tau in [0.,0.5, 0.8, 0.85, 0.9, 1.0]:
    p0i=list(p0r)
    p0i[3]=tau
    parinfo = [{'value':0., 'fixed':0, 'limited':[0,0], 'limits':[0.,0.]}
                   for i in range(5)]
    parinfo[3]['fixed'] = True
    parinfo[1]['limited']=[1,1]
    parinfo[1]['limits'][0]=65.
    parinfo[1]['limits'][1]=135.
    parinfo[2]['limited']=[0,1]
    parinfo[2]['limits'][1]=0.1
    for i in range(5): parinfo[i]['value']=p0i[i]
    result=mpfit(residuals, p0i, functkw=dict(use_log=False), iterfunct=None,
        parinfo=parinfo)
    ptaur.append(result.params)
    p0i=result.params
    print "I0=%.4g    a=%.4g    da=%.3g    tau=%.4g    dw_a=%.4g"%tuple(p0i)

# <codecell>

def fcc_dw_rad(p, H, K, L):
    I0=p[0]
    a=p[1]
    da=p[2]
    tau=abs(p[3])
    dw_a=p[4]
```

```
    DW=exp(-1./3.*dw_a**2*(Qr**2))
    uv_scale=sqrt((H*astar)**2+(K*astar)**2+(L*cstar)**2) # length of the unit vector in HKL direction
    Qx=Qr*H*astar/uv_scale
    Qy=Qr*K*astar/uv_scale
    Qz=Qr*L*cstar/uv_scale
    return I0*FFrcubes(Qx, Qy, Qz, a, da, tau)*DW

figure(figsize=(13,16))
for i, ptaui in enumerate(ptaur):
    plot_all(ptaui, 3, 2, i+1, datfile=folder+'/single_meso_refinement_rcubes_tau_%.2f.dat')
savefig(folder+"/single_meso_refinement_rcubes.png", dpi=300)

# <codecell>


IH00=fcc_dw_rad(ptaur[5], 1,0,0)
IHH0=fcc_dw_rad(ptaur[5], 1,1,0)
IH0H=fcc_dw_rad(ptaur[5], 1,0,1)
I2HHH=fcc_dw_rad(ptaur[5], 2,1,1)
IHH2H=fcc_dw_rad(ptaur[5], 1,1,2)
dw_a=ptaur[5][3]
DW=exp(-1./3.*dw_a**2*(Qr**2))

xlim((0.05, 0.18))
ylim((-1e-4,1.2e-3))
plot(Qr, 8.5e3*ffs(Qr, 120.08/2.)*DW*Qr**4, '-', color='#aaaaaa', lw=10, label='Analytic Sphere')
plot(Qr, IH00*DW*Qr**4, label='Numeric H00')
plot(Qr, IHH0*DW*Qr**4, label='Numeric HH0')
plot(Qr, IH0H*DW*Qr**4, label='Numeric H0H')
plot(Qr, I2HHH*DW*Qr**4, label='Numeric 2HHH')
plot(Qr, IHH2H*DW*Qr**4, label='Numeric HH2H')
legend()
savefig(folder+"/compare_rcubes_spheres.png", dpi=300)

# <codecell>

errorbar(Q,I*Q**4,dI*Q**4)
plot(Q, f(ptaur[3])*Q**4)
ylim((-1e-4,1.2e-3))
xlabel('Q [$AA^{-1}$]')
ylabel('I$cdot Q^4$');
savefig(folder+"/single_meso_result_rcubes.png", dpi=300)
export_gnuplot(folder+"/single_meso_result_rcubes.dat", Q,I*Q**4,dI*Q**4, f(ptaur[3])*Q**4)

a=107.7
x,y=mgrid[-resolution*a:resolution*a:400j, -resolution*a:resolution*a:400j]
figure(figsize=(11,10))
dens=normed_round_cube_realspace(0.85,400,resolution)
imshow(dens.sum(axis=2), cmap="gist_yarg", extent=[-resolution*a,resolution*a, -resolution*a, resolution*a])
xlim((-1.1*a,1.1*a))
ylim((-1.1*a,1.1*a))
xlabel('x [$AA$]')
ylabel('y [$AA$]')
savefig(folder+"/single_meso_realspace_projection_rcubes.png", dpi=300)
export_gnuplot(folder+"/single_meso_realspace_projection_rcubes.dat", x, y, dens.sum(axis=2))

figure(figsize=(11,10))
imshow(dens[:,:,200], cmap="gist_yarg", extent=[-resolution*a,resolution*a, -resolution*a, resolution*a])
xlim((-1.1*a,1.1*a))
ylim((-1.1*a,1.1*a))
xlabel('x [$AA$]')
ylabel('y [$AA$]')
savefig(folder+"/single_meso_realspace_shadow_rcubes.png", dpi=300)
```

```
export_gnuplot(folder+"/single_meso_realspace_shadow_rcubes.dat", x, y, dens
    [:,:,200])
del(dens)

# <markdowncell>

# Implementation of radial integrated form factor for SAXS refinement

# <codecell>

def FFrSAXS(Qr, a, da, tau):
    if not tau in Is_tau:
        dens=normed_round_cube_realspace(tau, 400, resolution)
        A=rfftn(dens)
        I=abs(A**2)
        Is_tau[tau]=I
    else:
        I=Is_tau[tau]
    # calculate Q-vectors normalized by a
    xsteps=2.*resolution/400.
    steps=200
    Qmax=pi/xsteps
    Qx,Qy,Qz=mgrid[0:Qmax:steps*1j,0:Qmax:steps*1j,0:Qmax:steps*1j]
    Qr_a=sqrt(Qx**2+Qy**2+Qz**2)
    Qr_high=Qr_a/maximum(1e-10, a-3.*da*a)
    Qr_low=Qr_a/(a+3.*da*a)
    Iout=zeros_like(Qr)
    for i,Qri in enumerate(Qr):
        region=where((Qr_low<=Qri)&(Qr_high>Qri))
        weights=lognorm(Qr_a[region]/Qri, a, da)
        Iout[i]=(I[region]*weights).sum()/weights.sum()
    return Iout


# <codecell>

Qr=linspace(0., 0.3, 200)
result=[FFrSAXS(Qr, 100., 0.05, 0.85), FFrSAXS(Qr, 100., 0.05, 0.50),
        FFrSAXS(Qr, 100., 0.10, 0.85), FFrSAXS(Qr, 100., 0.20, 0.85)]
export_gnuplot(folder+"/single_meso_rcubes_ff.dat", Qr, *result)
semilogy(Qr, result[0], label='tau = 0.85  sigma_a = 0.05')
semilogy(Qr, result[1], label='tau = 0.50  sigma_a = 0.05')
semilogy(Qr, result[2], label='tau = 0.85  sigma_a = 0.10')
semilogy(Qr, result[3], label='tau = 0.85  sigma_a = 0.20')
legend()
xlabel('Q [AA^-1]')
ylabel('I')
title('Radial integrated form factor of rounded cubes')
savefig(folder+"/single_meso_rcubes_ff.png", dpi=300);

# <markdowncell>

# Load the SAXS data and fit the form factor with tau=0.85.
#
# Afterwards, the result parameters are used to fit with different taus.

# <codecell>

data=loadtxt('saxsdata.dat')
Qr=data[:-1,0]
Ir=data[:-1,1]
dIr=data[:-1,2]
fitregion=where(Ir>0.)[0][50:-20]

# Residuals used for SAXS refinement
def resSAXS(p, fjac=None):
    I0=p[0]
    a=p[1]
    da=p[2]
    tau=p[3]
    BG=p[4]
    sigmaQ=p[5]
```

```
582     res=np.exp(-0.5*(Qr-Qr.mean())**2/sigmaQ**2)
583     res/=res.sum()
584     I=I0*FFrSAXS(Qr, a, da, tau)+BG
585     I=convolve(I,res,mode='same')[fitregion]
586     err=dIr[fitregion]/Ir[fitregion]
587     return 0, (log(Ir[fitregion])-log(I))/err
588 
589 pSAXS=[4.50215333e-09, 1.09122571e+02, 0.05067, 0.85, 0.00101633, 0.00379122]
590 parinfo = [{'value':0., 'fixed':0, 'limited':[0,0], 'limits':[0.,0.]}
591               for i in range(6)]
592 parinfo[3]['fixed'] = True
593 parinfo[4]['fixed'] = True
594 for i in range(6): parinfo[i]['value']=pSAXS[i]
595 
596 result=mpfit(resSAXS, pSAXS, parinfo=parinfo, maxiter=10, iterfunct=None)
597 
598 
599 def Isim(p):
600     I0=p[0]
601     a=p[1]
602     da=p[2]
603     tau=p[3]
604     BG=p[4]
605     sigmaQ=p[5]
606     res=np.exp(-0.5*(Qr-Qr.mean())**2/sigmaQ**2)
607     res/=res.sum()
608     I=I0*FFrSAXS(Qr, a, da, tau)+BG
609     I=convolve(I,res,mode='same')
610     return I
611 
612 ISAXSSim=Isim(result.params)
613 
614 # <codecell>
615 
616 figure(figsize=(12,10))
617 semilogy(Qr,Ir,label='data')
618 export_gnuplot(folder+'/single_meso_rcubes_ff_fit.dat', Qr, Ir, ISAXSSim)
619 semilogy(Qr, ISAXSSim, label='fit')
620 legend()
621 xlabel('Q [$AA^{-1}$]')
622 ylabel('I')
623 title('SAXS fit of rounded cubes')
624 savefig(folder+"/single_meso_rcubes_ff_fit.png", dpi=300);
625 
626 # <codecell>
627 
628 p0SAXS=result.params
629 pSAXStau=[]
630 
631 for tau in [0.85, 0.825, 0.8, 0.775, 0.75]:
632     pSAXS=list(p0SAXS)
633     pSAXS[3]=tau
634     parinfo = [{'value':0., 'fixed':0, 'limited':[0,0], 'limits':[0.,0.]}
635                   for i in range(6)]
636     parinfo[3]['fixed'] = True #0.025 # steps in tau used for refinement
637     parinfo[4]['fixed'] = True #0.025 # steps in tau used for refinement
638     for i in range(6): parinfo[i]['value']=pSAXS[i]#
639 
640     result=mpfit(resSAXS, pSAXS, iterfunct=None, maxiter=5, parinfo=parinfo)
641     pSAXStau.append(result.params)
642     print tau, result.fnorm
643 
644 print '\n'.join([("%10g "*6)%tuple(p) for p in pSAXStau])
645 
646 # <codecell>
647 
648 figure(figsize=(15,12))
649 p0i=[9e-10, 108.99, 0.058, 0.8, 0.04]
650 parinfo = [{'value':0., 'fixed':0, 'limited':[0,0], 'limits':[0.,0.]}
651               for i in range(5)]
652 parinfo[1]['fixed'] = True
653 parinfo[2]['fixed'] = True
```

```
parinfo[3]['fixed'] = True
for i in range(5): parinfo[i]['value']=p0i[i]
result=mpfit(residuals, p0i, functkw=dict(use_log=False), iterfunct=None,parinfo=
    parinfo)
result.params
plot_all(result.params, 2, 2, 1, datfile=folder+'/
    single_meso_refinement_rcubes_SAXSfit_tau_%.2f.dat')
plot_all(ptaur[3], 2, 2, 2)

subplot(223)
errorbar(Q,I*Q**4,dI*Q**4)
plot(Q, f(result.params)*Q**4)
ylim((-1e-4,1.2e-3))
xlabel('Q [AA^-1]')
ylabel('I cdot Q^4');
subplot(224)
errorbar(Q,I*Q**4,dI*Q**4)
plot(Q, f(ptaur[3])*Q**4)
ylim((-1e-4,1.2e-3))
xlabel('Q [AA^-1]')
ylabel('I cdot Q^4');
export_gnuplot(folder+"/single_meso_result_rcubes_after.dat", Q, I*Q**4,dI*Q**4, f(
    result.params)*Q**4)
savefig(folder+"/single_meso_result_rcubes_after.png", dpi=300)

# <codecell>
```

B.2 Laue function fit for single mesocrystal

```
from numpy import sqrt, sin, cos, arange, exp, newaxis, pi, linspace, zeros_like

class SpheresLaue(fit_data.FitFunction):
  name="Spheric FF+Laue"
  parameters=[1., 100., 0.01, 0.,
              150., 0., 20, 2, 0.1]
  parameter_names=['I', 'r', 'δr', 'Qx', 'c', 'δc', 'N', 'δN', 'Inc']
  parameter_description={'I': 'Scaling', 'r': 'Particle Radius', 'Qx': 'Q-offset'}
  fit_function_text='Moved Laue'


  def fit_function(self, p, x):
    I0, r, dr, Qx=p[0:4]

    c,dc,N,dN=p[4:8]
    Inc=p[8]

    R=linspace(r*(1.-3*dr), r*(1+3.*dr), 20)
    Pr=exp(-0.5*(R-r)**2/(r*dr)**2)
    Pr/=Pr.sum()
    Qr=sqrt(Qx**2+x**2)[:,newaxis]*R[newaxis,:]
    FF=I0*(Pr[newaxis,:]*((sin(Qr)-Qr*cos(Qr))**2/Qr**6)).sum(axis=1)

    L=zeros_like(x)
    scales=linspace(1-3*dc, 1+3*dc, 21)
    Ps=exp(-0.5*((scales-1)/dc)**2)
    Ps/=Ps.sum()
    for Pi, scale in zip(Ps, scales):
      Ql=x*c/2*scale
      L+=self.laue(Ql, N, dN)
    return FF*(L+Inc)

  def laue(self, Ql, N, dN):
    if dN>0:
      Nmin=min(int(N)-3, int(N-3*dN))
      Nmax=max(int(N)+3, int(N+3*dN))
      n=arange(Nmin, Nmax+1)
      P=exp(-0.5*((n-N)/dN)**2)
      P/=P.sum()

```

```
      Laue=abs((exp(1j*(Ql+pi))+1.)[:, newaxis]*sin(Ql[:, newaxis]*n[newaxis, :])/
          sin(Ql[:, newaxis]))**2
      L=(Laue*P[newaxis, :]).sum(axis=1)
    else:
      L=abs((exp(1j*(Ql+pi))+1.)*sin(Ql*int(N))/sin(Ql))**2
    return L



fit_data.FitSession.available_functions_2d[SpheresLaue.name]=SpheresLaue
```

B.3 Single mesocrystal modeling

```

# <codecell>

from numpy import *
from scipy.special import j1
from scipy.signal import fftconvolve
from pylab import *
from matplotlib.colors import LogNorm, LinearSegmentedColormap
import matplotlib
#matplotlib.rc('font', size=24)

folder='/home/josten/mesotest/'

#astar=2.*pi/235.
#cstar=2.*pi/280.
astar=0.046645771
cstar=0.041500563

h_MC=2150.
r_MC=22000.
DW_MC=5.
def F_MC(Qy, Qz):
    F=sinc(h_MC*Qz/pi)
    F[Qy!=0]*=j1(r_MC*Qy[Qy!=0])/(r_MC*Qy[Qy!=0])
    return F

r_NP=58.0
def F_NP(Q, r):
    Qr=Q*r
    return (sin(Qr)-Qr*cos(Qr))/Qr**3

# <codecell>

qy=linspace(-0.01,0.01,400)
qz=linspace(-0.01,0.01,400)
Qy,Qz=meshgrid(qy,qz)

I=abs(F_MC(Qy,Qz)**2)
figure(figsize=[14,10])
gca().set_xlim([-0.01,0.01])
gca().set_ylim([-0.01,0.01])
pcolormesh(Qy,Qz,I, norm=LogNorm(1e-7,1))
colorbar()
savefig(folder+'single_meso_simu_peakshape.png', dpi=300);

# <codecell>

qy=linspace(-0.01,0.21,2200)
qz=linspace(-0.01,0.21,2200)
Qy,Qz=meshgrid(qy,qz)

A=zeros_like(Qy)
for H in range(-1,5):
    for L in range(-1,5):
        if (H+L)%2==1:
            continue
```

```
57          A+=F_MC(Qy-H*astar,Qz-L*cstar)
58
59  IHOL=abs(A**2)
60
61  # <codecell>
62
63
64  A=zeros_like(Qy)
65  for HK in range(-1,3):
66      for L in range(0,6,2):
67          A+=F_MC(Qy-HK*sqrt(2.)*astar,Qz-L*cstar)
68
69  IHHL=abs(A**2)
70
71  # <codecell>
72
73  sigmax=0.00031
74  sigmay=0.00031
75  res=exp(-0.5*(((Qy-qy.mean())/sigmax)**2+((Qz-qz.mean())/sigmay)**2))
76  res/=res.sum()
77  IHOL_res=fftconvolve(res, IHOL, mode="same")
78  IHHL_res=fftconvolve(res, IHHL, mode="same")
79
80  # <codecell>
81
82  sigma_r=0.1
83  ri=linspace(-3*sigma_r,3*sigma_r,11)+r_NP
84  Pi=exp(-0.5*(r_NP-ri)**2/sigma_r**2)
85  Pi/=Pi.sum()
86  FF=zeros_like(Qy)
87  Qr=sqrt((Qy**2+Qz**2))
88  for rii, Pii in zip(ri, Pi):
89      FF+=Pii*F_NP(Qr, rii)**2
90
91  # <codecell>
92
93  DW=exp(-1./3.*DW_MC**2*(Qy**2+Qz**2))
94
95  # <codecell>
96
97  cmap=LinearSegmentedColormap.from_list('default', ['#0000ff', '#00ff00', '#ffff00',
98                                                     '#ff0000', '#ff00ff', '#000000'],
                                                          N=256)
99
100 L=4e-4*minimum(1e4, array([1./(Qz-0.11)**2, 1./(Qz-0.055)**2, 1./Qz**2, 1./(Qz
        +0.055)**2, 1./(Qz+0.11)**2]).max(axis=0))*minimum(1e3, 1./Qy**2)
101 C=500.
102
103 figure(figsize=[13,12])
104 imshow(((L*IHOL_res*DW+1e-3)*FF)*((Qy**2+Qz**2)>0.0008), cmap=cmap, norm=LogNorm(6e
        -6, 6e-2),
105        extent=[qy.min(), qy.max(), qz.max(), qz.min()])
106 title('HOL - Plane')
107 xlabel('Qy')
108 ylabel('Qz')
109 colorbar()
110 savefig(folder+'single_meso_simu_HOL.png', dpi=300);
111
112 # <codecell>
113
114 figure(figsize=[13,12])
115 imshow(((L*IHHL_res*DW+1e-3)*FF)*((Qy**2+Qz**2)>0.0008), cmap=cmap, norm=LogNorm(1e
        -5, 3e-2),
116        extent=[qy.min(), qy.max(), qz.max(), qz.min()])
117 title('HHL - Plane')
118 xlabel('Qy')
119 ylabel('Qz')
120 colorbar()
121 savefig(folder+'single_meso_simu_HHL.png', dpi=300);
122
123 # <codecell>
124
```

```
# export data
def export_gnuplot(fname, x, y, z):
    output=open(fname, 'wb')
    data=array([x,y,z])
    for i in range(Qy.shape[1]):
        savetxt(output, data[:,:,i].transpose())
        output.write('\n')
    output.close()

export_gnuplot(folder+'single_meso_simu_H0L.dat',
               Qy, Qz, ((C*IH0L_res*DW+1e-3)*FF)*((Qy**2+Qz**2)>0.0008))
export_gnuplot(folder+'single_meso_simu_HHL.dat',
               Qy, Qz, ((C*IHHL_res*DW+1e-3)*FF)*((Qy**2+Qz**2)>0.0008))

export_gnuplot(folder+'single_meso_simu_H0L_Lorentz.dat',
               Qy, Qz, ((L*IH0L_res*DW+1e-3)*FF)*((Qy**2+Qz**2)>0.0008))
export_gnuplot(folder+'single_meso_simu_HHL_Lorentz.dat',
               Qy, Qz, ((L*IHHL_res*DW+1e-3)*FF)*((Qy**2+Qz**2)>0.0008))

# <codecell>
```

B.4 Peak shape computation for in-situ experiments

```
#-*- coding: utf-8 -*-
'''
  Load a set of measurements and fit a peak function for each dataset.
'''

import os,sys
import shutil
import time
from glob import glob
from copy import deepcopy
from plot_script.read_data.kws2 import read_edf_file
from form_factors import FitSphereQres
from neue_funktion_final import PeakShapeResTilt


stdout=None

print """  Usage:
    -Open one dataset and make your correction:
        d=filter_dataset(dataset(), [0.,10.,0.,10.])
        session.active_file_data.append(d)
        remove_bg(d)
        remove_sphere(d)
        # <ctrl>+N

    -Fit the peak function with the desired xy-region and define the free parameters

    -Run the fits for all files in the active directory:
        z.B. plots_for_all(preset='s113')
          plots_for_all(fit_function=None,
                        name='Fits',
                        store_data=False,
                        correction=None,
                        remove_background=False,
                        preset=None)"""

SPHERE_PARAMS=[
                0.000577067, # I0
                0.,  # BG
                50.0518, # R
                0.0638503, # δR
                0.0035, # ΔΘ vorher
                1e-10, # Δλ
                4.51, # λ
                ]

```

```
                # 0.00135482, # ΔΘ vorher
CUBES_PARAMS=[
                 0.000577067, # I0
                 0.,  # BG
                 60.3707, # R
                 0.0556317, # δR
                 0.0035, # ΔΘ
                 1e-10, # Δλ
                 4.51, # λ
                 ]
        #  x-from x-to  y-from y-to
#BG_REGION=[0.15,  0.16, 0.21,  0.229]   #vorher
BG_REGION=[0.151,  0.161, 0.22,  0.229] #P321, P227



def iteration_update(step_add=None,info=''):
  '''
    Define a function which updates the user on the current fit iteration.
  '''
  stdout.write(info+'\n')
  stdout.flush()
  return 0

def fit_data_list(datasets, # list of file names
                  initial_fit=None, # Fit function to be used, if None uses fit-0 from active dataset
                  correction=None, # form factor correction function to be used
                  remove_background=False, # remove the background
                  plot_prefix='Result_', # name of session.file_data list to append datasets to
                  incregion=None, # region to extract incoherent scattering
                  ii_region=None, # region to calculate integrated intensity
                  param_file=None, # file to store the text data to
                  ):
  '''
    Starting from a given fit (if None uses the first
    fit of the active dataset) all datasets in a list of
    names are read and fit. The result parameters for each
    file are returned as a list.
  '''
  global stdout, do_plot
  if stdout is None:
    try:
      # open dialog for output
      stdout=plot_gui.status_dialog
      stdout.show_all()
      do_plot=True
      session.file_data['temp']=[None]
      session.active_file_data=session.file_data['temp']
      session.active_file_name='temp'
      plot_gui.measurement=session.file_data['temp']
      plot_gui.index_mess=0
    except:
      stdout=sys.stdout
      do_plot=False
  from config import gnuplot_preferences
  gnuplot_preferences.settings_3dmap+='set format cb "10^{%L}"\nset cblabel offset 1.5\n'
  gnuplot_preferences.plotting_parameters_3d='w points palette ps .1 pt 5'
  if do_plot:
    import gtk
    keep_running=gtk.CheckButton(label='Keep Running')
    keep_running.set_active(True)
    stdout.vbox.pack_end(keep_running, False)
    keep_running.show()
    stdout.present()
  if initial_fit is None:
    # get first fit from active dataset
    fit=dataset().fit_object.functions[0][0]
  else:
    fit=initial_fit
```

```
116   # create multiprocessing framework
117   fit.activate_multiprocessing()
118
119   if param_file is not None:
120     param_file=open(param_file+'.txt', 'w')
121     param_file.write( "\t".join(fit.parameter_names)+"\t"
122                       "\t".join(["δ"+name for name in fit.parameter_names])+
123                       "\t#\tTime\n"
124                     )
125     param_file.flush()
126
127   parameters=[]
128   ff=None # formfactor intensity array
129   incidxs=None
130   ii_idxs=None
131   first_time=None
132   for i, ds in enumerate(datasets):
133     # iterate through all datasets
134     stdout.write("  Reading %s...\n" % ds)
135     stdout.flush()
136     # read dataset and extract number and time
137     data=read_edf_file(ds)[0]
138     info=map(lambda line: map(str.strip, line.split(':',1)), data.info.splitlines())
139     info=dict(filter(lambda item: len(item)==2, info))
140     file_number=int(ds.rsplit('_',1)[1].split("ccd")[0])
141     gmtime=time.strptime(info['HMStartTime'].split('.')[0], '%Y-%m-%dT%H:%M:%S')
142     float_time=time.mktime(gmtime)
143     if remove_background:
144       stdout.write("    ...background...\n")
145       stdout.flush()
146       remove_bg(data)
147     if correction is not None:
148       stdout.write("    ...correcting...\n")
149       stdout.flush()
150       # filter the dataset for the fitted region
151       dataf=filter_dataset_fitregion(data, fit)
152       # clear all references to the data and delete the temporary file
153       data.store_data()
154       os.remove(data.tmp_export_file)
155       del(data)
156       data=dataf
157       if ff is None:
158         # calculate the form factor correction intensities on first call
159         ff=correction(data)
160       data.z/=ff
161     if incregion is not None:
162       stdout.write("    ...incoherent background...\n")
163       stdout.flush()
164       if incidxs is None:
165         incidxs=np.where((data.x>=incregion[0])&(data.x<=incregion[1])&
166                          (data.y>=incregion[2])&(data.y<=incregion[3]))
167       incdata=float(data.z[incidxs].sum())/len(data.z[incidxs])
168       bg_param_index=fit.parameter_names.index('BG')
169       fit.parameters[bg_param_index]=incdata
170       if bg_param_index in fit.refine_parameters:
171         fit.refine_parameters.remove(bg_param_index)
172
173       stdout.write("    ...=%g...\n"%incdata)
174       stdout.flush()
175
176
177     if ii_region is not None:
178       stdout.write("    ...integrated intensity")
179       stdout.flush()
180       if ii_idxs is None:
181         ii_idxs=np.where((data.x>=ii_region[0])&(data.x<=ii_region[1])&
182                          (data.y>=ii_region[2])&(data.y<=ii_region[3]))
183       ii_data=data.z[ii_idxs].sum()/len(data.z[incidxs])
184       if incregion is not None:
185         ii_data-=incdata
186       stdout.write(" %f\n"%(float(ii_data)))
187       stdout.flush()
```

```
188     stdout.write("    ...refineing...\n")
189     stdout.flush()
190     fitmsg, covar=fit.refine(data.x, data.y, data.z, None,#data.z.error, ##None=
            ignore errors, data.z.error=übercksichtigung
191                              progress_bar_update=iteration_update) #Fit Routine
192     errors=[]
193     if fitmsg!='':
194       stdout.write("Error in Fit: "+fitmsg)
195       stdout.flush()
196     errors=[np.sqrt(covar[i][i]) for i in range(len(fit.parameters))]
197     if first_time is None:
198       first_time=float_time
199     float_time-=first_time
200     if ii_region is None:
201       fit_parameters=list(fit.parameters)+errors+[file_number, float_time]
202     else:
203       fit_parameters=list(fit.parameters)+[float(ii_data)]+\
204                           errors+[float(ii_data.error)]+[file_number, float_time]
205     parameters.append(fit_parameters)
206     if param_file is not None:
207       param_file.write( "\t".join(["%g"%param for param in  fit_parameters])+"\n")
208       param_file.flush()
209
210     stdout.write("    ...result:\n  \t%s\n  \t%s\n+/-\t%s\n\n" % (
211                                             repr(fit.parameter_names),
212                                             repr(fit.parameters),
213                                             repr(errors)))
214     stdout.flush()
215     # create fit data for plotting
216     data.is_matrix_data=False
217     data.plot_options.xrange=[fit.x_from,fit.x_to]
218     data.plot_options.yrange=[fit.y_from,fit.y_to]
219     data.plot_options.zrange=[1.,1000.]
220     data.plot_together_zindex=-1
221     fit_data=mds.MeasurementData([],x=0,y=1,zdata=2)
222     fit_data.data.append(data.x)
223     fit_data.data.append(data.y)
224     fit_data.data.append(mds.PhysicalProperty(data.z.dimension, data.z.unit,
225                             fit(data.x,data.y)))
226     data.plot_together.append(fit_data)
227     data.sample_name=''
228     data.short_info='#%i'%file_number
229     session.picture_width='2400'
230     session.pictire_height='1200'
231     if do_plot:
232       # plot an image and copy the result
233       plot_gui.measurement[0]=data
234       replot()
235       shutil.copy(session.TEMP_DIR+'/plot_temp.png', plot_prefix+'%04i.png'%
              file_number)
236     else:
237       # directly plot as file
238       mdp.gnuplot_plot_script(session,
239                               [data],
240                                'temp_plot',
241                               '.png',
242                               data.short_info,
243                               [data.short_info],
244                               False,
245                               plot_prefix+'%04i.png'%file_number)
246
247     # clear all references to the data and delete the temporary file
248     data.store_data()
249     os.remove(data.tmp_export_file)
250     del(data)
251     if do_plot and not keep_running.get_active():
252       # stop iteration due to user input
253       break
254   # terminate other processes
255   fit.deactivate_multiprocessing()
256   if do_plot:
257     stdout.vbox.remove(keep_running)
```

```
258   return np.array(parameters).transpose()
259
260 def plots_from_paramlist(parameters, parameter_names):
261   # create plots of parameters
262   idx=mds.PhysicalProperty('File No.', '', parameters[-2])
263   tm=mds.PhysicalProperty('Time', 's', parameters[-1])
264   for i,name in enumerate(parameter_names):
265     ds=mds.MeasurementData(x=0,y=2)
266     ds.data.append(tm)
267     ds.data.append(idx)
268     if np.all(parameters[len(parameter_names)+i]==0):
269       ycol=mds.PhysicalProperty(name, '', parameters[i])
270     else:
271       ycol=mds.PhysicalProperty(name, '', parameters[i],
272                                         parameters[len(parameter_names)+i])
273     ds.data.append(ycol)
274     session.active_file_data.append(ds)
275
276 def plots_for_all(fit_function=None,
277                   name='Fits',
278                   store_data=True,
279                   correction=None,
280                   remove_background=False,
281                   param_file=None,
282                   preset=None):
283   '''
284     Perform analysis for all files in the active directory
285     starting from the last file. Options can be given
286     when called or using the preset name.
287   '''
288   global params, initial_fit
289   files=glob('*.edf')
290   files.sort()
291   files.reverse()
292   if preset is None:
293     initial_fit=None
294     incregion=None
295     ii_region=None
296   else:
297     preset=fit_presets[preset]
298     initial_fit=PeakShapeResTilt(list(preset['initial_fit']))
299     initial_fit.use_rotation=preset['use_rotation']
300     # add all peak regions and paramters
301     min_x=1000.
302     max_x=-1000.
303     min_y=1000.
304     max_y=-1000.
305     initial_fit.refine_parameters=range(8)+[13,14] #all free peak parameters +
          background and α_c
306     initial_fit.regions=[]
307     for xf,xt,yf,yt,Ii,Qyi,Qzi in preset['peaks']:
308       # set the fit region as maximum from all peak ranges
309       min_x=min(min_x, xf)
310       max_x=max(max_x, xt)
311       min_y=min(min_y, yf)
312       max_y=max(max_y, yt)
313       # add the peak to the fit function
314       i=len(initial_fit.regions)
315       initial_fit.add_region(xf, xt, yf, yt, Ii, Qyi, Qzi)
316       #if i in [0]:
317       initial_fit.refine_parameters+=[15+3*i] # free intensity
318       #else:
319       #  initial_fit.refine_parameters+=[15+3*i, 17+3*i] # free intensity and Qz
320     # constrain intensities to be >= 0
321     initial_fit.constrains[14]={'bounds': [0., None], 'tied': ''} # α_c>=0
322     for i in range(len(initial_fit.regions)):
323       if (15+3*i) in initial_fit.constrains:
324         initial_fit.constrains[15+3*i]['bounds'][0]=0.
325       else:
326         initial_fit.constrains[15+3*i]={'bounds': [0., None], 'tied': ''}
327     initial_fit.x_from=min_x
328     initial_fit.x_to=max_x
```

```
329       initial_fit.y_from=min_y
330       initial_fit.y_to=max_y
331       if preset['mirror_peaks']:
332         initial_fit.add_mirrors()
333       correction=preset['correction']
334       remove_background=preset['remove_background']
335       incregion=preset['incregion']
336       ii_region=preset['ii_region']
337       if param_file is None:
338         param_file=preset['param_file']
339       if name == 'Fits':
340         name=preset['name']
341     # fit all datasets
342     params=fit_data_list(files,
343                          correction=correction,
344                          remove_background=remove_background,
345                          initial_fit=initial_fit,
346                          plot_prefix=param_file+'_',
347                          ii_region=ii_region,
348                          incregion=incregion, param_file=param_file)
349     #if param_file is not None:
350     #  params[-1]-=params[-1].min()
351     #  np.savetxt(param_file+'.txt', params.transpose(), fmt='% 12g', delimiter='\t')
352     # create plots for parameters
353     session.file_data[name]=[]
354     session.active_file_data=session.file_data[name]
355     session.active_file_name=name
356     plot_gui.measurement=session.file_data[name]
357     plots_from_paramlist(params, initial_fit.parameter_names)
358     try:
359       plot_gui.rebuild_menus()
360       replot()
361     except:
362       pass
363
364   def remove_sphere(ds):
365     '''
366       Devide the measured intensity by the particle formfactor.
367     '''
368     ff=ff_sphere(ds)
369     ds.z/=ff
370
371   def ff_sphere(ds):
372     # sphere form factor
373     FF=FitSphereQres(SPHERE_PARAMS)
374     return FF(np.sqrt(ds.x**2+ds.y**2))
375
376   def remove_cube(ds):
377     '''
378       Devide the measured intensity by the particle formfactor.
379     '''
380     ff=ff_cube(ds)
381     ds.z/=ff
382
383     #öErhhung der Minimas zur Vermedung der Ringe
384     #Q=np.sqrt(ds.x**2+ds.y**2)
385     #ds.z/=ff+5*Q**(-3)+30000
386
387   def ff_cube(ds):
388     # cube form factor
389     FF=FitSphereQres(CUBES_PARAMS)
390     return FF(np.sqrt(ds.x**2+ds.y**2))
391
392   def remove_bg(ds):
393     '''
394       Subtract background.
395     '''
396     rg=BG_REGION
397     bg=ds.z[(ds.x>=rg[0])&(ds.x<=rg[1])&\
398                  (ds.y>=rg[2])&(ds.y<=rg[3])]
399     bg=bg.sum()/len(bg)
400     ds.z-=bg    #P231,P227
```

```
401   #ds.z-=8  #P225
402
403 def filter_dataset(ds, region):
404   '''
405     Get a new dataset for a region defined by [x0, x1, y0, y1]
406   '''
407   ids=np.where((ds.x>=region[0])&(ds.x<=region[1])&\
408                (ds.y>=region[2])&(ds.y<=region[3]))
409   return ds[ids]
410
411 def filter_dataset_fitregion(ds, fit):
412   '''
413     Get a new dataset for a region defined by PeakShapeResTilt peak regions.
414   '''
415   ids=ds.x!=ds.x # all False
416   for region in fit.regions:
417     ids=ids|((ds.x>=region[0])&(ds.x<=region[1])&(ds.y>=region[2])&(ds.y<=region[3])
          )
418   return ds[ids]
419
420
421 # Paramters for different Peaks
422 fit_presets={
423
424
425    'P231ai03': {                  # General peak parameters
426           'initial_fit': [  #'a*', 'c*', γ'_y', γ'_z'
427                             0.058643, 0.0208204, 0.000276603, 0.000432451,
428                             #σ'_tilt', σ'_r',
429                             4.92965, 0.0179373,
430                             #'Qy_off','Qz_off','Qphi_off' is fixed
431                             -0.00219964, 0.00659945, -0.577801,
432                             #'width' , 'height', 'decay' is fixed
433                             0.00497968, 0.000754677, 3195.79,
434                             #α'_i', α'_c'
435                             0.3, 0.0000244498,
436                             # BG
437                             27.,
438                           ],
439           'peaks': [  # parameters for each single peak
440                       # xfrom, xto, yfrom, yto,  I,   H/K     L
441                       [0.026, 0.09, 0.154, 0.185, 5e5, 1, 8], # 1 0 8
442                       [0.026, 0.087, 0.073, 0.11, 5e5, 1, 4],# 1 0 4
443                       [0.026, 0.087, 0.089, 0.127, 5e5, 1, 5],# 1 0 5
444                       [0.07, 0.116, 0.049, 0.0888199, 5e5, np.sqrt(3.), 3], # 1 1 3
445                       [0.09, 0.14, 0.067, 0.107, 5e5, 2, 4], # 2 0 4
446                       [0.07, 0.116, 0.104658385093, 0.146, 5e5, np.sqrt(3.), 6] # 1
                              1 6
447
448                     ],
449                     #  x-from, x-to, y-from, y-to
450            'mirror_peaks': True, # add peaks from the left side
451            'use_rotation': True,
452            'correction': ff_sphere,
453            'remove_background': True,
454            'param_file': 'P231_Spheres_short_ai03_timedependence_final',
455            'name': 'P231_Spheres_short_ai03',
456            'ii_region': [0.035, 0.08, 0.096, 0.13], # Integrated inteisity around 0
                 1 5
457            'incregion': [0.02 , 0.03, 0.095,   0.11],
458           },
459
460    'P226ai03': {                  # General peak parameters
461           'initial_fit': [ #'a*', 'c*', γ'_y', γ'_z'
462                             0.056734, 0.0200253, 0.0000322504, 0.000158157,
463                             #σ'_tilt', σ'_r',
464                             2.73872, 0.0162109,
465                             #'Qy_off','Qz_off','Qphi_off' is fixed
466                             -0.00189297, 0.00698159, -0.564942,
467                             #'width' , 'height', 'decay' is fixed
468                             0.00497968, 0.000754677, 3195.79,
469                             #α'_i', α'_c'
```

```
                            0.3, 0.0000244498,
                            # BG
                            27.,
                           ],
          'peaks': [  # parameters for each single peak
                      # xfrom, xto, yfrom, yto,  I,   H/K     L
                      [0.026, 0.09, 0.154, 0.185, 5e5, 1, 8], # 1 0 8
                      [0.026, 0.087, 0.073, 0.11, 5e5, 1, 4],# 1 0 4
                      [0.026, 0.087, 0.089, 0.127, 5e5, 1, 5],# 1 0 5
                      [0.07, 0.116, 0.049, 0.0888199, 5e5, np.sqrt(3.), 3], # 1 1 3
                      [0.09, 0.14, 0.067, 0.107, 5e5, 2, 4], # 2 0 4
                      [0.07, 0.116, 0.104658385093, 0.146, 5e5, np.sqrt(3.), 6] # 1
                          1 6

                     ],
                     #  x-from, x-to, y-from, y-to
           'mirror_peaks': True, # add peaks from the left side
           'use_rotation': True,
           'correction': ff_sphere,
           'remove_background': True,
           'param_file': 'P226_Spheres_middle_ai03_timedependence_final',
           'name': 'P226_Spheres_midlle_ai03',
           'ii_region': [0.035, 0.08, 0.095, 0.13], # Integrated inteisity around 0
               1 5
           'incregion': [0.02 , 0.03, 0.095,   0.11],
          },




  }
```

```
#-*- coding: utf-8 -*-
'''
  Definition of mesocrystal GISAXS peak shape including instrumental
  resolution function and structural tilt and size distribution.
  To work the data has to be defined on a regular grid, otherwise the
  FFT convolution algorithm won't work.

  The calculations can be performed with multiprocessing, splitting each
  peak calculation to the different processes.
'''

from numpy import sqrt, where, arctan2, abs, exp,pi, zeros_like, unique, minimum,
    sin, cos
from scipy.signal import fftconvolve
from plot_script.fit_data import FitFunction3D, register_class
from multiprocessing import Pool
import atexit

LAMBDA=4.51 # A

class PeakShapeResTilt(FitFunction3D):
  '''
    Fit a Gaussian or Lorentzian peak function with radial tilting distribution
    and a beam shape function convoluted with fft.
  '''

  # define class variables.
  name="Mesopeak + Resolution"
  # default parameters
  parameters=[0.058, 0.021, 0.0001, 0.0001,
              0., 0.001,
              0.,0.,0.,
              0.00531166, 0.000941805, 9233.57,
              0.3, 0.1,
              0.,
              ]
  # names of parameters
  parameter_names=['a*', 'c*', 'γ_y', 'γ_z', # peak parameters
```

```
                    'σ_tilt', 'σ_r', # tilt parameter in °
                    'Qy_off','Qz_off','Qphi_off', # instrumental offsets
                    'width' , 'height', 'decay', # instrumental parameters
                    'α_i', 'α_c',
                    'BG', # background
                    ]
    fit_function_text='Meso: a^*=[a*] c^*=[c*] γ_yγ=[_y|2] γ_zγ=[_z|2] σ_{tiltσ}=[_tilt
        |2]'
    parameter_description={'a*': 'Horizontal reciprocal lattice parameter',
                           'c*': 'Vertical reciprocal lattice parameter',
                           'Qy_off': 'Measurement Qy offset',
                           'Qz_off': 'Measurement Qz offset',
                           'Qphi_off': 'Measurement tilt offset',
                           'γ_y': 'Lorenz width in Qy-direction',
                           'γ_z': 'Lorenz width in Qz-direction',
                           'σ_tilt': 'Width of tilting angle',
                           'σ_r': 'Width of radial broughdening (distribution of
                               lattice size)',
                           'σ_y': 'Width of Qy broughdening (distribution of a
                               parameter)',
                           'σ_z': 'Width of Qz broughdening (distribution of c
                               parameter)',
                           'width': 'Beam width horizontal (window function)',
                           'height': 'Beam width vertical (widnow function)',
                           'decay': 'Speed of exponential intensity decay outside of
                               Beam window',
                           'BG': 'Background',
                           }

    use_rotation=True # default is an rotational average
    regions=None
    max_iter=50 # restrain the maximum number of iterations
    pool=None

    def __init__(self, initial_parameters=[], use_mp=False):
      FitFunction3D.__init__(self, initial_parameters)
      self.refine_parameters=[0,1,2,3,4,5]
      self.parameter_names=list(self.parameter_names)
      self.constrains={}
      if use_mp:
        # create a pool of worker processes
        self.activate_multiprocessing()

    def activate_multiprocessing(self):
      '''
        Create a worker pool.
      '''
      if self.pool is not None:
        self.deactivate_multiprocessing()
      self.pool=Pool()

    def deactivate_multiprocessing(self):
      '''
        Terminate the worker pool. Must be called before exiting
        the program, otherwise the processes stay alive and CTRL+c
        is needed to exit the program.
      '''
      if self.pool is not None:
        self.pool.close()
        self.pool.join()
        self.pool=None

    def add_region(self, xf, xt, yf, yt, Ii, Qyi, Qzi):
      '''
        Add an other peak with a defined fit region, intensity and position.
      '''
      if self.regions is None:
        self.regions=[]
      idx=len(self.regions)
      self.regions.append([xf, xt, yf, yt])
      self.parameters.append(Ii)
      self.parameters.append(Qyi)
```

```
105       self.parameters.append(Qzi)
106       self.parameter_names.append("I_%i"%idx)
107       self.parameter_names.append("Qy_%i"%idx)
108       self.parameter_names.append("Qz_%i"%idx)
109
110     def fit_function(self, p, x, y):
111       '''
112         Combined intensity function for several peak regions including
113         resolution and tilting.
114         Each peak is a convolution of the resolution function a
115         Gauusian/Lorentzian peak shape and a gaussian tilt and radial distribution.
116       '''
117       # get parameters by name
118       astar=p[0]
119       cstar=p[1]
120       gamma_y=p[2]
121       gamma_z=p[3]
122       sigma_tilt=p[4]/180.*pi
123       sigma_r=p[5]
124       Qy_off=p[6]
125       Qz_off=p[7]
126       Qphi_off=p[8]/180.*pi
127       width=p[9]
128       height=p[10]
129       decay=p[11]
130       alpha_i=p[12]*pi/180.
131       alpha_c=p[13]*pi/180.
132       BG=p[14]
133       if self.use_rotation:
134         self.parameter_names[4:6]=['σ_tilt', 'σ_r']
135       else:
136         self.parameter_names[4:6]=['σ_y', 'σ_z']
137       # if no region is defined the selected fit area is taken as region
138       if self.regions is None:
139         raise IndexError, "no peak defined"
140       else:
141         # each region has corresponding intensity, Qy- and Qz-position parameters
142         regions=[[reg[0], reg[1], reg[2], reg[3],p[15+3*i], p[16+3*i], p[17+3*i]] \
143                           for i,reg in enumerate(self.regions)]
144       I=zeros_like(x)
145       background=zeros_like(x)
146       I_list=[]
147       param_list=[]
148       res_list=[]
149       idx_list=[]
150       pix_size=None
151       # peaks for all regions
152       for xf, xt, yf, yt, Ii, HK, L in regions:
153         # get indices of points in the region
154         idx=where((x>=xf)&(x<=xt)&(y>=yf)&(y<=yt))
155         # calc position with phi offset
156         Qyi=HK*astar
157         Qzi=L*cstar
158
159         # reshape x and y to two dimensional array
160         ux=unique(x[idx])
161         uy=unique(y[idx])
162         xitems=len(ux)
163         yitems=len(uy)
164         if pix_size is None:
165           pix_size=(ux[1]-ux[0])*(uy[1]-uy[0])
166         # calculate pixel size for normaliztaion
167         Qy=x[idx].reshape(yitems, xitems)
168         Qz=y[idx].reshape(yitems, xitems)
169         # correct instrumental missalignment
170         # 0-offset
171         Qy=Qy-Qy_off
172         Qz=Qz-Qz_off
173         # sample tilting
174         Qytmp=Qy
175         Qy= cos(Qphi_off)*Qytmp+sin(Qphi_off)*Qz
176         Qz=-sin(Qphi_off)*Qytmp+cos(Qphi_off)*Qz
```

```
177
178         in_list=[Qy, Qz, Qyi, Qzi, gamma_y, gamma_z,
179                  sigma_tilt, sigma_r,
180                  width, height, decay,
181                  alpha_i, alpha_c,
182                  Ii, self.use_rotation]
183         idx_list.append(idx)
184         if self.pool is None:
185           # calculate one peak
186           I_list.append(calc_I(in_list))
187         else:
188           # send calculation of one peak to the multiprocessing pool
189           res_list.append(self.pool.apply_async(calc_I, args=(in_list,)))
190       if self.pool is not None:
191         # fetch the results of the multiprocessing calculations
192         I_list=map(lambda item: item.get(), res_list)
193       for idx, Ip in zip(idx_list, I_list):
194         # add peak intensity to output
195         I[idx]+=Ip.flatten()
196         background[idx]=BG
197       return I+background # add background
198
199     def to_list(self):
200       '''
201         Get all important parameters as a list.
202       '''
203       return [self.parameters, self.parameter_names,
204               self.regions, [self.x_from, self.x_to, self.y_from, self.y_to],
205               self.refine_parameters]
206
207     def from_list(self, param_list):
208       '''
209         Set all important parameters from a list.
210       '''
211       self.parameters=list(param_list[0])
212       self.parameter_names=list(param_list[1])
213       self.regions=list(param_list[2])
214       self.x_from,self.x_to,self.y_from,self.y_to=param_list[3]
215       self.refine_parameters=list(param_list[4])
216
217     def add_mirrors(self):
218       '''
219         For each region add the mirror peak on the other side of the specular line.
220       '''
221       regions=self.regions
222       regparams=[[self.parameters[15+3*i],self.parameters[16+3*i],self.parameters
              [17+3*i]]
223                  for i in range(len(regions))]
224       pstart=15+3*len(regions)
225       for i, regi, parami in zip(range(len(regions)), regions, regparams):
226         self.add_region(-regi[1], -regi[0], regi[2], regi[3], parami[0], -parami[1],
              parami[2])
227         # constrain all peak parameters to the original peak
228         self.constrains[pstart+3*i]={'bounds': [None, None], 'tied': '[I_%i]'%i}
229         self.constrains[pstart+1+3*i]={'bounds': [None, None], 'tied': '-[Qy_%i]'%i}
230         self.constrains[pstart+2+3*i]={'bounds': [None, None], 'tied': '[Qz_%i]'%i}
231         for j in range(3):
232           # fit parameter if original was selected
233           if (15+j+3*i) in self.refine_parameters:
234             self.refine_parameters.append(pstart+j+3*i)
235       self.x_from=-self.x_to
236
237   def Qz_obs(Qz, alpha_i, alpha_c):
238     k0=2.*pi/LAMBDA
239     return k0*(sin(alpha_i)+
240              sqrt(sin(alpha_c)**2+
241                  (Qz*LAMBDA/(2.*pi)-sqrt(sin(alpha_i)**2-sin(alpha_c)**2))**2
242                  ))
243
244
245   def gaussian_tilt(Qy, Qz, Qy0, Qz0, sigma_tilt, sigma_r):
246     '''
```

```
247       Return a peak with gaussian tilt and radius components.
248     '''
249     Qr=sqrt(Qy**2+Qz**2)
250     Qphi=arctan2(Qz,Qy)
251     Qr0=sqrt(Qy0**2+Qz0**2)
252     Qphi0=arctan2(Qz0,Qy0)
253     #tilt_norm=1./(2.*pi*sigma_r*sigma_tilt)
254     tilt_shape=exp(-0.5*(((Qr-Qr0)/(sigma_r*Qr0))**2+((Qphi-Qphi0)/sigma_tilt)**2))
255     return tilt_shape#*tilt_norm
256
257   def beam(x, y, width, height, fall=8000., pix_size=1e-10):
258     '''
259       Calculate a beam shape function as a window horizontal and
260       vertical widnow with exponentially decaying edges.
261     '''
262     px=exp(-fall*(abs(x)-width/2.))
263     py=exp(-fall*(abs(y)-height/2.))
264     if height<=pix_size:
265       pos=(y<=pix_size)&(y>=-pix_size)
266       py[pos]=minimum(1.-abs(y[pos])/pix_size,0.)
267     if width<=pix_size:
268       pos=(x<=pix_size)&(x>=-pix_size)
269       px[pos]=minimum(1.-abs(y[pos])/pix_size, 0.)
270     Peak=minimum(px, 1.)*minimum(py,1.)
271
272     return Peak#/Peak.sum()
273
274   def gaussian(x,y,sigma_x, sigma_y):
275     '''
276       Not normalized Gaussian peak shape function.
277     '''
278     #norm=1./(2.*pi*sigma_x*gamma_y)
279     G=exp(-0.5*((x/sigma_x)**2+(y/sigma_y)**2))
280     return G#*norm
281
282   def lorentzian(x,y,gamma_x, gamma_y, pix_size):
283     '''
284       Not normalized lorentzian peak shape function.
285     '''
286     #norm=1./((pi*gamma_x*gamma_y))
287     L=1./(1.+((x/gamma_x)**2+(y/gamma_y)**2))
288     # make sure the maximum of the function is not reduced by too small gamma values
289     if gamma_x<=pix_size and gamma_y<=pix_size:
290       L[(x<=pix_size/2.)&(x>=-pix_size/2.)&(y<=pix_size/2.)&(y>=-pix_size/2.)]=1.
291     elif gamma_x<=pix_size:
292       pos=(x<=pix_size/2.)&(x>=-pix_size/2.)
293       L[pos]=1./(1.+(y[pos]/gamma_y)**2)
294     elif gamma_y<=pix_size:
295       pos=(y<=pix_size/2.)&(y>=-pix_size/2.)
296       L[pos]=1./(1.+(x[pos]/gamma_x)**2)
297     return L#*norm
298
299   def calc_I(in_list):
300     '''
301       Calculate intensity on one region.
302     '''
303     Qy, Qz, Qyi, Qzi=in_list[:4]
304     gamma_y, gamma_z=in_list[4:6]
305     sigma_tilt, sigma_r=in_list[6:8]
306     width, height, decay=in_list[8:11]
307     alpha_i, alpha_c=in_list[11:13]
308     Ii=in_list[13]
309     use_rotation=in_list[14]
310     # calculate approx. pixe size
311     pix_size=(Qz.max()-Qz.min())/len(Qz)
312     if sigma_tilt==0:
313       # no tilting of mesos
314       # calculate peak shape function
315       Ip=lorentzian(Qy-Qyi,Qz-Qzi,gamma_y, gamma_z, pix_size)
316     else:
317       # tilting of mesos
318       # calculate peak shape function
```

```
319       peak_shape=lorentzian(Qy-Qy.mean(), Qz-Qz.mean(), gamma_y, gamma_z, pix_size)
320       if use_rotation:
321         # calculate tilt and radial distribution function
322         gauss_shape=gaussian_tilt(Qy,Qz,Qyi,Qzi, sigma_tilt, sigma_r)
323       else:
324         # calculate gaussian distribution in Qy and Qz direction
325         gauss_shape=gaussian(Qy-Qyi,Qz-Qzi, sigma_tilt*180./pi*Qyi, sigma_r*Qzi)
326       # convolute tilt and radial distribution with peak shape
327       Ip=fftconvolve(peak_shape, gauss_shape, 'same')
328     if height!=0 and width!=0:
329       # calculate beam shape function
330       # the peak position is moved due to refraction effects
331       Qzi_obs=Qz_obs(Qzi, alpha_i, alpha_c)
332       beam_shape=beam(Qy-Qy.mean(), Qz-Qz.mean()-Qzi_obs+Qzi, width, height, decay,
              pix_size)
333       # convolute peak shape with beam shape
334       Ip=fftconvolve(beam_shape, Ip, 'same')
335     return Ii*Ip/Ip.sum() # normalize to integrated intensity
336
337   class BeamResolution(FitFunction3D):
338     '''
339       A pure resolution function to refine the peak shape with
340       e.g. silicon total reflection measurement.
341     '''
342     name="Resolution"
343     parameters=[10000., 0., 0.177, 0.00531166, 0.000941805, 9233.57]
344     parameter_names=['I0', 'x0','y0','width','height','decay']
345     fit_function_text='Resolution'
346
347     def fit_function(self, p, x, y):
348       I0,x0,y0,w,h,d=p
349       return I0*beam(x-x0,y-y0,w,h,d)
350
351   # Add class to the available fit functions in Plot.py
352   register_class(PeakShapeResTilt)
353   register_class(BeamResolution)
354
355   #[0.031860800000000002, 0.055555899999999998, 0.10974299999999999,
          0.0018228000000000001, 0.0019904900000000001, 5.2483300000000002,
          0.00013660899999999999, 0.0028664099999999998, 0.0, 0.020954199999999999,
          0.058215099999999999, 0.089450399999999999]
356   #[[0.035, 0.08, 0.085, 0.13], [0.035, 0.08, 0.07, 0.115]]
```

B.5 GeniX plugin for a reflectivity simulation of an ensemble of mesocrystals

```
1   '''
2     Simulating nanoparticle assamblies.
3   '''
4   from numpy import *
5
6   import lib.paratt as Paratt
7   import lib.neutron_refl as MatrixNeutron
8   from lib.instrument import *
9   # Preamble to define the parameters needed for the models outlined below:
10
11  ModelID='SpecNX'
12
13  __pars__=['Layer', 'Stack', 'Sample', 'Instrument']
14  instrument_string_choices={'probe': ['x-ray', 'neutron', 'neutron pol', \
15      'neutron pol spin flip', 'neutron tof', 'neutron pol tof'], 'coords': ['q', 'tth
            '], \
16      'restype': ['no conv', 'fast conv', \
17       'full conv and varying res.', 'fast conv + varying res.'], \
18      'footype': ['no corr', 'gauss beam', 'square beam'], \
19      'pol': ['uu', 'dd', 'ud']}
20
21  InstrumentParameters={'probe':'x-ray', 'wavelength':1.54, 'coords':'q', \
```

```
22      'I0': 1.0, 'res': 0.001, 'coherence_length': 3000., \
23     'restype':'fast conv', 'respoints': 5, 'resintrange': 2, 'beamw':0.2, \
24      'footype': 'square beam', 'samplelen': 10.0, 'incangle': 0.0, 'pol': 'uu', \
25     'Ibkg': 0.0}
26
27  InstrumentGroups=[('General', ['wavelength', 'coords', 'I0', 'Ibkg', '
        coherence_length']),
28                    ('Resolution', ['restype', 'res', 'respoints', 'resintrange']),
29                    ('Neutron', ['probe', 'pol', 'incangle']),
30                    ('Footprint', ['footype', 'beamw', 'samplelen', ]),
31                    ]
32
33  InstrumentUnits={'probe':'', 'wavelength': 'AA', 'coords':'', \
34       'I0': 'arb.', 'res': '[coord]', 'coherence_length': 'AA', \
35     'restype':'', 'respoints':'pts.', 'resintrange':'[coord]', 'beamw':'mm', \
36      'footype': '', 'samplelen':'mm', 'incangle':'deg.', 'pol': '', \
37     'Ibkg': 'arb.'}
38
39  LayerParameters={'sigma':0.0, 'dens':1.0, 'd':0.0, 'f':(1.0+1.0j)*1e-20,
40       'b': 0.0+1.0J, 'xs_ai': 0.0, 'magn':0.0, 'magn_ang':0.0,
41       'np_z_position': 0.5, 'np_type': 0}
42  LayerUnits={'sigma': 'AA', 'dens': 'at./AA', 'd': 'AA', 'f':'el./at.',
43       'b': 'fm/at.', 'xs_ai': 'barn/at.', 'magn': 'mu_B/at.', 'magn_ang': 'deg.',
44       'np_z_position': '', 'np_type': '0/1'}
45  LayerGroups=[('Standard', ['f', 'dens', 'd', 'sigma']),
46                ('Neutron', ['b', 'xs_ai', 'magn', 'magn_ang']),
47                ('Particles', ['np_z_position', 'np_type'])]
48  StackParameters={'Layers':[], 'Repetitions': 1, 'slices': 10, 'is_meso': 0,
49                   'r_bottom': 1500., 'r_top': 1000., 'surface_density': 25.,
50                   'c_bottom': 100., 'c_top': 100., 'c_var_layers': 5, 'aspect_ratio':
                         1.,
51                   'f_matrix': 0.j, 'dens_matrix': 1., 'b_matrix': 0.j, 'magn_matrix':
                         0., 'magn_ang_matrix': 0.}
52  StackGroups=[('General', ['Repetitions', 'slices', 'is_meso']),
53                ('Meso Crylstals', ['r_top', 'r_bottom', 'surface_density']),
54                ('Unit Cell', ['c_top', 'c_bottom', 'c_var_layers', 'aspect_ratio']),
55                ('Meso Matrix', ['f_matrix', 'dens_matrix', 'b_matrix', 'magn_matrix'
                      , 'magn_ang_matrix']),
56                ]
57  StackUnits={
58               'Repetitions': '', 'slices': '', 'is_meso': '0/1',
59                 'r_bottom': 'AA', 'r_top': 'AA', 'surface_density': '%',
60                 'c_top': 'AA', 'c_bottom': 'AA', 'c_var_layers': '', 'aspect_ratio':
                       'c/a',
61                 'f_matrix': 'et./at.', 'dens_matrix': 'at./AA',
62                 'b_matrix': 'fm/at.', 'magn_matrix': 'mu_B/at.', 'magn_ang_matrix':
                       'deg.',
63               }
64  SampleParameters={'Stacks':[], 'Ambient':None, 'Substrate':None}
65
66
67  # define the density profiles for the different types of particles
68  # density is defined as particle surface in a layer
69  def profile_sphere(idp, d):
70    r=d/2.
71    return where(abs(idp)<r, (pi*(r**2-idp**2)), 0.)
72  def profile_cube(idp, a):
73    return (abs(idp)<=a)*a**2
74
75  DENSITY_PROFILES=[profile_sphere, profile_cube]
76  SINGLE_PART=-1
77
78  # A buffer to save previous calculations for spin-flip calculations
79  class Buffer:
80      Ruu=0
81      Rdd=0
82      Rdu=0
83      Rud=0
84      parameters=None
85
86  def Specular(TwoThetaQz, sample, instrument):
87      # calculate the reflectivity for the different parts of the sample
```

```
88      # which lie in one correlation area (top of meso, edges of mesos, bottom)
89      meso=None
90      for stack in reversed(sample.Stacks):
91        if stack.is_meso:
92          meso=stack
93          break
94
95      if meso is None:
96        # simulation without mesos
97        R=SpecRaw(TwoThetaQz, sample, instrument)
98        return SpecRes(TwoThetaQz, sample, instrument, R)
99
100     # calculate intensity for space between mesos
101     meso.dens_bottom=0.0
102     meso.dens_top=0.0
103     Rfree=SpecRaw(TwoThetaQz, sample, instrument)
104     # calculate intensity for meso edges
105     # if the slope is lower than the coherence length/2
106     # it gets calculated in several steps
107     if (meso.r_bottom-meso.r_top)>=(instrument.coherence_length/2.):
108       r_steps=arange(meso.r_top,
109                      meso.r_bottom+instrument.coherence_length,
110                      instrument.coherence_length/2.)
111       Pall=(meso.r_bottom+instrument.coherence_length/2.)**2/\
112             (meso.r_top-instrument.coherence_length/2.)**2
113       Psteps=(r_steps[1:]-r_steps[:-1])*2/Pall
114       Psteps/=Psteps[:-1].sum()
115       Redge=zeros_like(Rfree)
116       for i, ri in enumerate(r_steps[:-1]):
117         meso.dens_top=(meso.r_bottom**2-(ri+instrument.coherence_length/2.)**2)/(
              meso.r_bottom**2-meso.r_top**2)
118         meso.dens_bottom=(meso.r_bottom**2-(ri-instrument.coherence_length/2.)**2)/(
              meso.r_bottom**2-meso.r_top**2)
119         Redge+=Psteps[i]*SpecRaw(TwoThetaQz, sample, instrument)
120     else:
121       meso.dens_top=0.5*(1.-(meso.r_top/meso.r_bottom))
122       meso.dens_bottom=0.5*(1+(meso.r_top/meso.r_bottom))
123       Redge=SpecRaw(TwoThetaQz, sample, instrument)
124     # calculate intensity for meso center
125     meso.dens_bottom=1.0
126     meso.dens_top=1.0
127     Rtop=SpecRaw(TwoThetaQz, sample, instrument)
128     # combine intensities
129     meso_outer_area=(meso.r_bottom+instrument.coherence_length/2.)**2
130     meso_inner_area=min([meso.r_top-instrument.coherence_length/2., 0.])**2
131     full_area=meso_outer_area/meso.surface_density*100. # full area is mesocrystal/
            mc-density
132     free_area=full_area-meso_outer_area
133     edge_area=meso_outer_area-meso_inner_area
134     if SINGLE_PART<0:
135       # combined reflectivity
136       R=free_area/full_area*Rfree+meso_inner_area/full_area*Rtop+edge_area/full_area
              *Redge
137     elif SINGLE_PART==1:
138       R=Rfree
139     elif SINGLE_PART==2:
140       R=Redge
141     else:
142       R=Rtop
143     # for SLD use some kind of approximation
144     meso.dens_bottom=1.-free_area/full_area
145     meso.dens_top=(1.-free_area/full_area)*(meso.r_top**2/meso.r_bottom**2)
146     # Resolution corrections and return
147     return SpecRes(TwoThetaQz, sample, instrument, R)
148
149 def SpecRaw(TwoThetaQz, sample, instrument):
150     # preamble to get it working with my class interface
151     restype=instrument.getRestype()
152
153     if restype==2 or restype==instrument_string_choices['restype'][2]:
154         (TwoThetaQz, ignore)=ResolutionVector(TwoThetaQz[:], \
155               instrument.getRes(), instrument.getRespoints(), \
```

```
156                 range_=instrument.getResintrange())
157     # TTH values given as x
158     if instrument.getCoords()==instrument_string_choices['coords'][1]\
159      or instrument.getCoords()==1:
160         Q=4*pi/instrument.getWavelength()*sin(TwoThetaQz*pi/360.0)
161     # Q vector given....
162     elif instrument.getCoords()==instrument_string_choices['coords'][0]\
163      or instrument.getCoords()==0:
164         Q=TwoThetaQz
165     else:
166         raise ValueError('The value for coordinates, coords, is WRONG!'
167                          'should be q(0) or tth(1).')
168 
169     type_=instrument.getProbe()
170     pol=instrument.getPol()
171 
172     #lamda = instrument.getWavelength()
173     parameters=sample.resolveLayerParameters()
174     if type_==instrument_string_choices['probe'][0] or type_==0:
175         fb=array(parameters['f'], dtype=complex64)
176     else:
177         fb=array(parameters['b'], dtype=complex64).real*1e-5
178         abs_xs=array(parameters['xs_ai'], dtype=complex64)*(1e-4)**2
179 
180     dens=array(parameters['dens'], dtype=complex64)
181     d=array(parameters['d'], dtype=float64)
182     magn=array(parameters['magn'], dtype=float64)
183     #Transform to radians
184     magn_ang=array(parameters['magn_ang'], dtype=float64)*pi/180.0
185 
186     sigma=array(parameters['sigma'], dtype=float64)
187 
188 
189     if type_==instrument_string_choices['probe'][0] or type_==0:
190         sld=dens*fb*instrument.getWavelength()**2/2/pi
191     else:
192         wl=instrument.getWavelength()
193         sld=dens*(wl**2/2/pi*sqrt(fb**2-(abs_xs/2.0/wl)**2)-
194                                   1.0J*abs_xs*wl/4/pi)
195     # Ordinary Paratt X-rays
196     if type_==instrument_string_choices['probe'][0] or type_==0:
197         R=Paratt.ReflQ(Q, instrument.getWavelength(), 1.0-2.82e-5*sld, d, sigma)
198     #Ordinary Paratt Neutrons
199     elif type_==instrument_string_choices['probe'][1] or type_==1:
200         R=Paratt.ReflQ(Q, instrument.getWavelength(), 1.0-sld, d, sigma)
201     #Ordinary Paratt but with magnetization
202     elif type_==instrument_string_choices['probe'][2] or type_==2:
203         msld=2.645e-5*magn*dens*instrument.getWavelength()**2/2/pi
204         # Polarization uu or ++
205         if pol==instrument_string_choices['pol'][0] or pol==0:
206             R=Paratt.ReflQ(Q, instrument.getWavelength(), \
207                 1.0-sld-msld, d, sigma)
208         # Polarization dd or --
209         elif pol==instrument_string_choices['pol'][1] or pol==1:
210             R=Paratt.ReflQ(Q, instrument.getWavelength(), \
211                  1.0-sld+msld, d, sigma)
212         else:
213             raise ValueError('The value of the polarization is WRONG.'
214                 ' It should be uu(0) or dd(1)')
215     # Spin flip
216     elif type_==instrument_string_choices['probe'][3] or type_==3:
217         # Check if we have calcluated the same sample previous:
218         if Buffer.parameters!=parameters:
219             msld=2.645e-5*magn*dens*instrument.getWavelength()**2/2/pi
220             np=1.0-sld-msld
221             nm=1.0-sld+msld
222             wl=instrument.getWavelength()
223             (Ruu, Rdd, Rud, ignore)=MatrixNeutron.Refl(Q, wl, np, nm, d, magn_ang)
224             Buffer.Ruu=Ruu; Buffer.Rdd=Rdd; Buffer.Rud=Rud
225             Buffer.parameters=parameters.copy()
226         else:
227             pass
```

```
228         # Polarization uu or ++
229         if pol==instrument_string_choices['pol'][0] or pol==0:
230             R=Buffer.Ruu
231         # Polarization dd or --
232         elif pol==instrument_string_choices['pol'][1] or pol==1:
233             R=Buffer.Rdd
234         # Polarization ud or +-
235         elif pol==instrument_string_choices['pol'][2] or pol==2:
236             R=Buffer.Rud
237         else:
238             raise ValueError('The value of the polarization is WRONG.'
239                 ' It should be uu(0), dd(1) or ud(2)')
240 
241     # tof
242     elif type_==instrument_string_choices['probe'][4] or type_==4:
243         wl=4*pi*sin(instrument.getIncangle()*pi/180)/Q
244         sld=dens[:, newaxis]*(wl**2/2/pi*sqrt(fb[:, newaxis]**2-
245                                               (abs_xs[:, newaxis]/2.0/wl)**2)-
246                               1.0J*abs_xs[:, newaxis]*wl/4/pi)
247         R=Paratt.Refl_nvary2(instrument.getIncangle()*ones(Q.shape), \
248             (4*pi*sin(instrument.getIncangle()*pi/180)/Q), \
249                 1.0-sld, d, sigma)
250     # tof spin polarized
251     elif type_==instrument_string_choices['probe'][5] or type_==5:
252         wl=4*pi*sin(instrument.getIncangle()*pi/180)/Q
253         sld=dens[:, newaxis]*(wl**2/2/pi*sqrt(fb[:, newaxis]**2-
254                                               (abs_xs[:, newaxis]/2.0/wl)**2)-
255                               1.0J*abs_xs[:, newaxis]*wl/4/pi)
256         msld=2.645e-5*magn[:, newaxis]*dens[:, newaxis]\
257                 *(4*pi*sin(instrument.getIncangle()*pi/180)/Q)**2/2/pi
258         # polarization uu or ++
259         if pol==instrument_string_choices['pol'][0] or pol==0:
260             R=Paratt.Refl_nvary2(instrument.getIncangle()*ones(Q.shape), \
261                 (4*pi*sin(instrument.getIncangle()*pi/180)/Q), \
262                  1.0-sld-msld, d, sigma)
263         # polarization dd or --
264         elif pol==instrument_string_choices['pol'][1] or pol==1:
265             R=Paratt.Refl_nvary2(instrument.getIncangle()*ones(Q.shape), \
266              (4*pi*sin(instrument.getIncangle()*pi/180)/Q), \
267               1.0-sld+msld, d, sigma)
268         else:
269             raise ValueError('The value of the polarization is WRONG.'
270                 ' It should be uu(0) or dd(1)')
271     else:
272         print type_
273         raise ValueError('The choice of probe is WRONG')
274     return R
275 
276 def SpecRes(TwoThetaQz, sample, instrument, R):
277     # preamble to get it working with my class interface
278     restype=instrument.getRestype()
279 
280     if restype==2 or restype==instrument_string_choices['restype'][2]:
281         (TwoThetaQz, weight)=ResolutionVector(TwoThetaQz[:], \
282               instrument.getRes(), instrument.getRespoints(), \
283                range_=instrument.getResintrange())
284     # TTH values given as x
285     if instrument.getCoords()==instrument_string_choices['coords'][1]\
286      or instrument.getCoords()==1:
287         Q=4*pi/instrument.getWavelength()*sin(TwoThetaQz*pi/360.0)
288     # Q vector given....
289     elif instrument.getCoords()==instrument_string_choices['coords'][0]\
290      or instrument.getCoords()==0:
291         Q=TwoThetaQz
292     else:
293         raise ValueError('The value for coordinates, coords, is WRONG!'
294                          'should be q(0) or tth(1).')
295 
296 #     type_=instrument.getProbe()
297 #     pol = instrument.getPol()
298 #
299 #     lamda = instrument.getWavelength()
```

```
#     parameters = sample.resolveLayerParameters()
#     if type_ ==  instrument_string_choices['probe'][0] or type_==0:
#         fb = array(parameters['f'], dtype = complex64)
#     else:
#         fb = array(parameters['b'], dtype = complex64).real*1e-5
#         abs_xs = array(parameters['xs_ai'], dtype = complex64)*(1e-4)**2
    #FootprintCorrections

    foocor=1.0
    footype=instrument.getFootype()
    beamw=instrument.getBeamw()
    samlen=instrument.getSamplelen()
    theta=arcsin(Q*instrument.getWavelength()/4.0/pi)*180/pi
    if footype==1 or footype==instrument_string_choices['footype'][1]:
        foocor=GaussIntensity(theta, samlen/2.0, samlen/2.0, beamw)
    elif footype==2 or footype==instrument_string_choices['footype'][2]:
        foocor=SquareIntensity(theta, samlen, beamw)
    elif footype==0 or footype==instrument_string_choices['footype'][0]:
        pass
    else:
        raise ValueError('The choice of footprint correction, footype,'
            'is WRONG')

    #Resolution corrections
    if restype==instrument_string_choices['restype'][1] or restype==1:
        R=ConvoluteFast(TwoThetaQz, R[:]*foocor, instrument.getRes(), \
             range_=instrument.getResintrange())
    elif restype==instrument_string_choices['restype'][2] or restype==2:
        R=ConvoluteResolutionVector(TwoThetaQz, R[:]*foocor, weight)
    elif restype==instrument_string_choices['restype'][3] or restype==3:
        R=ConvoluteFastVar(TwoThetaQz, R[:]*foocor, instrument.getRes(), \
            range_=instrument.getResintrange())
    elif restype==instrument_string_choices['restype'][0] or restype==0:
        R=R[:]*foocor
    else:
        raise ValueError('The choice of resolution type, restype,'
            'is WRONG')

    return R*instrument.getI0()+instrument.getIbkg()


def OffSpecularMingInterdiff(TwoThetaQz, ThetaQx, sample, instrument):
    raise NotImplementedError('Not implemented use model interdiff insteads')
    return TwoThetaQz, ThetaQx

def SLD_calculations(z, sample, inst):
    ''' Calculates the scatteringlength density as at the positions z
    '''
    parameters=sample.resolveLayerParameters()
    dens=array(parameters['dens'], dtype=complex64)
    f=array(parameters['f'], dtype=complex64)
    b=array(parameters['b'], dtype=complex64)
    type_=inst.getProbe()
    magnetic=False
    mag_sld=0
    if type_==instrument_string_choices['probe'][0] or type_==0:
        sld=dens*f
    elif type_==instrument_string_choices['probe'][1] or type_==1 or\
        type_==instrument_string_choices['probe'][4] or type_==4:
        sld=dens*b
    else:
        magnetic=True
        sld=dens*b
        magn=array(parameters['magn'], dtype=float64)
        #Transform to radians
        #magn_ang=array(parameters['magn_ang'], dtype=float64)*pi/180.0
        mag_sld=2.645*magn*dens

    d=array(parameters['d'], dtype=float64)
    d=d[1:-1]
    # Include one extra element - the zero pos (substrate/film interface)
    int_pos=cumsum(r_[0, d])
```

```
372     sigma=array(parameters['sigma'], dtype=float64)[:-1]+1e-7
373     if z==None:
374         z=arange(-sigma[0]*5, int_pos.max()+sigma[-1]*5, 0.5)
375     if not magnetic:
376         rho=sum((sld[:-1]-sld[1:])*(0.5-\
377             0.5*erf((z[:, newaxis]-int_pos)/sqrt(2.)/sigma)), 1)+sld[-1]
378         dic={'real sld': real(rho), 'imag sld': imag(rho), 'z':z}
379     else:
380         sld_p=sld+mag_sld
381         sld_m=sld-mag_sld
382         rho_p=sum((sld_p[:-1]-sld_p[1:])*(0.5-\
383             0.5*erf((z[:, newaxis]-int_pos)/sqrt(2.)/sigma)), 1)+sld_p[-1]
384         rho_m=sum((sld_m[:-1]-sld_m[1:])*(0.5-\
385             0.5*erf((z[:, newaxis]-int_pos)/sqrt(2.)/sigma)), 1)+sld_m[-1]
386         dic={'real sld +': real(rho_p), 'imag sld +': imag(rho_p), \
387                 'real sld -': real(rho_m), 'imag sld -': imag(rho_m), 'z':z}
388     return dic
389
390 SimulationFunctions={'Specular':Specular, \
391                      'OffSpecular':OffSpecularMingInterdiff, \
392                      'SLD': SLD_calculations\
393                     }
394
395 import lib.refl as Refl
396 (Instrument, Layer, Stack, Sample)=Refl.MakeClasses(InstrumentParameters, \
397     LayerParameters, StackParameters, SampleParameters, SimulationFunctions, \
398     ModelID)
399
400 def resolveLayerParameter(self, parameter):
401   # if stack type includes nanoparticles, the parameters consist of slices
402   if self.is_meso:
403     # c-parameter variation from bottom to top, lower layers stay constant
404     c_all=[self.c_bottom]*int(max([(self.Repetitions-self.c_var_layers), 0]))+\
405           linspace(self.c_bottom, self.c_top, min([self.c_var_layers, self.
                Repetitions])).tolist()
406     if parameter=='d':
407       par=[]
408       for ci in c_all:
409         par+=[ci/self.slices]*int(self.slices)
410     elif parameter=='dens':
411       par=[1.0]*int(self.Repetitions*self.slices)
412     elif parameter=='sigma':
413       par=[]
414       for ci in c_all:
415         par+=[ci/self.slices/2.]*int(self.slices)
416     elif parameter in ['b', 'f', 'magn', 'magn_ang']:
417       par=[]
418       SLD_matrix=getattr(self, parameter+'_matrix')*self.dens_matrix
419       # The mesos can be more dens on bottom than on top
420       # the dens_bottom and dens_top parameters are set during the intensity
              calculations.
421       # The density of the lowest layer is always 1.
422       dens_all=[1./(self.c_bottom/self.aspect_ratio)**2]+\
423                         linspace(getattr(self, 'dens_bottom', 1.)/(self.c_bottom/
                              self.aspect_ratio)**2,
424                                  getattr(self, 'dens_top', 1.)/(self.c_top/self.
                                       aspect_ratio)**2,
425                         self.Repetitions).tolist()
426       for i, dens_from_to in enumerate(zip(dens_all[:-1], dens_all[1:])):
427         dens=linspace(dens_from_to[0], dens_from_to[1], self.slices)
428         pari=(SLD_matrix*dens)
429         for lay in self.Layers:
430           # add SLDs of all particles in the unit cell
431           lay.calculate_slices(parameter, c_all[i], pari, SLD_matrix*dens[0], dens,
432                                bottom=(i==0), top=(i==(self.Repetitions-1)))
433         par+=pari.tolist()
434     else:
435       par=[0.]*int(self.Repetitions*self.slices)
436   else:
437     par=[lay.__getattribute__(parameter)+0.0 for lay in self.Layers]*self.
          Repetitions
438   return par
```

```
439
440 def calculate_slices(self, parameter, c, slices, matrix, dens, bottom=True, top=
        False):
441   ''' Calculate the SLD profile for one nanoparticle layer as a
442       sum of all profiles from the particles inside.
443   '''
444   SLD=getattr(self, parameter)*self.dens
445   d=c/len(slices)
446   sigma=self.sigma # smear out the position of the particles
447   if sigma==0:
448     d_pos=[0.]
449     P_pos=[1.]
450   else:
451     d_pos=arange(-2*sigma, 2*sigma+d/2., d/2.)
452     P_pos=exp(-0.5*d_pos**2/sigma**2)
453     P_pos/=P_pos.sum()
454   # structure types
455   profile=DENSITY_PROFILES[int(self.np_type)]
456   # calculate SLDs
457   if bottom:
458     dens=[dens[0]]*len(dens)
459   tmp_slice=zeros_like(slices)
460   pos=arange(len(slices))*d
461   for deli, Pi in zip(d_pos, P_pos):
462     # position of the slice
463     # center position of the nanoparticle
464     np_pos=self.np_z_position*c+deli
465     idp=pos-np_pos
466     tmp_slice+=Pi*(SLD-matrix)*profile(idp, self.d)*dens
467     if not bottom:
468       # particle parts sticking out from the lower lying UC
469       tmp_slice+=Pi*(SLD-matrix)*profile(idp+c, self.d)*dens
470     if not top:
471       # particle parts sticking out from the hight lying UC
472       tmp_slice+=Pi*(SLD-matrix)*profile(idp-c, self.d)*dens
473   slices+=tmp_slice
474 #  for i in range(len(slices)):
475 #    tmp_slice=0.
476 #    for deli, Pi in zip(d_pos, P_pos):
477 #      # position of the slice
478 #      pos=i*d
479 #      # center position of the nanoparticle
480 #      np_pos=self.np_z_position*c+deli
481 #      idp=pos-np_pos
482 #      tmp_slice+=Pi*(SLD-matrix)*profile(idp, self.d)*dens[i]
483 #      if not bottom:
484 #        # particle parts sticking out from the lower lying UC
485 #        tmp_slice+=Pi*(SLD-matrix)*profile(idp+c, self.d)*dens[i]
486 #      if not top:
487 #        # particle parts sticking out from the hight lying UC
488 #        tmp_slice+=Pi*(SLD-matrix)*profile(idp-c, self.d)*dens[i]
489 #    slices[i]+=tmp_slice
490
491 Layer.calculate_slices=calculate_slices
492 Stack.resolveLayerParameter=resolveLayerParameter
493
494 if __name__=='__main__':
495     pass
```

Appendix C

Bibliography

Books

[1] S. Blügel, D. Bürgler, M. Morgenstern, C. M. Schneider, and R. Waser (eds.), *Spintronics - From GMR to Quantum Information*, Forschungszentrum Jülich GmbH Institut für Festkörperforschung, (2009)

[2] S. Blundell, *Magnetism in Condensed Matter (Oxford Master Series in Physics)*, Oxford University Press, USA, December 2001

[3] T. Brückel, G. Heger, D. Richter, and R. Zorn (eds.), *Neutron Scattering*, vol. 5, Forschungszentrum Jülich GmbH, (2008)

[4] W. Demtröder, *Experimentalphysik 2 Elektrizität und Optik*, Springer-Lehrbuch, Springer Berlin Heidelberg, (2006)

[5] W. Demtröder, *Experimentalphysik 1 Mechanik und Wärme*, Springer-Lehrbuch, Springer Berlin Heidelberg, (2008)

[6] H. Fuess, T. Hahn, H. Wondratschek, U. Müller, U. Shmueli, A. Authier, V. Kopský, D. B. Litvin, M. G. Rossmann, E. Arnold, S. Hall, and M. B., *International tables for crystallography*, T. Hahn (ed.), Wiley, New York, (1983)

[7] C. Giacovazzo, *Fundamentals of crystallography*, Oxford University Press, Oxford; New York, (2011)

[8] A. Guimarães, *Principles of Nanomagnetism*, Springer Berlin / Heidelberg, (2009)

[9] T. L. Hill, *Statistical Mechanics: Principles and Selected Applications*, Dover Books on Physics, Dover Publications, (1987)

[10] J. N. Israelachvili, *Intermolecular and Surface Forces: With Applications to Colloidal and Biological Systems (Colloid Science)*, Academic Press, (1992)

[11] W. Kleber, H.-J. Bautsch, J. Böhm, and D. Klimm, *Einführung in die Kristallographie*, Verlag Technik, (1998)

[12] L. Néel and N. Kurti, *The Selected Works of Louis Neel*, Gordon & Breach Publishing Group, (1984)

[13] L. Reimer and G. Pfefferkorn, *Raster-Elektronenmikroskopie*, 2. neubearb. und erw. aufl. ed., Springer-Verlag, Berlin, (1977)

Articles

[14] A. Ahniyaz, Y. Sakamoto, and L. Bergström, *Magnetic field-induced assembly of oriented superlattices from maghemite nanocubes*, Proceedings of the National Academy of Sciences **104** (2007), no. 45, 17570–17574

[15] A. Ahniyaz, G. A. Seisenbaeva, L. Häggström, S. Kamali, V. G. Kessler, P. Nordblad, C. Johansson, and L. Bergström, *Preparation of iron oxide nanocrystals by surfactant-free or oleic acid-assisted thermal decomposition of a Fe(III) alkoxide*, Journal of Magnetism and Magnetic Materials **320** (2008), no. 6, 781–787

[16] S. J. Andrews, J. E. Hails, M. M. Harding, and D. W. J. Cruickshank, *The mosaic spread of very small crystals deduced from Laue diffraction patterns*, Acta Crystallographica Section A **43** (1987), no. 1, 70–73

[17] S. J. Andrews, M. Z. Papiz, R. McMeeking, A. J. Blake, B. M. Lowe, K. R. Franklin, J. R. Helliwell, and M. M. Harding, *Piperazine silicate (EU 19): the structure of a very small crystal determined with synchrotron radiation*, Acta Crystallographica Section B **44** (1988), no. 1, 73–77

[18] M. N. Baibich, J. M. Broto, A. Fert, F. N. Van Dau, F. Petroff, P. Etienne, G. Creuzet, A. Friederich, and J. Chazelas, *Giant Magnetoresistance of (001)Fe/(001)Cr Magnetic Superlattices*, Phys. Rev. Lett. **61** (1988), no. 21, 2472–2475

[19] E. Bauer, *Phänomenologische Theorie der Kristallabscheidung an Oberflächen. I*, Zeitschrift für Kristallographie - Crystalline Materials **110** (1958), no. 1-6, 372–394

[20] S. Bedanta and W. Kleemann, *Supermagnetism*, Journal of Physics D: Applied Physics **42** (2009), no. 1, 013001

[21] K. Bian, J. J. Choi, A. Kaushik, P. Clancy, D.-M. Smilgies, and T. Hanrath, *Shape-Anisotropy Driven Symmetry Transformations in Nanocrystal Superlattice Polymorphs*, ACS Nano **5** (2011), no. 4, 2815–2823

[22] T. P. Bigioni, X.-M. Lin, T. T. Nguyen, E. I. Corwin, T. A. Witten, and H. M. Jaeger, *Kinetically driven self assembly of highly ordered nanoparticle monolayers*, Nat Mater **5** (2006), no. 4, 265–270

[23] G. Binasch, P. Grünberg, F. Saurenbach, and W. Zinn, *Enhanced magnetoresistance in layered magnetic structures with antiferromagnetic interlayer exchange*, Phys. Rev. B **39** (1989), no. 7, 4828–4830

[24] K. J. M. Bishop, C. E. Wilmer, S. Soh, and B. A. Grzybowski, *Nanoscale Forces and Their Uses in Self-Assembly*, Small **5** (2009), no. 14, 1600–1630

[25] M. Bjorck and G. Andersson, *GenX: an extensible X-ray reflectivity refinement program utilizing differential evolution*, Journal of Applied Crystallography **40** (2007), no. 6, 1174–1178

[26] P. G. Bolhuis, D. Frenkel, S.-C. Mau, and D. A. Huse, *Entropy difference between crystal phases*, Nature **388** (1997), no. 6639, 235–236

[27] P. Busch, M. Rauscher, D.-M. Smilgies, D. Posselt, and C. M. Papadakis, *Grazing-incidence small-angle X-ray scattering from thin polymer films with lamellar structures - the scattering cross section in the distorted-wave Born approximation*, Journal of Applied Crystallography **39** (2006), no. 3, 433–442

[28] M. J. Campolongo, S. J. Tan, D.-M. Smilgies, M. Zhao, Y. Chen, I. Xhangolli, W. Cheng, and D. Luo, *Crystalline Gibbs Monolayers of DNA-Capped Nanoparticles at the Air-Liquid Interface*, ACS Nano **5** (2011), no. 10, 7978–7985

[29] J. J. Choi, K. Bian, W. J. Baumgardner, D.-M. Smilgies, and T. Hanrath, *Interface-Induced Nucleation, Orientational Alignment and Symmetry Transformations in Nanocube Superlattices*, Nano Lett. **12** (2012), no. 9, 4791–4798

[30] D. K. G. de Boer, *X-ray reflection and transmission by rough surfaces*, Phys. Rev. B **51** (1995), no. 8, 5297–5305

[31] R. D. Deegan, *Pattern formation in drying drops*, Phys. Rev. E **61** (2000), no. 1, 475–485

[32] R. D. Deegan, O. Bakajin, T. F. Dupont, G. Huber, S. R. Nagel, and T. A. Witten, *Capillary flowasthe cause of ring stains fromdried liquid drops*, NATURE **VOL 389** (1997)

[33] S. Disch, E. Wetterskog, R. P. Hermann, G. Salazar-Alvarez, P. Busch, T. Bruckel, L. Bergstrom, and S. Kamali, *Shape Induced Symmetry in Self-Assembled Mesocrystals of Iron Oxide Nanocubes*, Nano Letters **11** (2011), no. 4, 1651–1656

[34] S. Disch, E. Wetterskog, R. P. Hermann, A. Wiedenmann, U. Vainio, G. Salazar-Alvarez, L. Bergström, and T. Brückel, *Quantitative spatial magnetization distribution in iron oxide nanocubes and nanospheres by polarized small-angle neutron scattering*, New Journal of Physics **14** (2012), no. 1, 013025

[35] S. Disch, E. Wetterskog, R. P. Hermann, D. Korolkov, P. Busch, P. Boesecke, O. Lyon, U. Vainio, G. Salazar-Alvarez, L. Bergstrom, and T. Bruckel, *Structural diversity in iron oxide nanoparticle assemblies as directed by particle morphology and orientation*, Nanoscale (2013)

[36] A. Dong, J. Chen, P. M. Vora, J. M. Kikkawa, and C. B. Murray, *Binary nanocrystal superlattice membranes self-assembled at the liquid-air interface*, Nature **466** (2010), no. 7305, 474–477

[37] W. Dong, X. Li, L. Shang, Y. Zheng, G. Wang, and C. Li, *Controlled synthesis and self-assembly of dendrite patterns of Fe 3 O 4 nanoparticles*, Nanotechnology **20** (2009), no. 3, 035601

[38] D. Dunphy, H. Fan, X. Li, J. Wang, and C. J. Brinker, *Dynamic Investigation of Gold Nanocrystal Assembly Using In Situ Grazing-Incidence Small-Angle X-ray Scattering*, Langmuir **24** (2008), no. 19, 10575–10578

[39] M. Eckert, *Disputed discovery: the beginnings of X-ray diffraction in crystals in 1912 and its repercussions*, Acta Cryst. A **68** (2012), no. 1, 30–39

[40] A. Einstein, *Über die von der molekularkinetischen Theorie der Wärme geforderte Bewegung von in ruhenden Flüssigkeiten suspendierten Teilchen*, Ann. Phys. **322** (1905), no. 8, 549–560

[41] P. C. Fannin and S. W. Charles, *The study of a ferrofluid exhibiting both Brownian and Neel relaxation*, Journal of Physics D: Applied Physics **22** (1989), no. 1, 187–

[42] B. Faure, G. Salazar-Alvarez, and L. Bergstroöm, *Hamaker Constants of Iron Oxide Nanoparticles*, Langmuir **27** (2011), no. 14, 8659–8664

[43] F. M. Fowkes, Y. C. Huang, B. A. Shah, M. J. Kulp, and T. B. Lloyd, *Surface and colloid chemical studies of gamma iron oxides for magnetic memory media*, Colloids and surfaces **29** (1988), no. 3, 243–261

[44] A. Gabriel, *Position sensitive x-ray detector*, Rev. Sci. Instrum. **48** (1977), no. 10, 1303–1305

[45] R. Ganapathy, M. R. Buckley, S. J. Gerbode, and I. Cohen, *Direct Measurements of Island Growth and Step-Edge Barriers in Colloidal Epitaxy*, Science **327** (2010), no. 5964, 445–448

[46] S. C. Glotzer and M. J. Solomon, *Anisotropy of building blocks and their assembly into complex structures*, Nat Mater **6** (2007), no. 7, 557–562

[47] M. Gonuguntla and A. Sharma, *Polymer Patterns in Evaporating Droplets on Dissolving Substrates*, Langmuir **20** (2004), no. 8, 3456–3463

[48] Harding and M., *Recording Diffraction Data for Structure Determination for Very Small Crystals*, Journal of Synchrotron Radiation **3** (1996), no. 6, 250–259

[49] J. He, R. Tangirala, T. Emrick, T. P. Russell, A. Böker, X. Li, and J. Wang, *Self-Assembly of Nanoparticle-Copolymer Mixtures: A Kinetic Point of View*, Adv. Mater. **19** (2007), no. 3, 381–385

[50] S. Heitkam, W. Drenckhan, and J. Fröhlich, *Packing Spheres Tightly: Influence of Mechanical Stability on Close-Packed Sphere Structures*, Phys. Rev. Lett. **108** (2012), no. 14, 148302

[51] S. Hosur, L. Naik, and N. Badiger, *Study of the real part (f') of anomalous scattering factors for the elements of atomic number from Z = 64 to 73 using HPGe detector*, **128** (2013), no. 5, 1–9

[52] L. Häggström, S. Kamali, T. Ericsson, P. Nordblad, A. Ahniyaz, and L. Bergström, *Mössbauer and magnetization studies of iron oxide nanocrystals*, **183** (2008), no. 1-3, 49–53

[53] Z. Jiang, X.-M. Lin, M. Sprung, S. Narayanan, and J. Wang, *Capturing the Crystalline Phase of Two-Dimensional Nanocrystal Superlattices in Action*, Nano Lett. **10** (2010), no. 3, 799–803

[54] T. Junno, K. Deppert, L. Montelius, and L. Samuelson, *Controlled manipulation of nanoparticles with an atomic force microscope*, Appl. Phys. Lett. **66** (1995), no. 26, 3627–3629

[55] S. Kamali, M. Itou, A. Kodama, P. Stroeve, and Y. Sakurai, *Orientational order of self-assembled magnetic nanocrystals*, Phys. Rev. B **85** (2012), no. 2, 024506–

[56] J. C. Kendrew, G. Bodo, H. M. Dintzis, R. G. Parrish, H. Wyckoff, and D. C. Phillips, *A Three-Dimensional Model of the Myoglobin Molecule Obtained by X-Ray Analysis*, Nature **181** (1958), no. 4610, 662–666

[57] H. Kubbinga, *Crystallography from Haüy to Laue: controversies on the molecular and atomistic nature of solids*, Acta Cryst. A **68** (2012), no. 1, 3–29

[58] Y. Lalatonne, J. Richardi, and M. P. Pileni, *Van der Waals versus dipolar forces controlling mesoscopic organizations of magnetic nanocrystals*, Nat Mater **3** (2004), no. 2, 121–125

[59] B. Lengeler, C. G. Schroer, B. Benner, A. Gerhardus, T. F. Gunzler, M. Kuhlmann, J. Meyer, and C. Zimprich, *Parabolic refractive X-ray lenses*, Journal of Synchrotron Radiation **9** (2002), no. 3, 119–124

[60] X. Lin, C. Sorensen, and K. Klabunde, *Digestive Ripening, Nanophase Segregation and Superlattice Formation in Gold Nanocrystal Colloids*, **2** (2000), no. 2, 157–164

[61] F. C. Meldrum and H. Coelfen, *Controlling mineral morphologies and structures in biological and synthetic systems*, ChemInform **40** (2009), no. 5

[62] N. C. Miller, E. Cho, M. J. N. Junk, R. Gysel, C. Risko, D. Kim, S. Sweetnam, C. E. Miller, L. J. Richter, R. J. Kline, M. Heeney, I. McCulloch, A. Amassian, D. Acevedo-Feliz, C. Knox, M. R. Hansen, D. Dudenko, B. F. Chmelka, M. F. Toney, J.-L. Brédas, and M. D. McGehee, *Use of X-Ray Diffraction, Molecular Simulations, and Spectroscopy to Determine the Molecular Packing in a Polymer-Fullerene Bimolecular Crystal*, Adv. Mater. **24** (2012), no. 45, 6071–6079

[63] A. Moser, K. Takano, D. T. Margulies, M. Albrecht, Y. Sonobe, Y. Ikeda, S. Sun, and E. E. Fullerton, *Magnetic recording: advancing into the future*, Journal of Physics D: Applied Physics **35** (2002), no. 19, R157

[64] S. Murthy, Z. Wang, and R. Whetten, *Thin films of thiol-derivatized gold nanocrystals*, Philosophical Magazine Letters **75** (1997), no. 5, 321–328

[65] S. Narayanan, J. Wang, and X.-M. Lin, *Dynamical Self-Assembly of Nanocrystal Superlattices during Colloidal Droplet Evaporation by in situ Small Angle X-Ray Scattering*, Phys. Rev. Lett. **93** (2004), no. 13, 135503

[66] L. Néel, *Théorie du traînage magnétique des ferromagnétiques en grains fins avec applications aux terres cuites*, Annales de Géophysique **5** (1949), 99–136

[67] P. C. Ohara, D. V. Leff, J. R. Heath, and W. M. Gelbart, *Crystallization of Opals from Polydisperse Nanoparticles*, Phys. Rev. Lett. **75** (1995), no. 19, 3466–3469

[68] J. Park, K. An, Y. Hwang, J.-G. Park, H.-J. Noh, J.-Y. Kim, J.-H. Park, N.-M. Hwang, and T. Hyeon, *Ultra-large-scale syntheses of monodisperse nanocrystals*, Nat Mater **3** (2004), no. 12, 891–895

[69] L. G. Parratt, *Surface Studies of Solids by Total Reflection of X-Rays*, Phys. Rev. **95** (1954), no. 2, 359–369

[70] J. S. Pedersen, *Determination of size distribution from small-angle scattering data for systems with effective hard-sphere interactions*, Journal of Applied Crystallography **27** (1994), no. 4, 595–608

[71] J. S. Pedersen, *Analysis of small-angle scattering data from colloids and polymer solutions: modeling and least-squares fitting*, Advances in Colloid and Interface Science **70** (1997), no. 0, 171–210

[72] V. Petkov, P. D. Cozzoli, R. Buonsanti, R. Cingolani, and Y. Ren, *Size, Shape, and Internal Atomic Ordering of Nanocrystals by Atomic Pair Distribution Functions: A Comparative Study of gamma-Fe2O3 Nanosized Spheres and Tetrapods*, Journal of the American Chemical Society **131** (2009), no. 40, 14264

[73] M. P. Pileni, *Nanocrystal Self-Assemblies: Fabrication and Collective Properties*, J. Phys. Chem. B **105** (2001), no. 17, 3358–3371

[74] F. X. Redl, K.-S. Cho, C. B. Murray, and S. O'Brien, *Three-dimensional binary superlattices of magnetic nanocrystals and semiconductor quantum dots*, Nature **423** (2003), no. 6943, 968–971

[75] G. Renaud, R. Lazzari, C. Revenant, A. Barbier, M. Noblet, O. Ulrich, F. Leroy, J. Jupille, Y. Borensztein, C. R. Henry, J.-P. Deville, F. Scheurer, J. Mane-Mane, and O. Fruchart, *Real-Time Monitoring of Growing Nanoparticles*, Science **300** (2003), no. 5624, 1416–1419

[76] S. V. Roth, T. Autenrieth, G. Grubel, C. Riekel, M. Burghammer, R. Hengstler, L. Schulz, and P. Muller-Buschbaum, *In situ observation of nanoparticle ordering at the air-water-substrate boundary in colloidal solutions using x-ray nanobeams*, Appl. Phys. Lett. **91** (2007), no. 9, 091915–3

[77] G. Scapin, *Structural biology and drug discovery*, Current Pharmaceutical Design **12** (2006), no. 17, 2087–2097

[78] W. W. Schmahl and W. Steurer, *Laue centennial*, Acta Cryst. A **68** (2012), no. 1, 1–2

[79] D. Schwarzenbach, *The success story of crystallography*, Acta Cryst. A **68** (2012), no. 1, 57–67

[80] O. H. Seeck, C. Deiter, K. Pflaum, F. Bertam, A. Beerlink, H. Franz, J. Horbach, H. Schulte-Schrepping, B. M. Murphy, M. Greve, and O. Magnussen, *The high-resolution diffraction beamline P08 at PETRA III*, Journal of Synchrotron Radiation **19** (2012), no. 1, 30–38

[81] E. V. Shevchenko, D. V. Talapin, N. A. Kotov, S. O'Brien, and C. B. Murray, *Structural diversity in binary nanoparticle superlattices*, Nature **439** (2006), no. 7072, 55–59

[82] P. Siffalovic, E. Majkova, L. Chitu, M. Jergel, S. Luby, I. Capek, A. Satka, A. Timmann, and S. V. Roth, *Real-Time Tracking of Superparamagnetic Nanoparticle Self-Assembly*, Small **4** (2008), no. 12, 2222–2228

[83] P. Siffalovic, E. Majkova, L. Chitu, M. Jergel, S. Luby, A. Satka, and S. V. Roth, *Self-assembly of iron oxide nanoparticles studied by time-resolved grazing-incidence small-angle x-ray scattering*, Phys. Rev. B **76** (2007), no. 19, 195432

[84] S. Singamaneni and V. Bliznyuk, *Fabrication of Ni nanoparticles and their size-selective self-assembly into chains under external magnetic field*, Appl. Phys. Lett. **87** (2005), no. 16, 162511–3

[85] D. M. Smilgies, *Geometry-independent intensity correction factors for grazing-incidence diffraction*, Review of Scientific Instruments **73** (2002), no. 4, 1706–1710

[86] Q. Song, Y. Ding, Z. L. Wang, and Z. J. Zhang, *Formation of Orientation-Ordered Superlattices of Magnetite Magnetic Nanocrystals from Shape-Segregated Self-Assemblies*†, J. Phys. Chem. B **110** (2006), no. 50, 25547–25550

[87] E. C. Stoner and E. P. Wohlfarth, *A Mechanism of Magnetic Hysteresis in Heterogeneous Alloys*, Philosophical Transactions of the Royal Society of London. Series A, Mathematical and Physical Sciences **240** (1948), no. 826, 599–642

[88] H. Sun, H. Wei, H. Zhang, Y. Ning, Y. Tang, F. Zhai, and B. Yang, *Self-Assembly of CdTe Nanoparticles into Dendrite Structure: A Microsensor to Hg2+*, Langmuir **27** (2010), no. 3, 1136–1142

[89] S. Sun, C. B. Murray, D. Weller, L. Folks, and A. Moser, *Monodisperse FePt Nanoparticles and Ferromagnetic FePt Nanocrystal Superlattices*, Science **287** (2000), no. 5460, 1989–1992

[90] J. R. Thomas, *Preparation and Magnetic Properties of Colloidal Cobalt Particles*, J. Appl. Phys. **37** (1966), no. 7, 2914–2915

[91] J. V. I. Timonen, M. Latikka, L. Leibler, R. H. A. Ras, and O. Ikkala, *Switchable Static and Dynamic Self-Assembly of Magnetic Droplets on Superhydrophobic Surfaces*, Science **341** (2013), no. 6143, 253–257

[92] K. Vegso, P. Siffalovic, E. Majkova, M. Jergel, M. Benkovicova, T. Kocsis, M. Weis, S. Luby, K. Nygård, and O. Konovalov, *Nonequilibrium Phases of Nanoparticle Langmuir Films*, Langmuir **28** (2012), no. 28, 10409–10414

[93] K. Vegso, P. Siffalovic, M. Weis, M. Jergel, M. Benkovicova, E. Majkova, L. Chitu, Y. Halahovets, S. Luby, I. Capek, and A. Satka, *In situ GISAXS monitoring of Langmuir nanoparticle multilayer degradation processes induced by UV photolysis*, Phys. Status Solidi A **208** (2011), no. 11, 2629–2634

[94] G. M. Whitesides and B. Grzybowski, *Self-Assembly at All Scales*, Science **295** (2002), no. 5564, 2418–2421

[95] L. V. Woodcock, *Entropy difference between the face-centred cubic and hexagonal close-packed crystal structures*, Nature **385** (1997), no. 6612, 141–143

[96] K. W. Yung, P. B. Landecker, and D. D. Villani, *An Analytic Solution for the Force Between Two Magnetic Dipoles*, Magnetic and Electrical Separation **9** (1998), no. 1, 39–52

[97] E.-Y. Zhang and C.-R. Wang, *Fullerene self-assembly and supramolecular nanostructures*, Current Opinion in Colloid & Interface Science **14** (2009), no. 2, 148–156

[98] J. Zhang, Z. Luo, B. Martens, Z. Quan, A. Kumbhar, N. Porter, Y. Wang, D.-M. Smilgies, and J. Fang, *Reversible Kirkwood-Alder Transition Observed in Pt3Cu2 Nanoctahedron Assemblies under Controlled Solvent Annealing/Drying Conditions*, J. Am. Chem. Soc. **134** (2012), no. 34, 14043–14049

[99] R. K. Zheng, H. Gu, B. Xu, K. K. Fung, X. X. Zhang, and S. P. Ringer, *Self-Assembly and Self-Orientation of Truncated Octahedral Magnetite Nanocrystals*, Adv. Mater. **18** (2006), no. 18, 2418–2421

Other Publications

[100] Agilent Technologies, *AFM Almanac - Imaging Modes*, http://www.home.agilent.com/upload/cmc_upload/All/AFMAlmanac_010510a.pdf?&cc=DE&lc=ger

[101] Agilent Technologies, *Agilent 5400 AFM/SPM - Data Sheet*, (2007), http://www-omcs.materials.ox.ac.uk/uploads/AGILENT%205400%20tech%20sheet.pdf

[102] Bruker AXS GmbH, *NANO STAR - Small Angle X-ray Scattering Solutions*, (2010), http://www.bruker.com/fileadmin/user_upload/8-PDF-Docs/X-rayDiffraction_ElementalAnalysis/XRD/Brochures/NANOSTAR_DOC-B88-EXS011_low.pdf

[103] S. Disch, *The spin structure of magnetic nanoparticles and in magnetic nanostructures*, Ph.D. thesis, RWTH Aachen University, (2010)

[104] FEI, *MagellanTM XHR SEM*, (2009), http://www.fei.com/uploadedFiles/DocumentsPrivate/Content/magellan_ds.pdf

[105] FEI, *An introduction to electron microscopy*, (2010), http://www.fei.com/uploadedFiles/Documents/Content/Introduction_to_EM_booklet_July_10.pdf

[106] GPS Division Analytical Facility, *ZEISS 1550VP Field Emission SEM - Imaging capabilities discription*, http://www.gps.caltech.edu/facilities/analytical/sem.html

[107] S. P. Gubin, *Introduction*, Magnetic Nanoparticles, Wiley-VCH Verlag GmbH & Co. KGaA, (2009), pp. 1–23

[108] G. B. Khomutov and Y. A. Koksharov, *Organized Ensembles of Magnetic Nanoparticles: Preparation, Structure, and Properties*, Magnetic Nanoparticles, Wiley-VCH Verlag GmbH & Co. KGaA, (2009), pp. 117–195

[109] J. P., *X-ray Data Collection Course*, (2006), http://xray0.princeton.edu/ phil/Facility/Guides/XrayDataCollection.html

[110] W. Schweika, *X-ray and neutron diffraction*, Electronic Oxides (S. Blügel, T. Brückel, R. Waser, and C. M. Schneider, eds.), Forschungszentrum Jülich GmbH, (2010)

[111] synchrotron ESRF, *ID01 - Microdiffraction imaging - beamline homepage*, http://www.esrf.eu/UsersAndScience/Experiments/StructMaterials/ID01

[112] synchrotron Soleil, *SWING beamline - homepage*, http://www.synchrotron-soleil.fr/portal/page/portal/Recherche/LignesLumiere/SWING

Appendix D

List of Figures

Appendix E

List of Tables

Appendix F

List of Symbols, Abbreviations and Definitions

F.1 Symbols

	Mathematic Symbols
δ	delta-distribution
∂	partial derivative
Δx	difference of $x_2 - x_1$
$\vec{v}$	vector
$\hat{e}_v$	unit vector parallel to $\vec{v}$
$a \circledast b$	convolution of a and b
$\mathfrak{F}(f)$	Fourier transform of function f
$\mathfrak{F}^{-1}(F)$	Fourier back transform
	Physical Nomenclature
a	average in-plane lattice constant of the nanoparticle superstructure from an ensemble of mesocrystals
A	magnetic exchange constant
a_{DW}	mean squared displacement of the lattice position by the Debye-Waller factor term
a_{NP}	edge length of a cubic nanoparticle
c	average out-of-plane lattice constant of the nanoparticle superstructure from an ensemble of mesocrystals

	Physical Nomenclature (continued)
D	diffusion coefficient
$f(\vec{Q})$	atomic form factor
$F_{NP}^{Shape}(\vec{Q})$	nanoparticle form factor for different shapes (spheres, T-Cubes or R-Cubes)
$H_{\perp}$	low magnetic field with field gradient pointing away from the substrate
H_{γ}	low magnetic field with field gradient pointing to the substrate
$H_{\succeq}$	low magnetic field with field gradient pointing in an in-plane direction of the substrate
$H_{\underline{\perp}}$	strong magnetic field with field gradient pointing away from the substrate
$H_{\underline{\gamma}}$	strong magnetic field with field gradient pointing to the substrate
$H_{\underline{\succeq}}$	strong magnetic field with field gradient pointing in an in-plane direction of the substrate
h	height of the droplet measured by the light-band micrometer
H	external applied field
hkl	Miller indices
$H_{\underline{\rightrightarrows}}$	homogeneous magnetic field in in-plane direction to the substrate
$H_{\underline{\uparrow\uparrow}}$	homogeneous magnetic field in out-of-plane direction to the substrate
I	measured scattering intensity
K	uniaxial anisotropy constant
$\vec{k}_{i/f}$	incident and outgoing wave vector with $k = \frac{2\pi}{\lambda}$
k_B	Boltzmann constant
L(x)	Langevin function
m	magnetic moment of a nanoparticle
M(H)	average magnetic moment of a sample
M_s	saturation magnetization
n	natural number $\mathbb{N}$, refractive index
N_A	Avogadro constant ($6,02214129 \cdot 10^{23}$ mol^{-1})
N_L	number of repetitions of the unit cell by a Laue function
N_{NP}	number of nanoparticles in the sample
P_{MC}	parameter determined from the single mesocrystal diffraction experiment
$\vec{Q} = \vec{k}_f - \vec{k}_i$	scattering vector
$Q_{x/y/z}$	x/y/z component of the scattering vector
R	ideal gas constant ($= N_A \cdot k_B = 8.3144621 \frac{J}{mol\,K}$)
$\vec{r}$	real space vector
r_c	critical radius below particles act as a single domain particle
r_e	classical electron radius ($2.81 \cdot 10^{-15}$ m)
r_{NP}	average radius of a spherical nanoparticle determined from a solution by SAXS
r_{shell}	average radius of the organic shell thickness determined from a solution by SAXS and SANS
$S(\vec{Q})$	structure factor
t	time
T	temperature

	Physical Nomenclature (continued)
T_B	blocking temperature
t_0	starting time of the nucleation
V	particle volume
$V(\vec{r})$	scattering potential
x_{MC}	parameter x measured at a single mesocrystal (MC)
$\alpha_{\mathrm{i/f/c}}$	incident/outgoing/critical angle
γ	half-width at half-maximum (HWHM) of the Lorentz function, natural linewidth of an ensemble of mesocrystals
$\gamma_{y/z}$	in-plane/out-of-plane mesocrystal half-width at half-maximum
$\varepsilon_{\mathrm{y/z}}$	in-plane/out-of-plane mesocrystal correlation length averaged over the ensemble statistic
η	friction coefficient
λ	wavelength
μ	absorption length
μ_0	vacuum permeability
ρ	density
σ	depending on context: standard deviation describing a Gaussian distributed variation or scattering cross-section
$\sigma_{\mathrm{a_{NP}/r_{NP}}}$	standard deviation describing a Gaussian distributed variation of the edge length of a cubic/ radius of a spherical nanoparticle
$\sigma_{\mathrm{c_{MC}}}$	standard deviation describing a Gaussian distributed variation of the lattice parameter c in a single mesocrystal
$\sigma_{\mathrm{N_L}}$	standard deviation describing a Gaussian distributed variation of the number of repetitions of the unit cell in one mesocrystal
$\sigma_{\mathrm{r/t}}$	standard deviation describing a random variation of the mesocrystal lattice parameters/ a Gaussian distributed tilting of the c-axis away from the substrate surface (ensemble of mesocrystals)
τ	degree of truncation
τ_0	characteristic attempt time
τ_m	time scale of the experiment
τ_N	Néel relaxation time
$\tau_{\mathrm{Round/Trunc}}$	degree of truncation for the rounded/truncated cube model
$[\mathrm{uvw}]$	specific direction in a lattice
(hkl)	specific plane in a lattice
$\langle \mathrm{x} \rangle$	mean value x
Ψ	wave function

	Sample Emblems
M_S^I	single mesocrystal with spherical building blocks
M_C^I	single mesocrystal with cubic building blocks
$S_S^{8.4}$	nanoparticle solution of spheres with a concentration of $8.4{\cdot}10^{14}$ NP/ml
$S_C^{8.4}$	nanoparticle solution of cubes with a concentration of $8.4{\cdot}10^{14}$ NP/ml
$D_{S,\,5.01}^{Lg1.68\perp 80}$	example for a sample with an ensemble of mesocrystals formed from spherical building blocks self-assembled under a magnetic field of 80 mT and gradient up

F.2 Abbreviations

	Instruments
D8	Bruker laboratory x-ray reflectometer (in house)
ID01	X-ray diffraction and scattering beamline for coherent x-ray diffraction, SAXS and GISAXS experiments at the ESRF synchrotron in Grenoble, France
MARIA	Magnetic reflectometer with high incident angle for polarized neutron reflectometry and GISANS at the MLZ neutron center in Garching, Germany
P08	High resolution diffraction beamline at the PETRAIII synchrotron in Hamburg, Germany
SWING	X-ray diffraction and scattering beamline for SAXS and GISAXS experiments at the SOLEIL synchrotron in Saclay, France
4-circle	Huber laboratory 4-circle diffractometer (in house)

	Methods
AFM	Atomic force microscope
FIB	Focused ion beam
GISANS	Grazing incidence small angle neutron scattering
GISAXS	Grazing incidence small angle x-ray scattering
HRTEM	High resolution transmission electron microscopy
SANS	Small angle neutron scattering
SAXS	Small angle x-ray scattering
SEAD	Selected area (electron) diffraction
SEM	Scanning electron microscopy
TEM	Transmission electron microscopy
XRD	X-ray diffraction
XRR	X-ray reflectometry

	Materials
Co	cobalt
Cu	copper
Fe	iron
NaI	sodium iodide
Pt	platinum
Si	silicon
γ-Fe_2O_3	Maghemite
	Abbreviations for theory
BA	Born Approximation
DWBA	distorted wave Born approximation
FF	form factor
SF	structure factor
SLD	scattering length density
vdW	van der Waals
	General abbreviations
bct	body-centered tetragonal
BG	background
BSE	backscattered electrons
ETD	Everhart Thornley detector
fcc	face-centered cubic
FT	Fourier transform
hcp	hexagonal close-packed
HWHM	half-width at half maximum
ICSD	Inorganic Crystal Structure Database
LBM	light-band micrometer
MC	single mesocrystal
N_L	number of repetitions of the unit cell/oscillations for the Laue function
NP	nanoparticle
SD	standard deviation
SE	secondary electrons
TLD	through the lens detector
TPCL	triple phase contact line
vCD	low-voltage high-contrast solid state detector

F.3 Definitions

truncation	general term for "truncation" of the edges by cubic particles
nanocrystal	other word for single crystalline nanoparticle
nanoparticle structure	atomic crystal structure of one single nanoparticle
mesocrystal	3 dimensionally highly ordered ensemble of nanoparticles
mesocrystal structure	supercrystal structure or nanoparticle superstructure inside one mesocrystal
rounded	spherical truncation by cubic particles
single mesocrystal	one mesocrystal isolated from an ensemble of mesocrystals
truncated	flat truncation by cubic particles
2D powder	sample with arbitrary orientated in-plane crystals, but with a preferred c-direction

Acknowledgement

Ganz zum Schluss möchte ich mich ganz herzlich bei allen Leuten bedanken, die mich im Laufe der Dissertation begleitet, in jeder Hinsicht tatkräftig unterstützt und ohne die eine solche Arbeit gar nicht möglich gewesen wäre.

Prof. Thomas Brückel danke ich ganz besonders für die Möglichkeit der Promotion in seiner Arbeitsgruppe. Exzellente Forschungsbedingungen haben mir viele Möglichkeiten eröffnet. Mein besonderer Dank gilt ihm für die detaillierten Anmerkungen zur vorliegenden Dissertation.

Prof. Uwe Klemradt danke ich für die Übernahme der Zweitkorrektur.

Ulrich Rücker danke ich herzlich für wissenschaftliche Betreuung und Unterstützung während meiner Doktorandenzeit. Zu ihm konnte ich mit allen Fragen kommen und speziell im Experimentellen hat Ulrich fast immer Recht.

Artur Glavic, Gennady Pospelov, Walter van Herck und Joachim Wuttke danke ich für die tolle Zusammenarbeit im Bereich der Programmierung der Streusimulationen.

Prof. Lennart Bergström, Erik Wetterskog and German Salazar-Alvarez I would like to thank for providing high quality nanoparticles for this PhD thesis.

Doris Meertens und Andras Kovacs für die herzliche Aufnahme ins ERZ und die stetige Unterstützung bei der FIB Präparation und den TEM Aufnahmen. Zusätzlich möchte ich **Prof. Rafal E. Dunin-Borkowski** danken, der diese Zusammenarbeit erst möglich gemacht hat.

Elke Brauweiler-Reuters und Hans Peter Bochem für eine tolle Zusammenarbeit und die stetige, schnelle Unterstützung bei den SEM-Aufnahmen.

Frank Gossen, der mich bei bei den verschiedensten Angelegenheiten, als auch beim Bau komplexer Versuchsaufbauten immer unterstützt hat.

I would like to thank all instrument scientists at various facilities for their help and assistance at our beamtimes:

Stefan Mattauch danke ich für die tolle Betreuung und Hilfe bei der Durchführung der Neutronenstreuexperimente am TREFF und MARIA. Natürlich nicht zu vergessen **Harald Schneider**, der immer eine exzellente Probenumgebung zur Verfügung gestellt hat.

Eugen Weschke and Enrico Schierle für die Betreuung bei der Soft X-ray Messzeit an BESSY.

Valeria Lauter for the scientific support during and after the neutron beamtime at the SNS.

Jens Wenzel Andreasen for the possiblity to measure at a brilliant GISAXS lab-source in Risø, even within only a few days notice.

Florian Meneau for the scientific support during the GISAXS beamtime in Soleil.

Peter Boesecke und Tobias Schulli für die hervorragende Unterstützung bei dem in-situ Experiment an der ESRF.

Oliver Seeck für die Unterstützung bei dem aufwendigen Single-Mesokristall-Experiment an Petra III.

Natürlich finden solche Messzeiten nicht ohne Unterstützung von Kollegen statt. Danke an **Manuel Angst, Paul Zakalek, Artur Glavic, Artem Feoktystov, Zhendong Fu, Denis Korolokov, Raphaël P. Hermann, Subhankar Bedanta und Alice Klapper** für die tolle Unterstützung auf den jeweiligen Messzeiten.

Ich möchte mich bei allen Mitarbeitern des Instituts für Streumethoden für die freundschaftliche Aufnahme, die angenehme Arbeitsatmosphäre und die große Hilfsbereitschaft bedanken, die mir in den letzten Jahren zuteil wurde. Insbesondere danke ich Barbara Köppchen für die große Hilfe bei allen organisatorischen Fragen und beim IT-Team, Josef Heinen, Guido Vehres und Christel Horriar-Esser für die stetige Hilfe bei verschiedensten MAC Problemchen. Claire Ryalls danke ich für das sprachliche Korrekturlesen von Einleitung und Zusammenfassung. Weiterhin gilt mein Dank den Werkstättenteams (Glasbläserei und IFF) . Meinen Zimmerkollegen auch den besten Dank, für die vielen netten und aufheiternden Stunden, die wir gemeinsam im Büro verbracht haben. Zudem möchte ich noch Rainer Link danken, der mich im gesamten Zeitraum meiner Dotorarbeit moralisch unterstützt hat und viele gute Anregungen eingebracht hat. Zu guter Letzt möchte ich meinem Freund und meinen Eltern danken, die immer für mich da waren und sind.

Band / Volume 98
Cryogenic Break-Junction Characterization of Single Organic Molecules
T. Grellmann (2014), VI, 86 pp
ISBN: 978-3-95806-015-9

Band / Volume 99
Interacting Interactions: A Study on the Interplay of Molecule-Molecule and Molecule-Substrate Interactions at Metal-Organic Interfaces
M. Willenbockel (2014), IX, 245 pp
ISBN: 978-3-95806-018-0

Band / Volume 100
Microwire crossbar arrays for chemical, mechanical, and thermal stimulation of cells
P. Rinklin (2015), xii, 184 pp
ISBN: 978-3-95806-022-7

Band / Volume 101
Modification and characterization of potential bioelectronic interfaces
K. Greben (2015), 76 pp
ISBN: 978-3-95806-028-9

Band / Volume 102
Extending the precision and efficiency of the all-electron full-potential linearized augmented plane-wave density-functional theory method
G. Michalicek (2015), 195 pp
ISBN: 978-3-95806-031-9

Band / Volume 103
Metabolic engineering of *Escherichia coli* for the production of plant phenylpropanoid derived compounds
P. V. van Summeren-Wesenhagen (2015), V, 92 pp
ISBN: 978-3-95806-039-5

Band / Volume 104
Spin-reorientation transition in epitaxial Ni_xPd_{1-x} fims on Cu(001): a microscopic analysis
D. Gottlob (2015), x, 134 pp
ISBN: 978-3-95806-049-4

Band / Volume 105
Resonant Magnetic Scattering Studies using Synchrotron Radiation and Laser-Generated Extreme Ultraviolet Light
C. M. Weier (2015), vii, 143 pp
ISBN: 978-3-95806-052-4

Band / Volume 106
Neutron Scattering
Lectures of the JCNS Laboratory Course held at Forschungszentrum Jülich and at the Heinz-Maier-Leibnitz Zentrum Garching
edited by Th. Brückel, D. Richter, G. Roth, A. Wischnewski and R. Zorn (2015), ca 300 pp
ISBN: 978-3-95806-055-5

Band / Volume 107
Neutron Scattering
Experimental Manuals of the JCNS Laboratory Course held at Forschungszentrum Jülich and at the Heinz-Maier-Leibnitz Zentrum Garching
edited by Th. Brückel, D. Richter, G. Roth, A. Wischnewski and R. Zorn (2015), ca 150 pp
ISBN: 978-3-95806-056-2

Band / Volume 108
STM-based quantum transport through molecular wires
N. Fournier (2015), ix, 295 pp
ISBN: 978-3-95806-059-3

Band / Volume 109
Study on the electroforming and resistive switching behaviour of nickel oxide thin fims for non-volatile memory applications
R. Weng (2015), xxi, 159 pp
ISBN: 978-3-95806-062-3

Band / Volume 110
Microswimmers – From Single Particle Motion to Collective Behaviour
Lecture Notes of the DFG SPP Summer School 2015
edited by G. Gompper, C. Bechinger, S. Herminghaus, R. E. Isele-Holder, U.B. Kaupp, H. Löwen, H. Stark, R. G. Winkler (2015)
ISBN: 978-3-95806-083-8

Band / Volume 111
Long range order in 3D nanoparticle assemblies
E. Josten (2015), 238 pp
ISBN: 978-3-95806-087-6

Schlüsseltechnologien /
Key Technologies
Band / Volume 111
ISBN 978-3-95806-087-6